MODELLING AND PERFORMANCE EVALUATION OF COUPLED MICRO RESONATOR ARRAY FOR ARTIFICIAL NOSE

By

Nor Hayati Saad

A thesis submitted to
The University of Birmingham
for the degree of
DOCTOR OF PHILOSOPHY

School of Mechanical Engineering
The University of Birmingham
August 2010

ABSTRACT

This research presents a new sensor structure, the coupled micro resonator array (CMRA) as an approach to reduce the complexity of large artificial nose sensing system. The aim is to exploit multiple resonant sensors with a simplified readout. The CMRA working principle is based on mass loading frequency response effect; the frequency response of the coupled resonators is a signature for the multiple sensors.

The key research outputs are balanced effective mass of the coupled resonators for measurable response and broke the structure symmetry for unique frequency response pattern and stable structure eigenvectors to enhance the system odour discrimination.

To develop the CMRA, the structure is modelled and analysed using finite element and lumped mass analysis. Using silicon-on-insulator material, the CMRA is fabricated in order to evaluate the performance. The effect of mass loading is tested by platinum mass deposition using focused ion beam technology (FIB). The inverse eigenvalue analysis was used to estimate the mass change pattern of the CMRA structure. The research also investigates effect of the manufacturing variations on the CMRA structure performance.

With the finger print of the coupled frequency response, the output signal of N multiple resonant sensors is monitored by a single processor; hence, reducing the complexity of readout and signal processing system.

To my husband Abdul Rahim and
my daughters Nur Aisyah Damia and Nurin Safwani

ACKNOWLEDGEMENTS

It is a great pleasure to acknowledge all assistance and support that I directly or indirectly receive from individual or group of people throughout the whole of my research time until the completion of this research study.

This research work would not have been produced without my supervisor Michael CL Ward. I am very grateful and thankful for his enthusiastic support and guidance, for all research ideas, and for support in order for me to complete this research thesis. Many thanks as well to my second supervisor Raya K. Al-Dadah for her moral support when I started my research and until the research has been completed.

Special thank to Carl J. Anthony for his invaluable ideas, tips and support throughout my time in the clean room to fabricate the structure. Many thanks to my research colleague Xueyong Wei for his help in HF released process and platinum mass deposition using focused ion beam machine (FIB); thank you to David Chenelar for his help in gold metallization; Simon Pyatt (Physics Department) for structure wire bonding; Mike Lancaster and Donna Holdom (Electrical Engineering Department) in allowing me to use the wafer dicing saw machine; Paul Stanley and Morris Theresa (Metallurgy Department), and Hossein Ostadi for their help in using the scanning electron microscope.

I would like to specially thank Ross Turnbull, research colleague from Oxford University, who was responsible for the establishment of the electronic testing setup; other research fellow Bhaskar Choubey, and Steve Collins for their research knowledge and support. To thank to QinetiQ for the aluminium metallization, the Engineering and Physical Sciences Research Council (EPSRC) which indirectly or directly finance some of the research cost.

Thank you as well to other fellow researchers, Mi Yeon Song, Jason Teng, Martin J Prest and Peng Bao in sharing some research knowledge. Not to forget all research colleagues in Micro Technology Group, Emma Carter, Sam, Haseena, Ali, and Sahand who cheered up my time and shared their research ideas.

Thank you so much to all my family members, my husband Abdul Rahim, my mother Fatimah who supported me throughout my research time.

Finally, I would like to gratefully acknowledge the MARA University of Technology (UiTM) Shah Alam and the Malaysian Ministry of Higher Education for sponsoring my PhD study.

LIST OF PUBLICATION

1) Nor Hayati Saad, Michael C L Ward, Raya Al-Dadah, Carl Anthony, Bhaskar Choubey, and Steve Collins. Performance Analysis of A Coupled Micro Resonator Array Sensor. *Eurosensors XXII, Dresden, Germany, ISBN 978-3-00-025218-1*, pp. 60 – 63, 2008.

2) Nor Hayati Saad, Raya K. Al-Dadah, Carl J. Anthony, and Michael C.L. Ward. MEMS Mechanical Spring in Coupling and Synchronizing Coupled Micro resonator Array Sensor (Extended Abstract). *34th International Conference on Micro & Nano Engineering, Athens, Greece*, 2008.

3) Nor Hayati Saad, Raya K. Al-Dadah, Carl J. Anthony, and Michael C.L. Ward. Analysis of MEMS Mechanical Spring for Coupling Multimodal Micro Resonators Sensor. *Microelectronic Engineering*, 86(4-6):1190-1193, 2009.

4) Nor Hayati Saad, Xueyong Wei, Carl Anthony, Hossein Ostadi, Raya Al-Dadah, and Michael C.L. Ward. Impact of Manufacturing Variation on the performance of Coupled Micro Resonator Array for Mass Detection Sensor. *Eurosensors XXIII*, Switzerland; or *Procedia Chemistry*, 1(1): 831-834, 2009.

5) Nor Hayati Saad, Carl J. Anthony, Raya Al-Dadah, Michael C.L. Ward. Exploitation of Multiple Sensor Arrays in Electronic Nose. *2009 IEEE Sensors*, pp.1575-1579, 2009.

6) Nor Hayati Saad, Carl J. Anthony, Michael C.L. Ward, Bhaskar Choubey, Ross Turnbull, and Steve Collins. Manufacturing Variation in MEMS: Fabrication of Micro Array Resonators. *Second STIMESI Workshop on MEMS and Microsystems Research and Teaching, Berlin-Brandenburg Academy of Sciences and Humanities, Germany*, 2008.

TABLE OF CONTENTS

CHAPTER 1 - INTRODUCTION

CHAPTER 2 - LITERATURE REVIEW

CHAPTER 3 - DESIGN, MODELLING AND FINITE ELEMENT ANALYSIS OF CMRA-V1

CHAPTER 6 - FABRICATION AND PACKAGING

LIST OF FIGURES

LIST OF TABLES

LIST OF ABBREVIATIONS

A-F:	Amplitude-Frequency
BAW:	Bulk Acoustic Wave
BOX:	buried oxide layer
CMOS:	Complementary metal–oxide–semiconductor
CMRA:	coupled micro resonator array
CMRA-v1:	coupled micro resonator array (first version)
CMRA-v2:	coupled micro resonator array (second version)
CP:	Conducting Polymer
DAQ:	data acquisition system
DOF:	degree of freedom
DRIE:	dry reactive ion etching
ESEM:	environmental scanning electron microscope
FEA:	finite element analysis
FIB:	focused ion beam
FMS:	fingerprint mass spectrometer
IEA:	Inverse eigenvalue analysis
LMA:	lumped mass analysis
MEMS:	micro electromechanical systems
MOS:	Metal-Oxide-Semiconductor
MOSFET:	Metal-Oxide-Silicon-Field-Effect-Transistor
NEM:	nano electromechanical
OM:	optical microscope
PARC:	pattern recognition engine
QCM:	Quartz Crystal Microbalance
Q-factor:	Quality factor
R:	resonator
RF:	radio frequency
SAS:	multi sensor array system
SAW:	Surface Acoustic Wave
SEM:	scanning electron microscope
singleR-v1:	single resonator-first version (fixed-fixed beam resonator)
singleR-v2:	single resonator-second version (comb-drive resonator)
SOI:	silicon-on-insulator
VOC:	volatile organic compound

CHAPTER 1 - INTRODUCTION

1.1 Introduction to the Artificial Nose

An artificial nose or electronic nose is a system used to mimic the biological nose in detecting or distinguishing different types of material species or odours. The material species can be in the form of a simple odour or a complex odour. The complex odour is a collection of two or more different volatile chemical compounds that together produces a smell [1]. The artificial nose provides consistent, low cost, and rapid sensory information for long term applications compared to the human biological nose. Due to its features, the artificial nose has been used to replace the human biological nose in some industrial areas applications. For example, it is used for quality assurance in the food, beverage and health care industries. It is also employed in space and military applications for autonomous mobile sensing systems and in environmental monitoring to monitor unpleasant or hazardous agents.

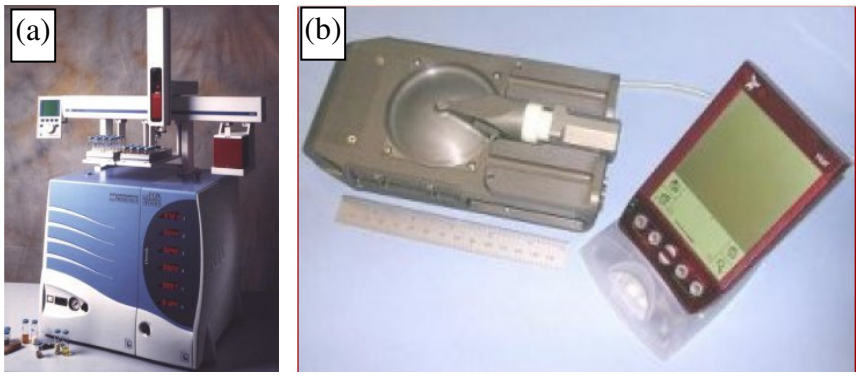

Figure 1.1 (a) Electronic Nose Prometheus by Alpha MOS, France [2]; (b) Second generation of electronic nose developed by NASA [3]

Figure 1.1(a) and (b) show examples of commercial artificial nose available in the market. The Electronic Nose Prometheus illustrated in Figure 1.1(a) is an odour and VOC (volatile organic compound) analyzer [2], which combines a highly sensitive fingerprint mass

spectrometer (FMS) and multi sensor array system (SAS) technologies. The Prometheus [2] is used for quality assurance of raw materials, intermediates and finished products in food, beverage, pharmaceutical, cosmetics, chemical and petrochemical industries. Figure 1.1(b) portrays an image of the electronic nose developed by NASA (National Aeronautics and Space Administration) [3]. The device uses 16 different polymer film sensors for detecting compounds such as ammonia.

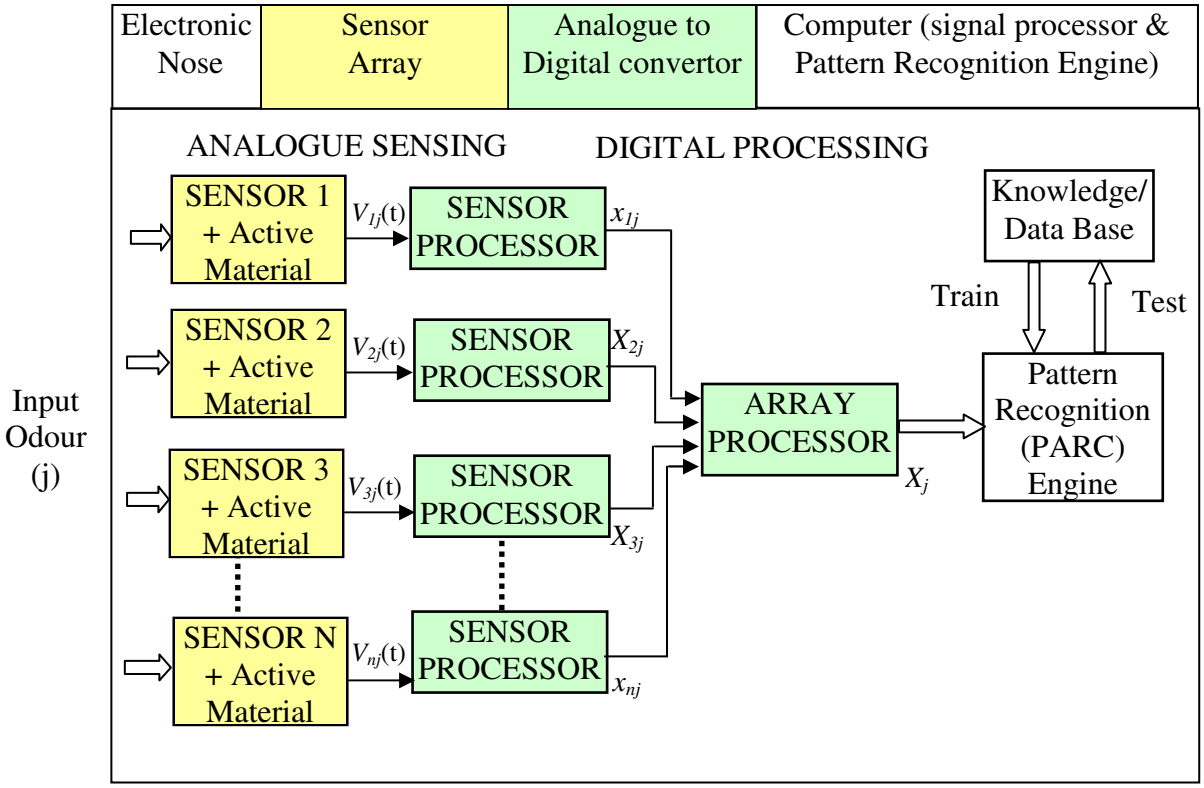

Figure 1.2 Architecture of artificial nose system [1]

Figure 1.2 shows a typical architecture of the artificial nose. It consists of an array of sensors, a signal processing system and a pattern recognition engine (PARC) [1, 4]. An odour is presented to the active material of a sensor, which converts a chemical input into an electrical signal, V_{ij}(t). Each of the signals from N sensors is then digitised to a digital signal, X_j. The response of the output signals are then analysed using the pattern-recognition (PARC) engine. The PARC characterises the responses of the sensor array by using mathematical rules that

relate the response output from a known odour to a set of descriptors held in a Data/ Knowledge Base. The response from an unknown odour is tested against the Knowledge Base and a prediction of the class of the material is specified.

1.2 Problem Statement

The sensors and the pattern recognition engine system (PARC) play an important role in determining the performance of the artificial nose [5] . In order to increase the sensitivity and flexibility of the artificial nose many sensors are required. Adding to the number of sensors can enhance the odour mixture recognition, which will improve the artificial nose performance [6]. Table 1-1 lists the types of sensor arrays and number of sensors employed in the artificial nose in different application areas.

Table 1-1: Type and number of sensing elements applied in different application of the artificial nose

Sensor Array Type	Number of Sensors	Application
Bulk Acoustic Wave	8	Distinguishing different food flavours [7]
Conducting Polymer	12	Differentiating 3 type of beers [8, 9]
Mixed sensors type	15	Effect of ageing for ground pork/ beef [7]
Quartz resonator	16	Discriminating 3 type of fragrances mixture [4]
-	32	Diagnosing 3 different conditions of Cattle (34 measurement of breath samples) [10]
Polymer carbon black nano-composite	32	Detecting 6 bacteria [11]
Chemoresistive micro-sensor array	80	Discriminating between 2 simple odours and essential oil [12]

From the above table, it can be observed that, more sensors are required to detect a complex odours or a large mixture of different types of materials. Undoubtedly, the information

content of the signals from multiple sensor arrays are significantly greater than those from single sensor systems [13]. For example, 12 sensors were used to differentiate between 3 types of beer [9] and 32 sensors were applied to detect 6 different types of bacteria [10]. At least 16 quartz resonators sensor were needed to discriminate between 3 different types of fragrance mixtures [4]. Covington *et al.* [12] concluded that closer emulation of the olfactory mucosa and nasal cavity could yield a better odour discrimination. They replicated the basic structure of the olfactory mucosa system with 80 chemo-resistive micro sensors and an integrated fluidic channel to act as the nasal cavity. They were successful in discriminating between 2 simple odours and a set of complex odours (i.e. essential oils).

Consider the performance of a sensor in terms of a detection limit or detection threshold of the odours; the detection limit of a typical sensor can range from parts per million levels (ppm, 10^6) down to parts per billion (ppb, 10^9) or to more lower odour concentrations, parts per trillion (ppt, 10^{12}) or below in air. The detection limit of a sensor can be improved by reducing the noise which may be suffered by the sensors from interfering signals due to fluctuations in ambient temperature, humidity or pollution. The sensors also may be affected by a drift as a result of poisoning or aging of the sensors. Increasing the number of sensors improves the signal-to-noise level by providing some level of redundancy and permitting signal averaging to take place [7, 14-17].

Sensor arrays are important in measuring complex odour mixtures, since it is not necessary to break the complex odour down into its individual components [17]. Several industries such as the food and beverage industry require the sensor for comparing the quality of the processed products between different batches. The sensors arrays provide non-invasive technique which will benefit the industries. Therefore, the quality assurance process is simplified and all non-value added activities are removed.

As discussed earlier, employing a large number of sensors helps to improve the performance of the artificial nose. However, it also adds greatly to the complexity of the sensing system and cost of the device. Increasing the number of sensors will complicate the readout system of the sensors, since each sensor in the array must be individually monitored. More processors are required to process the individual output signals. Any requirements to integrate the output signal patterns of the individual sensors for tracing the signature of the material species will complicate the signal processing system and the pattern recognition engine system (PARC).

This research seeks an approach to reduce the complexity of large artificial nose sensor systems by exploiting a new sensor structure which is called Coupled Micro Resonator Array (CMRA).

1.3 Coupled Micro Resonator Array (CMRA)

The CMRA structure design is based on an array of coupled resonators. Figure 1.3 illustrates the conceptual design of the CMRA sensor structure. It consists of three main elements: (1) an array of micro resonators (e.g. R1 to R5), (2) mechanical springs, (3) comb actuators. Each individual resonator represents a micro-mass sensor and the array is coupled together with the mechanical springs. The comb actuators are used to drive and readout the output signal of the sensors based on an electrostatic excitation and a capacitive detection method respectively.

The CMRA sensor structure applies the concept of mass loading-frequency shift effect working principle. Conceptually, the surface area on the resonator which will be designed for the active material[1] [18, 19] is sensitive to any small amount of the adsorbed mass such as odour molecules. An odour is passed over the resonator, then the odour molecules will be

[1] a chemically sensing membrane material which will absorb odorant molecules when the odour or aroma sample is passed over the membrane

selectively absorbed into the surface of the resonator. Each resonator will react selectively to particular substances by increasing its mass, so the characteristic-frequency of the sensor will reduce. The shift in frequency is approximately proportional to the total mass of the adsorbed odour molecules. Since each resonator may have different selectivity, the frequency shift pattern across the array may be used as a signature of the odour.

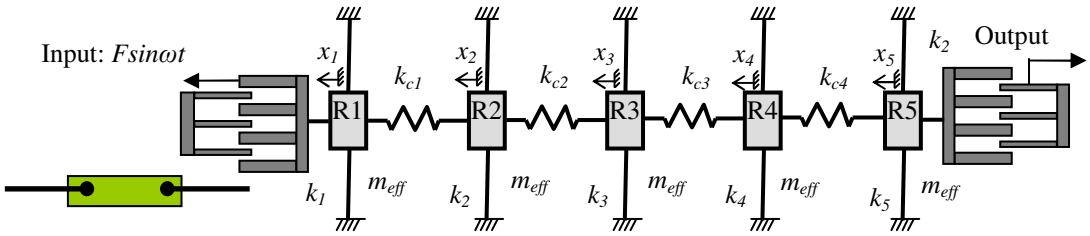

Figure 1.3 Schematic diagram of design concept of coupled resonator array sensor structure

Since the resonators are mechanically coupled together, the state of each resonator can be monitored simply by measuring the resonant frequencies of the coupled system. Thus, in principle with N sensors, just two connections are required to monitor the sensors; one for a drive connection and another for a pick off connection; thus, greatly reduce the complexity of the readout measurement. The signal processing system is also simplified since only a single processor is required to process the output signal as compared to the conventional system [20, 21]. Using the CMRA, the necessity to monitor and integrate different output signals from individual sensors is eliminated. So, the complexity of the pattern recognition engine (PARC) system used to identify the signature of the odours is significantly reduced. By simplifying the readout measurement, signal processing system and pattern recognition system, the manufacturing costs of large sensors are expected to reduce. Therefore, with the CMRA sensor structure, it is expected to reduce the overall cost of the artificial nose.

1.4 Manufacturing Process Variation versus CMRA Performance

Manufacturing variation in MEMS (Micro Electro Mechanical Systems) is inevitable [22, 23]. The variation can be considered as a noise, which normally the manufacturer does not have control of. The source of this noise or variation can come from many factors. It includes external sources such as environmental factors, different batches of wafers, tolerances in the fabricated mask, and internal sources of the fabrication processes. The fabrication processes induce wafer to wafer as well as variation across a single wafer [24]. The variations in processing time and process temperature have a critical influence in most of MEMS processes. A slight difference in processing time and temperature may vary the geometrical dimensions of the fabricated structure.

The variations in the geometrical parameter may affect the response pattern and performance of the coupled resonator sensors. The variations in the geometrical parameter will change the effective mass and stiffness of the resonators. As a result, the resonant frequency of the resonators will change. This research quantifies the manufacturing variations and analyzes its effect on the performance of the CMRA. The variation is quantified by measuring the geometrical parameter of the fabricated structures and comparing it to the designed structure. A simple model of lumped mass parameters of the CMRA is developed to analyze the possible effect of the manufacturing variations on the performance of the designed CMRA sensor structure. The manufacturing variations may reduce the CMRA sensor performance or help to stabilise the resonant modes of the system and enhance the system odour discrimination. The research observes the effect of manufacturing variation on the performance of the fabricated CMRA structure.

1.5 Objectives

The main aim of the research is to exploit a new sensor structure of a coupled micro resonators array (CMRA) for the artificial nose. The research objectives:-

1.5.1 To model and analyze the performance of the CMRA structure

1.5.2 To fabricate and evaluate the performance of the CMRA structure

1.5.3 To observe the effect of manufacturing process variation on the CMRA structure performance

1.6 Scope and Methodology

The research focuses on the realization of the CMRA by modelling the geometrical structure of the CMRA and evaluating its performance using finite element analysis and numerical analysis. The research explores and studies the possibility of the CMRA sensor structure generating distinctive output signal patterns for any mass changes absorbed by the resonators. These distinctive signal patterns are vitally important for the artificial nose in identifying different types of odours and materials absorbed by the sensors. For an improved CMRA (CMRA version 2, CMRA-v2), the research models and analyzes design alternatives of the CMRA to examine the measurability of the output signals. The research demonstrates the inverse eigenvalue analysis used to determine the mass change patterns absorbed by the resonator sensor. An analysis is carried out to examine the effects of stability of the CMRA structure's eigenvectors on the determination of masses absorbed by the sensors. The simulated CMRA structures are fabricated and tested to examine the performance of the structure. To study the effect of the absorbed mass on the structure frequency response, a mass is deposited on the fabricated CMRA and its singleton using a Focused Ion Beam (FIB)

technology. Hence, the fabricated CMRA structure and its singleton should be sensitive to detect the FIB mass. A separate analysis is performed to analyse the effect of the manufacturing process variations on the geometrical parameter of the fabricated structure. The research uses the scanning electron microscope (SEM) to measure the geometrical parameters of the fabricated micro resonators on INTEGRAM chips (out-sourced fabrication). The measured data is compared to the designed structure; and the analysed data is used to predict the impact of the manufacturing variations on the designed CMRA. The results of the frequency response measurement of the fabricated CMRA and its singleton are analysed to examine the performance of the CMRA sensor structure and observe how the manufacturing variations may impact the performance of the fabricated CMRA.

1.7 Outline of Thesis

This thesis consists of eight chapters:-

Chapter 1 describes the artificial nose, introduces the CMRA and highlights the possible effect of the manufacturing process variation on the CMRA.

Chapter 2 reviews the current technology status of works relevant to the development of the CMRA.

Chapter 3 describes the modelling, numerical and finite element analysis of the first version of the CMRA (CMRA-v1). This chapter analyses each structure elements of the CMRA-v1 which includes fixed-fixed beam resonators, butterfly shaped mechanical coupling spring designs, and comb drive actuators. The performance of the simulated CMRA-v1 are analyzed and discussed.

Chapter 4 explains the eigenvalue and eigenvector analysis of the CMRA using a lumped mass model. This chapter re-evaluates the performance of the CMRA-v1 and highlights the

key structure improvements of the CMRA sensor structure. The lumped mass model alternatives of the CMRA which include constant mass CMRA and staggered CMRA are examined and discussed.

Chapter 5 focuses on the design and modelling of the second version of the CMRA (CMRA-v2). This chapter compares the performance of three CMRA(s) designs; Constant Mass CMRA, Staggered Mass CMRA, and Staggered Stiffness CMRA. This chapter also discusses the inverse eigenvalue analysis used to determine the pattern of mass changes absorbed by the resonators. Furthermore, Chapter 5 introduces and describes the analysis of the effect of manufacturing process variations on the geometrical dimension of the fabricated micro resonator structure (INTEGRAM chips). Further analysis is carried out to examine the effect of the quantified manufacturing variations on the structure performance.

Chapter 6 covers all manufacturing processes to fabricate the CMRA sensor structures and its singleton (integrated comb-drive resonator and single fixed-fixed beam resonator). This chapter observes the fabricated CMRA and discusses all constraints in the fabrication processes. This chapter also explains the processes and preparations for the frequency response measurement of the fabricated structure.

Chapter 7 includes electronic testing setup, testing samples and all procedures used to test the frequency response of the structure. This chapter presents and discusses the frequency measurement result of the single resonator and the CMRA structure. The overall performance of the CMRA sensor structure and the effect of the manufacturing process variation are presented.

Chapter 8 concludes the achievement of the research and highlights recommendations for future research.

CHAPTER 2 - LITERATURE REVIEW

2.1 Introduction

This chapter reviews topics related to the main subject matter of the thesis. Section 2.2 highlights the nature of the human biological nose architecture compared to the artificial nose, the odour detection processes in the biological nose, and the importance of the artificial nose in industrial applications. Section 2.3 reviews type of sensors employed in the artificial nose including functional features and performance. Sections 2.4 and 2.5 cover subjects related to the performance of the resonant micro sensors and methods of excitation and readout. Sections 2.6 and 2.7 review past researches associated to the coupled micro resonator structure and the comb-drive actuator respectively. Section 2.8 highlights manufacturing process variation researches in MEMS and Section 2.9 summarizes the overall position.

2.2 Biological Nose versus Artificial Nose

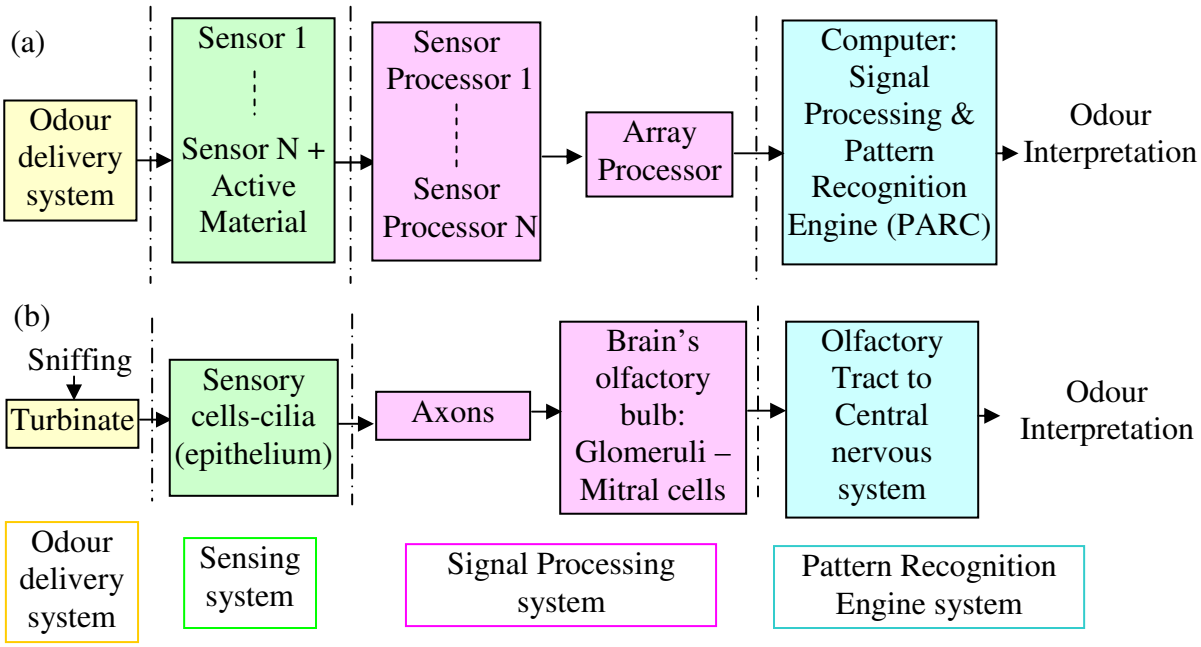

Figure 2.1 (a) A simplified architecture of the conventional artificial nose system; (b) Human olfactory system

Figure 2.1(a) and (b) illustrate the schematic diagrams of the simplified architecture of the artificial nose system and the human olfactory system respectively. Comparing between the two systems, both systems consist of an odour delivery system, a sensing system, a signal processing system and a pattern recognition engine system. Figure 2.2 shows illustrations of the detail of odorant receptors of the human olfactory system [25].

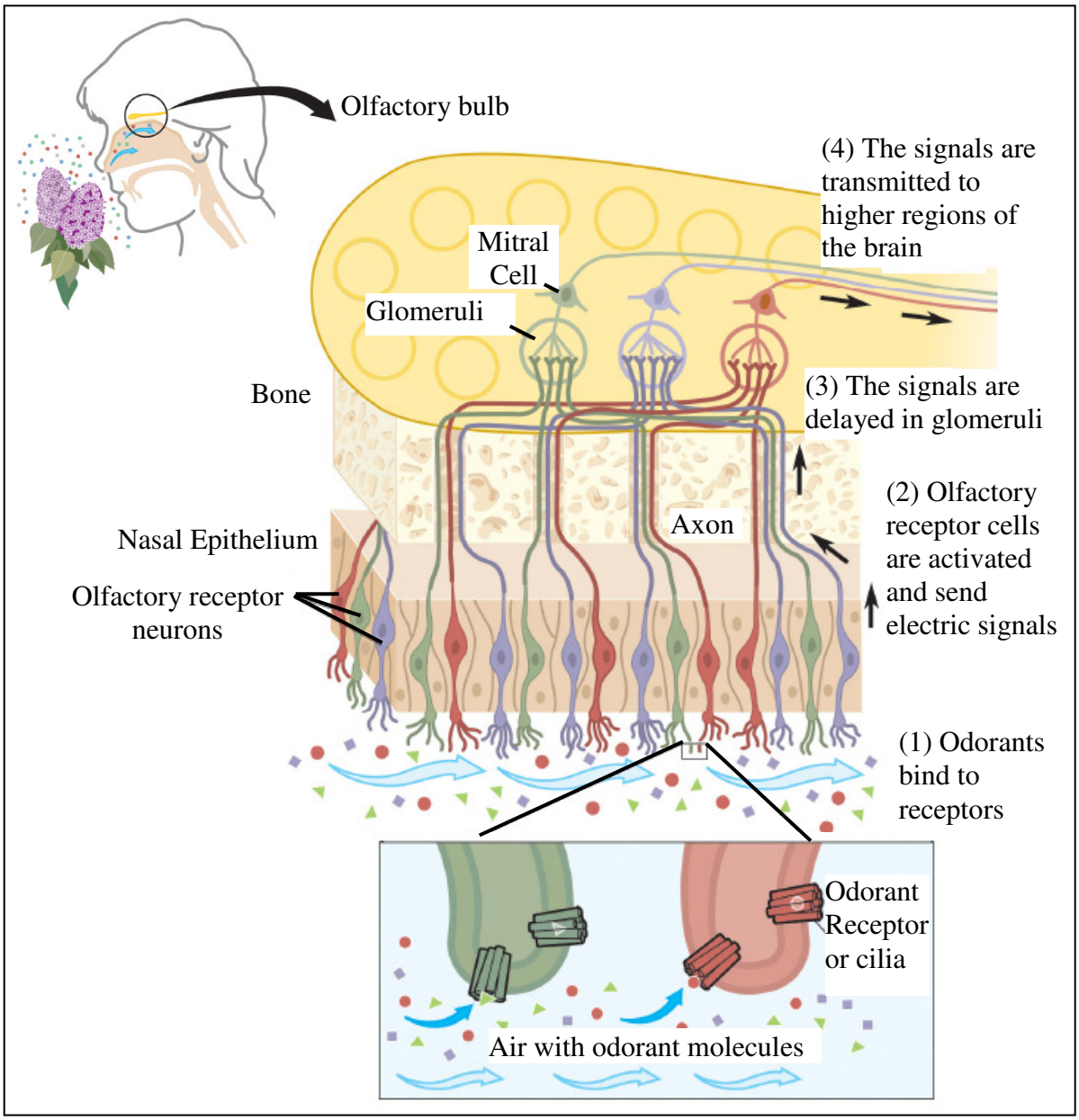

Figure 2.2 Odorant receptors and the organization of the human olfactory system [25]

The odour detection process in the artificial nose starts when a sample(s) of odour is passed over an array of sensors. The odour detection process in the human olfactory system starts when we sniff. Air samples that contain molecules of odours pass curved bony structures (turbinate) . The turbinate creates a turbulent airflow pattern that carry the mixture of volatile compounds to the thin mucus coating of the nose olfactory epithelium (Figure 2.2) [14]. In humans, the olfactory epithelium is located about 7 cm up and into the nose from the nostrils [26].

Hair cells in the olfactory epithelium are the receptors that act as sensory cells that respond to particular chemicals. There are about 50 millions primary sensory receptor cells or neurons on a small area of 2.5 square centimetres olfactory region in humans [27]. Each sensory receptor neurons have 20-30 projected small hairs called cilia [28]. The cilia are whip-like extensions of 30-200 microns in length [27]. The olfactory chemo receptors are located on these cilia [29]. While, in the artificial nose, the sensor surface area with the coated active material will act as a receptor where selective molecular reception of the odorant occurs and sensory transduction starts.

At rest, ions are pumped within the cell membrane of the olfactory epithelium to keep the cells polarized (at around 90mV) [14]. When the odorant molecules bind to a receptor protein, it initiates a cascade of enzymatic reactions and results in depolarization of the cells membrane [28, 30]. The change in the polarity state creates signals, which then are transmitted to the olfactory bulb along neural 'wires' called axons [31]. Axons are bundled in groups of 10-100 to penetrate the ethmoidal cribriform plate of bone, reaching the olfactory bulb of the brain [27, 29]. From the mitral cells (i.e. contacts with the next level of nerve cells) the information is sent directly to the higher levels of the central nervous system in the brain; the signalling process is interpreted and olfactory response occurs [27, 32].

2.2.1 The Importance of the Artificial Nose

The sensitivity of human nose is undoubtedly greater than that of any electronic equipment. But, the variability in results is also far greater and practical difficulties arise in using human panels for many operations [33]. Comparing the artificial nose and the human biological nose, the human nose is unavoidably affected by the state of the health and mood of the inspectors [4]. The testing results may vary depending on the individual conditions in terms of mental states and adaptability to the equipment and environment. Due to the nature of the human biological nose, it cannot be used routinely for 100% product control in applications such as the monitoring of perfume in soaps and cosmetics bases, the monitoring of body odours in deodorant development and the monitoring of aroma in the food industry [34]. Therefore, the use of the artificial nose will be more productive and cost effective for any long-term business strategy.

There are many industries which require the application of the artificial nose technology. Bourgeois *et al.* [35] reviewed the use of the sensor arrays in environmental monitoring. Many industries such as paper and waste processing industry, food and beverage processing and perfumes industries may be exposed to pollutions due to the nature of their industrial activities. The emitted toxic gases and volatile organic compounds which are in the form of complex odour mixtures make it impossible to monitor using a single sensor or using the biological nose.

Natural smells, perfumes and flavours are invariably complex mixtures of chemicals containing at least tens and more frequently hundreds of constituent odorants. Differences in ratio of the constituent chemicals affect the odour or flavour. In some instances the odour of a natural material is dominated by one odorant and other odorants presence serve to give nuance the odour [36]. The use of the artificial nose to detect one odorant in a complex

chemical is more effective and feasible. Considering the capability of the biological nose, the threshold of the odorant molecules that can be detected by a normal healthy person is limited [37]. Furthermore, the biological nose produces only the qualitative information compared to the artificial nose which can provide quantitative information [9]. Therefore the electronic nose is important for such applications to replace the biological nose.

The use of the artificial nose in some medical applications for synthesizing the biological samples is practical. For example the artificial nose was used to detect glucose level in blood plasma samples [36] in order to diagnose diabetes. The electronic nose was successfully employed to distinguish the CSF (cerebrospinal fluid) from serum in cultures sample and to detect tuberculosis in sputum samples [38]. The use of the artificial nose in these medical applications is more efficient and may help to expedite the clinical decision making processes [39].

2.3 Sensor Technologies Used in the Artificial Noses

2.3.1 Sensor Type and Features

Most sensors arrays were designed or constructed in the form of individual sensors or individually packaged sensors [13]. Some applications of the multiple sensors are in the form of a hybrid array, where different types of sensors are used together to discriminate different type of odours [15]. Table 2-1 lists the different type of sensor arrays commonly used in the artificial nose. Each sensor is categorized, based on its operation principles such as piezoelectricity, resonance, electrical conductivity, capacitive charge coupling, and optical based sensing.

Table 2-1 Sensor technologies applied in the artificial nose

Sensor Type
Quartz Crystal Microbalance (QCM)
Surface Acoustic Wave (SAW)
Bulk Acoustic Wave (BAW)
Micro cantilever beams
Metal-Oxide-Semiconductor (MOS)
Conducting Polymer (CP) and Intrinsically Conducting Polymers (ICPs)
Metal-Oxide-Silicon-Field-Effect-Transistor arrays (MOSFET arrays)
Optical sensing array

QCM [40], SAW [41, 42], BAW and micro cantilever beam sensors [43, 44] operate based on a resonance principle. Figure 2.3(a) shows an example of QCM sensor [21]. It consists of quartz crystal oscillator covered with a gas-sensitive material. Adsorption of volatile compounds changes the sensor resonant frequency and the response amplitude of oscillation. The frequency shift, Δf was used to determine the amount of mass deposited or removed from QCM sensor [45].

MOS and CP sensor applies an electrical conductivity operation principle. Tin oxide (SnO_2) is an example of MOS sensor (Figure 2.3(b) and (c)). When the sensor is exposed to air, the SnO_2 surface absorbs oxygen. The oxygen absorption creates a space-charge layer on the surface of each SnO_2 grain; the space-charge creates a potential barrier to conduction at each grain boundary and increases the sensor electrical resistance [15, 21]. Figure 2.3(d) depicts an example of CP sensor. It consists of conductive fillers such as carbon black or polypyrrole [46, 47] and nonconductive organic polymers as the insulating matrix. When the composite sensors are exposed to an odorant, the composites will swell; the degree of swelling depends on the polymer and odorant interactions and results in a change in the conductivity of the composite film [21].

MOSFETs are gas sensitive field effect device with catalytic metal gates (e.g. palladium, platinum, and iridium) [48] (Figure 2.3 (e)). When molecule gas such as hydrogen

adsorbs to the gate and diffuses to the SiO_2 layer, it forms a dipole layer. The charging of the gate results in voltage change in the sensor signal. An optical fibre sensor is an example of optical sensing array. It employs analyte-sensitive indicators such as fluorescence intensity for detecting odour species [15].

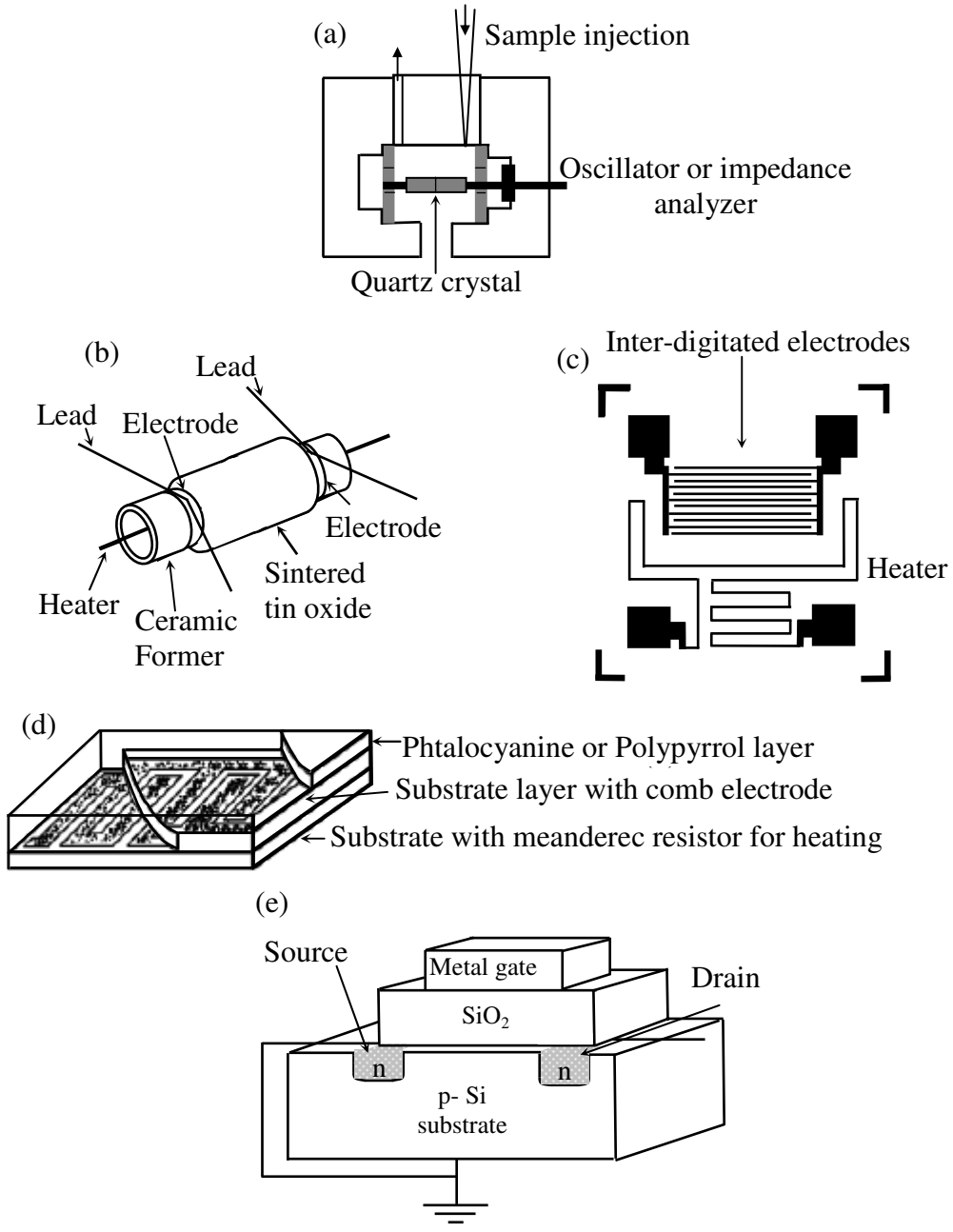

Figure 2.3 (a) QCM sensor [21]; (b) an individual packaged of the SnO_2 sensor [15]; (c) the array of SnO_2 sensor [15]; (d) Conducting Polymer sensor [21]; (e) MOSFET sensor [15]

Considering several sensor types which are discussed earlier, the resonant sensor is capable of producing a direct digital output signal [49]. The approach offers long term stability [40]. Due to its high sensitivity, the cantilever resonant sensor has been used as a mass sensors to detect vapour such toluene, methanol and its mixture [44]. MOS sensors have a disadvantage, since it needs to dope with metal to increase the surface sensitivity [15]. While, CP sometimes difficult to operate and time consuming to electro-polymerize the active materials. Taking advantages offered by the resonant sensor, this research investigates mechanically coupling the resonant sensors and seeks to simplify the multiple sensors system for the artificial nose applications.

2.3.2 Performance of Current Sensors and Artificial Noses

To date, compared to a rich experience odour assessor, the artificial nose is still limited in capabilities [4, 50-55]. The performance of the artificial nose relies on the specific sensor characteristics, an evaluation technique of a sensor response (PARC, Pattern recognition engine) [56] and mathematical modelling to characterize and integrate the multiple sensors response. As an example, 16 quartz resonator sensor at 20MHz frequency and supported with an automated pattern recognition system of FLVQ (Fuzzy Learning Vector Quantification) was able to distinguish 3 mixtures of fragrances (0 to 70% concentration) at only 79% recognition rate [4].

Daqi and Wei [50] argued that a single type of mathematical function approximation model cannot simultaneously determine many different kinds of odour classes and concentrations. They used 16 commercial TGS sensors and four different function approximation models (i.e. multivariate logarithmic regression (MVLR), quadratic multivariate logarithmic regression (QMVLR), multilayer perceptron (MLP) , and support

vector machine (SVM)) to classify 4 types of fragrances at 21 different concentrations (i.e. between 1 to 10000ppm). Szczurek and Maciejewska [54] claimed that they successfully transformed responses of a MOS sensor array to an intensity of odour (mixture of 0-346.4mg/m^3 toluene and 0-180.4mg/m^3 ethyl acetate) using a generalized regression network (GRN) neural model. Feng *et al.* [55] employed Quartz crystal microbalance sensors and MIPs (Molecular Imprinting techniques) for determination of formaldehyde; they revealed a linear relationship between frequency shifts and concentrations of analyte in the range of 1.25 to 14.25µM.

The performance of each sensor technology can be compared in terms of their functional features: (i) limit of detection (sensor sensitivity); (ii) selectivity; (iii) repeatability and reproducibility of the output signal; (iv) any temperature and humidity dependence; (v) operating temperature level; (vi) response time, recovery time and lifetime of the sensors [57]. *Detection limit* or *sensor sensitivity* is referred to the ratio of the number of odorants to the total number of molecules in the gas sample being analyzed [14, 21]. The sensor sensitivity may range from a low to high detection limit (e.g. part per million 10^{-6} (ppm) to part per trillion 10^{-12} (ppt)). *Selectivity* or *Specificity is* the ability of sensors to detect the specific compound within a complex headspace (i.e. mixture of hundred compounds) [14].

Boholt *et al.* [57] reviewed the performance of five different types of sensors in terms of their functional features (i.e. MOS, MOSFET, CP, QCM, and SAW); comparing between the five sensors types, the QCM and SAW sensor, which are grouped under resonant sensors, have higher selectivity compared to other sensors. The SAW can work at the highest limit of detection (i.e. ppb) and comparable with other sensors in terms of low humidity dependence. The SAW works in the ambient temperature and QCM at a slight elevated temperature (i.e. an average of 30 -40^{o}C) compared to the MOSFET and MOS which can only work at least at

100 – 200^{o}C. However, a slight disadvantage of the QCM and SAW is that performance of both sensors are temperature dependence; one of the reasons is that the sensitivity of the sensor response decreases at an elevated temperature due to reduction of sorption strength of the gas-sensitive material coated on the sensor surface [58].

2.4 Resonant Sensors Performance

Resonant sensors are based upon the principle of the resonant frequency or the frequency distribution produced in a mechanical structure, which is measured and related to the property to be determined. Resonator sensors are suitable for the measurement of mass flow, density, viscosity, rotation rate, pressure, force, and acceleration [42].

Resonator sensors often have a relatively high mechanical quality factor (Q-factor), which leads to a high resolution of frequency and hence high sensitivity [59]. A high Q-factor also implies low energy losses from the resonator and therefore low power requirements to maintain the resonance, which simplifies the operating electronics.

Another advantage of frequency domain sensors is that the signal output is essentially 'digital' in contrast to analogue signal output [60]. Therefore, the detected signal can be directly connected to digital circuits, which ensures high accuracy detection and simplicity compared with other type of sensors.

However, as argued by Kaajakari *et al.* [61] there are few major problems which needs to be overcome in order to further improve the performance of the resonant sensors: (i) maintaining and measuring the prime mode of vibration of the mechanical structure; (ii) improving measurement reliability by considering the influences of material consistency and manufacturing tolerances; and (iii) the application of sophisticated mathematical modelling techniques to understand fully the modes of vibration.

Stemme [62] raised important considerations in designing high performance of resonant sensors:-

- High quality (Q) factor;
- Having a sufficient input parameter selectivity and sensitivity of resonance frequency;
- Low temperature sensitivity of the resonance frequency;
- Selection of type of resonator design and mode of vibration;
- Reducing mode coupling (i.e. the interference of unwanted vibration modes in the excitation of the wanted modes).

2.4.1 Quality Factor

Q is known as the quality factor of the resonator. Loosely, it describes the number of oscillations of the system before it is damped out [63]. Q factor can be defined as the total energy stored in the structure divided by the sum of energy losses from the vibrating element per cycle. In forced vibration Q is related to a measure of the sharpness of resonance. Consider a single degree-of-freedom mass spring damping system in Figure 2.4.

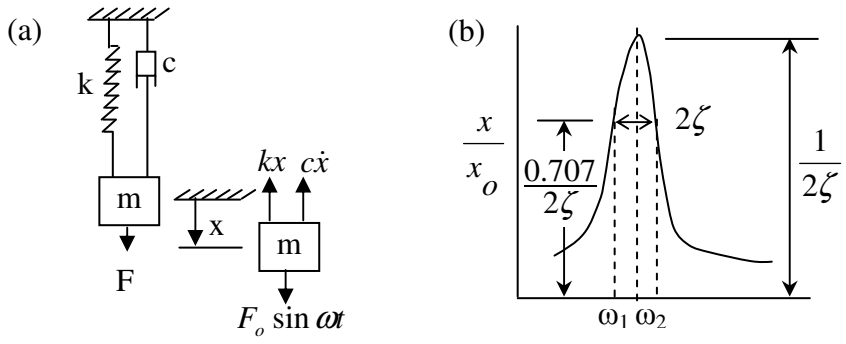

Figure 2.4 [64] (a) Viscously damped system with harmonic excitation; (b) Sharpness of resonance

Differential equation of motion: $m\ddot{x} + c\dot{x} + kx = F_o \sin \omega t$ (Equation 2-1)

Amplitude of oscillation; $X = \frac{F_o}{\sqrt{\left(k - m\omega^2\right)^2 + (c\omega)^2}}$ (Equation 2-2)

Phase of displacement; $\phi = Tan^{-1} \frac{c\omega}{k - m\omega^2}$ (Equation 2-3)

Natural frequency of undamped oscillation, $\omega_n = \sqrt{\frac{k}{m}}$ (Equation 2-4)

Critical damping; $c_c = 2m\omega_n$ (Equation 2-5)

Damping factor; $\zeta = \frac{c}{c_c}$ (Equation 2-6)

Quality factor, $Q = \frac{\omega_n}{\omega_2 - \omega_1} = \frac{f_n}{f_2 - f_1} = \frac{1}{2\zeta}$ (Equation 2-7)

Where, $F_o sin\omega t$: is the harmonic excitation force; ω: excitation frequency; ω_1 and ω_2: two frequencies of resonance sidebands which was found at half-power points of the resonance amplitude (X_{res}) $X = 0.707X_{res}$ [64].

The Q factor depends on different damping mechanisms; to get high Q factors, the damping must be low. The damping mechanisms may be due to structure imbalances which cause energy losses into the surroundings, viscous and acoustic damping losses and internal material related losses.

The internal losses depend on the purity, dislocations and thermo-elastic losses of the material [62]. The thermo-elastic losses are due to irreversible heat conduction resulting from the structure flexural motion. Single crystal materials such as single crystalline silicon and quartz have excellent resonating properties in terms of very high intrinsic Q-factors [62]. As emphasized by Nguyen and Howe [65], the intrinsic Q of a micro resonator is also a function of the anchor design and is temperature dependant. The Q factor also can be increased by increasing the vibration balance for example by using a double or triple beam and bridge

structures in the resonance mode configuration. In addition, Huang *et al.* [66] observed a strong correlation between surface roughness of silicon carbide thin film material and the quality factor of the resonators made from it.

High Q factor is very important because [63]:

- Simplify the feedback control electronics (i.e. require a low energy to maintain the vibration).
- Allow precise measurement of the resonator response.
- Give high accuracy and long term stability (i.e. low sensitivity to mechanical disturbances).

However, Kaajakari *et al.* [61] claimed that a high quality factor makes micro resonators susceptible to nonlinearities.

2.4.2 Nonlinear Effect

MEMS resonators exhibit two kinds of nonlinearities, a mechanical stiffening and an electrical softening. At low biased voltages, the capacitive forces are weak and the mechanical stiffening effect may dominate. This causes right hand side bending of the frequency response [67] (Figure 2.5(a)). At high biased voltage, the nonlinearities in capacitive forces are dominant, causing the electrically induced softening effect. This causes left side bending of the frequency response curve [67] (Figure 2.5(b)). The mechanical nonlinearity is due to geometrical and material effects in the resonating element while the capacitive nonlinearity is due to capacitive coupling mechanism (i.e. the design of the capacitor element) [68]. As an example the use of boron-doped material enhances the nonlinear mechanical responses of the resonator [69].

The nonlinear amplitude frequency effect limits the maximum sustainable amplitude and reduces the maximum signal-to-noise ratio that can be achieved. Beyond the sustainable amplitude, the resonator amplitude and phase response exhibit duffing bifurcation instabilities as well as excess of phase noise induced by the amplitude noise [67]. In a severe condition, the nonlinear effect can cause a damage and fatigue to the device [70]. Langdon [71] claimed that for the force and mass sensing applications, the resonator should be designed to have small displacements to avoid the nonlinearity. The nonlinear frequency response causes inaccuracy of mass determinations due to unstable frequency shifts and resonator response amplitude.

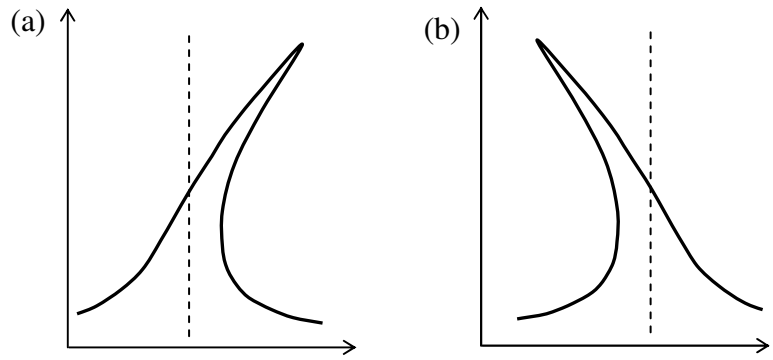

Figure 2.5 [67] (a) Nonlinear – mechanical stiffening; (b) Nonlinear – electrical softening

2.4.3 Resonance Frequency- Temperature Sensitivity

The temperature sensitivity of the resonant frequency can be controlled by selecting the resonator material, type of vibration mode (resonator shape and design), type of excitation and frequency detection and reducing any thermal expansion mismatch [62]. In selecting the resonator material, the properties of the material such as density, thermal expansion, Poisson's ratio and elastic constant are important since all of these properties affect the resonant frequency.

Low temperature sensitivity can be achieved if the resonators are made from a single-crystalline material. The introduction of extra layers of material will result the bimetallic effect, which will induce thermal stress and increase the temperature sensitivity.

Silicon is an example of good electronic material used in integrated circuits. It provides excellent mechanical properties of single-crystal silicon in terms of high purity and low defect density. The high mechanical quality of silicon and the resonance of an element make it possible to make stable, high resolution and high sensitivity resonant silicon sensors [72, 73].

2.4.4 Resonator Design and Vibration Mode

The resonator can be designed in various shapes. Each shape can have several vibration modes such as transversal, longitudinal, torsional and lateral [63]. Each mode has its own displacement patterns, resonant frequency and Q-factor. Normally the resonant frequency of the modes is designed to be dependent of change of resonator mass (mass loading), internal forces or stress and change of stiffness of resonator.

An unbalanced resonator design yields energy losses at the mount due to reaction forces required to maintain the unbalanced resonator vibration which reduces the Q-factor. In order to be perfectly balanced, a vibrating structure must have a fixed centre of gravity and the sum of forces and moments resulting from the vibration should be zero [62].

2.5 Excitation and Detection Methods of Resonant Sensor

The *excitation* drives the resonator into vibration and the *detection* measures the response of the resonator. There are a few considerations in selecting the excitation method [74]: (i) Material effect; (ii) The size of actuation force; (iii) The fractional stroke (displacement per unit length) of the actuator; and (iv) Any temperature dependence. It is very important to

make sure that the selected excitation and the detection arrangement does not introduce any deterioration in the Q-factor in terms of residual stresses and damping [62].

As shown in Figure 2.6, there are several types of excitation techniques with their associated detection methods [62, 63].

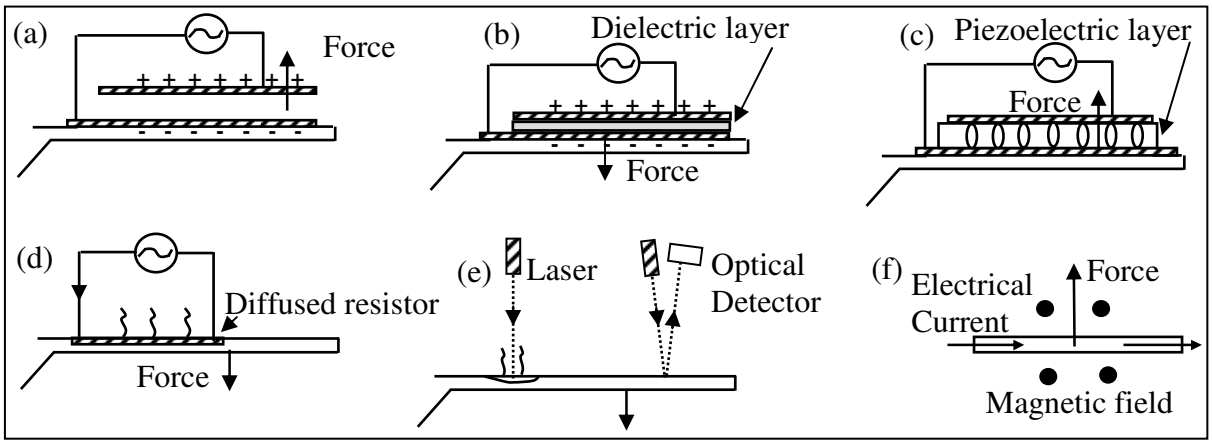

Figure 2.6 Excitation and detection technique of resonant sensor [62] (a) electrostatic - capacitive; (b) dielectric technique; (c) piezoelectric [62, 74]; (d) Resistive Heating-piezoresistive; (e) Optical heating-detection; (e) magnetic excitation-detection

2.5.1 Electrostatic Excitation and Capacitive Detection

The technique requires two electrodes arranged in a close proximity, where one of the electrodes is the resonator (Figure 2.6(a)). Applying an alternating voltage across the electrodes results in an alternating electrostatic force on the resonator element. The capacitive detection is based on the fluctuation of the charged capacitor (i.e. electrodes with varying distance) which causes a current [63]. Converting the current to a voltage and sweeping through the resonator frequency will determine the resonator response.

2.5.2 Dielectric Excitation and Detection

The technique uses of a sandwich structure consisting of a thin dielectric layer between an upper and a lower electrode (i.e. the resonator element) (Figure 2.6(b)). An applied voltage creates attraction forces between the two electrodes, which will deform the dielectric material. The layer deformation causes lateral stresses to the dielectric material which results in a bending action of the multilayer structure. The response of vibration can be detected by measuring the change of capacitances due to the change in dielectric layer thickness of the material [62].

2.5.3 Piezoelectric Excitation and Detection

A piezoelectric material has built in dipole charges. The material produces a voltage when a mechanical stress is applied or conversely will deform if it is subjected to a voltage [15, 63] (Figure 2.6(c)).

2.5.4 Resistive Heating Excitation and Piezoresistive Detection

As shown in Figure 2.6(d), a thermal heating can be accomplished by heat dissipations in an integrated diffused resistor. The heat creates a local material expansion which results in a resonator element deflection. The resonator deflection will induce stresses to the silicon structure; the resonator vibration is measured accordingly based on a change in material resistance .

2.5.5 Optical Heating and Detection

A periodically activated laser focused on the resonator is used to generate thermal stresses and induce the vibration (Figure 2.6(e)). A typical setup of an array of vertical cavity surface

emitting lasers, collimating optics and a position-sensitive detector (PSD) may be used to measure resonance frequency; The PSD will capture the laser beam reflected from the tip of the vibrating resonator [75].

2.5.6 Magnetic Excitation and Detection

The force resulting from the interaction between the electrical current through the structure and a magnetic field (external magnetic field) has been used for resonator excitations (Figure 2.6(f)). The vibration of the resonator (a conductor) in a magnetic field creates an induced voltage, which can be used to measure the vibration responses [62].

Comparing between the six techniques, the electrostatic and capacitive technique was chosen to drive and readout the CMRA sensor structure. Although, the dielectric approach is a promising technique, it is only suitable for the materials with a very high dielectric constant such as PZT [62, 63]. The piezoelectric is an effective excitation technique; however, since silicon will be used to fabricate the CMRA, a piezoelectric material such as zinc oxide has to be deposited on the silicon layer. The technique increases risk of Q factor reduction due to increase of the temperature sensitivity as a result of thermal expansion coefficient mismatch between different material layers [62, 74].

Considering resistive heating - piezoresistive detection technique, the approach is limited only to out of plane motions. Furthermore, the heating process may change the material properties as the temperature rises and may affect the resonator performance. The optical heating approach is an attractive technique; however, measurement of motion is not very accurate due to the noise induced by the optical laser beam (shot noise and non-linear heating) [62, 76]. While the magnetic excitation and detection technique can be easily

realized with the help of an external magnetic field; the technique becomes quite weak on a micro-scale device.

The electrostatic excitation and capacitive detection technique is a simple approach to exploit in the concept of the CMRA sensor structure. The technique can be realized using comb drive actuators, which can be incorporated in the design of the coupled resonators. However, the comb drive actuator need to be properly designed in ensuring a sufficient capacitance in order to drive and readout the resonator output signal.

2.6 Coupled Resonators

To date most of the research on coupled resonators have been used to improve the performance of a micro-electromechanical system (MEMS) or nano-electromechanical system (NEMS) [70, 77-80]. The collective behaviours of the coupled resonator arrays structure was used to enhance the performance of devices such as a single resonator for oscillator applications [77] [78, 79], RF filters [81-87], magnetometers and mass sensors [43, 44, 88, 89]. In addition, the coupled resonator structure also had been employed to study the nonlinear effect of an array of resonators [90] and nonlinear phenomenon such as intrinsic localized modes (ILMs) [91]. For all the applications, the resonator coupling has been achieved either by using capacitive couplings [81, 83, 84, 90, 92] or mechanical spring couplings [70, 77, 78, 82, 85, 88, 89, 93, 94].

Considering the application of the coupled resonators for an ultra-sensitive mass sensing [88, 89]; the research employed micro cantilever resonators which are coupled together by an overhang (Figure 2.7). A concept of mode localization of the coupled resonator was applied in order to analyse the sensor performance. The concept is realized in the sense that in each eigenmode one structure oscillates more than the other; and the change

in eigenmode are unique to the cantilever to which mass is added. The research used the unique eigenmode as a characteristic 'fingerprint' that identifies the particular cantilever where mass has been added.

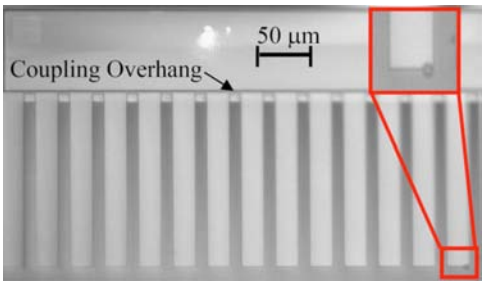

Figure 2.7 Photograph of the array of fifteen coupled cantilevers [88]

Research led by DeMartini *et al.* [43] also used the mode localization concept of overhang coupled cantilevers to present a number of frequency-mistuned micro beam resonator mass sensors. Each cantilever resonator which is individually functionalized for a specific analyte were coupled to a common shuttle mass for actuation and readout measurement purposes. The sensors rely on the strong mode localization to ensure effective mass sensing. In the presence of strong mode localization any change of mass induces a markedly shift in the resonance frequency associated with the altered resonator, which is then used to determine the species of the analyte. With 4 mistuning micro beams sensors [44] the research was able to distinguish between toluene, methanol vapours and mixture of the two vapours. Comparing to the work in [43, 44, 88, 89] which used the mode localization approach (shift of the response amplitude), the CMRA used the resonant frequency shift as the approach for mass detection.

The coupled resonators approach is also employed to improve the filter performance due to manufacturing process variations effect. Wang and Nguyen [82] demonstrated the use of coupled resonators to suppress pass-band distortion due to finite-mass and process mismatch nonlinearities. A 2D array structure strongly coupled in one direction and weakly

coupled in the other direction was used to reduce the effect of vibration localization in filters due to the effect of manufacturing process mismatch nonidealities [86].

2.7 Comb-Drive

The comb-drive actuator is normally used for performing tasks that can be easily integrated within a chip. It is easily controlled and consumes little power [95]. It can perform tasks such as positioning devices, probes and heads; it has been employed in micro grippers, force-balanced accelerometers, laterally oscillating gyroscopes and radio frequency (RF) filters [96]; it may be designed as a resonator sensor with servo feedback for readout or self-test.

The comb-drive based on the electrostatic actuator has low temperature dependence and the performance is material independence. The performance of the comb-drive purely depends on the geometrical dimension of the fingers and the effect of the input voltage. The fabrication processes of the structure is compatible with CMOS processes. The operation of the comb drive is easy to understand and it produces a force that scales well to the micro dimension [74]. Due to features of the comb-drive, it provides a simple and cheap approach to drive and readout the CMRA sensor structure. Hence, the structure is selected and will be incorporated in the CMRA design structure.

2.7.1 Important Design Criteria of Comb-Drive

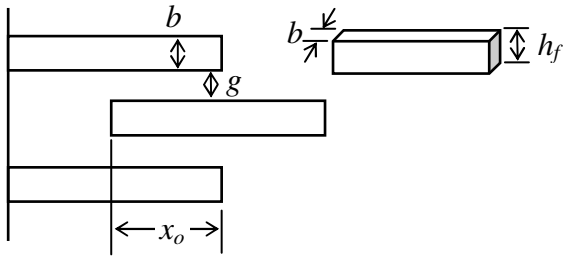

Figure 2.8 Important design geometry of comb drive

A comb-drive actuator consists of moving and fixed conductive fingers. The comb-drive working principle is based on an electrostatic force that is generated between biased inter-digitated conductive combs [97]. The magnitude of electrostatic force depends on the applied voltage as well as the geometry of the fingers (Figure 2.8).

The most common comb design consists of rectangular fingers (Figure 2.8) which exhibit constant force output over a wide range of displacement and allow capacitances to vary linearly with engagements [97-99]. The electrostatic forces increase with increasing size of beam width (b), number of comb fingers [100], and initial overlapping between moving and fixed comb fingers (x_o) [101], and with decreasing gap spacing (g) [102-104].

The electrostatic force, F_{el} [100] is calculated as:

$$Fel = \frac{1}{2}\frac{\delta C}{\delta x}v^2 = \frac{n.\varepsilon_o.b}{g}.v^2 \qquad \text{(Equation 2-8)}$$

Where $\delta C/\delta x$: change of capacitance [F/m]; v: input voltage [v]; n: total number of fingers; ε_o: permeability in free space = 8.85 x 10^{-12} Cb^2/Nm^2 ; b: width of finger [m] ; and g: gap between fingers [m].

A comb displacement, x[m] when the electrostatic force is acting on the spring used to anchor the comb-drive, and the capacitance between the fixed and moving comb fingers, C [F] are [100]:

$$x = \frac{n.\varepsilon_o.b}{k_x.g}.v^2 \qquad \text{(Equation 2-9)}$$

$$C = \frac{2.n.\varepsilon_o.b(x + x_o)}{g} \qquad \text{(Equation 2-10)}$$

Where k_x: stiffness of anchor spring in the direction of comb drive displacement.

In normal cases, the comb drive design should obtain a large displacement (x) and provide continuous motion capability (i.e. stable motion) [105].

2.7.2 Comb Drive Design for Large and Stable Displacement

A large comb displacement is important to generate a large capacitance or electrostatic force to drive the comb. While, a stable displacement is important to ensure continuous comb drive motions without any finger 'sticking' due to side instability [101, 104].

Referring to Equation 2-9, the comb displacement may be increased by decreasing the gap design, g or increasing the input voltage. However, with the small gap spacing or too high input voltage the comb actuator became unstable [102, 106]. The equivalent negative spring constant, when the moving comb is placed at the centre of the comb gap, k_e is given by [107]:

$$k_e = \frac{\delta F y}{\delta y} = \frac{2\varepsilon_o h_f x_o V^2}{g^3} \qquad \text{(Equation 2-11)}$$

The mechanical spring constant which linked to the comb drive, k_y (y-axis is a direction perpendicular to the comb drive movement) keeps the position of the moving comb against the instability of the electrostatic force. The comb stays stable if k_y is larger than k_e , or :

$$\left|k_y\right| \rangle \left|\frac{2\varepsilon_o h_f x_o V^2}{g^3}\right| \qquad \text{(Equation 2-12)}$$

Hence, the stability can be increased if the gap size (g) is increased, or the comb thickness (h_f), initial overlapping of comb (x_o) and applied voltage (V) are decreased. Otherwise, the suspension to anchor the comb-drive needs to be redesigned to increase the spring constant of k_y.

Several design alternatives of suspension systems used to anchor the comb-drive had been proposed for increasing the displacement and stability of the comb-drive [100, 103-107]. The suspension system must be compliant in the direction of the comb displacement and stiff in the orthogonal directions.

Legtenberg *et. al* [100] proposed a folded flexure beam suspension system which was connected to the centre of the beam that is able to hold a large number of comb fingers

(Figure 2.9(a)) . The system produces a large displacement comb drive at low driven voltage and reduces the side instability. Elata and Leus [103] proposed the use of folded beam suspensions with pre-curved beams; the moving comb can then be constrained to move only in the primary direction and the side pull-in instability can practically be avoided.

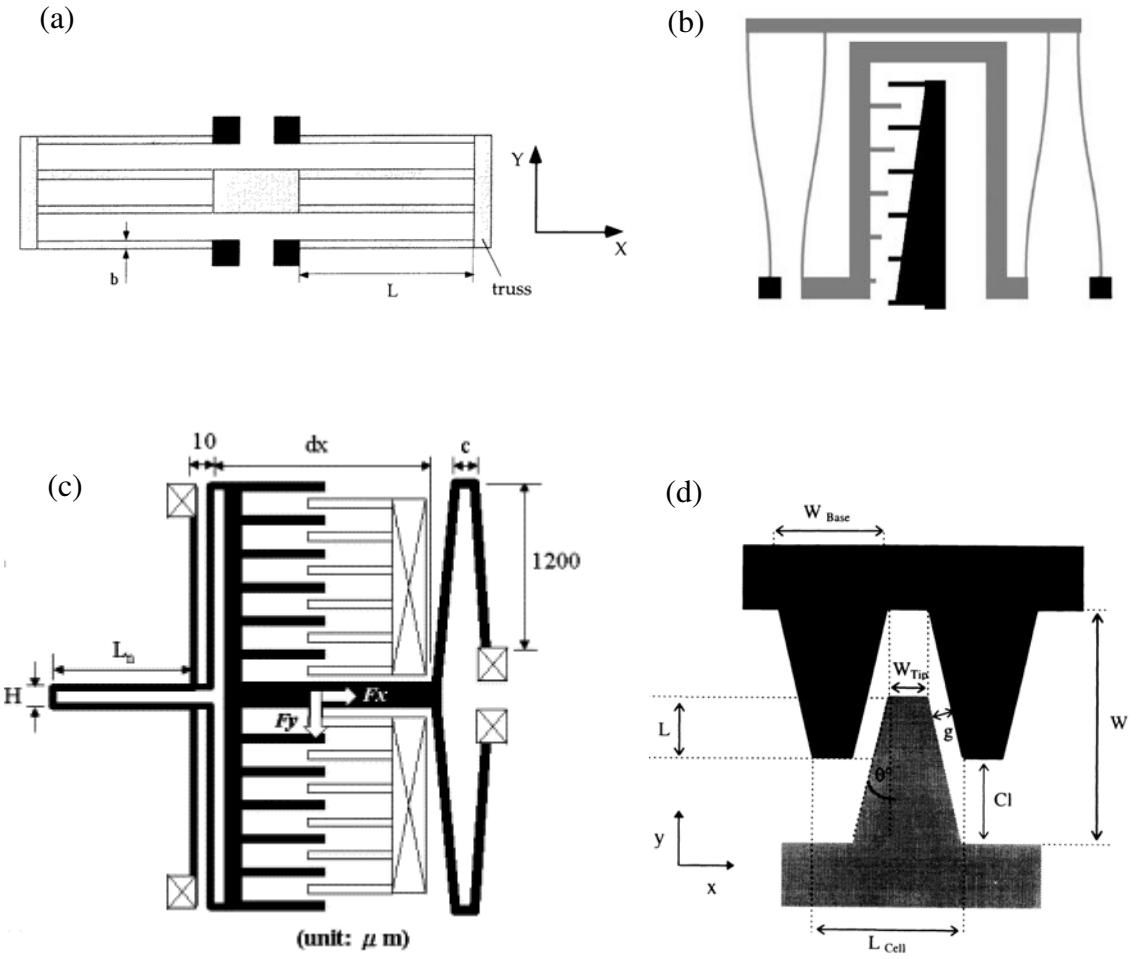

Figure 2.9 Suspensions and comb finger designs (a) Folded Flexure Beam [100]; (b) An initially bent suspension beam [104]; (c) a hybrid spring with a n-shaped joint [105]; (d) Angled comb finger [108, 109]

Grade *et al.* [104] proposed a customized suspension, where the beam was fabricated in an initially bent configuration (Figure 2.9(b)) . They claimed the instability decreases over the range of actuation by a factor of 30%. For maximum static displacement of comb drive actuator, Chen and Lee [105] proposed a new hybrid spring with a n-shaped joint (Figure

2.9(c)). The research used an equivalent spring constant, k_{sy} at the centre of overlap, instead of *ky* to accurately simulate the maximum static x-displacement. By using k_{sy} the stability of comb drive due to torsion effects was considered.

Other researchers focus on the comb finger design for improving the comb-drive displacement and stability; Lee *et al.* [110] claimed that by making the ratio of height of fingers, h_f to the height of anchor spring, h_s significantly greater than one helps to achieve high displacement of the comb actuator. Increasing the h_f increases the generated capacitance; hence, the comb displacement will be increased.

Rosa *et al.* proposed a new angled comb finger design (Figure 2.9(d)) [108, 109]. They claimed that the structure achieved twice displacement of a standard rectangular comb finger and demonstrated twice force generation capability and at the same time maintaining overall device stability.

2.8 Manufacturing Variation in MEMS

With the present micro fabrication techniques, process variation is inevitable which leads to variability in the product features and product performance [111]. As revealed by Adams *et al.* [112], identical micromechanical resonators will always have variations in resonant frequency even when fabricated on the same die.

Many research studies have been carried out related to the manufacturing variations in MEMS. Most previous studies focused on reducing the performance variability of MEMS at design stages [24, 111, 113-118]. Other research introduced robust mechanical couplings to minimize the effect of inherent disorders in resonator arrays due to the fabrication variation [77, 78, 84, 86, 90, 119]. Few research studies have been conducted to estimate the

performance variation of the MEMS devices [120] and approaches to quantify the process variations [121].

2.8.1 Reducing the Performance Variability of MEMS at the Design Stage

Mawardi and Pitchumani [111] developed analytical models for the variability in the resonance frequency as the function of the parameter uncertainty (i.e. geometrical structure and material property). Their target was to minimize the variance of the natural frequencies and also satisfy target performance requirements.

Dewey *et al.* [113] presented robust design that minimizes the effects of parametric variability on overall performance of electrostatic comb-drive micro resonator. The research presented the formulation of statistical noise-sensitivity reduction for optimizing design performance stability and assessed the relative contribution of each design parameter to the optimized performance variability. Codreanu *et al.* [117] performed a deterministic modelling and simulation (i.e. Monte Carlo Simulation) using the ANSYS software in order to study the influence of the variability of design parameters on the performance of micro-comb resonators.

Zhu *et al.* [118] proposed robust control laws for a parallel plate electrostatic micro actuator in the presence of uncertainties. In order to ensure the stability of the actuator, the research included the parasitic capacitance (due to layout, fringing field, or deformation of moveable plate) and the parameter variations in the design of MEMS control systems.

2.8.2 Performance Variation Estimation and Process Variation Quantification

Schenato *et al.* [120] presented approaches to estimate performance variations for general planar suspended MEMS structure for low frequency applications. Two approaches were

discussed, based on Monte Carlo Method (probabilistic) and robust optimization and semidefinite programming (SDP) approximation.

Wittwer *et al.* [122] analysed and predicted the performance of the cantilever beam before fabrication by treating the material properties and dimensional parameters of the structure as random variables. The research concluded that the gauge uncertainties due to variations in material properties and dimensional parameters were found to be significant when compared with measurement repeatability especially for large cantilever deflections.

Li *et al.* [123] researched and discussed the origins of various DRIE fabrication tolerances together with its effect on the performance of a lateral comb drive actuator in terms of electrostatic force, mechanical stiffness, stability and displacement.

Hong *et al.* [124] studied the feasibility of the resonators as a vibrating microgyroscope with self-tuning capability. From their research they found that the fabricated resonator of a particular design has process-induced non-uniformities that cause different resonant frequencies and the sensitivity of microgyroscope was low due to process-induced non-uniformities.

Monitoring MEMS fabricated geometries is important to observe the change of the structure geometrical dimension due to the manufacturing variation effect. Gupta [121] explored an approach to quantify variation by using an optical microscope. He relies on the optical microscope and standard electronic test equipment used at the wafer level for independent measurements of geometry.

As discussed above, the effect of process variations on the MEMS fabricated devices is inevitable. Many researchers were focused to reduce the effect of the process variation in order to improve the device performance. This research will examine the effect of process variation by measuring the geometrical dimension of the fabricated resonator; the possible

effect of the variation on the coupled resonators is analysed. The variation may reduce some response of the coupled resonators or it may enhance a uniqueness of the CMRA to facilitate the system odour discrimination.

2.9 Summary and Focus of Thesis

As discussed the artificial nose is significantly important to replace the biological nose in certain industrial applications. This is due to the nature of the biological nose which is inconsistent in the detection performance and inherent conditions of the liquid and vapour which in the form of complex, volatile and hazardous compound.

Many sensor technologies have been integrated in the artificial nose based on different working principles as described in Section 2.3. Among those sensors, the resonant sensor such as QCM showed the highest sensor selectivity. Other resonant sensors provided room for further improvement in terms of sensitivity and response time. Many approaches are available to drive and readout the resonant sensor as reviewed in Section 2.5. The research of the CMRA structure will demonstrate the use of electrostatic excitation and capacitive detection to drive and readout the response of the coupled resonant sensor.

As presented in Section 2.6, the coupled resonators (i.e. overhang coupled cantilevers) has been employed as mass sensors; it have been used to improve the performance of band pass filters, reduce the manufacturing process non-idealities, and to study the effect and phenomenon of non-linear behaviour in MEMS devices. This research will exploit the approach of the coupled resonators as an alternative to simplify the complexity of a large artificial nose sensing system. The frequency response pattern of the coupled resonators may be used to monitor a state of each multiple resonant sensors.

The comb-drive actuator can be observed as one of the most versatile and robust MEMS structure. From the review in Section 2.7, the comb drive can be integrated for on-chip application and designed to suit certain MEMS requirement. However, the performance and stability of the comb drive are limited by its geometrical design parameter, design of its anchor spring and the input voltage to drive the resonator. This thesis will discuss the use of the comb drive as an actuator to drive the first version of the CMRA structure (CMRA-v1) in Chapter 3 and the application of the comb drive as a resonator sensor element of the second version of the CMRA in Chapter 4 and 5.

As reviewed in Section 2.8, the presence of manufacturing variation significantly may reduce the performance of MEMS devices. However, the process variation itself may inherently help to improve some performance of the MEMS device such as in the case of coupled micro resonator array sensor structure (CMRA) [125]. Further analysis will be presented and discussed in Chapter 5; how the process variation may affect the performance of the CMRA sensor structure.

In consequent to the reviews, Chapter 3 will discuss considerations and constrains of the design elements of the first version of the CMRA (CMRA-v1) which is fixed-fixed beam resonators coupled together with butterfly shape coupling springs. An improved CMRA-v2 structure which is based on an integrated coupled comb-drive resonators is modelled and analysed in Chapter 4 and 5. The fabrication processes of the CMRA are explained in Chapter 6. Overall measured frequency response of the CMRA and the CMRA sensor performance are discussed in Chapter 7.

CHAPTER 3 - DESIGN, MODELLING AND FINITE ELEMENT ANALYSIS OF CMRA-V1

3.1 Introduction

This chapter presents the modelling, finite element analysis (FEA) and performance evaluation of the first version of the coupled micro resonator array sensor structure (CMRA-v1). Section 3.2 highlights design elements of the structure and justify all the design constraints and considerations of the sensor structure. The detail design, modelling and performance evaluation of the CMRA-v1 structure (including fixed-fixed beam resonator, butterfly shaped coupling spring and tilted folded comb drive actuator) are described and discussed in Section 3.3, 3.4 and 3.5 respectively. Section 3.6 analyses and discusses a design of the single fixed-fixed beam resonator coupled with a simple comb drive actuator for frequency response measurement and analysis of the single resonator (singleR-v1). Section 3.7 summarizes the performance of the simulated CMRA-v1 structure element and overall achievement in Chapter 3.

3.2 Constraints and Design Considerations

As introduced in Chapter 1, the coupled micro resonator array (CMRA-v1) structure consists of 3 structural elements which are:-

- Resonator sensor
- Mechanical coupling spring
- Comb drive actuators

In order to design and model the CMRA-v1 structure, this research includes all the possible constraints and considerations which may affect the final geometrical design parameters of the structure.

3.2.1 Drive-Readout System Constraint

(a)

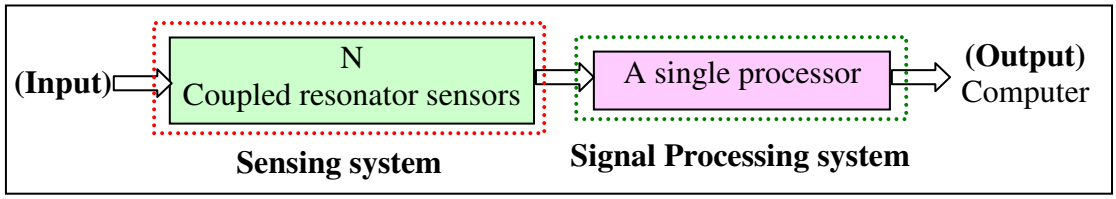

(b)

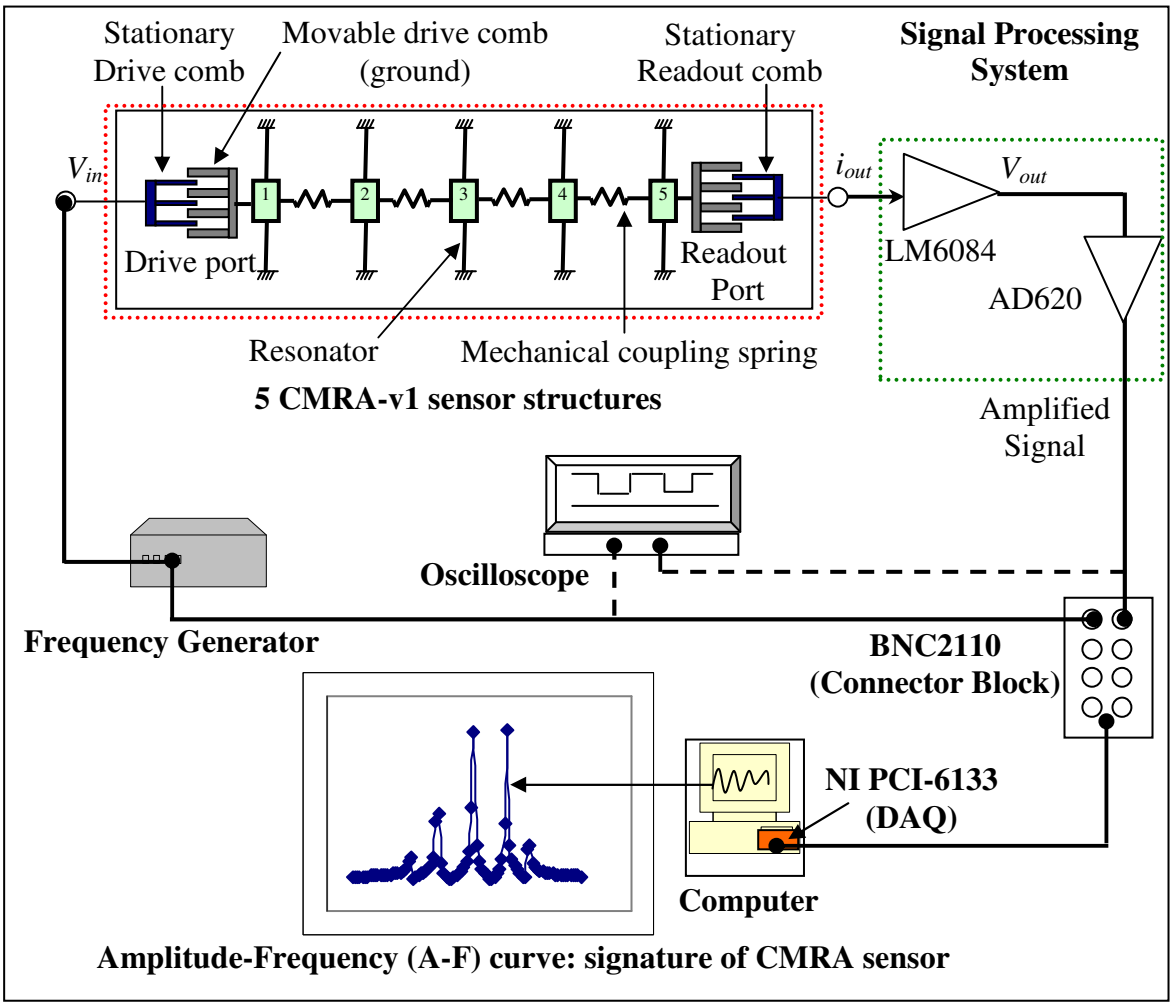

Figure 3.1 (a) A simplified schematic of sensing and processing system of an artificial nose using CMRA sensor structure; (b) Schematic of CMRA-v1 with 2 ports input/output (I/O) connections to measure the frequency response of the sensor structure

Figure 3.1 (a) and (b) illustrate the CMRA-v1 structure and the drive-readout connections in order to monitor the output signal of the structure. As illustrated in Figure 3.1(b) the CMRA-

v1 requires an input voltage, V_{in} (V_{AC}) to drive the structure electrostatically. A difference in voltage between the stationary and movable drive comb generates an electrostatic force to excite and vibrate the movable driven comb and the structure coupled to it. The movement of the movable readout comb generates a current (i_{out}) at the stationary readout comb due to the fluctuation of the capacitance between the two readout combs. The i_{out} is converted to a voltage (V_{out}) by using the transimpedance amplifier. The output signal is further amplified before it is measured.

The resonant frequencies of the CMRA can be observed by connecting the amplified signal to the oscilloscope and sweeping through the range of natural frequencies of the CMRA using a frequency generator. The frequency response of the CMRA structure (Amplitude-Frequency (A-F) curve) is measured and monitored on the computer by automatically sweeping the frequencies of the coupled structure via the shielded connector block (NI BNC2110) [126] and the data acquisition system (DAQ) (NI PCI-6133) [127]. The research focuses on a development of the CMRA structure (as highlighted in Figure 3.1(b) with red dotted line) and uses the readout measurement system (signal processing system) which was developed by Ross Turnbull, Oxford University.

The developed readout system uses LM6084 transimpedance amplifier to convert the generated current at the readout port (i_{out}) to an output voltage, V_{out} (Figure 3.1(b)). An AD620 Instrumentation amplifier was used to further amplify the signal to V_{INA}. Some requirements of these amplifiers are:-

- The input bias current for the LM6084 [128] must be at least 1nA. The LM6084 amplifier turns the current to 1mV voltage. Then the AD620 amplifiers [129] amplifies the 1mV voltage into 10 to 20 mV final output voltage which required by the readout facilities.

- From design specifications, the amplifiers are suitable to be used for a low frequency bandwidth application, i.e. between 10 to 100 kHz. Increase in the frequency response reduces the performance of the amplifier. For example, by increasing the frequency from 10 to 100 kHz, the output voltage of the AD620 amplifier, V_{INA} reduces from 28 to 4 Volts p-p. The CMR (Common Mode Rejection) and PSRR (Power Supply Rejection Ratio) of the AD620 are also decreased about 20 dB [129].

The use of data acquisition system (DAQ), NI PCI-6133 [127] with 2.5 Ms/sec may also limit the frequency of the CMRA structure. As an example, at the maximum of 200 kHz, the system only manages to measure around 12 points per cycle. For more accurate measurement, the structure frequency must be reduced, to increase number of points that can be measured by the DAQ per cycle.

Taking into consideration the requirements and constraints of the readout facilities [129], the first version of the CMRA structure (CMRA-v1) was designed with the 5 eigenfrequencies lie on a centre frequency around 50 kHz.

3.2.2 Expected CMRA Output Signal

3.2.2.1 Distinctive (Unique) Response Pattern

It is important for the CMRA structure to have a unique frequency response pattern as a finger-print or a signature to represent each single or multiple resonator sensors . Since the CMRA sensor structure is designed to selectively absorb a particular mass; so the signature can be used to associate the mass and the resonators which absorb the mass. Hence, the identity of the mass can be traced.

3.2.2.2 Coupling Modes

The frequency response pattern of the 5 coupled resonators depends on the 5 modal eigenfrequencies of the structure. These eigenfrequencies correspond to the 5 eigenmodes of the coupled resonators. The CMRA structure must be designed to ensure that no unwanted coupling modes between the 5 main wanted modes. The fundamental frequency of each element connected to the resonator (i.e. the mechanical coupling spring and the comb actuator) must be designed to be outside the range of the main 5 eigenfrequencies of the CMRA. The unwanted coupling modes may decouple the synchronization of the structure movement. In turn, it may reduce the sensitivity of sensor response and the measurability of the main response pattern of the sensor structure.

3.2.2.3 Measurable (Readable) Signal

The measurability of the CMRA output signal relies on the sensitivity of the readout measurement facilities, which in turn depends on the amount of the generated current, i_{out} at the readout port (refer to Figure 3.1(b)). The current, i_{out} is a proportion to the induced capacitance between the movable and stationary readout combs. It is related to the overall displacement of the coupled structure and the geometrical design of the comb fingers. Therefore, to ensure the output signal of the structure is measurable, the design of the CMRA-v1 is guided by an aim to ensure the structure generates enough capacitance to satisfy at least the minimum amount of the i_{out} at the readout port.

3.2.3 Fabrication Constraints

The main constraint deals with the limit of the lithography machine to transfer patterns of the structure design to the wafer. The research uses a Canon Mask Aligner PLA-501FA in the

lithography process. A minimum of 2 to 3μm structure size is proposed to be used for good resolution of the transferred patterns [130, 131]. In addition, the mask which is out-sourced also limits the geometrical dimensions of the CMRA structure. The practical resolution of the design to be written on the mask is at least 1μm [132]. To include the constraints of the mask design and the mask aligner machine, the research designs the CMRA-v1 with a minimum of 2.5μm geometrical structure dimension.

3.3 Design and Finite Element Analysis of the Fixed-Fixed Beam Resonator

3.3.1 Design Considerations

In order to reduce any possibility of energy losses (for high Q-resonator), the fixed-fixed beam with a lateral prime mode vibration was chosen as the resonator element of the CMRA-v1. Comparing the fixed-fixed beams (a bridge), and cantilever beam resonators, the fixed-fixed beam is more sensitive to a change of a mass [133]. The lateral mode vibration may help to reduce energy losses due to viscous and acoustic damping.

The damping losses can be reduced by facilitating the movement of gas surrounding the vibrating beam. This is accomplished by reducing the effective surface area of the resonator which is perpendicular to the resonator movement. This section analyses the structure performance based on a 5μm structure thickness.

3.3.2 Fixed-Fixed Beam Resonator Design

Figure 3.2 illustrates a schematic of the top view layout of the fixed-fixed resonator and its geometrical design parameters. The final geometrical design parameters was confirmed by examining how the geometrical design parameters may affect the natural frequency, effective mass and effective stiffness of the resonator using numerical analyses.

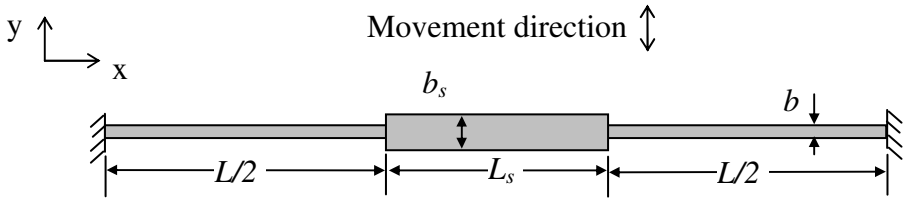

Figure 3.2 Schematic of a fixed-fixed beam resonator (top view)

The natural frequency, ω_n of the beam was determined by [63, 90, 134]:-

$$\omega_n = \sqrt{\frac{k_b}{m_{eff}}}\ ; \qquad \text{(Equation 3-1)}$$

Where, k_b is an effective resonator stiffness *and* m_{eff} is an effective mass of the resonator; The effective stiffness of the resonator, k_b was estimated as follows [135, 136]:-

$$k_b = \frac{192EI}{L_{eff}^{\ 3}}; \qquad I = \frac{hb^3}{12}; \qquad \text{and} \qquad L_{eff} = L - L_s \qquad \text{(Equation 3-2)}$$

Where E: Young's Modulus of the beam material (Silicon = $170\text{x}10^9$ [Pa]); and I: Second moment of area of the fixed-fixed beam; h: thickness of the beam.

The effective mass of the resonator, m_{eff}, was determined using the Rayleigh – Ritz method [134]. Rayleigh's principle is a common method used to find the natural frequency of vibrating systems. The accuracy of Rayleigh's method depends on how closely one can estimate the dynamic deflection curve. The static deflection curve is often used to approximate the dynamic deflection for the fundamental mode [134, 137]:-

$$m_{eff} = m_c + \frac{13}{35} m_b \qquad \text{(Equation 3-3)}$$

Where, m_c: a concentrated mass at the midspan of the beam ($m_c = b_s L_s h \rho_{silicon}$); and m_b: mass of beam of the resonator ($m_b = b\ Lh \rho_{silicon}$); $\rho_{silicon} = 2329$ kg/m^3.

Details of the design parameter of the fixed-fixed beam resonator are presented in Table 3-1.

Table 3-1 Details of the geometrical design parameter of a fixed-fixed beam resonator

Geometrical Design Parameter	Dimension [μm]
Length of beam, L	500
Width of resonator, b	3
Length of controlled surface area, L_s	200
Width of controlled surface area, b_s	10

3.3.3 Modelling and Finite Element Analysis (FEA)

The finite element analysis (FEA) was used to further model and analyse the structure performance. The modelling was performed using COMSOL Multiphysics Software to determine the performance of the resonator including the natural frequency, the effective stiffness and mass, and frequency response (Amplitude-Frequency curve) of the single resonator. Appendix A highlights the important considerations in FEA using COMSOL software which includes the simulation processes using the predefined physics modes and the effect of stability and mesh quality on the simulation result.

3.3.3.1 Eigenfrequency of Single Resonator

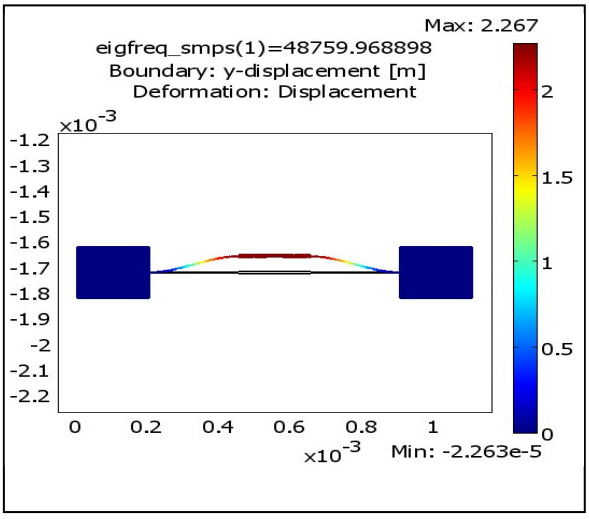

Figure 3.3 Eigenfrequency analysis result of fixed-fixed beam resonator

The natural frequency and mode shapes in COMSOL are determined using eigenfrequency analysis. The eigenfrequencies in COMSOL are related to eigenvalues, λ; ($\lambda = \omega^2$). By setting the material properties of the structure (i.e. silicon), boundary constraints (fixed and free elements), solver parameters and initializing structure mesh, the solver returned the frequency, f value through Equation 3-4 [138]. Figure 3.3 shows the result of the eigenfrequency analysis of the beam (f ~ 48760 Hz), with neglected damping condition.

$$f = \frac{\sqrt{\lambda}}{2\pi} \qquad \text{(Equation 3-4)}$$

3.3.3.2 Effective Mass and Stiffness of Single Resonator

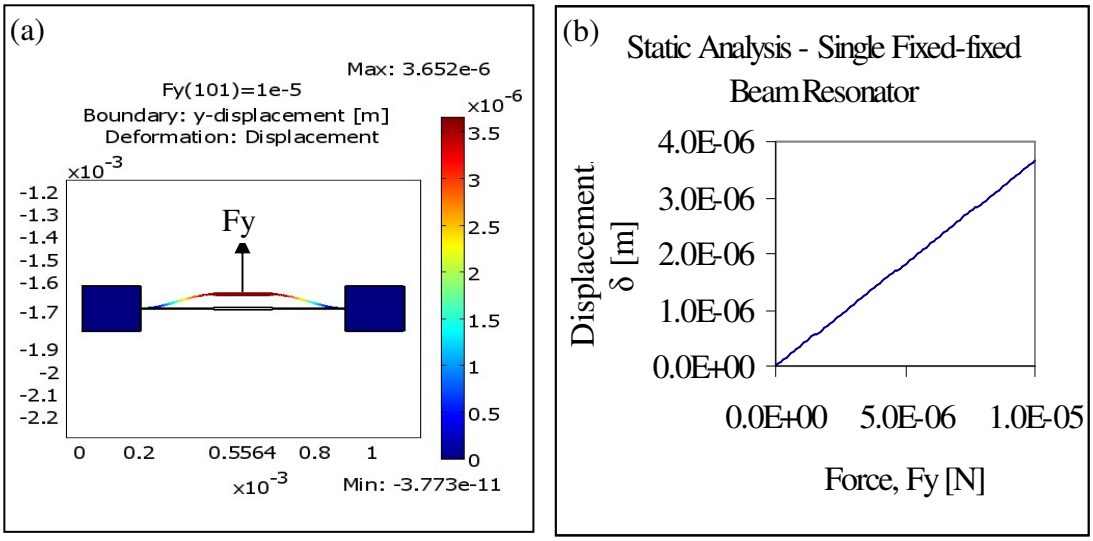

Figure 3.4 Static analysis result of the fixed-fixed beam resonator

The spring constant (stiffness) of the resonator, k can be found from a linear relationship between force, F_y and displacement, δ:-

$$k = F_y / \delta \qquad \text{(Equation 3-5)}$$

In COMSOL the analysis was performed using static analysis and the parametric solver, which required multiple inputs or a range of input forces. As shown in Figure 3.4 (a), by

setting the input force *Fy* at the midspan of the beam, the solver returns the static displacement of the beam Figure 3.4 (b). Equation 3-5 is used to calculate the spring constant of the fixed-fixed beam resonator. The effective mass was calculated by substituting the spring constant and natural frequency of the resonator in Equation 3-1, which returns m_{eff} = 2.92 x 10^{-11}kg.

3.3.3.3 Frequency Response of the Fixed-Fixed Beam Resonator

This analysis was performed using the parametric solver to determine the Amplitude-Frequency (A-F) curve of the resonator. The frequency response, $F_{freq,}$ in COMSOL is calculated using Equation 3-6 [138]:-

$$F_{freq}=FF_{Amp}(f)\cos\left(2\pi ft+F_{Ph}(f)\frac{\pi}{180}\right) \qquad \text{(Equation 3-6)}$$

The software solves for a steady state response from harmonic excitation loads, *F*, with a range of excitation frequency, *f* near the fundamental frequency of the resonator (which is determined from the eigenfrequency analysis). To analyse the response of the fixed-fixed resonator, the analysis assumed and set *F*= 1x10^{-6}N and *f* = 45000-55000Hz. F_{Amp} is an amplitude factor and $F_{ph,}$ is a phase shift, which were set to 1 and 0 (based on default value) respectively.

The frequency response curve also depends on the damping parameter, c. In COMSOL modelling, the damping parameter c is expressed in the form of mass, *m* and stiffness, *k* based on the Rayleigh Damping Model:-

$$c=\alpha_{dM}m+\beta_{dK}\kappa \qquad \text{(Equation 3-7)}$$

Where, α_{dM}: Mass damping parameter; and β_{dK}: Stiffness damping parameter. The relationship between Rayleigh damping parameter and damping factor or damping ratio, ξ [138]:-

$$\xi = \frac{1}{2}\left(\frac{\alpha_{dM}}{2\Pi f} + \beta_{dK}\, 2\Pi f\right) \quad ; \; \xi = \frac{c}{c_C} = \frac{c}{2m\omega_n} = \frac{1}{2.Q} \qquad \text{(Equation 3-8)}$$

Where, c_C: critical damping; f: excitation frequency; ω_n: natural frequency of the structure and Q: the resonator quality factor. By setting the value of α_{dM} and β_{dK} the appropriate damping condition can be modelled in COMSOL. This section examines the performance of the fixed-fixed beam at different damping factors, ξ. = 5e-5, 5e-4, 5e-3, 0.05 (or Q = 10000, 1000, 100, 10 respectively) and at no damping condition.

3.3.4 Performance of the Fixed-Fixed Beam Resonator

Table 3-2 Performance parameter of the fixed-fixed beam resonator

Description of Performance Parameter	Numerical Analysis	Simulation
Natural frequency, f [Hz]	49990.00	48759.97
Effective stiffness of beam, k_b [N/m]	2.94	2.74
Effective mass of beam, m_{eff} [kg]	2.98 x 10^{-11}	2.92 x 10^{-11}
Force, F [N] (at δy = 1x10^{-6} [m])	2.9 x 10^{-6}	2.8 x 10^{-6}

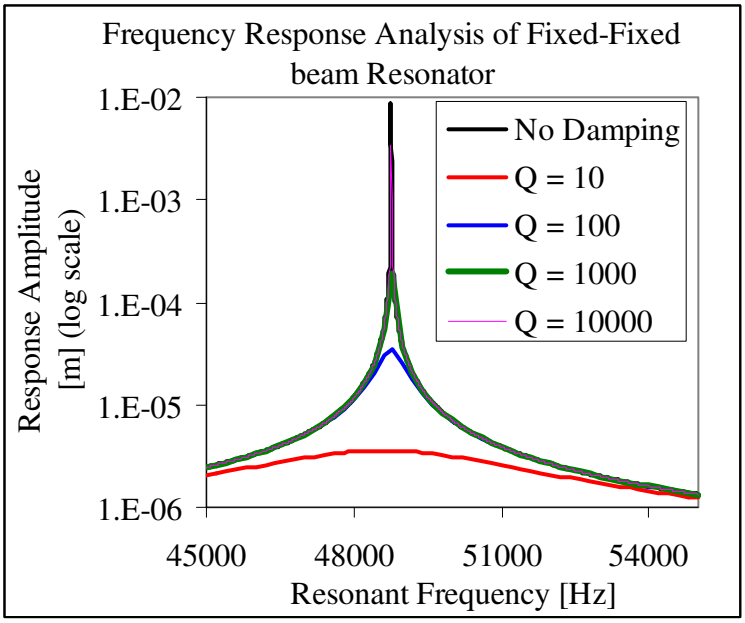

Figure 3.5 Frequency response analysis of fixed-fixed beam resonator

Table 3-2 lists the analysed performance of the fixed-fixed beam resonator using numerical analysis and FEA. As can be observed, the parameter which was analysed using numerical analysis is slightly higher compared to the FEA result. This is expected due to over estimation of the effective mass and stiffness of the resonator which was evaluated based on static deflection curve. From the analysis, the beam requires at least 2.8μN forces to displace the resonator to 1μm.

Figure 3.5 shows the frequency response analysis result for the fixed-fixed beam resonator at different quality factors, Q (10, 100, 1000 and 10000) and at no damping condition. Increasing the damping factor, ξ reduces the response amplitude and increases the response bandwidth of the resonator. For example, increasing the damping factor from 5 x 10^{-5} to 5 x 10^{-4} (10x) reduces the amplitude of the beam to a factor of 17. The damping diminishes the Q-factor of the resonator and flattens the A-F curve of the resonator. This research mitigates the effect of damping by measuring the response of the resonator in a vacuum condition.

3.4 Mechanical Spring Coupling

3.4.1 Design Considerations

The performance of the sensor structure mainly depends on the displacement of the sensor along the excitation axis. Therefore, the spring must be more flexible along the excitation axis and rigid in the perpendicular axis. To ensure the CMRA works effectively, the mechanical springs must be designed so that not to introduce any unwanted eigenmodes within the main modal frequencies of the coupled structure.

To date most of the existing micro springs reported in the literature [119, 139-143] do not meet these requirements. For example with simple zigzag shape spring (Figure 3.6), the

spring may introduce spurious responses due to torsion and elongation of the spring element in Y-axis during the operation [144]. As a consequence the response amplitude (X-axis) of the sensors structure may be reduced.

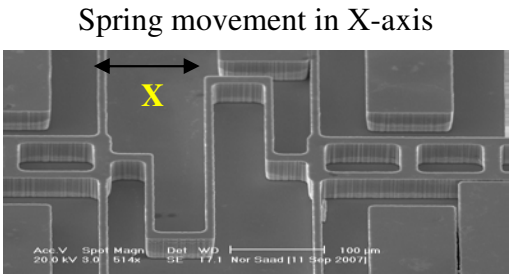

Figure 3.6 Scanning Electron Microscope (SEM) image of zigzag coupling spring

Overall frequency bandwidth of the response relies on the mechanical coupling [145] between each resonator. The spring should be designed, so that the stiffness can be controlled easily by configuring the design parameters of the spring. Considering all the constraints, this research introduces a new closed loop butterfly shape spring, in order to couple the resonator array sensor structure together.

3.4.2 Closed Loop Butterfly Shape Spring Design

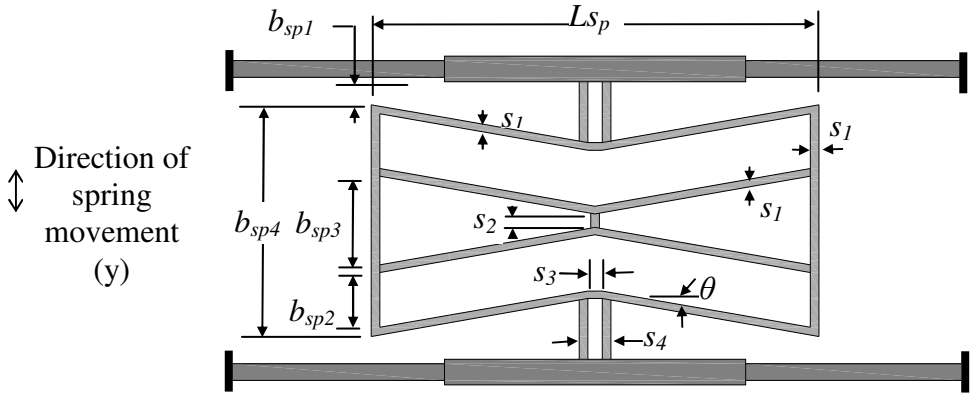

Figure 3.7 Schematic of a closed loop butterfly spring design used to couple 2 fixed-fixed beam resonators

Figure 3.7 shows a schematic diagram of the butterfly spring design. The spring was designed with joined-tilted beams in order to increase the displacement of the springs along the excitation axis. Any possibilities of the torsion and elongation of the spring elements in x-axis are reduced by fixing the middle of the spring structure. Table 3-3 highlights the detail geometrical design parameter of the spring.

Table 3-3 Details of geometrical design parameter of butterfly spring (Figure 3.7)

Geometrical Design Parameter	Dimension [μm]
Width of spring element 1, S_1	2.5
Width of spring element 2, S_2	7.9
Width of spring element 3, S_3	10
Width of spring element 4, S_4	15
Tilted angle of element 1, θ	11^o
Spring width 1, b_{sp1}	10
Spring width 2, b_{sp2}	71
Spring width 3, b_{sp3}	103
Spring width 4, b_{sp4}	255
Spring length, L_{sp}	500

3.4.3 Performance of Butterfly Spring using FEA

Table 3-4 Performance parameter of butterfly spring

Performance Parameter	Value [unit]
Natural Frequency, $\omega_{n(sp)}$	30545.6 [Hz]
Spring constant, k_{csp} (y), k_{csp} (x)	(y) 0.4578 [N/m]; (x) 2.772 x10^4 [N/m]
Static displacement , Y (at maximum 1e-5 force [N])	22 [μm]
Spring effective mass, m_{effsp}	1.2429 x10^{-11} [kg]

Finite element analysis using COMSOL Multiphysics was used to examine the performance parameter of the butterfly spring, which includes the natural frequency and mode shape of the

structure, the spring constant and effective mass of the structure. The analyses were performed as discussed earlier in Section 3.3.3.

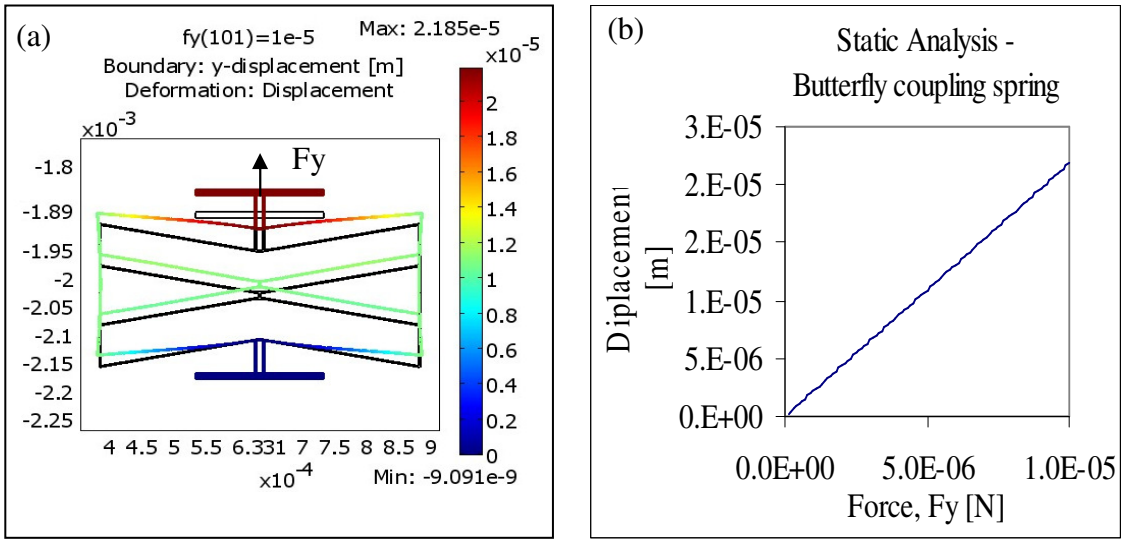

Figure 3.8 Static analysis result of butterfly coupling spring

Table 3-4 highlights the simulated parameter of the designed butterfly spring; with the fundamental mode of the spring is 30.546 kHz. The stiffness ratio of the spring ($k_{csp(x)}$/ $k_{csp(y)}$) is 6.06 x10^4. From the static analysis result (Figure 3.8 (b)), at 1μN force the spring displaces at 2.18μm.

To examine whether any possibility of unwanted eigenmodes may be introduced by the designed butterfly spring within the main modal frequencies of the coupled structure, the first six eigenmodes of the structure were observed (from eigenfrequency analysis). Figure 3.9 illustrates the first 6 eigenmodes (of the 6 eigenfrequencies) of the simulated butterfly spring. From the analysis, it was observed that only the second mode of the spring (f(2) = 61.116 kHz, Figure 3.9(b)) is quite close to the targeted range of the designed frequency of the CMRA (i.e. 50 kHz). At this mode the spring starts to twist (Figure 3.9 (b)); however, the fixed mid-joined beams helped to reduce any displacement of the spring in x-axis. Further

analysis is required to examine the effect of the coupling constant on the frequency response (A-F curve) of the coupled structure.

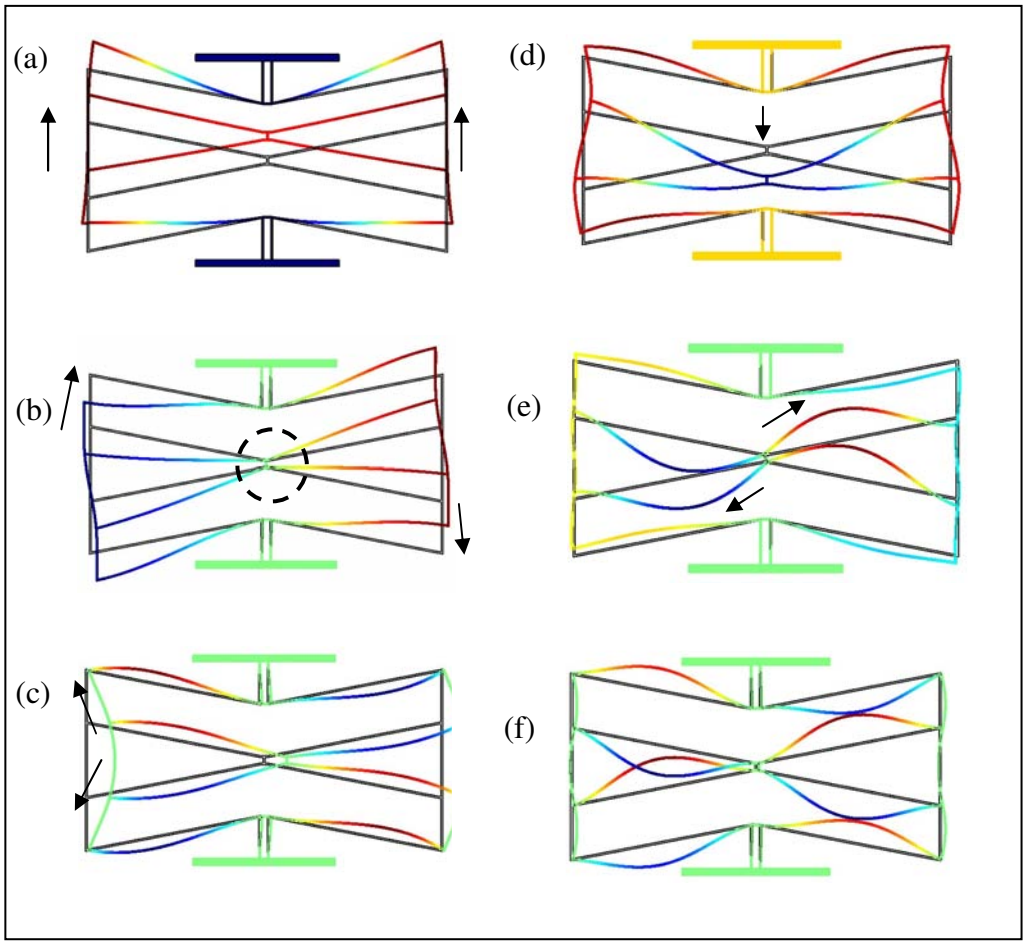

Figure 3.9 Eigenfrequency analysis result of the first 6 eigenmodes of butterfly spring: (a) mode1: 30.546 kHz (fundamental mode); (b) mode2: 61.116 kHz; (c) mode3: 119.592 kHz; (d) mode4: 139.639 kHz; (e) mode5: 235.256 kHz; (f) mode6: 291.452 kHz.

3.4.4 Effect of Coupling Constant

In analyzing the effect of coupling stiffness, k_c on the frequency response of the coupled system, two designs of the butterfly spring (sp_1 and sp_2) with varied coupling stiffness were considered and compared with the coupling spring which was presented in Section 3.4.2.; k_c (sp_1)= 0.1149N/m, k_c(sp_2)= 0.6746, and k_c($sp_{CMRA\text{-}v1}$, Section 3.4.2)= 0.4578 N/m.

Table 3-5 Geometrical design parameters of the coupling spring (All dimensions in µm unit)

Geometrical Parameter Description	sp_1	sp_2
Width of spring element 1, S_1 [µm]	1	1
Width of spring element 2, S_2 [µm]	10.7	10.5
Width of spring element 3, S_3 [µm]	10	10
Width of spring element 4, S_4 [µm]	12	12
Tilted angle of element 1, θ	11°	11°
Spring width 1, b_{sp1} [µm]	23	36.5
Spring width 2, b_{sp2} [µm]	53	53
Spring width 3, b_{sp3} [µm]	72	45
Spring width 4, b_{sp4} [µm]	182	155
Spring length, L_{sp} [µm]	312	175
Spring thickness, h [µm]	5	5
Natural Frequency, ω_n [Hz]	29930.3	84449.9
Effective mass, m_{eff} (x 10^{-11}) [Kg]	0.32	0.24
Coupling stiffness, k_{csp} [N/m]	0.1149	0.6746
Stiffness ratio (k_b: k_{csp})	25.6:1	4.1:1

To design sp_1 and sp_2 the geometrical dimensions of the butterfly spring in Figure 3.7 (Section 3.4.2) were modified. The spring length (L_{sp}) and the spring width (b_{sp}) were adjusted to produce the required spring constant. Table 3-5 highlights the final geometrical dimension of the 2 springs including its spring constant and a coupling stiffness ratio between the fixed-fixed beams resonator (k_b = 2.74 N/m) and the coupling spring, k_{csp} (k_b: k_{csp}). Please note that the coupling stiffness of each spring was determined using FEA.

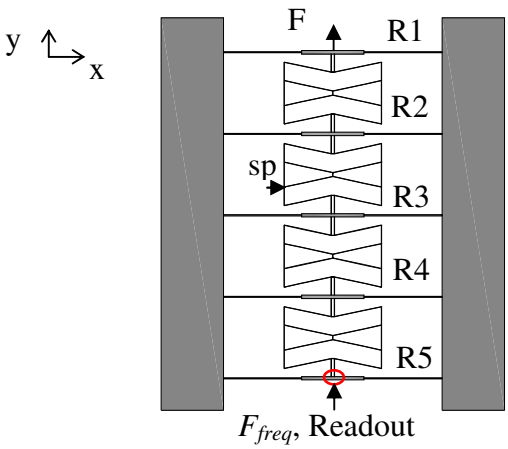

Figure 3.10 Schematic of 5 fixed-fixed beam resonators (R1(resonator 1), R2, R3, R4 and R5) coupled with butterfly coupling spring, sp

To examine the effect of coupling stiffness and coupling ratio on the coupled resonators, each coupling spring (sp_1, sp_2, and $sp_{CMRA\text{-}v1}$) was coupled to 5 fixed-fixed beam resonators (refer to Section 3.3.2; the design of the fixed-fixed beam resonator). An example of the coupled structure is illustrated in Figure 3.10.

Using COMSOL Multiphysics software, eigenfrequency analysis was performed to determine the modal frequencies (f_M) of the coupled resonators. The frequency response analyses were conducted to examine the overall pattern of the frequency bandwidth, separation of the modal frequencies and the response amplitude of the coupled structures. Each analysis was conducted at no damping condition with the excitation frequency, f within the range between the first and fifth modes of the natural frequency of the system as determined by the eigenfrequency analysis. The harmonic excitation, F was assumed to be 1μN, pulling in the +y-axis at R1 (Figure 3.10). The frequency response (F_{freq}) of the coupled structure was monitored at another end of the coupled resonators, R5.

Table 3-6 Eigenfrequency analysis result of the coupled structure using FEA

Spring k_c [N/m]	Modal frequency of coupled resonators, f_M [kHz]				
	mode1 f_{M1}	mode2 f_{M2}	mode3 f_{M3}	mode4 f_{M4}	mode5 f_{M5}
sp_1, 0.1149	48.2	48.6	49.4	50.2	50.8
$sp_{CMRA\text{-}v1}$, 0.4578	48.5	49.6	51.8	53.8	55.1
sp_2, 0.6746	39.9	43.6	49.8	56.4	62.2

As presented in Table 3-6, the five modal frequencies of the coupled resonators rely on the stiffness of the coupling spring. Stiffer spring increases the bandwidth of the frequency response and reduces the amplitude of the responses. For example when the resonators (f_R = 48.760kHz) were coupled with sp_1 (k_c = 0.1149N/m) the bandwidth of the 5 ripples is 2600 Hz. However, when the resonators were coupled using sp_2 (k_c = 0.6746N/m) the overall

bandwidth drastically increases to 22300Hz (Figure 3.11). Comparing between the stiffness of the spring and the maximum amplitude responses of the coupled structure (Figure 3.11); a 6x increase in the coupling constant, reduced 12x the response amplitude of the coupled structure.

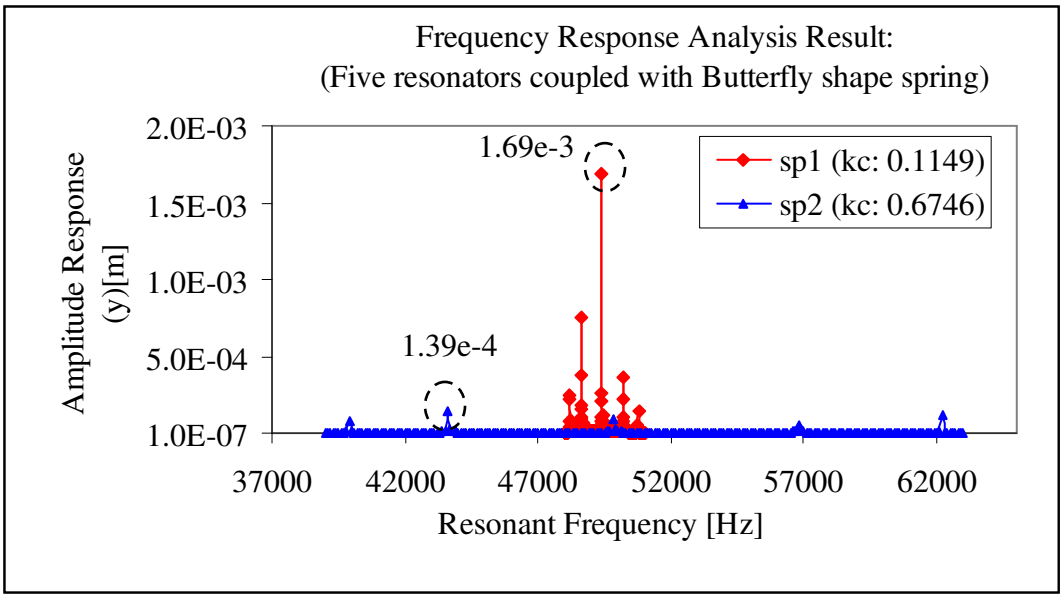

Figure 3.11 The effect of coupling constant on the response amplitude of the coupled resonators

By properly configuring the design parameters of the butterfly spring, the coupling stiffness can easily be controlled so as to adjust the separation of the modal frequencies and overall frequency bandwidth to suit with the application.

3.4.5 Uniqueness of CMRA Frequency Response Pattern Analysis using FEA

The performance of the CMRA mainly depends on the distinctiveness of the output signal when either any single or coupled resonators sensor absorbs the mass. To analyse the uniqueness of the response pattern of the CMRA-v1, consider the 5 fixed-fixed beam

resonators which were coupled with the sp_1 butterfly shaped spring (refer to Figure 3.10 and Table 3-5).

Using COMSOL FEA, two type of analysis were performed (refer to Section 3.4.4); Eigenfrequency analysis was used to determine the frequency shift of the sensor structure when each of the resonator sensors mass is changed and frequency response analysis for the overall frequency response pattern of the CMRA structure. Six tests were conducted (T0, T1-T5). Test T0 determined the initial condition, where no mass was added to any of the resonators. Five tests T1, T2, T3, T4 and T5 were conducted by separately adding a mass of 0.5% of m_c (concentrated mass at the midspan of the beam, ~2.33 x 10^{-13} kg) to the mass of each resonator R1, R2, R3, R4 and R5 respectively. Table 3-7 highlights the shift of the 5 modal frequencies of the coupled structure when each resonator (R1, R2, R3, R4, and R5) absorbs similar amount of mass separately.

Table 3-7 Frequency response analysis result using FEA; the shift of 5 eigenfrequencies when the single resonator absorbs 2.33 x 10^{-13} kg mass separately

Testing Condition	Modal frequency of Coupled resonators, f_M [Hz]				
	f_{M1}	f_{M2}	f_{M3}	f_{M4}	f_{M5}
T0: Initial condition (no added mass)	48638	48638	49407	50209	50772
T1: +m @ R1 (mass added at R1 only)	48197	48615	49385	50196	50769
T2: +m @ R2	48192	48626	49406	50189	50757
T3: +m @ R3	48191	48638	49381	50209	50750
T4: +m @ R4	48192	48626	49406	50189	50757
T5: +m @ R5	48197	48615	49385	50196	50769

As can be observed from Table 3-7, the shift of the modal frequency of the structure are always similar between R1 and R5 , or R2 and R4 when they absorbed similar amount of

mass. Figure 3.12 shows an example of the frequency response pattern of the coupled structure for test 2 (T2) and test 4 (T4).

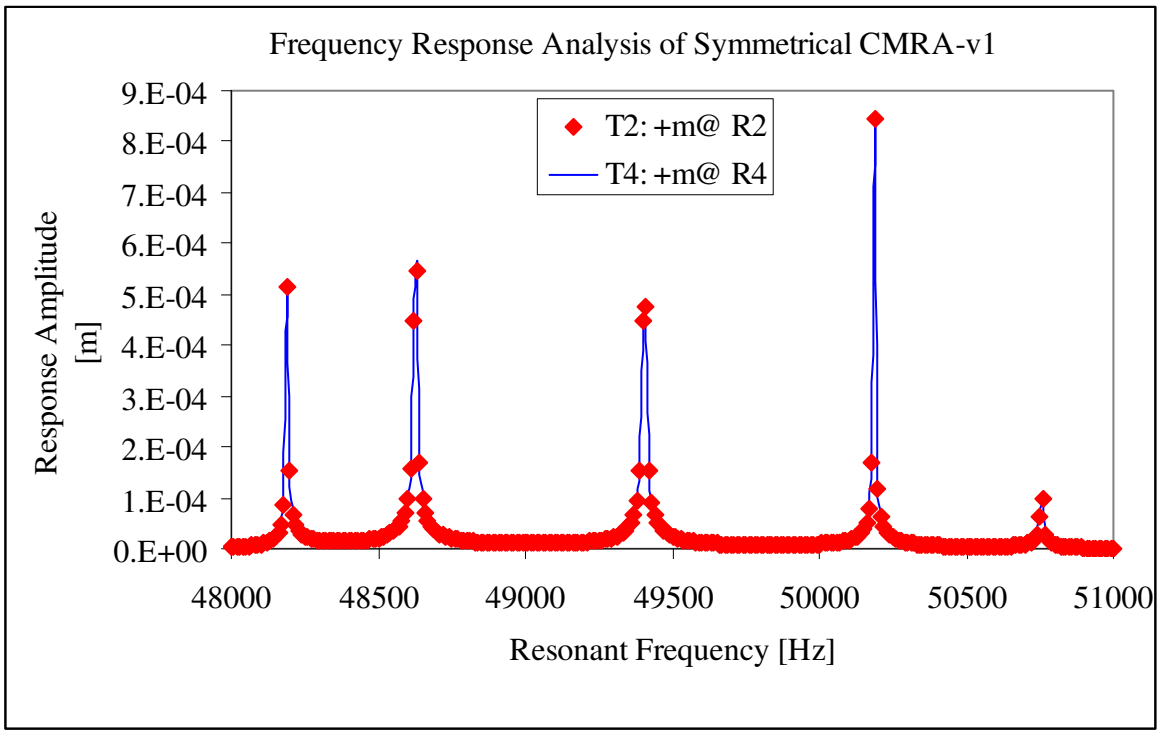

Figure 3.12 Frequency response analysis result of constant mass CMRA

From Figure 3.12, it can be seen that due to a symmetrical CMRA design with the constant resonator mass or identical resonators the response pattern of the first half of the resonator always mirrors the response pattern of the second half of the CMRA (i.e. R1 mirrors R5 and R2 mirrors R4).

The constant CMRA produced a potential problem, where the effect of mass changes on the single resonator is ambiguous. The change of the mass is difficult to associate with a particular resonator. As a result the identity of the absorbed mass cannot be traced. Further analysis is required to improve the CMRA design by breaking the structure symmetry to ensure a unique frequency response pattern either for a single or multiple resonator sensors. The CMRA structure improvement will be discussed in Chapter 4 and 5.

3.5 Comb Actuator

3.5.1 Design Considerations

The comb actuator was employed to drive and measure the output signal of the 5 CMRA-v1. The comb drive actuator should be designed so that enough capacitance is produced between the moving and fixed fingers. The induced capacitance is important to stimulate the electrostatic force to drive the coupled structure and to generate the current at the readout port, i_{out}. At least 1nA current is required in order to measure the response of the CMRA-v1 (see Section 3.2.1).

As analyzed in Section 3.4.4, the main 5 eigenfrequencies of the coupled structure lay between 48.5kHz and 55.1kHz when coupled with the selected butterfly spring ($sp_{CMRA\text{-}v1}$). The eigenfrequency of the comb actuator should be designed outside of the main frequency range to reduce any unwanted mode couplings. To ensure larger displacement of actuator for measurable response, the comb actuator must be flexible in the direction of movement (y-direction). Any possibility of side instability must be avoided by ensuring the actuator rigid in the x-direction.

3.5.2 Comb Actuator Design

Figure 3.13 depicts the schematic of the designed comb actuator for the drive and readout port and Table 3-8 highlights the main geometrical design parameters of the actuator. The research used a tilted-folded beam to anchor the comb actuators. The tilted-folded beam was employed to improve the stability of the comb actuator and enhancing the stable travel range [107]. The increase of width of comb finger b, and number of fingers, increases the electrostatic driving force. However, the design needs to consider the effect of the design

parameters on the effective mass and the final size of the comb actuator. Decreasing the gap also increased the generated electrostatic force. However, too small gap may reduce the stability of the travel range of the actuator.

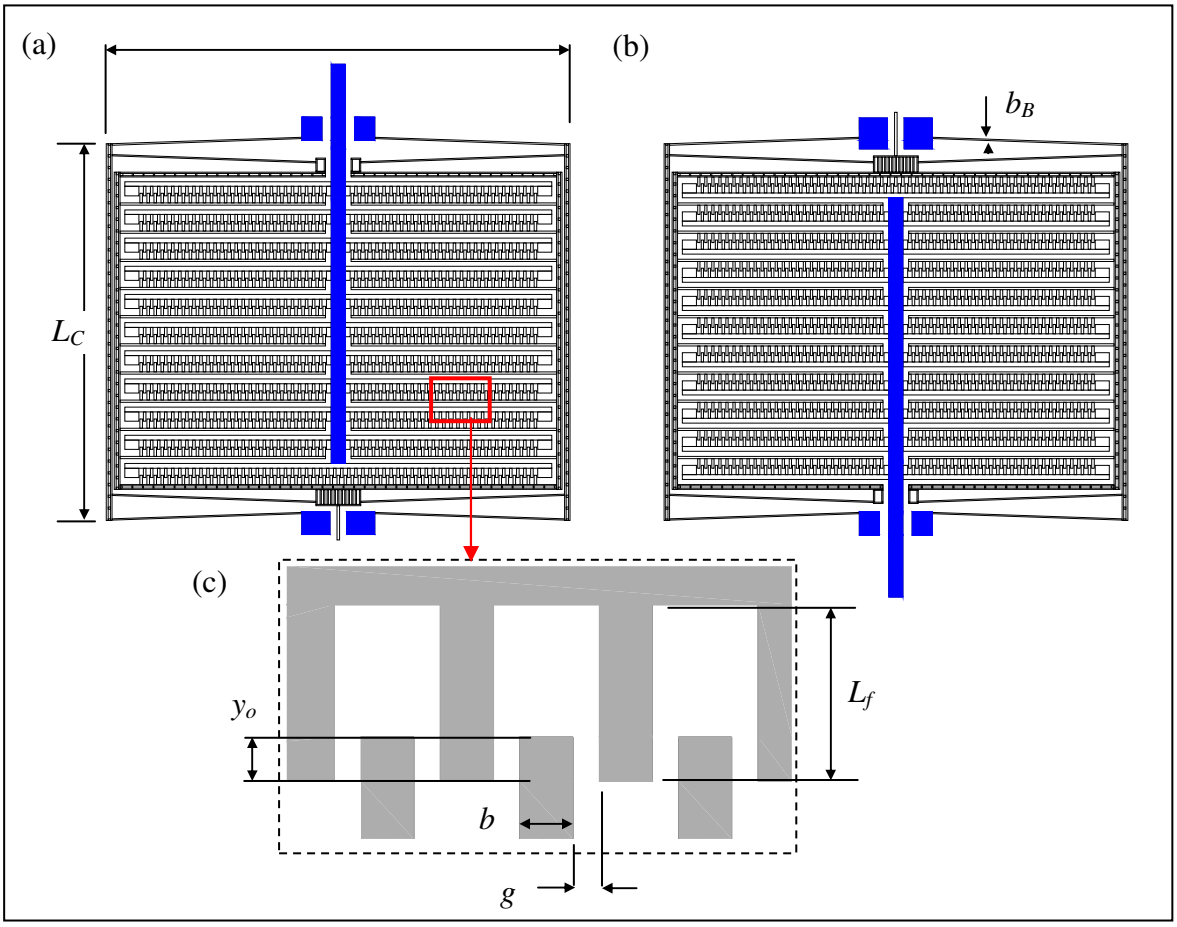

Figure 3.13 (a) Driven comb actuator; (b) readout comb actuator; (c) Geometrical design parameter of the comb fingers

Table 3-8 Main geometrical design parameter of the comb actuator

Description of Geometrical Comb Actuator Parameter	Dimension [μm]
Length of driven comb = Length of readout comb, L_C	802
Width of driven comb = width of readout comb, b_C	988
Width of tilted-folded beam, b_B	3
Width of comb finger, b	5
Length of comb finger, L_f	20
Overlapping distance of finger, y_o	6
Gap between fingers, g	2.5
Total number of fingers, n; Driven comb ; readout comb	1173

Hence, it is important to estimate the effect of the selected geometrical dimensions on the performance of the comb actuator. The research used the analytical analysis proposed by Rob *et al.* [100] based on a static behaviour of a comb drive in order to guide the comb actuator design:-

The lateral electrostatic force, F_{el} stimulated in the y-direction at the driven comb can be estimated using Equation 3-9:-

$$F_{el} = \frac{1}{2}\frac{\delta C}{\delta y}v^2 = \frac{n.\varepsilon_o.b}{g}.v^2 \qquad \text{(Equation 3-9)}$$

Where v: applied dielectric potential [v]; n: total number of fingers; ε_o: permeability in free space = 8.85 x 10^{-12} Cb^2/Nm^2; b: width of finger [m] ; and g: gap between fingers [m]. This electrostatic force is acting on the spring used to anchor the comb actuator, resulting in a deflection:-

$$y = \frac{n.\varepsilon_o.b}{k_y.g}.v^2 \qquad \text{(Equation 3-10)}$$

The capacitance between the fixed and moving comb actuator can be expressed:-

$$C = \frac{2.n.\varepsilon_o.b(y + y_o)}{g} \qquad \text{(Equation 3-11)}$$

Where, y_o: Initial overlapping between fixed and moving fingers;

The generated current (i_{out}) due to the change of the capacitance (dc/dy) can be calculated from:-

$$Q = C.V_s \qquad \text{(Equation 3-12)}$$

$$i_{out} = \frac{dQ}{dt} = \frac{d(C.V_s)}{dt} = V_s.\frac{dC}{dy}.\frac{dy}{dt} = V_s.\frac{dC}{dy}.\omega \qquad \text{(Equation 3-13)}$$

Where, Q: stored charge in capacitor [coulomb]; V_s: Sense voltage [v]; ω: natural frequency of the structure [rad/s].

A stable comb operation is bounded by $|k_x| > |k_e|$; where k_x is the stiffness of the spring to anchor the comb actuator in perpendicular to the actuator movement; k_e is the equivalent negative spring constant, when the moving comb is placed at the centre of the comb gap [102].

$$k_e = \frac{2.n.\varepsilon_o.b.(y + y_o)}{g^3}.v^2 \qquad \text{(Equation 3-14)}$$

The comb actuator also becomes unstable when the driving voltage exceeds the side instability (V_{si}), leading to side sticking of the moving and fixed fingers.

$$V_{si} = \frac{g^2.k_y}{2.n.\varepsilon_o.b}.\left[\sqrt{2.\frac{k_x}{k_y} + \frac{(y_o)^2}{g^2}} - \frac{y_o}{g}\right] \qquad \text{(Equation 3-15)}$$

The maximum displacement of the comb actuator that can be obtained before side sticking, y_{si} is:-

$$y_{si} = g.\left[\sqrt{\frac{k_x}{2.k_y}} - \frac{y_o}{2}\right] \qquad \text{(Equation 3-16)}$$

3.5.3 Finite Element Analysis of Comb Actuator

Due to the complexity of the design, FEA was used to analyse further performance parameters of the comb actuator which include the effective stiffness and mass of the actuator, the eigenfrequency and eigenmodes of the structure and the generated capacitance between the fixed and moving comb fingers.

3.5.3.1 Effective Mass, Stiffness, and Eigenfrequency

As presented in Section 3.3.3 and 3.4.3 the static analysis with parametric solver was used to estimate the stiffness of the actuator (k_y and k_x). Figure 3.14 (a) and (b) presents the static analysis result of the driven comb actuator. The actuator requires a minimum of 0.6μN force

to make 1µm displacement in y direction of movement. Figure 3.15 illustrates an example of the eigenfrequency analysis result of the readout comb. It was confirmed that the fundamental frequency of the comb actuators are outside the main frequency of the CMRA (48.5 – 55.1 kHz).

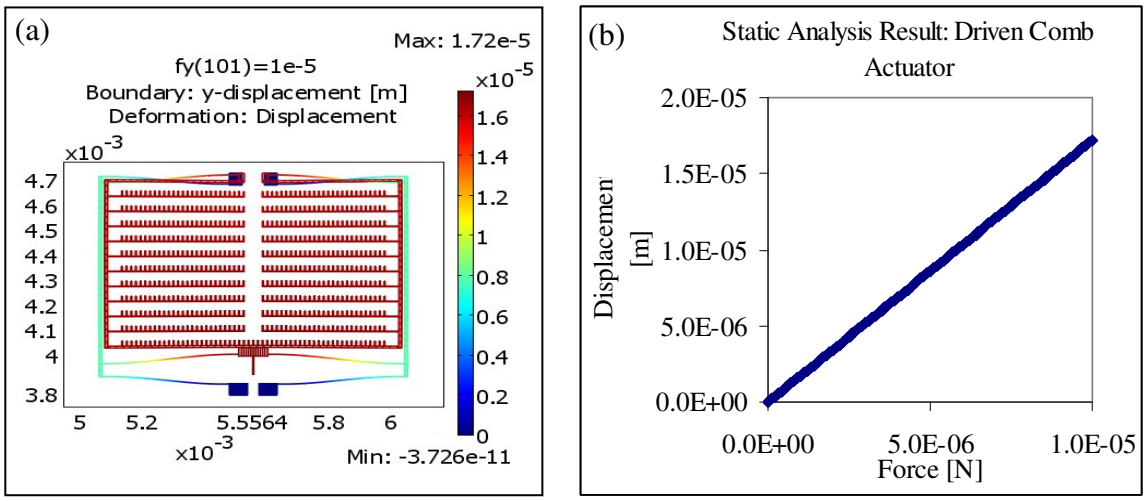

Figure 3.14 Static analysis result of the driven comb actuator

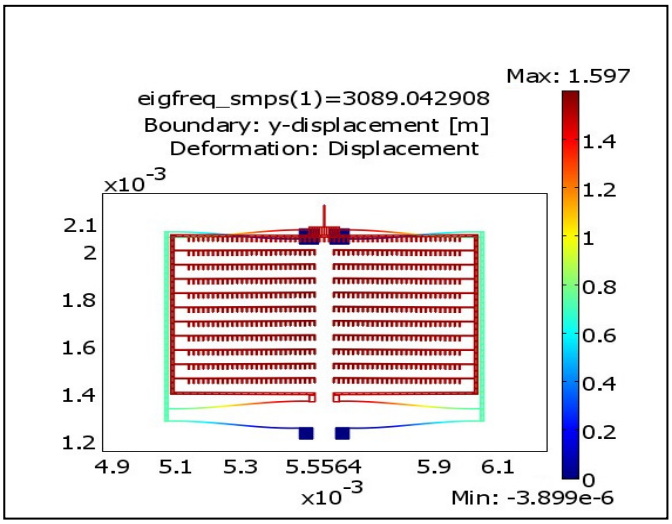

Figure 3.15 Eigenfrequency analysis result of comb actuator (fundamental mode of the readout comb (f = 3089.0 Hz))

3.5.3.2 Generated Capacitance

In COMSOL a capacitance generation can be simulated in an electrostatic module using a stationary or parametric solver. To simplify the modelling process the research analysed the

electrostatic field based on a two dimensional structure analysis. In COMSOL the electrostatic field is related to the total energy required to charge a related capacitor [146]:-

$$We = \frac{Q^2}{2.C} = \int_{\Omega} (D.E)d\Omega \quad ; \quad C = \frac{Q}{\Delta V} \qquad \text{(Equation 3-17)}$$

Where, Q: charge on the two conductive plate; C: Capacitance; ΔV: voltage difference across the plate; We: The stored electric energy in the capacitor, is readily available in the electrostatic application mode. The software calculates We by integrating across D (electric displacement) and E (electric field). To calculate C, Equations 3-17 are simplified relating between the stored energy and the voltage across the capacitor:-

$$C = \frac{Q^2}{2.We} = \frac{C^2 \cdot \Delta V^2 \cdot}{2.We}; \quad C = \frac{2.We}{\Delta V^2} \qquad \text{(Equation 3-18)}$$

The electrostatic field modelling relies on two subdomain settings; i.e. (1) the conductive plate (moving and fixed actuator) and (2) the surrounding air (Figure 3.16). Alternatively, the capacitance can be analysed using the energy method. It requires one of the actuators to be set to a 'port' boundary, where a unit of voltage will be forced to the boundary. By setting the boundary of the second set of actuator and the air boundary to a ground and zero charge, and initializing the structure mesh, the solver returns the value of the capacitance.

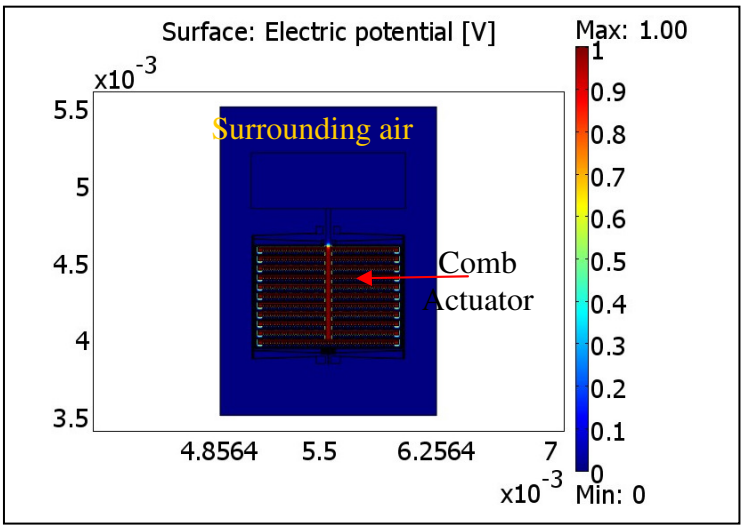

Figure 3.16 Capacitance analysis in electrostatic module with two subdomain setting of surrounding air and comb actuator

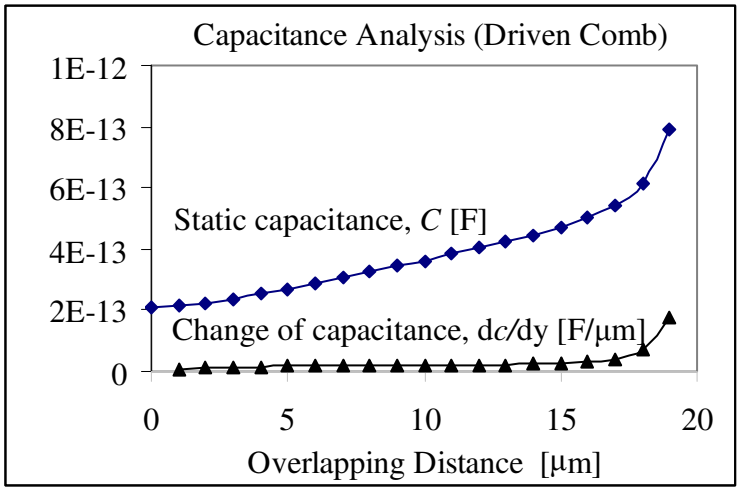

Figure 3.17 Static capacitance and dc/dy of driven comb analysed using FEA

Figure 3.17 presents the analysis result of the change of the capacitance (dc/dy) for the driven actuator at different relative displacements (finger overlapping) between fixed and moving actuators. At 6µm the initial overlapping, the related dc/dy is around 2 x 10^{-14}F/µm.

3.5.4 Performance of Comb Actuator

Table 3-9 Performance parameter of the driven and readout comb actuator (*Note: * simulated result; ** numerical analysis result*)

Performance Parameter of comb actuator	Value [unit]
Natural Frequency ω_n [Hz]	*3089.0
Effective stiffness of actuator, k_y; k_x [N/m]	*0.5855; *38140
Electrostatic force, F_{el} [N] (at 5 V input voltage, driven comb)	$^{**}0.52 \times 10^{-6}$
Displacement , Y [m] (at 5 V input voltage, driven comb)	$^{**}0.89 \times 10^{-6}$
Generated capacitance, [F] (driven comb)	$^{**}2.45 \times 10^{-13}$
Generated current, i_{out} [A] (readout comb)	3.12×10^{-9}
Effective mass of actuator [kg]	1.554×10^{-9}

Table 3-9 highlights the performance parameter of the comb actuator which was analyzed using numerical and finite element analyses. From the analysis, with 5V input voltage the

driven comb actuator displaces at least by 0.89μm. The actual resonant amplitude of the structure may be estimated by multiplying the static displacement of the actuator with the Q-factor of the structure. Assuming, a corresponding change of capacitance, at least 3nanoA current is expected to be measured at the readout port. Hence, it satisfies the requirement of the readout measurement facilities.

3.5.5 Driving the CMRA-v1 using the Designed Actuator

To ensure the measurability of the output signal of the coupled resonators, the drive and readout actuator were rigidly coupled to the first and fifth resonator of the CMRA structure. The Eigenfrequency analysis was performed to determine the mode shape of the coupled structures. Particular attention was given to the mode shape, where the comb drive actuator moves to pull the coupled resonators and the readout actuator. The movement of the readout comb actuator will confirm the measurability of the output signal of the CMRA-v1.

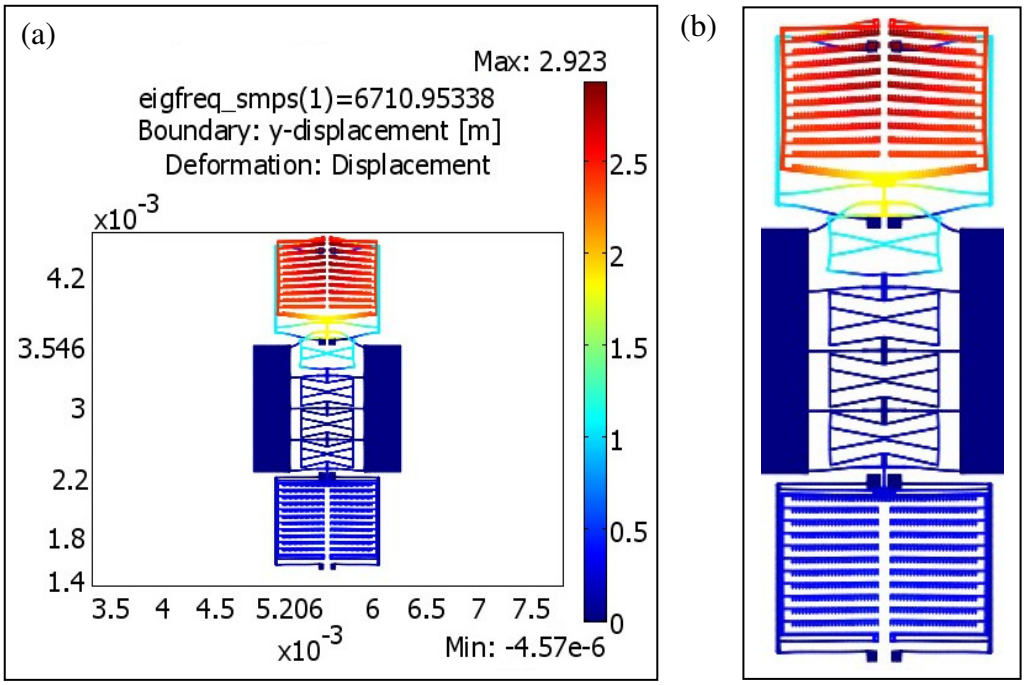

Figure 3.18 Eigenfrequency analysis result of CMRA-v1 (mode 1)

Figure 3.18 shows the eigenmode of the coupled structure. As can be observed from Figure 3.18(b), the comb drive was displaced at a maximum movement (dark red colour) in y-direction. However, due to the large mass of the comb drive actuator compared to the mass of the resonator (1.554×10^{-9} >>> 2.92×10^{-11} kg), a node was created at R2 which caused a very small amplitude of the resonator. Hence no displacement was observed at the readout resonator (dark blue colour).

In order to measure the frequency response pattern of the CMRA, the structure needs to be redesigned so that the mass of actuator and the mass of the resonator are significantly balanced (i.e. need to be designed with antinodes at the ends; will be discussed in Chapter 4).

3.6 Single Fixed-Fixed Beam Resonator for Frequency Response Measurement

A single fixed-fixed beam resonator with a simplified comb actuator was designed in order to measure the frequency response of the first version of the single resonator (singleR-v1). Figure 3.19 depicts the schematic of the structure.

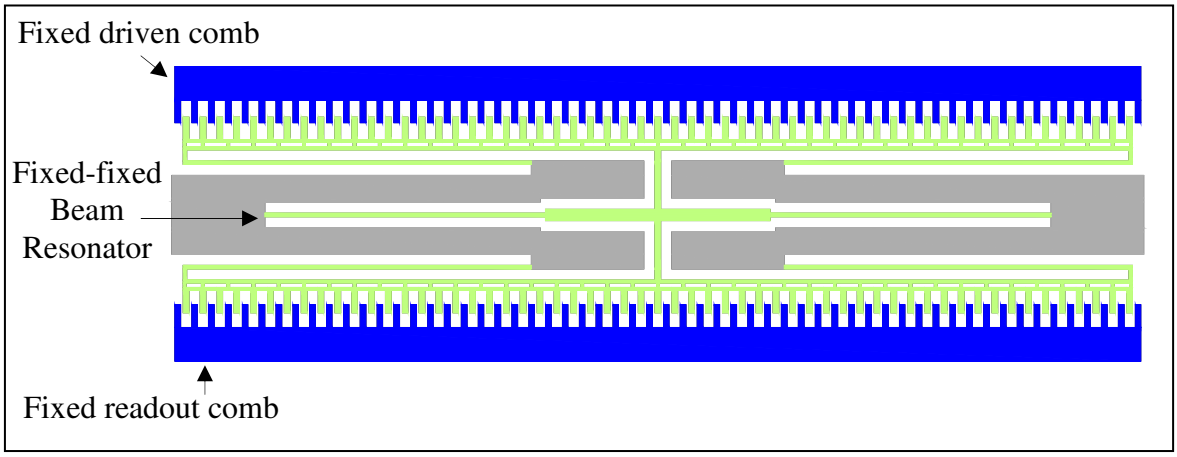

Figure 3.19 Schematic of a fixed-fixed beam resonator which rigidly coupled to a simple drive and readout comb actuator (singleR-v1)

3.6.1 Finite Element Analysis of the singleR-v1

Table 3-10 List of analyses conducted using FEA to examine the performance of the singleR-v1 structure

Type of Analysis/ Solver	Evaluated Performance Parameter
1) Static/ parametric	Structure stiffness
2) Eigenfrequency/ eigenfrequency	Eigenfrequency, eigenmode and effective mass
3) Capacitive/ stationary solver	capacitance
4) Parametric/parametric solver	Electrostatic force, structure displacement

Table 3-10 summaries all the conducted analyses. All analyses 1 to 3 are conducted similar to the analyses presented earlier in Section 3.3.3 and 3.4.3.

The electrostatic force in COMSOL is modelled using 3 combinations of application modes which include Plane Stress, Moving Mesh (ALE) and electrostatic module. The final model was simulated using a parametric analysis and parametric solver with the Plane stress mode controls the overall ruling of the modes. In this model an electric potential is applied to the fixed driven comb and the moving structure is grounded (Figure 3.19); the conditions were set in the electrostatic module. COMSOL solves the electrostatic equation [147]:-

$$-\Delta.(\varepsilon \nabla V) = 0 \qquad \text{(Equation 3-19)}$$

The electrostatic force density is

$$F_{el} = \frac{\varepsilon . E^2}{2} \qquad \text{(Equation 3-20)}$$

Where, ε: material permittivity, V: voltage potential [v], and E: Electric field.

The electrostatic forces attract the moving comb to the fixed comb, where the movement changes the electric field between them. COMSOL uses the Arbitrary Lagrangian-Eulerian (ALE) application mode to keep track the movement of the structure. Refer to Figure 3.22 in Section 3.6.2 for the electrostatic force analysis result.

3.6.2 Performance of the SingleR-v1 Structure

Table 3-11 Performance parameter analysis result of the single fixed-fixed beam resonator (SingleR-v1)

Performance Parameter of comb actuator	Value
Structure stiffness k_y [N/m]	5.234
Natural Frequency ω_n[Hz]	22127.1
Effective mass, m_{eff} [kg]	2.708×10^{-10}
Change of capacitance,dc/dy [F/μm]	2.09×10^{-15}
Electrostatic force, F_{el} [N] (at 5 v voltage potential)	1.07×10^{-4}
Generated current, i_{out} [A] (assuming at 8 V sense voltage)	2.32×10^{-9}

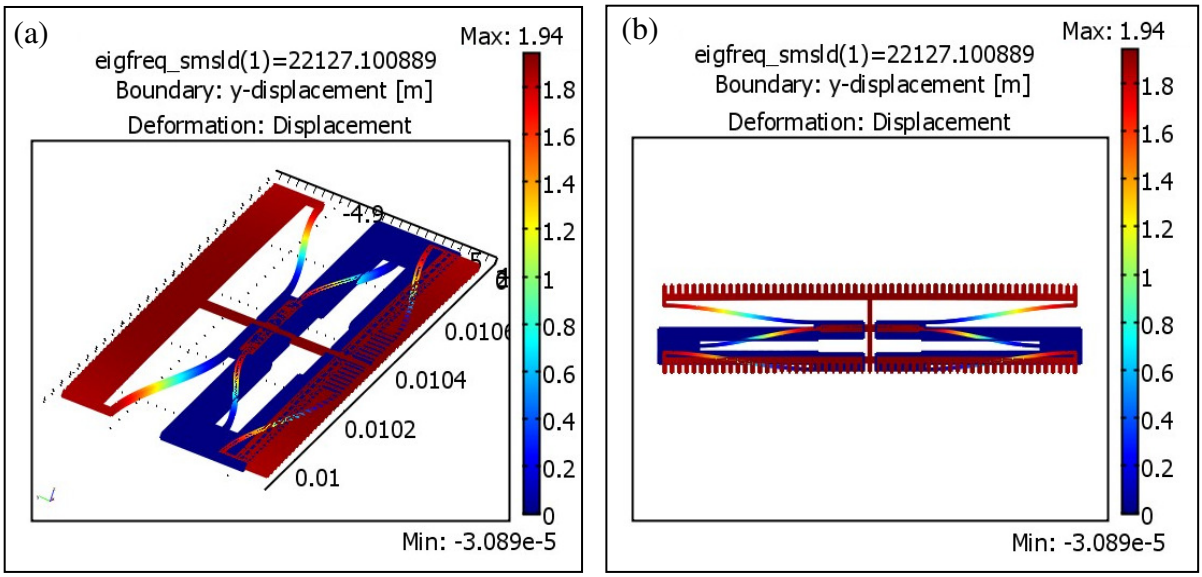

Figure 3.20 Fundamental eigenfrequency of the fixed-fixed beam resonator (SingleR-v1), (a) 3D view of structure analysis (x-y-z plane); (b) Top view (x-y plane)

Table 3-11 presents the overall performance of the SingleR-v1 Structure. By rigidly coupled the beam to the driven and readout comb, the stiffness of the structure increases from 2.74 N/m (for single fixed-fixed beam only) to 5.234 N/m. From the eigenfrequency analysis result (Figure 3.20) the fundamental eigenfrequency of the structure is 22127.1 Hz. In this frequency mode, the comb actuator and the resonator move forward together in the y-direction of movement. Equation 3-1 which relates the effective stiffness, mass and natural frequency of the structure was used to calculate the effective mass of the singleR-v1 structure.

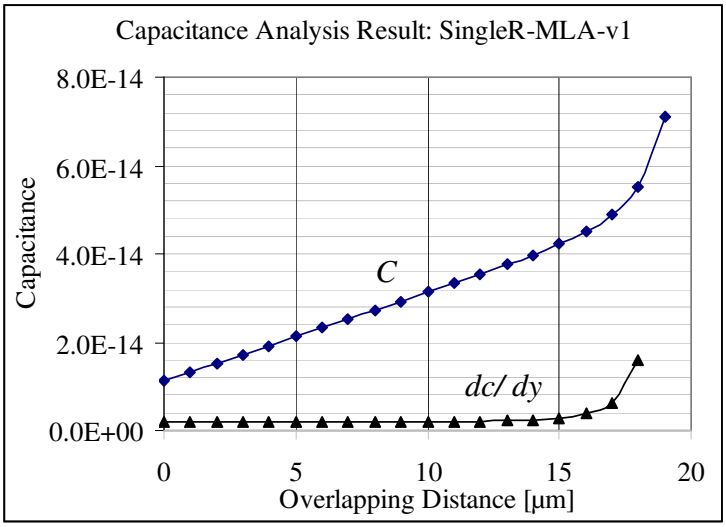

Figure 3.21 Static capacitance and change of capacitance (dc/dy) of the SingleR-v1 structure

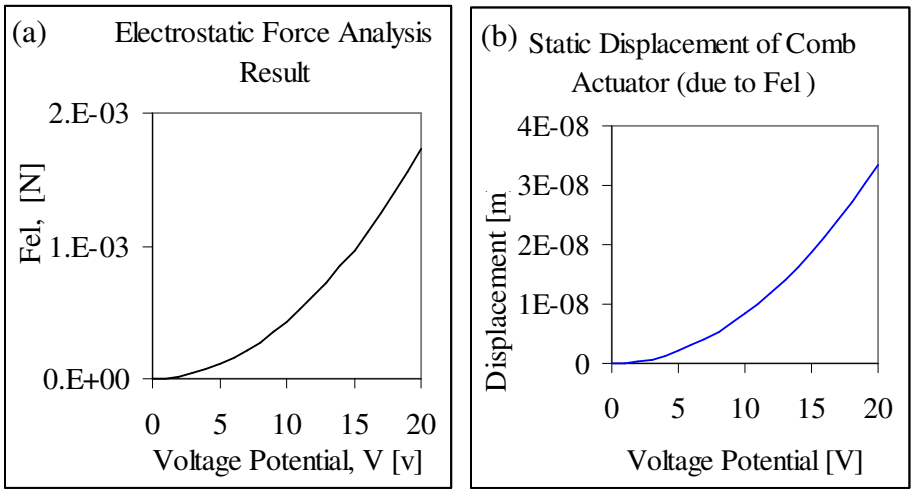

Figure 3.22 (a) Generated electrostatic force [N] at different voltage potential [v]; (b) Static displacement due to the generated electrostatic force.

From the capacitance analysis result (Figure 3.21), with a 5µm initial overlapping structure fingers, the static capacitance is approximately 2.12 x 10^{-14}F. With 5V potential differences between the fixed and moving fingers, the structure generates 1.07 x 10^{-4}N electrostatic force (Figure 3.22(a)), which causes 2.097 x 10^{-9}m structure movement (Figure 3.22 (b)). Due to the comb movement and fluctuation of the capacitance, it generates a current around 2.32nanoA at the readout port. With the amount of the generated current, the response of the

singleR-v1 Structure is expected to be measurable (refer to Chapter 6 and 7 for structure fabrication and frequency response measurement result).

3.7 Summary and Conclusion

The coupled micro resonator array (CMRA) was designed and modelled so that it can be fabricated (using in-house facilities) and the output signal can be measured using the available readout measurement facilities. Therefore all the constraints of the expected output signal, the measurement and fabrication were included in the design stage of the structure (Section 3.2).

The output signals of the CMRA which in the form of frequency response pattern of the coupled structure are related to the effective mass and stiffness of the coupled elements. The effectiveness of the CMRA-v1 relies on the functionality of the fixed-fixed beam resonator, coupling stiffness of the butterfly spring to synchronize the motion of the resonators and the comb actuator to drive and readout the output signal. The structure was designed to ensure no unwanted coupling in between the five main eigenfrequencies of the structure.

The stiffness of the coupling spring affects the overall frequency response pattern of the CMRA. From the finite element analysis result of the butterfly spring (Section 3.4.4), increasing the coupling stiffness increases the peak to peak response bandwidth and the overall bandwidth of the 5 ripples frequency response and decreases the amplitude of the response. The frequency response of the CMRA is also affected by the damping condition (viscous and acoustic damping). From finite element analysis of the single fixed-fixed beam resonator, the increase of damping factors reduced the response amplitude of the output signal and widened the bandwidth of the response.

A unique frequency response pattern for a single or multiple sensor is a key aspect of the CMRA structure. As analysed and discussed in Section 3.4.5, the response of the first half of

the sensor structure of the symmetrical coupled fixed-fixed beam resonators are always identical to the response of the second half of the structure when the structure absorbs similar amount of mass. To enhance the uniqueness of the frequency response of the coupled resonators for CMRA sensor structure, further analysis will be discussed in Chapter 4.

To ensure the output signal of the CMRA is measurable, at least 1nanoA of current (i_{out}) needs to be generated at the readout port of the comb actuator. The i_{out} generation is controlled by the change of the capacitance (dc/dy) and the flexibility of the readout comb actuator to fluctuate in the y-direction of movement. From the numerical and finite element analysis around 3nanoA current was estimated to be generated at the readout comb actuator. Based on the generated current, the structure is expected to be measurable.

When the comb drive actuator was coupled to the resonator (R1), the actuator failed to drive the CMRA structure. The large designed mass of the comb drive actuator (i.e. 53x more than the mass of resonator) created a standalone node at the next resonator (R2). Hence, it is important to further examine the mass of the 5 coupled resonators and the actuators to ensure measurable output signals. The overall effect of the mass and stiffness of the CMRA structure elements on the measurability of the output signal will be further analysed in Chapter 4 using a lumped mass model analysis.

Although other methods of excitation and detection (e.g. piezoelectric excitation and optical detection) may be used as an alternative to excite and readout the response of the 5 coupled fixed-fixed beam resonators; but, it is outside the research scope. To keep the electrostatic excitation and the capacitive detection scheme to detect the response pattern of the CMRA, the research improved the CMRA structure design by using an integrated coupled comb-drive resonator as the main structure element of the second version of the CMRA (will be discussed in Chapter 4 and Chapter 5).

CHAPTER 4 IMPROVEMENT OF CMRA USING LUMPED MASS MODEL ANALYSIS

4.1 Introduction

This chapter evaluates and analyses the performance of the coupled micro resonator array (CMRA) structure using the lumped mass model approach. Section 4.2 explains the overall lumped mass model of the CMRA structure which is based on an eigenvalue and eigenvector analysis. Section 4.3 briefly presents re-evaluation of the CMRA-v1 structure using the lumped mass model. Section 4.4 examines two alternatives of the lumped mass CMRA structures in order to improve the measurability of the CMRA structure output signal. To establish the improved CMRA structures, Section 4.5 highlights keys design improvement of the structure. Section 4.6 evaluates, and discusses the alternatives of the staggered lumped mass CMRA structures in terms of the measurability of output signals, uniqueness of frequency response patterns and stability of system eigenvectors. Section 4.7 summarizes the overall achievement in Chapter 4.

4.2 Lumped Mass Model of CMRA

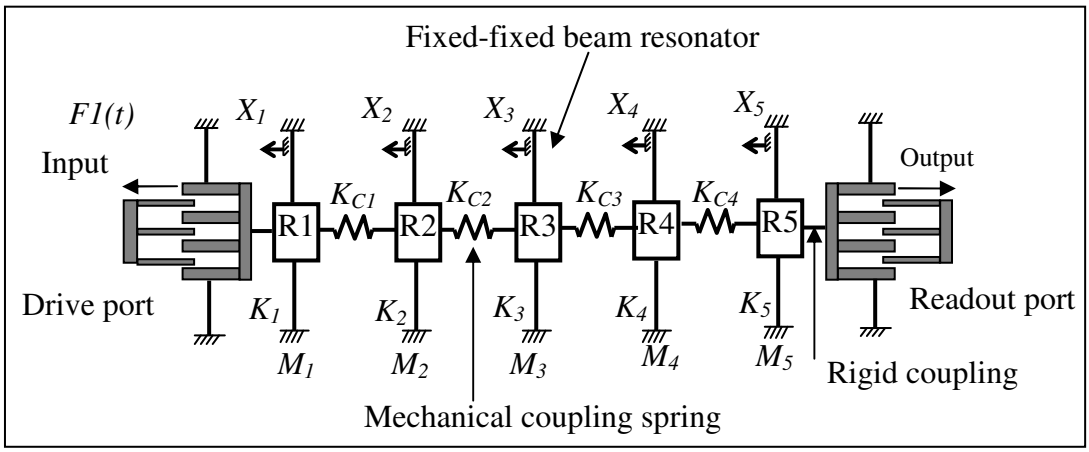

Figure 4.1 Schematic of the 5 CMRA-v1 sensor structures

Figure 4.1, a schematic of the first version of the coupled micro resonator array (CMRA-v1) which was discussed earlier in Chapter 3. The structure consists of 5 coupled resonators (R1, R2, R3, R4, and R5), and 4 mechanical coupling springs to couple the resonators together. To drive and readout the output signal of the structure, 2 sets of comb actuators were rigidly coupled to both end of the resonators array.

To re-evaluate the structure performance using the lumped mass analysis, the CMRA-v1 structure is considered as a five degrees-of-freedom (DOF) system. The structure is represented by 5 coordinates to describe its motion; i.e. x_1, x_2, x_3, x_4, and x_5. The 5-DOF system has 5 natural frequencies; each natural frequency is characterized by a natural state of vibration with a displacement configuration which is called normal mode [137, 148]. In mathematics they are referred to eigenvalues and eigenvectors.

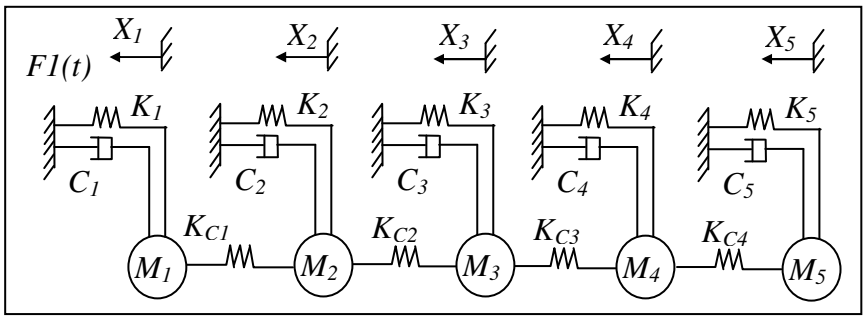

Figure 4.2 Free body diagram of the five CMRA structure

The relationship between eigenfrequencies and eigenvectors is established from the equations of motion of the system. Referring to the coupled resonators in Figure 4.1, consider a free body diagram of the system (Figure 4.2). The equations of motion of the system in Figure 4.2 are as follows:-

At M_1:

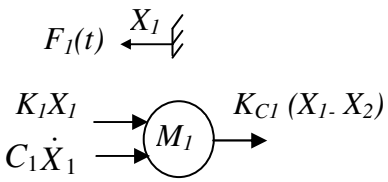

$$M_1\ddot{X}_1 + C_1\dot{X}_1 + (K_1 + K_{C1})X_1 - K_{C1}X_2 = F_1$$

(Equation 4-1)

At M_2:

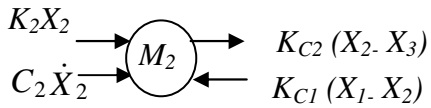

$$M_2\ddot{X}_2 + C_2\dot{X}_2 - K_{C1}X_1 + (K_2 + K_{C1} + K_{C2})X_2 - K_{C2}X_3 = 0$$

(Equation 4-2)

At M_3:

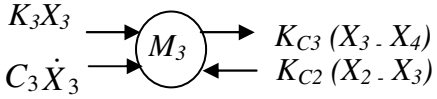

$$M_3\ddot{X}_3 + C_3\dot{X}_3 - K_{C2}X_2 + (K_3 + K_{C2} + K_{C3})X_3 - K_{C3}X_4 = 0$$

(Equation 4-3)

At M_4:

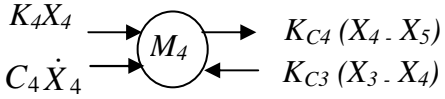

$$M_4\ddot{X}_4 + C_4\dot{X}_4 - K_{C3}X_3 + (K_4 + K_{C3} + K_{C4})X_4 - K_{C4}X_5 = 0$$

(Equation 4-4)

At M_5:

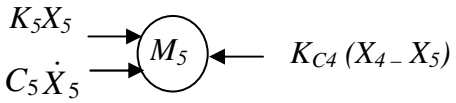

$$M_5\ddot{X}_5 + C_5\dot{X}_5 - K_{C4}X_4 + (K_5 + K_{C4})X_5 = 0$$

(Equation 4-5)

The above equations of motion (4-1 – 4-5) of the system are simplified in a matrix form as:

$$\begin{bmatrix} M1 & 0 & 0 & 0 & 0 \\ 0 & M2 & 0 & 0 & 0 \\ 0 & 0 & M3 & 0 & 0 \\ 0 & 0 & 0 & M4 & 0 \\ 0 & 0 & 0 & 0 & M5 \end{bmatrix} \begin{bmatrix} \ddot{X}1 \\ \ddot{X}2 \\ \ddot{X}3 \\ \ddot{X}4 \\ \ddot{X}5 \end{bmatrix} + [C] \begin{bmatrix} \dot{X}1 \\ \dot{X}2 \\ \dot{X}3 \\ \dot{X}4 \\ \dot{X}5 \end{bmatrix} + [K] \begin{bmatrix} X1 \\ X2 \\ X3 \\ X4 \\ X5 \end{bmatrix} = [F]$$

(Equation 4-6)

Where, $[C]$ is a damping matrix; $[K]$ is a stiffness matrix; and $[F]$ is a force matrix;

$$[F] = \begin{bmatrix} F1 \\ 0 \\ 0 \\ 0 \\ 0 \end{bmatrix}; \qquad [C] = \begin{bmatrix} C1 & 0 & 0 & 0 & 0 \\ 0 & C2 & 0 & 0 & 0 \\ 0 & 0 & C3 & 0 & 0 \\ 0 & 0 & 0 & C4 & 0 \\ 0 & 0 & 0 & 0 & C5 \end{bmatrix};$$

$$[K] = \begin{bmatrix} K1+KC1 & -KC1 & 0 & 0 & 0 \\ -KC1 & K2+KC1+KC2 & -KC2 & 0 & 0 \\ 0 & -KC2 & K3+KC2+KC3 & -KC3 & 0 \\ 0 & 0 & -KC3 & K4+KC3+KC4 & -KC4 \\ 0 & 0 & 0 & -KC4 & K5+KC4 \end{bmatrix}$$

In order to determine the natural frequencies and modes shape of the CMRA, the above system is examined under a free vibration and treated as an undamped system; where $F_1(t) = 0$ and $[C] = 0$. The system in Figure 4.2 is simplified as follows:

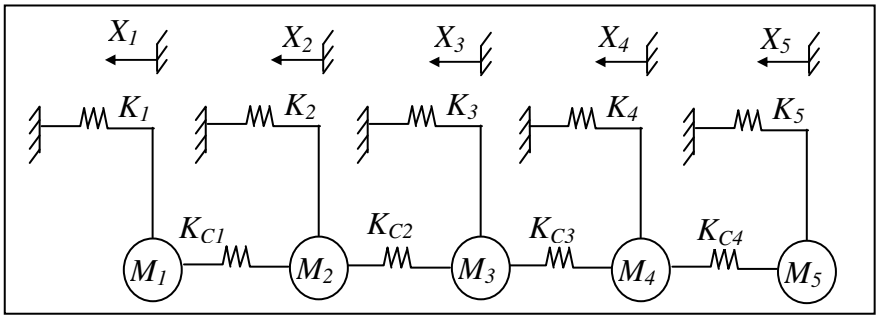

Figure 4.3 Free body diagram of undamped CMRA structure

For normal mode motion of the system, every point of motions is assumed to be harmonic. To solve the harmonic motion, X_1, X_2, X_3, X_4 , and X_5 were substituted with a harmonic constant:-

$$\begin{aligned}
&X_1 = A_1 \sin\omega t; && \dot{X}_1 = -\omega A_1 \cos\omega t; && \ddot{X}_1 = -\omega^2 A_1 \sin\omega t;\\
&X_2 = A_2 \sin\omega t; && \dot{X}_2 = -\omega A_2 \cos\omega t; && \ddot{X}_2 = -\omega^2 A_2 \sin\omega t;\\
&X_3 = A_3 \sin\omega t; && \dot{X}_3 = -\omega A_3 \cos\omega t; && \ddot{X}_3 = -\omega^2 A_3 \sin\omega t;\\
&X_4 = A_4 \sin\omega t; && \dot{X}_4 = -\omega A_4 \cos\omega t; && \ddot{X}_4 = -\omega^2 A_4 \sin\omega t;\\
&X_5 = A_5 \sin\omega t; && \dot{X}_5 = -\omega A_5 \cos\omega t; && \ddot{X}_5 = -\omega^2 A_5 \sin\omega t;
\end{aligned} \qquad \text{(Equation 4-7)}$$

Substituting Equation 4-7 into Equations 4-6 and rearranging in a matrix form:-

$$\omega^2 \cdot \begin{bmatrix} x1 \\ x2 \\ x3 \\ x4 \\ x5 \end{bmatrix} = [M^{-1}][K] \cdot \begin{bmatrix} x1 \\ x2 \\ x3 \\ x4 \\ x5 \end{bmatrix} \qquad \text{(Equation 4-8)}$$

$$\omega^2 [X] = [M^{-1}][K][X] \qquad \text{(Equation 4-9)}$$

Where; [M] is the mass matrix, [K] is the stiffness matrix and [X] is the displacement matrix of the system in Figure 4.3. The simplified Equation 4-9 denotes the matrix form of the eigenvalue problem.

$$M = \begin{bmatrix} M1 & 0 & 0 & 0 & 0 \\ 0 & M2 & 0 & 0 & 0 \\ 0 & 0 & M3 & 0 & 0 \\ 0 & 0 & 0 & M4 & 0 \\ 0 & 0 & 0 & 0 & M5 \end{bmatrix};$$

$$K = \begin{bmatrix} K1+K_{C1} & -K_{C1} & 0 & 0 & 0 \\ -K_{C1} & K2+K_{C1}+K_{C2} & -K_{C2} & 0 & 0 \\ 0 & -K_{C2} & K3+K_{C2}+K_{C3} & -K_{C3} & 0 \\ 0 & 0 & -K_{C3} & K4+K_{C3}+K_{C4} & -K_{C4} \\ 0 & 0 & 0 & -K_{C4} & K5+K_{C4} \end{bmatrix}$$

Knowing the value of mass and stiffness matrices, MATLAB may be used to solve the eigenvalue problem and so obtain the value of the five natural frequencies and the mode

shapes of the CMRA structure can be estimated. For example, using the MATLAB, the eigenvalues and eigenvectors are determined using a function of [V, d] = eig(E). Where V contains the eigenvectors, d contains the eigenvalues and E = $[M^{-1}]$ [K] (refer to Appendix B for the example of MATLAB codes).

4.3 Re-evaluation of the CMRA-v1

As discussed in Section 3.5.5 (Chapter 3), due to the very large mass of the actuator, the actuator failed to drive the coupled resonators. As a result the readout comb actuator was unable to detect the frequency response of the coupled resonators. To evaluate the performance of the CMRA-v1 using the lumped mass model analysis, the value of the effective mass, and stiffness of the resonators, comb actuators and coupling springs were obtained from the finite element analysis in Section 3.3.4 (Table 3-2), Section 3.4.3 (Table 3-4), and Section 3.5.4 (Table 3-9). Table 4-1 summarizes the effective mass and stiffness of the CMRA-v1 structure elements.

Using MATLAB the value of the effective mass and stiffness of the CMRA-v1 structure elements in Table 4-1 were substituted in Equation 4-9 in order to solve for the 5 eigenvalues and 5 eigenvectors of the coupled structure. Figure 4.4 shows the plot of the 5 eigenvectors of the CMRA-v1 structure for 5 structure eigenmodes.

The measurability of the structure output signal is associated with the absolute movement of the structure (response amplitude) at the particular drive or readout point. As can be observed at R1 (drive point) and R5 (readout point) the 2 large resonators displacement (mode 1 and mode 2) are only associated to the movement of the large mass of the actuators which was coupled to the structure array. For mode 3, 4, and 5 the resonators approach zero displacement at both ends of the array. The large masses have created nodes between

actuators and resonators. As a result the output signal of the structure at R5 is unable to be measured.

Table 4-1 A summary of the effective mass and stiffness of the CMRA-v1 structure elements (Note: *Kc1*= *Kc2*= *Kc3*=*Kc4*= 0.4578N/m)

Structure Elements	Effective Mass Parameter [kg]	Effective Stiffness Parameter [N/m]
Resonator 1 (R1) and Driven comb actuator	*M1*: 1.5832 x 10^{-9}	*K1*: 3.3255
Resonator 2 (R2)	*M2*: 2.92 x 10^{-11}	*K2*: 2.74
Resonator 3 (R3)	*M3*: 2.92 x 10^{-11}	*K3*: 2.74
Resonator 4 (R4)	*M4*: 2.92 x 10^{-11}	*K4*: 2.74
Resonator 5 (R5) and readout comb actuator	*M5*: 1.5832 x 10^{-9}	*K5*: 3.3255

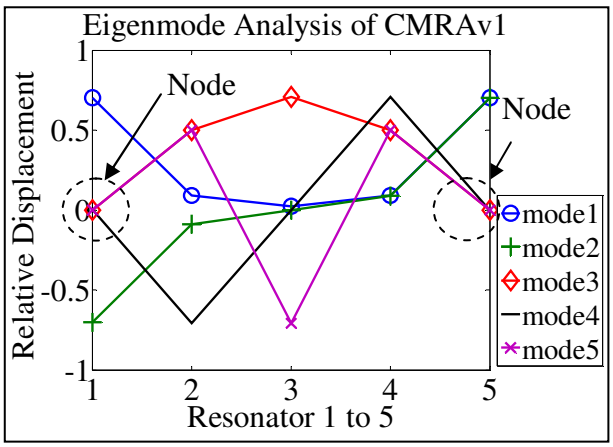

Figure 4.4 Eigenmode analysis result of CMRA-v1

4.4 Analysis of Improved Design

In order to ensure a measurable output signal of the structure (i.e. drive at R1, readout at R5), the nodes at both end of the structure array need to be removed. The research explores several alternative structures by modifying the mass and stiffness of the CMRA-v1 structure (in Table 4-1). Two alternatives are discussed:-

- Alternative 1: The original stiffness were retained, but the masses of the coupled elements were changed, so that they are equivalent to *M1* (Table 4-1).

- Alternative 2: The masses and stiffness of the coupled elements were changed, so that they have similar masses (*M1*) and similar stiffness (*K2*).

Having resonators and actuators which have similar masses may balance the relative displacement of the coupled structure. Hence, the node between the actuators and resonators may be removed. Two alternatives were compared and the effect of the change of mass and resonator stiffness on the structure eigenvalues and eigenvectors were observed. Table 4-2 summarizes the modification of the effective mass and stiffness of the 5 coupled elements for the two structure alternatives. Note that the 4 coupling stiffness used to couple the 5 structure elements remained 0.4578 N/m.

Table 4-2 Modified effective mass and stiffness of the 5 coupled structures for structure improvement analysis

Structure Elements	Effective mass, *M* and stiffness, *K* [N/m] of the 5 coupled elements Note: * (x 10^{-9}) [kg]			
	Alternative 1		Alternative 2	
	M	*K*	*M*	*K*
1	1.5832*	3.3255	1.5832*	2.74
2	1.5832*	2.74	1.5832*	2.74
3	1.5832*	2.74	1.5832*	2.74
4	1.5832*	2.74	1.5832*	2.74
5	1.5832*	3.3255	1.5832*	2.74

Using MATLAB, the lumped mass analyses were performed to determine the eigenvectors and eigenfrequencies of the coupled structures based on the two alternatives mass and stiffness parameters in Table 4-2. Figure 4.5 shows the plots of the eigenmodes analysis result for each of the two alternatives. Table 4-3 lists the 5 eigenfrequencies of the uncoupled structure and modal eigenfrequencies of the coupled structures for the two alternatives and CMRA-v1. Table 4-4 highlights the normalized eigenvectors of the two structure alternatives compared to the CMRA-v1.

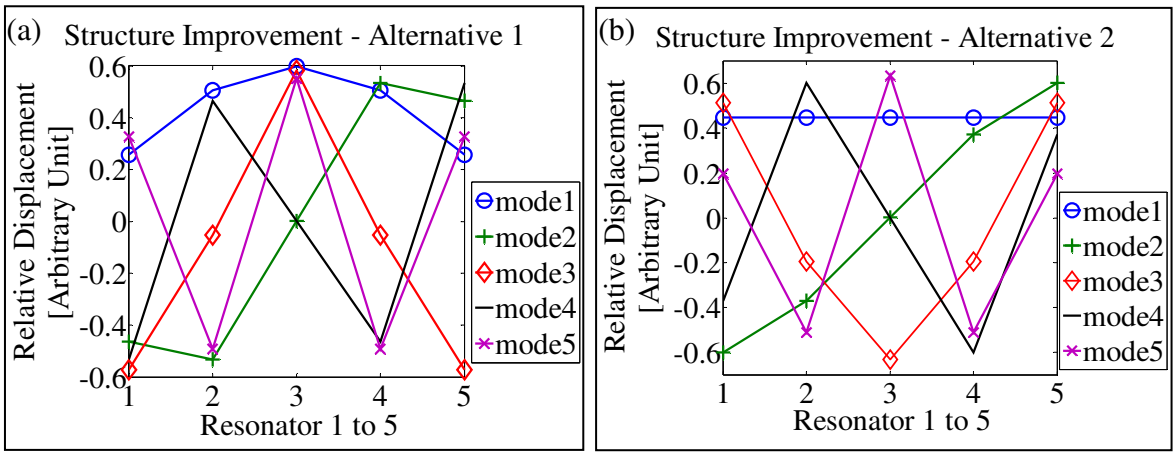

Figure 4.5 Eigenmode analysis result of 2 alternatives structure improvement of CMRA-v1

Table 4-3 Eigenfrequencies (f_R) and modal eigenfrequencies (f_m) of the CMRA-v1 and structure alternatives

	CMRA-v1		Alternative1		Alternative2	
	f_R	f_m	f_R	f_m	f_R	f_m
f_{R1}, f_{m1}	7294	7718	7294.3	6790.0	6621.1	6621.1
f_{R2}, f_{m2}	48753	7720	6621.1	7219.0	6621.1	6829.1
f_{R3}, f_{m3}	48753	51089	6621.1	7735.7	6621.1	7345.8
f_{R4}, f_{m4}	48753	56321	6621.1	8179.5	6621.1	7938.2
f_{R5}, f_{m5}	7294	61100	7294.3	8459.3	6621.1	8386.8

Table 4-4 Eigenvectors analysis result of the CMRA-v1 and structure alternatives

Alternative /Resonator (R)		Normalized Eigenvectors (of 5 coupled structure)				
		Mode1	Mode2	Mode3	Mode4	Mode5
CMRA-v1	R1	29.7	-7.8	-1	1	-1
	R2	4	-1	356.9	-415.9	500.2
	R3	1	0	505.4	0	706.9
	R4	4	1	356.9	415.9	500.2
	R5	29.7	7.8	-1	-1	-1
Alternative 1	R1	1	-1	-10.6	-1.1	1
	R2	2	-1.1	-1	1	-1.5
	R3	2.3	0	10.8	0	1.7
	R4	2	1.1	-1	-1	-1.5
	R5	1	1	-10.6	1.1	1
Alternative 2	R1	1	-1.6	2.6	-1	1
	R2	1	-1	-1	1.6	-2.6
	R3	1	0	-3.2	0	3.2
	R4	1	1	-1	-1.6	-2.6
	R5	1	1.6	2.6	1	1

For alternative 1 (Figure 4.5(a)), when the mass of the resonators are similar, the displacement of the resonators drastically is improved at R1 and R5. As can be observed in Table 4-3 and Table 4-4, by having small differences between the eigenfrequencies of the uncoupled resonators, improved the relative displacement of the resonators. Although, the actual relative displacement of the resonator depending on the mass and stiffness configuration of that particular resonator.

Referring to alternative 2 (Figure 4.5(b) and Table 4-4), with the uniform mass and stiffness configuration (similar eigenfrequencies for the 5 uncoupled elements), differences of the proportion of the relative displacement between the 5 coupled resonators are small (i.e. balanced relative displacement). Hence, no standalone node is created between the 5 resonators. Therefore, the measurability is confirmed at R1 and R5 for all the modes when the structures are coupled together.

From the above analysis results, the measurability of the coupled resonators depends on the eigenfrequencies, the mass and stiffness configuration of the uncoupled elements. A large mass differences between the coupled elements will cause the standalone node at the particular resonator. The large mass will reduce the relative displacement of the resonator, and hence the responses of the resonators are unable to be measured at that particular resonator. The mass and stiffness configuration of the resonators determined the range of the modal frequencies of the coupled structures and the range of frequencies which dominate the movement of the coupled structures.

Overall, the pattern or mode shape of the 5 coupled structures is directly related to the eigenfrequencies of each uncoupled element (f_R) and the eigenvectors of the coupled resonators. Therefore, we may configure the mass or stiffness of the resonator in order to control the eigenfrequencies of the coupled elements and modify the structure mass to control

the relative displacement (eigenvector) of the coupled structures. With the harmonization of the relative displacement of the couple structures and the eigenfrequencies of the coupled elements will determine the measurability of the output signal of the structure as well as the final frequency response pattern of the coupled structures.

4.5 Key Structure Improvement of the CMRA-v2

4.5.1 Measurability of Output Signal

The measurability of the output signal of the CMRA sensor structure relies on the balanced effective mass, stiffness of the coupled resonators, the mechanical coupling spring, and the actuators. As discussed in Section 4.4, the measurability of the coupled structure is definitely improved when the mass and stiffness of the resonators and actuators are similar (constant mass and stiffness). The main design challenge is to alter the mass and stiffness of the resonators and actuators, so that they are more or less similar. The mass modification needs to be configured without compromising the amount of capacitance generated in the system (for the readout measurement).

4.5.2 Unique Frequency Response Pattern

As discussed in Chapter 3 (Section 3.2.2.1) a unique frequency response pattern is important as a signature to identify which single or multiple resonators absorbs mass. As analysed in Section 3.4.5, with the symmetrical CMRA design (constant mass coupled resonators), the structure does not have a unique frequency response pattern for individual resonator mass changes. The frequency response pattern of the individual resonator in the first half of the array are always similar to the resonators in the second half of the array, when the resonator absorbs similar amount of mass separately (i.e. the response pattern of R1 mirrors R5 and R2 mirrors R4).

Since the mass and stiffness of the coupled structures control the modal eigenfrequencies of the resonator, the symmetrical mass and stiffness configuration of the 5 resonators may be broke (e.g. staggering the resonators mass) for a distinguishable frequency response pattern. However, it is very important to consider, the degree to which the 5 resonators are staggered. The staggered mass must not create a large change between the proportion of the relative displacements of the 5 coupled structures; a large difference between the 5 eigenvectors, will increase risk that the response of some of the resonators with low relative displacement will not be measurable.

4.5.3 Stability of Eigenvectors

An eigenvector describes the relative displacement of any point on the structure as the structure vibrates in a single mode [136]. When one of the resonators of the CMRA absorbs a mass, the change of the mass may be identified by using an inverse eigenvalue analysis. This requires knowledge of the perturbed eigenvalues (eigenfrequency after the structure absorbs the mass) and perturbed eigenvectors. Since the perturbed eigenvectors are complicated to measure, the unperturbed eigenvectors will be used in the estimation of the mass changes pattern of the CMRA. To reduce errors in mass estimation, it is important to ensure that the eigenvectors are stable against mass changes (i.e. comparable eigenvectors or comparable eigenmodes before and after mass is absorbed).

4.6 Lumped Mass Model of the CMRA-v2 and Structural Analysis

4.6.1 CMRA-v2 for Measurability of Output Signal

To ensure measurable frequency responses, the research considers a new configuration of the CMRA structure based on the integrated coupled comb-drive resonators (Figure 4.6). The use

of the comb-drive to replace the fixed-fixed beams resonators and simultaneously acts as actuators will solve the problem of large mass differences between the actuators and resonators and ensure sufficient electrostatic forces and capacitances for the drive and readout requirement.

The new CMRA structure with balanced mass configurations between the resonators and actuators (i.e. constant mass and stiffness) will help to ensure measurability of the CMRA frequency response.

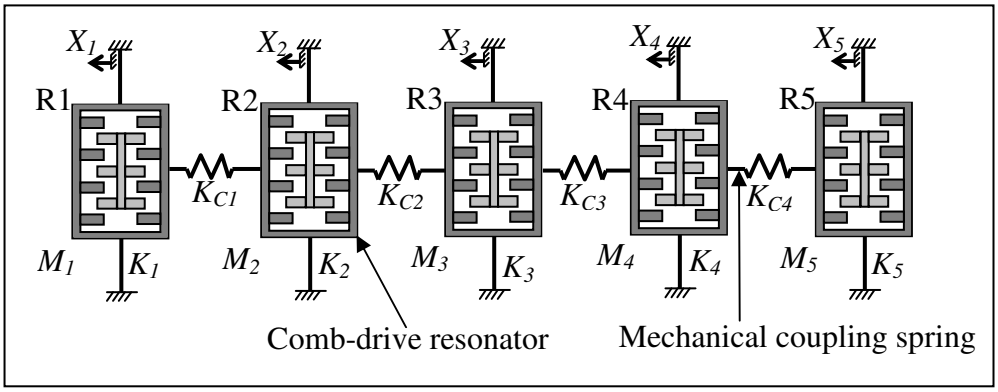

Figure 4.6 The schematic of the improved version of CMRA-v2 structure

4.6.2 Breaking Structure Symmetry for Performance Improvement of CMRA

Six alternatives were analysed in order to determine effective ways to stagger the coupled resonators; so that the structure is measurable, produces a unique frequency response, has stable eigenvectors before and after mass is perturbed at each of the single resonator.

- Alternative(1) and Alternative(2): 0.1 and 1 percent uniform step staggered mass of 5 CMRA respectively. The analyses examine the effect of 0.5% and 5% total staggered mass on the change of the eigenvectors of the 5 resonators. Note that a larger stagger (more than 1%) may result in a reduced measurability of the output; any smaller less than 0.1% causes the absorbed mass or manufacturing variations would dominate.

- Alternative(3) and Alternative(4): An unsymmetrical, but balanced mass distribution between the first half and second half of the structure array (sum of R1 and R2 mass is equal to the sum of mass of R4 and R5). With the unsymmetrical but balanced mass distribution approach, the amount of the total staggered mass may be increased without reducing the measurability of the structure output signal. The analyses compare the effect of 7% total staggered mass on the change of the eigenvectors when the heaviest mass is positioned in the middle (Alternative(3)) and at both ends of the structure array (Alternative(4)). Positioning the heaviest mass at the middle of the structure array may help to effectively balance the relative displacement of the coupled resonators for measurable output signal; constraining the heaviest mass at the end of the structure array may help to stabilize the eigenmodes of the perturbed CMRA.
- Alternative(5): Unsymmetrical, but balanced stiffness distribution between the first half and second half of the structure array (K1 + K2 is equal K4 + K5). The most stiff resonator is positioned in the middle of the array (R3).
- Alternative(6): 0.1 percent step staggered stiffness of 5 CMRA.

Table 4-5 lists the details of mass and stiffness configuration of the alternative structures. The mass (*M*) and stiffness (*K*) value of resonators is based on a comb-drive resonator from a group research project, which was designed by Anthony [125, 149]. The mass and stiffness of the resonators are evaluated using finite element analysis, which are discussed in Chapter 5. Note that the four coupling constants for all the structure alternatives is 0.3118 N/m.

Table 4-5 Mass and stiffness configurations of 6 alternatives of the staggered CMRA

Coupled Resonators	Effective mass, *M* and stiffness, *K* of the 5 coupled elements Note: *M* =3.8267nanokg; *K* = 24.9741N/m					
	Alternative(1)		Alternative(2)		Alternative(3)	
	M	*K*	*M*	*K*	*M*	*K*
R1	*M* + 0.1%*M*	*K*	*M* + 1%*M*	*K*	*M* - 4%*M*	*K*
R2	*M* + 0.2%*M*	*K*	*M* + 2%*M*	*K*	*M* - 1%*M*	*K*
R3	*M* + 0.3%*M*	*K*	*M* + 3%*M*	*K*	*M*	*K*
R4	*M* + 0.4%*M*	*K*	*M* + 4%*M*	*K*	*M* - 2%*M*	*K*
R5	*M* + 0.5%*M*	*K*	*M* + 5%*M*	*K*	*M* - 3%*M*	*K*
	Alternative(4)		Alternative(5)		Alternative(6)	
	M	*K*	*M*	*K*	*M*	*K*
R1	*M* + 4%*M*	*K*	*M*	*K* - 4%*K*	*M*	*K* + 0.1%*K*
R2	*M* + 1%*M*	*K*	*M*	*K* - 1%*K*	*M*	*K* + 0.2%*K*
R3	*M*	*K*	*M*	*K*	*M*	*K* + 0.3%*K*
R4	*M* + 2%*M*	*K*	*M*	*K* - 2%*K*	*M*	*K* + 0.4%*K*
R5	*M* + 3%*M*	*K*	*M*	*K* - 3%*K*	*M*	*K* + 0.5%*K*

As discussed in Section 4.3 and 4.4, the lumped mass analysis of the CMRA was performed using MATLAB programming. By substituting the value of mass and stiffness of the structures in Equation 4-9, the analysis returns the value of 5 eigenfrequencies and 5 eigenvectors of the coupled structure. The measurability of the structure output signal is determined by observing the eigenvectors of the structure alternatives at R1 and R5. Once the measurability of the structure output signal is confirmed, the eigenvalue and eigenvector analysis is repeated to examine the uniqueness of frequency response pattern and the stability of system eigenvectors.

A series of five tests were performed where a mass of 3.8267 x 10^{-12}kg (~0.1%) was added to R1, R2, R3, R4 and R5 separately. The eigenfrequencies and the eigenvectors of the unperturbed structure (i.e. initial condition) and perturbed structure (after the mass was added) were observed and compared. The stability of the eigenvectors of the CMRA with the constant mass (*M1* = *M2* = *M3* = *M4* = *M5* = *M* =3.8267nanokg) and constant stiffness (*K1* =

K2 = K3 = K4 = K5 = K = 24.9741N/m) was also analysed by adding the same amount of mass to R1, R2 , R3, R4, and R5 separately.

4.6.3 Result and Discussion

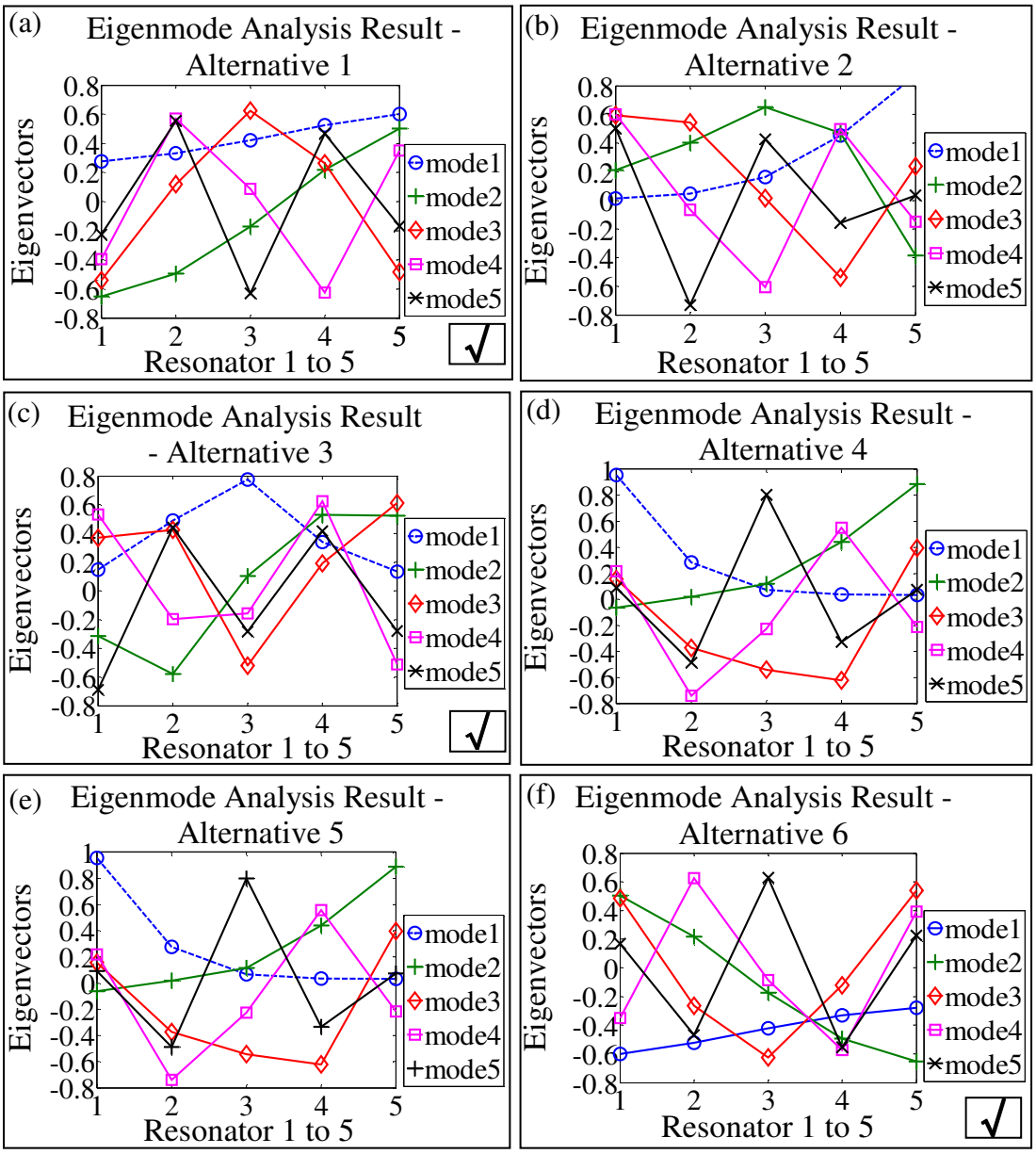

Figure 4.7 Eigenmode analysis result of 6 alternatives of Staggered CMRA

Figure 4.7 shows the eigenmodes analysis result of the 6 alternatives of the staggered CMRA. If we observe the eigenvectors at resonator 1 (R1) and R5 only 3 structure alternatives, (a):

Alternative(1), (c):Alternative(3), and (f):Alternative(6) (with '√' mark on Figure 4.7) are considered measurable since they all have an anti-node at the ends of the array.

Referring to alternative(1) (Figure 4.7(a)) and alternative(2) (b) with the uniform step-staggered mass approach; at a small amount of staggered mass (i.e. 0.1%**M* step increments) all the 5 eigenmodes are measurable. However, with a slightly larger amount of the step-staggered mass (i.e. 1%**M* increment), the mode 1 and 5 (Figure 4.7 (b)) approached zero. Therefore, mode 1 and 5 for alternative(2) expected unable to be measured.

Consider alternative(3) ((Figure 4.7(c)) and alternative(4) (Figure 4.7(d)) with the unsymmetrical but balanced mass distribution between the first half and the second half of the structure array. At a maximum of 7% total staggered mass on the structure array and with the heaviest mass positioned in the middle, all the 5 modal frequencies of the structure are measurable at R1 and R5. Positioning the heaviest mass at the end of the array (R1 and R5), (Figure 4.7 (d)) reduces the measurability of the structure output signal since the eigenvectors of the structure at R1 and R5 restrained to zero.

For alternative(5) (Figure 4.7(e)) and alternative(6) (Figure 4.7(f)), where the structure stiffness were staggered; with the unsymmetrical but balanced stiffness distribution for the alternative(5), placing the most stiff resonator at the middle of array (R3) and the least stiff resonator at the end of the array caused ineffective resonator displacement at R1 and R5. Hence, most of the eigenmodes at R1 and R5 approached zero. For alternative 6, with small uniform step-staggered stiffness (0.1%**K*) all the structure eigenmodes at R1 and R5 are measurable.

For the uniqueness of the frequency response pattern, consider the 5 modal frequencies of the staggered structure in Table 4-6, when the 5 resonators absorbs a mass separately. Comparing the 5 tests; although, some of the 5 modal frequencies of the structure alternatives

were identical when the single resonator (R1, R2, R3, R4 and R5) absorbs a mass (3.8267 x 10^{-12} kg) separately, but none of the test results completely mirror each other. Hence, it can be claimed that by breaking the structure symmetry using the staggered mass or staggered stiffness approaches (as exemplified by alternative(1), (3), and (6)) a unique frequency response pattern can be produced for a single resonator mass changes.

Table 4-6 Eigenfrequency analysis result of the staggered CMRA (Alternative(1), (3), and (6)); Note: identical colour for each structure alternative highlights similar eigenfrequencies value

Alternative of 5 CMRA		Modal Eigenfrequencies (f_M) [Hz]					
		Initial	+m @R1 (Test 1)	+m @R2 (Test 2)	+m @R3 (Test 3)	+m @R4 (Test 4)	+m @R5 (Test 5)
Alternative 1	f_{M1}	12836	12835	12835	12834	12834	12833
	f_{M2}	12871	12868	12869	12870	12870	12869
	f_{M3}	12949	12947	12949	12946	12948	12947
	f_{M4}	13046	13045	13044	13046	13044	13045
	f_{M5}	13125	13125	13123	13123	13124	13125
Alternative 3	f_{M1}	12932	12932	12930	12928	12931	12932
	f_{M2}	13054	13053	13051	13054	13052	13052
	f_{M3}	13111	13110	13109	13109	13110	13108
	f_{M4}	13234	13232	13234	13234	13232	13233
	f_{M5}	13256	13253	13255	13256	13255	13256
Alternative 6	f_{M1}	12874	12872	12872	12873	12873	12874
	f_{M2}	12909	12908	12909	12909	12908	12906
	f_{M3}	12987	12986	12987	12985	12987	12985
	f_{M4}	13085	13084	13082	13085	13083	13084
	f_{M5}	13164	13164	13162	13161	13162	13164

Figure 4.8 exemplifies the stability analysis result of structure eigenvectors for mode 2, before and after mass was added to the single resonator separately (refer to Appendix C for a complete eigenvectors stability analysis result for alternatives 1 to 6).

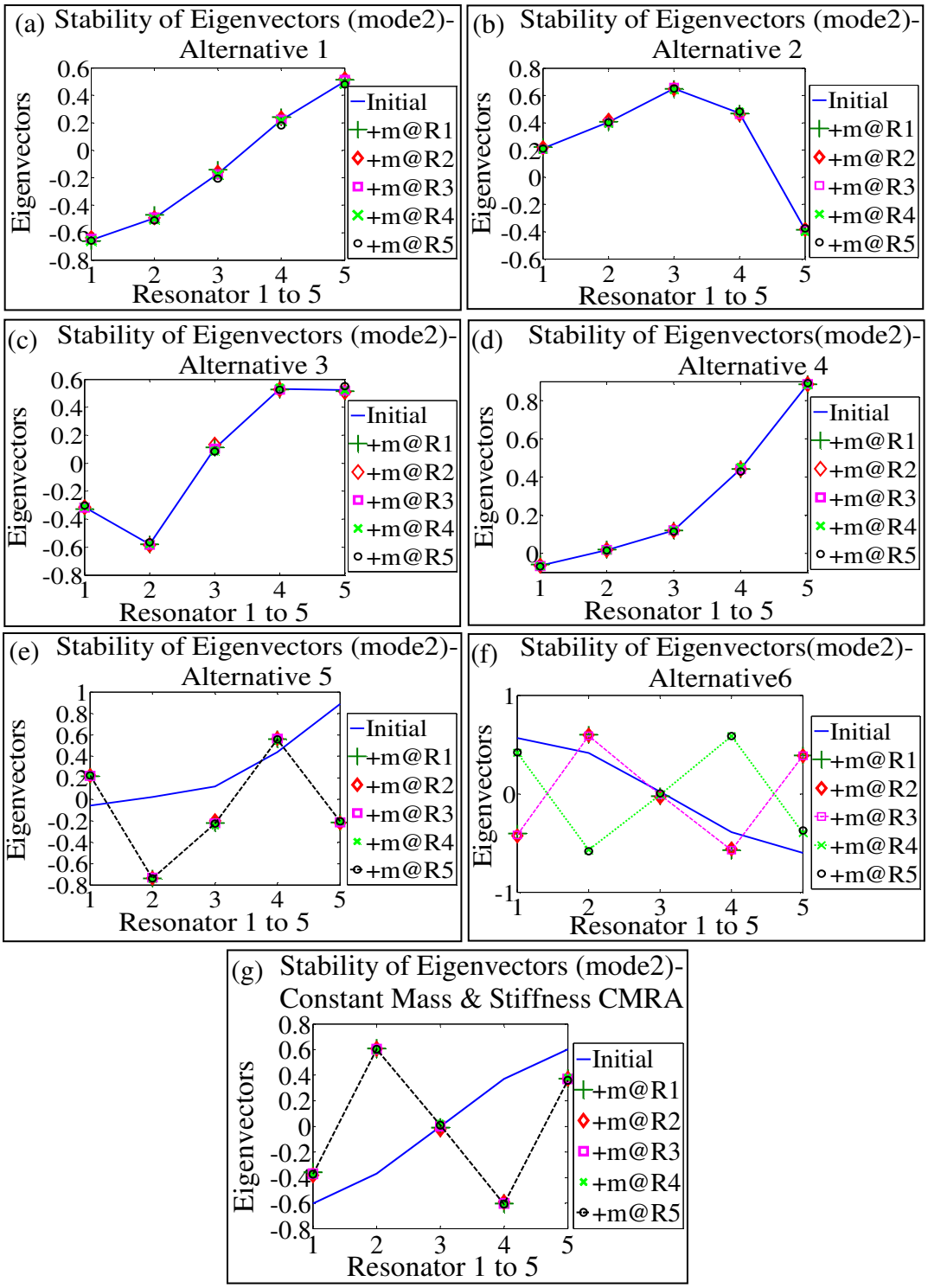

Figure 4.8 Stability of eigenvectors analysis result: example for mode 2; (a)-(f) six staggered structure alternatives; (g) constant mass and stiffness CMRA

Consider alternative(1) and (2) (Figure 4.8(a), (b) and Appendix C); by uniformly staggering the mass all the perturbed eigenvectors are stable (i.e. comparable eigenmodes) compared to the unperturbed eigenvectors.

For alternative(3) and (4) (unsymmetrical staggered mass - balanced mass distribution between the first and second half of the structure array), when the heaviest mass was positioned in the middle of the structure array (Figure 4.8(c), Appendix C) all the perturbed eigenvectors are stable except when mass is added at R1 (for mode 1 and mode 5). However when the heaviest masses were restrained at both ends of the structure array (Figure 4.8(d), Appendix C) all the perturbed eigenvectors are stable compared to unperturbed eigenvectors. Hence, it can be claimed that by constraining the relative displacement of the end resonator (i.e. positioning the heaviest mass at the end of the structure array) helped to stabilize the structure eigenvectors.

When the structure stiffness was staggered (i.e. for Alternative(5) and (6); Figure 4.8(e), and (f)); all the perturbed eigenvectors are unstable. Hence, it can be argued that, by only staggering the stiffness of the resonators, we are unable to stabilize the perturbed eigenvectors. Figure 4.8(g) depicts the stability of eigenvectors analysis result of 5 constant mass and constant stiffness coupled resonators. With the constant mass resonators all the perturbed eigenvectors are always different (unstable) compared to the unperturbed eigenvectors.

From the overall analyses result, the staggered mass and staggered stiffness approaches helped to break the structure symmetry of the 5 constant CMRA. As a result the structure (Alternatives 1, 3, and 6) produced unique modal frequencies for the single resonator mass changes.

The approach used to stagger the structure is very important to ensure a measurable output signal and stable eigenvectors. Although, the uniform step staggered mass produced stable eigenvectors, but at maximum of 1% staggered mass between each resonator the eigenvectors at R1 and R5 for mode 1 and 5 approached zero. The Alternative(3) with the unsymmetrical staggered mass but with balance mass distribution between the first half and second half of the structure array (heaviest mass in the middle) is considered an effective way to stagger the mass. At 7% total staggered mass (i.e. between R1 and R2, R1//R2: 3%, R2//R3:1%, R3//R4:2%, and R4//R5:1%) the eigenvectors at R1, R2, R3, R4 and R5 are measurable for all the 5 structure eigenmodes. Although, the eigenvectors were slightly unstable when mass was added at R1, but the perturbed eigenvectors were stable for the other 4 single resonator mass changes. Positioning the heaviest mass at the end of the structure array stabilized the eigenvectors for all the 5 resonator mass changes; but some of eigenvectors at R5 (mode 1 and mode 5) reduced to zero.

Staggering only the resonator stiffness, did not stabilize the eigenvectors of the perturbed structure. However, when we refer to the actual CMRA design, either by staggering the mass or stiffness of the resonator, we in fact change the mass of resonators. Hence both alternatives are used to stagger the CMRA (will be discussed in Chapter 5).

4.7 Summary and Conclusion

This chapter discusses the performance improvement of the CMRA using the lumped mass model analysis. Re-evaluation of the CMRA-v1 in Section 4.3 confirmed that the two large mass of the comb actuators which were rigidly coupled to R1 and R5 caused the standalone node at R1 and R5. The large mass of the comb drive actuator restrained the displacement of the R1 and R5. As a result, no movement was made to pull the adjacent resonators and the

readout comb actuator. Hence, the frequency response of the 5 coupled resonators is unable to be measured at R5.

From the structure improvement analysis in Section 4.4, the measurability of the structure output signal relies on the modal eigenfrequencies of the coupled structure and system eigenvectors. The modal frequency and the eigenvectors depend on the fundamental frequencies of the coupled structure, which was directly related to the mass and stiffness configuration of the resonators. The eigenvectors of the structure which are controlled by the configuration of the mass and resonator stiffness determined the final measurability of the structure at a specific measurement point. With constant mass and constant stiffness resonators the measurability of the 5 eigenmodes at R1 or R5 are confirmed. However, only half of the single resonator sensor structure produced unique frequency response pattern; and the perturbed eigenvectors for all single resonator mass changes were always unstable compared to the unperturbed eigenvectors.

The main challenge of the CMRA-v2 is to ensure the structure is measurable, having a unique frequency response pattern and stable perturbed eigenvectors compared to the unperturbed structure. The unique frequency response pattern is very important in order to detect the species absorbed by the resonator. The stable perturbed eigenvectors is important if the unperturbed eigenvectors will be used to estimate the mass changes pattern absorb by the resonators using the inverse eigenvalue analysis (will be discussed in Chapter 5).

Section 4.6 analyses and discusses few alternatives to break the structure symmetry of the constant CMRA in order to produce a unique frequency response pattern, stabilize the system eigenvectors and ensure the measurability of the structure output signal. Staggering the mass or stiffness of resonators produced unique frequency response patterns. To ensure the measurability of the coupled structure, the approach to stagger the structure and the

amount of the staggered mass is important. For example, the amount of the staggered mass for the uniform step staggered mass alternative must be less than 1%*M in order to ensure a measurable output signal of the 5 CMRA eigenmodes at both ends of the structure array. The research finally selects the alternative(3) as the basis to stagger the mass and stiffness of the 5 constant mass CMRA in Chapter 5. With the 7% total staggered mass for 5 resonators and the heaviest mass positioned in the middle of the structure array, the alternative(3) maintained the measurability of the CMRA structure.

CHAPTER 5 - MODELLING, FINITE ELEMENT ANALYSIS AND PERFORMANCE EVALUATION OF CMRA-V2

5.1 Introduction

This chapter presents an improved design of the coupled micro resonator array (CMRA-v2). The designs of the CMRA-v2 include a Constant CMRA, a Staggered Mass and a Staggered Stiffness CMRA are briefly explained in Section 5.2. Using COMSOL Multiphysics Finite Element Analysis (FEA), the performance of the structure is analysed and discussed in Section 5.3. Using a lumped mass model, Section 5.4 compares the performance of the designed structures in terms of the measurability of the output signal, uniqueness of frequency response pattern and stability of system eigenvectors. To further evaluate the stability of the system eigenvectors, Section 5.5 presents an inverse eigenvalue analysis; the mass change pattern of the CMRA-v2 single resonator sensor is estimated using the unperturbed design eigenvectors and the evaluated perturbed eigenfrequencies from the eigenvalue and eigenvectors derived for the perturbed structure in Section 5.4. This chapter also discusses the research work related to the manufacturing variation analysis. Section 5.6 presents an approach to quantify the manufacturing variation, discusses the result of the quantified data and presents an analysis of the impact of manufacturing variation on the designed Constant Mass CMRA.

5.2 Improved Design of CMRA-v2

This section presents the improved design of the CMRA-v2 structure which includes:-

- 5 Constant Mass CMRA
- 5 Staggered Mass
- 5 Staggered Stiffness CMRA

As discussed in Chapter 4, the Constant Mass CMRA design always produces a measurable frequency response for all the 5 eigenmodes of the structure. However, the structure does not produce a unique frequency response pattern for a single resonator mass perturbations and the perturbed structure eigenvectors are always unstable (dissimilar) compared to unperturbed eigenvectors. The 5 Constant Mass CMRA was designed in order to study and examine how the manufacturing variation may naturally stagger the stiffness or mass of the coupled resonators, and hence the final frequency response pattern of the structure.

As discussed in Section 4.6 (Chapter 4), with the staggered mass and staggered stiffness approaches, a unique frequency response pattern was produced. With the staggered mass approach the system eigenvectors of the CMRA was stabilized. Since the eigenvectors were stabilized against the perturbation mass, the staggered stiffness approach alone could not stabilize the eigenvectors. However, in reality when we stagger the stiffness of the resonator (i.e. increasing or decreasing the length of resonator anchor spring) we actually stagger the mass as well. Hence two approaches of the staggered mass (i.e. staggering linked masses of the resonators, Section 5.2.2) and staggered stiffness (i.e. staggering the length of the anchor spring) were chosen to improve the performance of the CMRA.

5.2.1 Five Constant Mass CMRA

Figure 5.1 shows the schematic of the second version of the 5 constant coupled micro resonator array structure. The 5 Constant Mass CMRA consists of 5 constant mass comb-drive resonators which were coupled with a narrowed S-shape or zigzag coupling spring. Each single resonator is anchored with 4 semi zigzag anchor spring. The zigzag spring was selected instead of butterfly spring to reduce the space occupied by the coupling spring. As discussed in Section 3.4.1 the spurious responses introduced by the spring were reduced by

increasing the length of the spring (L_{CSP}); a domination of the mass of the CMRA-v2 also help to reduce the unwanted response. With the CMRA-v2, the structure was designed to ensure the response pattern of the structure can be easily measured. The single resonator (Figure 5.1(b)) was designed with four sets of fixed comb-drives. The first 2 sets of the comb were designed for driving the structure (*Vin*) and the last 2 sets of the comb for reading the output signal of the structure (i_{out}). The measurement can be done either by using a single drive-a single readout measurement or a differential drive-differential readout measurement, or vice versa. Table 5-1 highlights the main geometrical dimensions of the structure.

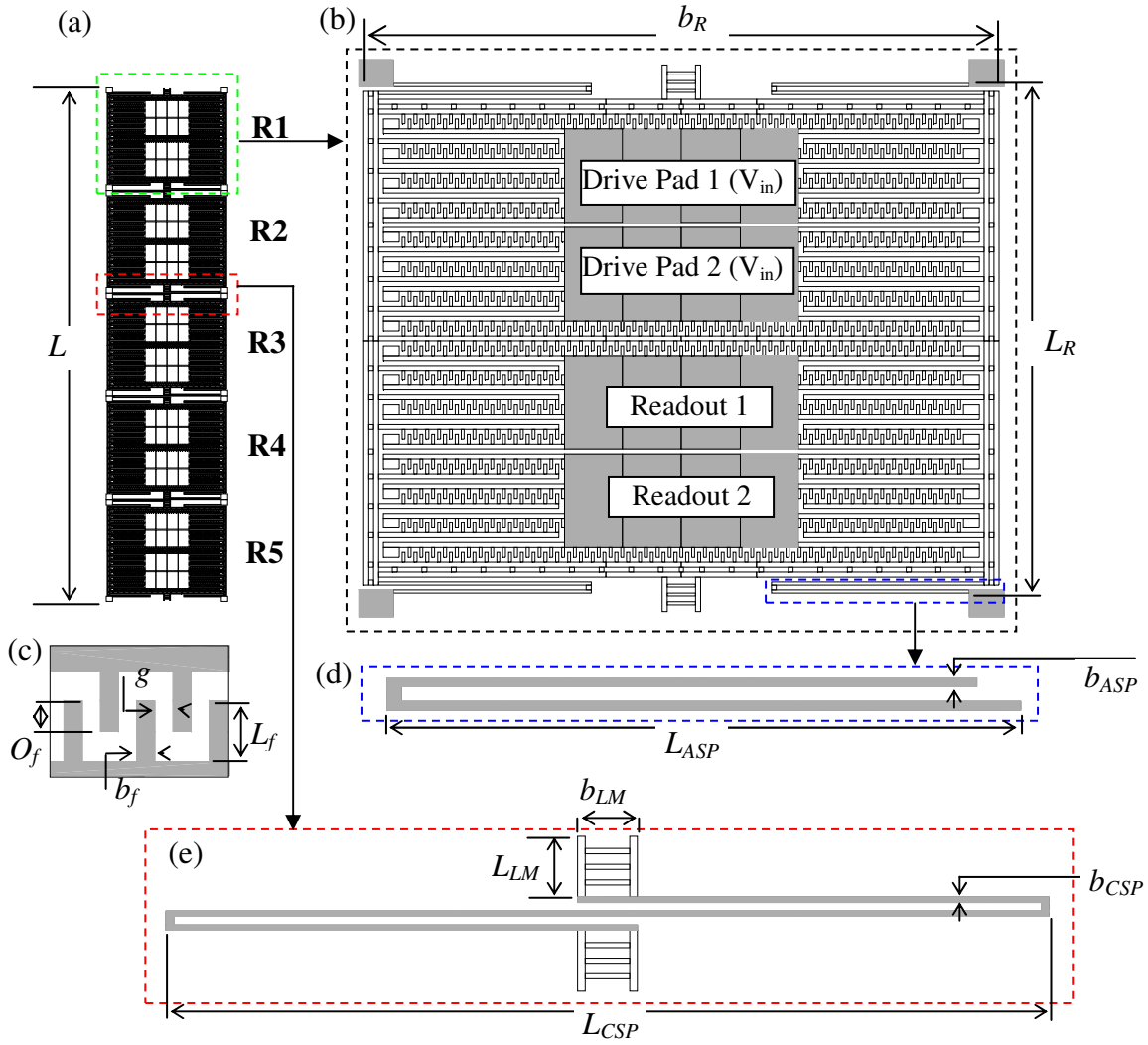

Figure 5.1(a) 5 Constant CMRA-v2; (b) Enlarged single resonator (singleR-v2); (c) Comb fingers; (d) semi-S shape anchor spring; (e) S-shape coupling spring and constant linked mass

Table 5-1 Main geometrical design parameter of the 5 Constant CMRA

No. Design Parameter	Description of Geometrical Comb Resonator Parameter	Dimension [μm]
1	Length of Single R, L_R	517
2	Width of Single R, b_R	645
3	Length of 5 Constant CMRA, L	2818
4	Length of anchor spring, L_{ASP}	216
5	Width of anchor spring, b_{ASP}	3
6	Length of coupling spring, L_{CSP}	575
7	Width of coupling spring, b_{CSP}	3
8	Length of Linked mass, L_{LM}	35
9	Width of Linked mass, b_{LM}	39
10	Length of comb finger, L_f	10
11	Width of comb finger, b_f	3
12	Gap between finger, g	3
13	Overlapping distance, O_f	5
14	Total number of fingers, n	5260 fingers

5.2.2 Five Staggered Coupled Micro Resonator Array (Staggered CMRA)

In order to improve the performance of the CMRA, this research proposes 2 design alternatives of the Staggered CMRA: (1) 5 Staggered Mass CMRA and (2) 5 Staggered Stiffness CMRA. As discussed in Section 4.6, by breaking the symmetry of the structure, both alternatives improved the distinguishability of the frequency response pattern of the CMRA. Either the staggered mass (i.e. modifying the resonator linked mass) or the staggered stiffness design alternatives (i.e. modifying length of the resonator anchor spring), the mass of the coupled resonators are modified. Hence both alternatives are used to stabilize the system eigenvectors.

For the 5 Staggered Mass CMRA, the main geometrical dimensions of the structure were the same as the 5 Constant CMRA, except for the width of the linked mass (b_{LM}, Figure 5.2(d)) which was used to connect the resonator and the coupling spring (design parameter no 9, Table 5-1). Figure 5.2 illustrates the schematic of the 5 Staggered Mass CMRA.

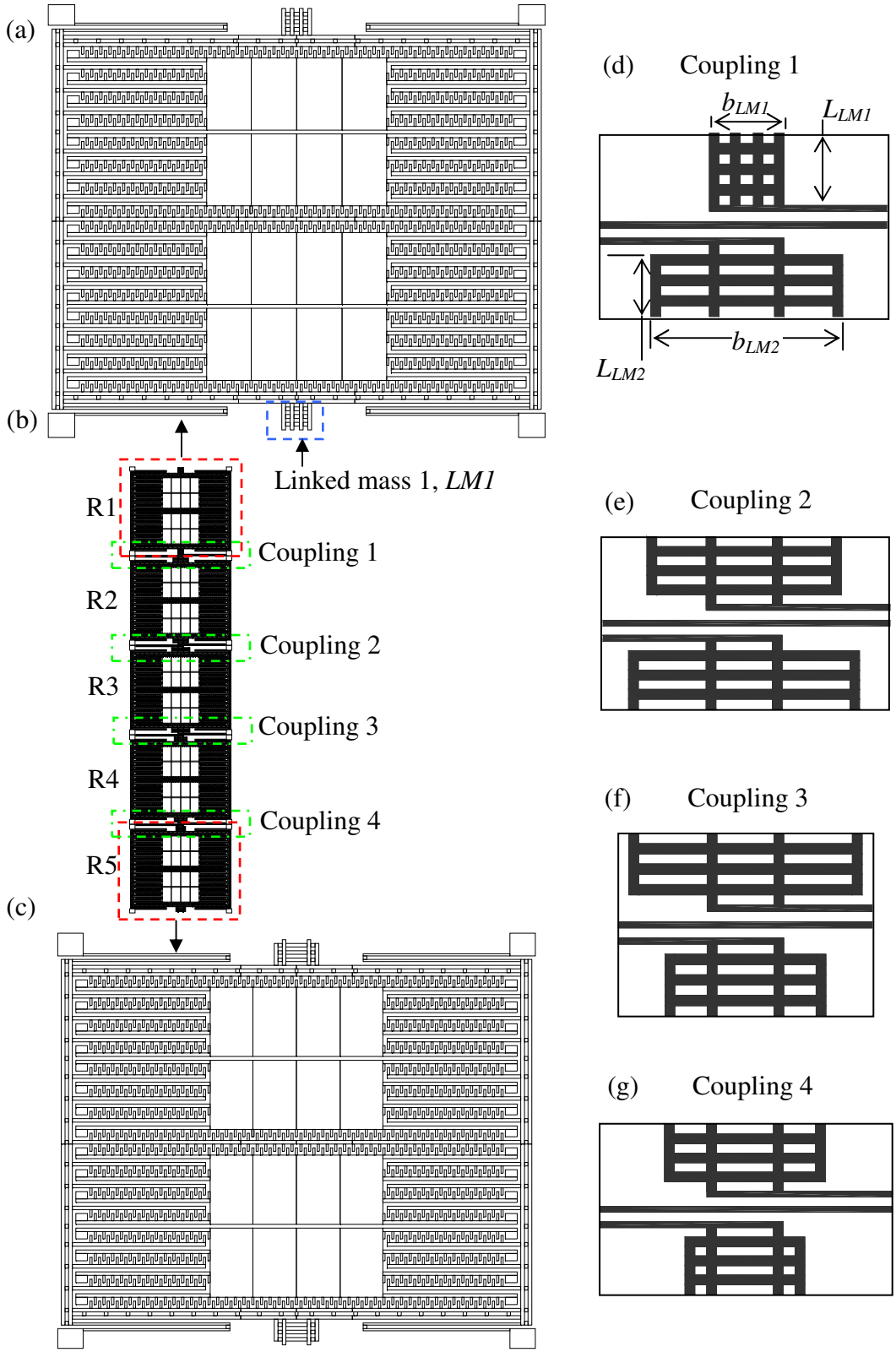

Figure 5.2 (a) Resonator 1, R1 (highlighted linked mass 1, *LM1*); (b) Schematic of Staggered Mass CMRA; (c) R5; (d) Coupling 1- linked mass 1 and 2; (e) Coupling 2- linked mass 2 and 3; (f) Coupling 3- linked mass 3 and 4; (g) Coupling 4- linked mass 4 and 5

To break the symmetry of the constant CMRA, the Staggered Mass CMRA was designed with a slight unsymmetrical mass distribution between all resonators. As discussed in Chapter 4, to ensure the structure vibrates efficiently generating a measurable output signal, all masses in the first half of the structure array (sum of R1 and R2) and the second half of the array (sum of R4 and R5) remained balanced with the heaviest mass positioned in the middle of the structure. The approach will help to effectively stagger the resonator mass and balance the relative displacement of the 5 resonators for measurability of the structure output signal (i.e. at R1 and R5). The length (L_{LM}) of the linked mass for all resonators remained 35μm (Figure 5.2(d) – (g)). The width (b_{LM}) of the linked mass for R1, R2, R3 and R5 were designed to be 39μm, 100, 119, 82, and 61μm respectively.

For the second alternative of the 5 Staggered Stiffness CMRA, the stiffness of the resonators was varied by modifying the length (L_{ASP}) of the 4 anchor springs for each resonator design parameter no.4, from Table 5-1. The least stiff resonator was positioned in the middle of the coupled structure and the stiffer resonator at the end of the structure array. Positioning the least stiff resonator which has the heaviest resonator mass (i.e. the longest anchor spring) at the middle of the structure will help to ensure effective structure movement for measurability of the output signal. The anchor spring length of the least stiff resonator R3 remained at 216μm and the other anchor springs for R1, R2, R4 and R5 were modified to 214.5μm, 215, 215.5 and 214μm respectively. All other geometrical design parameters remained the same as the 5 Constant CMRA.

5.3 Modelling and Finite Element Analysis (FEA) of CMRA-v2

FEA using COMSOL Multiphysics was used to determine the performance of the designed CMRA, i.e. the fundamental frequencies, the structure eigenmodes, the effective mass and

effective stiffness of the resonators, the capacitance generated by the comb-drive resonator and the frequency response of the unperturbed CMRA.

5.3.1 Eigenfrequency and Eigenmode

To determine the fundamental frequency and the eigenmodes of the structure, an eigenfrequency analysis was performed in the Plane Stress application mode of the COMSOL FEA using the eigenfrequency solver. Table 5-2 lists the fundamental frequency of the analysed CMRA structure.

Table 5-2 the eigenfrequency of comb-drive resonator (SingleR-v2) and fundamental modal frequencies of the three designed CMRA(s) analysed using the FEA

Frequency of SingleR-v2 [Hz]	Modal Eigenfrequencies [Hz] of the CMRA-v2		
	5 Constant Mass CMRA	5 Staggered Mass CMRA	5 Staggered Stiffness CMRA
12857.3	f_{M1} = 12543.5	f_{M1} = 12340.2	f_{M1} = 12574.8
	f_{M2} = 12651.4	f_{M2} = 12502.2	f_{M2} = 12725.6
	f_{M3} = 12792.2	f_{M3} = 12638.2	f_{M3} = 12874.5
	f_{M4} = 12922.6	f_{M4} = 12806.1	f_{M4} = 13032.2
	f_{M5} = 13009.5	f_{M5} = 12848.2	f_{M5} = 13076.8

As can be seen in Table 5-2, all of the devices have fundamental frequencies centred around 12000 Hz. Comparing the five eigenfrequencies of the 5 Staggered Mass CMRA are slightly lower than the 5 Constant CMRA, due to the extra mass. While, the 5 eigenfrequencies of the Staggered Stiffness CMRA were slightly higher compared to the 5 Constant Mass CMRA, this was due to the stiffer springs which were designed to anchor the structure.

Figure 5.3, 5.4 and 5.5 show the 5 eigenmodes of the CMRA structure for the 5 Constant CMRA, 5 Staggered Mass CMRA and 5 Staggered Stiffness CMRA respectively. The 5 eigenmodes of the structure represent the relative movement of the coupled resonators either in phase or anti-phase. The relative displacement values are summarized and tabulated in Table 5-3, 5-4, and 5-5 respectively.

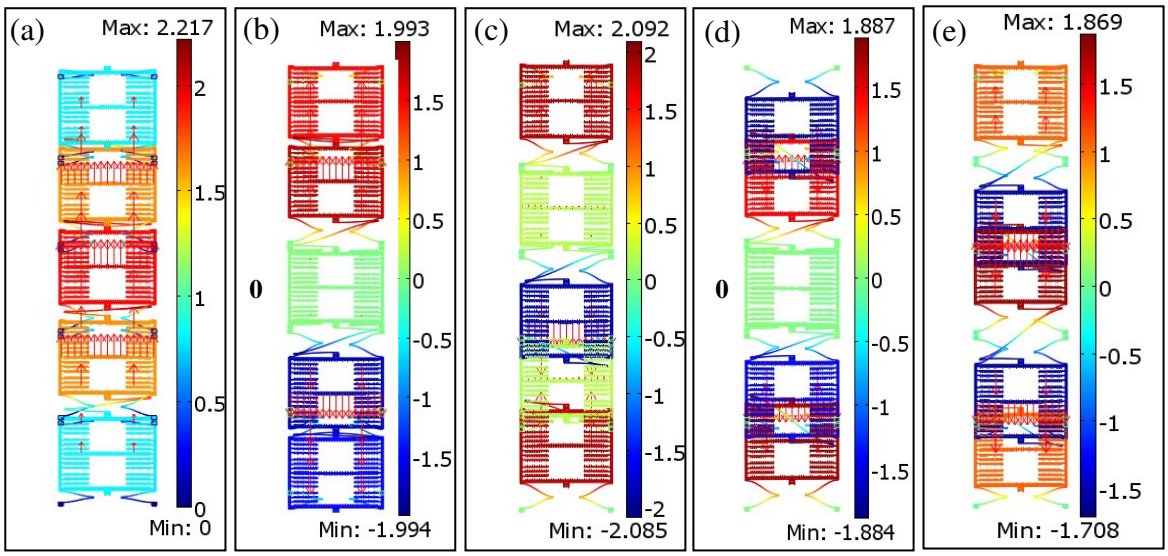

Figure 5.3 Eigenmodes analyses of 5 Constant Mass CMRA : (a) mode1; (b) mode2; (c) mode3; (d) mode4; (e) mode5

Table 5-3 the relative displacement of the resonators (associated to different colour shown on a scale bar) from the eigenmode analysis of 5 Constant Mass CMRA (in Figure 5.3)

	Mode 1 (a)	Mode 2 (b)	Mode 3 (c)	Mode 4 (d)	Mode 5 (e)
R1	+0.81	+1.48	+1.86	-1.76	+1.09
R2	+1.63	+1.74	+0.21	+1.47	-1.58
R3	+1.94	0	-1.88	0	+1.76
R4	+1.63	-1.74	+0.21	-1.47	-1.58
R5	+0.81	-1.48	+1.86	+1.76	+1.09

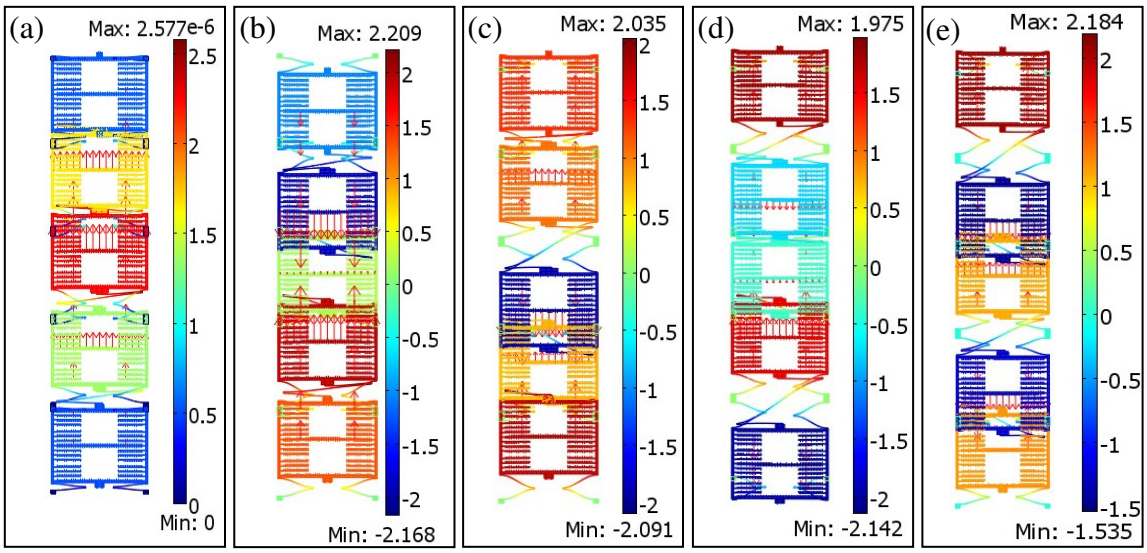

Figure 5.4 Eigenmodes analysis result of 5 Staggered Mass CMRA: (a) mode1; (b) mode2; (c) mode3; (d) mode 4; (e) mode5

Table 5-4 the relative displacement of the resonators (associated to different colour shown on a scale bar) from the eigenmode analysis of 5 Staggered Mass CMRA (Figure 5.4)

	Mode 1 (a)	Mode 2 (b)	Mode 3 (c)	Mode 4 (d)	Mode 5 (e)
R1	+0.54	-1.06	+1.34	+1.82	+2.06
R2	+1.66	-1.93	+1.07	-0.75	-1.46
R3	+2.27	+0.20	-1.93	-0.37	+1.10
R4	+1.36	+1.95	+0.79	+1.58	-1.27
R5	+0.50	+1.33	+1.79	-2.02	+1.18

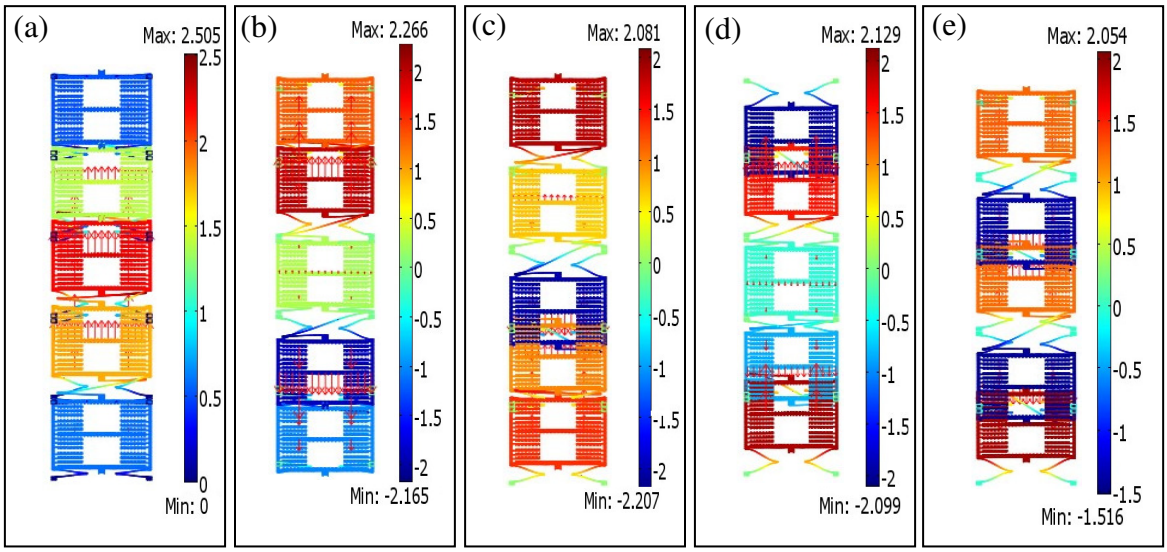

Figure 5.5 Eigenmodes analysis result of 5 Staggered Stiffness CMRA: (a) mode1; (b) mode2; (c) mode3; (d) mode 4; (e) mode5

Table 5-5 the relative displacement of the resonators (associated to different colour shown on a scale bar) from the eigenmode analysis of 5 Staggered Stiffness CMRA (in Figure 5.5)

	Mode 1 (a)	Mode 2 (b)	Mode 3 (c)	Mode 4 (d)	Mode 5 (e)
R1	+0.52	+1.32	+1.82	-1.96	+1.25
R2	+1.39	+1.99	+0.69	+1.50	-1.36
R3	+2.19	+0.25	-2.01	-0.34	+1.23
R4	+1.77	-1.91	+0.98	-0.83	-1.43
R5	+0.58	-1.03	+1.36	+1.95	+1.92

As can be observed for the three CMRA(s), each resonator shows synchronized movements either in-phase or out of phase for the 5 eigenmodes of the structure (i.e. no standalone

resonator). Hence all the 5 modal eigenfrequencies for the three CMRA(s) are expected to be measurable.

5.3.2 Frequency Response Pattern of the Unperturbed CMRA

The frequency response analysis (neglecting damping) was employed to determine the frequency response pattern of the unperturbed CMRA. Since the CMRA prime vibration mode is in lateral direction (i.e. x-y plane), the analysis was done in a Plane Stress application mode using a parametric solver (assuming no out-of-plane stress). By fixing an excitation force (e.g. F= $1x10^{-6}$ N) to drive the Constant CMRA structure (e.g. drive at R1, Figure 5.6) and sweeping through the excitation frequency (i.e. the range of modal frequencies of the structure, f_{M1}-f_{M5} = 12300-13100), the software solves for the frequency response of the structure. With the second version of the CMRA, we can drive or readout the response either at R1, R2, R3, R4 or R5.

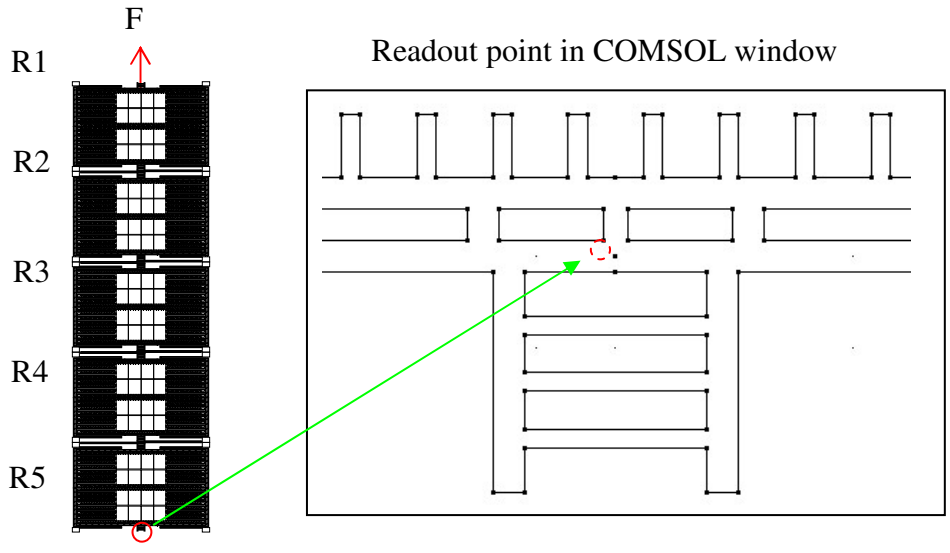

Figure 5.6 Schematic of 5 Constant Mass CMRA ; an example of drive point at R1 and readout point at R5 for frequency response analysis

Figure 5.7 shows the frequency response pattern of the 3 CMRA(s) structure designs, which were driven at R1 and Readout at R5. With different mass and stiffness configurations the 3

CMRA(s) show different frequency response patterns. The frequency response pattern agrees with the eigenmode analysis (see Section 5.3.1). For example for the 5 Constant CMRA (Figure 5.7(a)), the 5 frequency response peaks were observed with the highest and lowest response at the third and first eigenfrequency respectively. Referring to the resonator 5 (R5) for the eigenmodes of the structure (Figure 5.3(a) – (e), and Table 5-3); the R5 on the eigenmode 3 shows the highest relative displacement (+1.86) and the R5 on the eigenmode 1 shows the least relative displacement (+0.81). Referring to Figure 5.7(a), the absolute response of the first modal frequency is 6.51µm, which is considered detectable by the electronics readout.

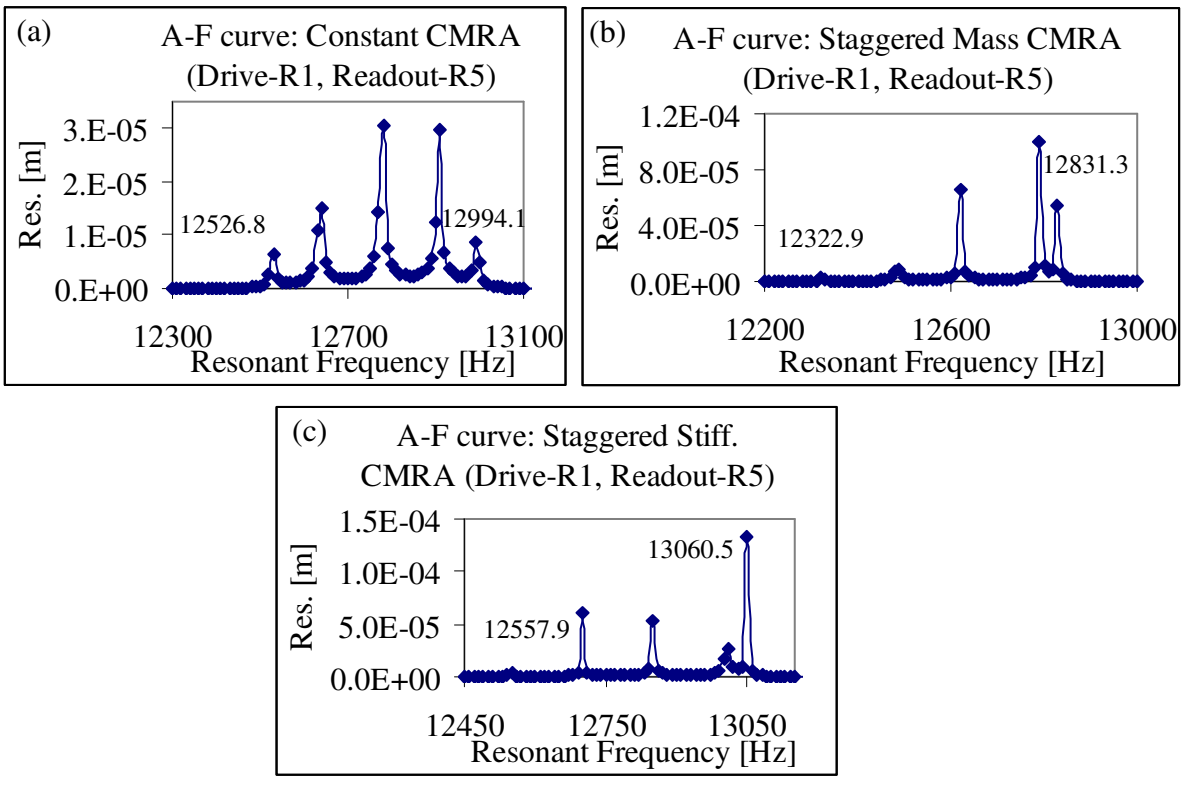

Figure 5.7 Frequency response analysis result of the CMRA (drive at R1, readout at R5); (a) 5 Constant CMRA; (b) 5 Staggered Mass CMRA; (c) 5 Staggered Stiffness CMRA.

For the Staggered Mass CMRA (Figure 5.7 (b)), 5 peaks also were observed with the lowest response and the highest response occurs at modal frequency 1 and 4 respectively. It can be

explained that the occurrence of the lowest and highest response may be due to the CMRA design configuration (i.e. heaviest mass at R3 and lightest mass at R1 and R5) and the drive and readout point of the structure (i.e. R1-R5); referring to the eigenmode analysis of the Staggered Mass CMRA (Figure 5.4, Table 5-4), the R5 in eigenmode 1 and eigenmode 4 displays the least and the maximum relative displacement respectively.

It is important to emphasize that at different drive and readout points a particular CMRA structure will present different frequency response patterns. Figure 5.8 shows examples of the frequency response pattern of the Constant CMRA when the response was driven and measured at R1-R3 and R3-R2 respectively. Due to the symmetrical structure, either driving the structure at R3 or measuring the response at R3 only 3 frequency response peaks are observed. The two missing eigenfrequencies are modal frequency 2 (f_{M2}) and modal frequency 4 (f_{M4}). Referring to the eigenmode 2 and 4 for the Constant CMRA (Figure 5.3 (b) and (d)), the third resonator, R3 has a zero displacement (a node). Hence, when the structure is driven or readout at R3 the response of the two eigenmodes turns to zero.

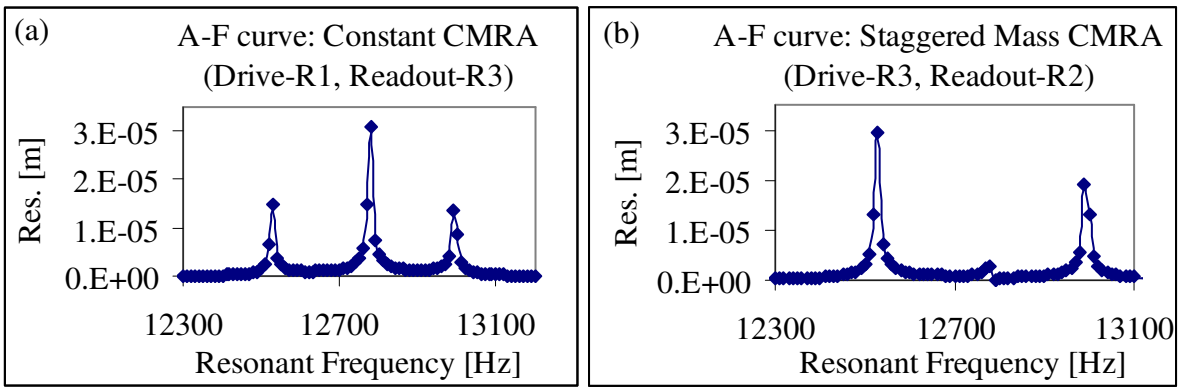

Figure 5.8 Frequency response analysis result of 5 Constant CMRA using FEA at different drive and readout points (a) Drive at R1 and Readout at R3; (b) Drive at R3 and readout at R2

5.3.3 Effective Mass and Effective Stiffness

In order to examine the performance of the perturbed CMRA , the structure is analysed using a lumped mass model. The model requires inputs of effective mass and effective stiffness of the coupled elements. The effective mass of the resonator (m) was calculated based on the resonant frequency of each uncoupled structure ($\omega_n^2 = k/m$); where k is the effective stiffness of the structure element, and ω_n is the structure resonant frequency.

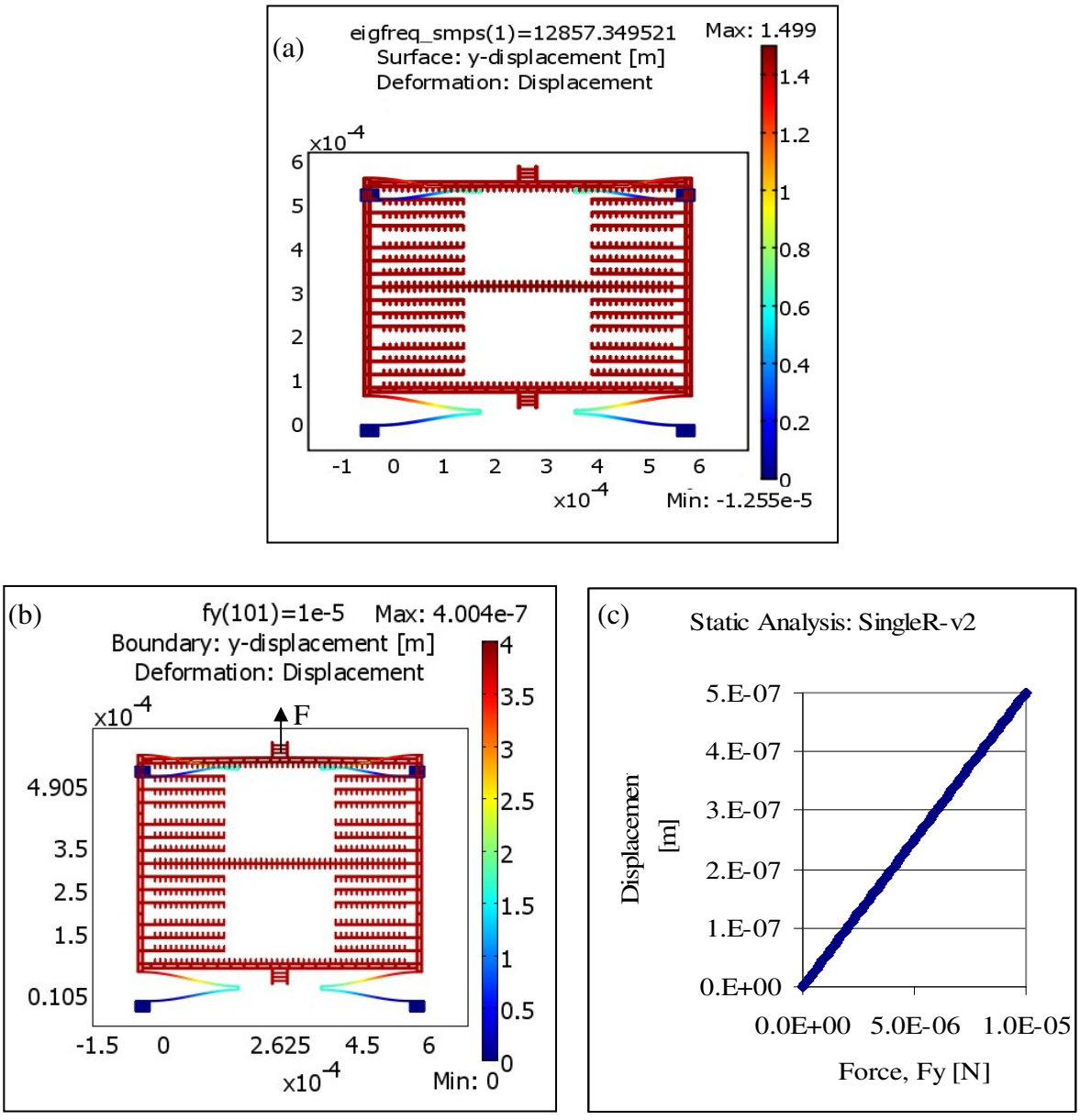

Figure 5.9 (a) Eigenfrequency of a single comb-drive resonator; (b), (c) Static displacement analysis result of comb-drive resonator

The resonant frequency of each uncoupled resonator is determined using an eigenfrequency analysis (Section 5.3.1). As presented in Chapter 3 (Section 3.3.3.2), the stiffness of the structure is evaluated in COMSOL Multiphysics using the Static analysis and parametric solver. By using a static input force, F, the software returns the static displacement of the structure. The stiffness of the structure is calculated by relating the static input force, F and static displacement of the structure, δ; ($k = F/\delta$; Equation 3-5). Figure 5.9 shows an example of the resonant frequency and static analysis result of the single comb-drive resonator from the FEA. Table 5-6 summarizes the effective stiffness and effective mass of each 5 resonators of the three CMRA(s).

Table 5-6 Effective mass and stiffness of the CMRA structure elements evaluated using COMSOL FEA (Note: the three CMRA was coupled with 4 constant coupling spring; k_{csp1}= k_{csp2}= k_{csp3}= k_{csp4}= 0.2495 N/m and effective mass, m_{csp} = 4.116 x 10^{-12}kg)

Designed Parameter	Single resonator	5 Constant Mass CMRA	5 Staggered Mass CMRA	5 Staggered Stiffness CMRA
Resonator stiffness [N/m]	19.9796	k_{R1} = 19.9796 k_{R2} = 19.9796 k_{R3} = 19.9796 k_{R4} = 19.9796 k_{R5} = 19.9796	k_{R1} = 19.9954 k_{R2} = 20.1343 k_{R3} = 20.1665 k_{R4} = 20.0868 k_{R5} = 20.0414	k_{R1} = 20.3029 k_{R2} = 20.1807 k_{R3} = 19.9796 k_{R4} = 20.0109 k_{R5} = 20.4824
Resonator mass, m [nanokg]	3.0615	m_{R1} = 3.0615 m_{R2} = 3.0615 m_{R3} = 3.0615 m_{R4} = 3.0615 m_{R5} = 3.0615	m_{R1} = 3.0941 m_{R2} = 3.1932 m_{R3} = 3.2241 m_{R4} = 3.1616 m_{R5} = 3.1263	m_{R1} = 3.0590 m_{R2} = 3.0596 m_{R3} = 3.0615 m_{R4} = 3.0607 m_{R5} = 3.0575

5.3.4 Change in Comb-Drive Capacitance

The comb drive capacitance is important since it determines the output of current (i_{out}) which is generated at the readout port of the structure. As discussed in Section 3.5.3.2, in COMSOL the capacitance was evaluated in the electrostatic application mode using the stationary solver. Figure 5.10 (a) and (b) show the capacitance analysis result of the single comb resonator. In

the analysis, the moving comb was grounded and the voltage input (V_{in}) was supplied to the first set of the fixed comb fingers.

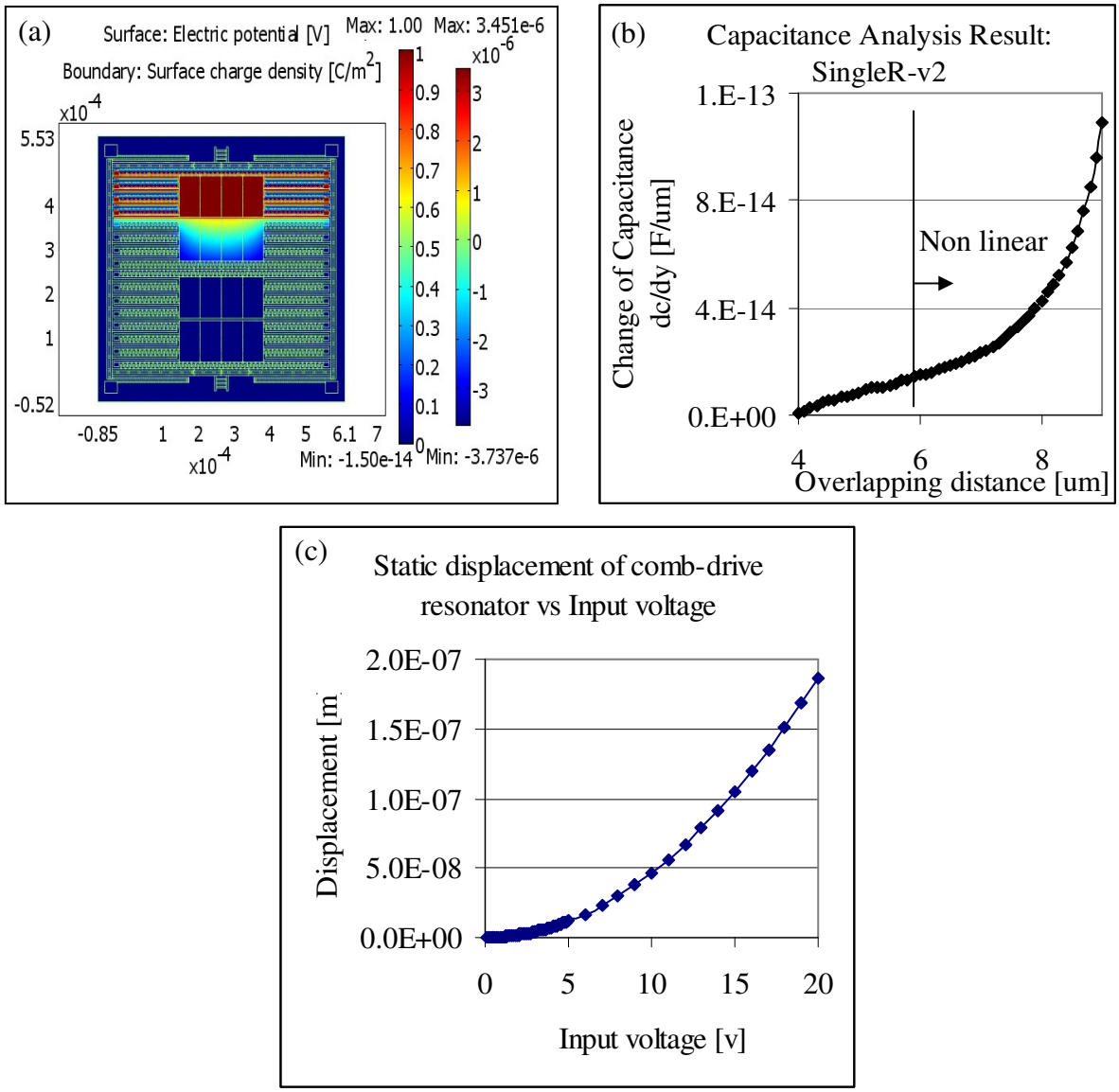

Figure 5.10 (a), (b) Capacitance analysis result of single comb-drive resonator using COMSOL FEA; (c) A static displacement of the comb-drive resonator

As can be observed (Figure 5.10 (b)) the change of the capacitance (dc/dy) of the resonator is linear when the overlapping distance is increased from 4 to 6µm. However, above the 6µm overlapping distance, the change of the capacitance becomes non-linear. From the analysis, at around 5µm overlapping distance of the fixed and moving fingers (Figure 5.10(b)), the

generated capacitance was 1.2 x 10^{-14}F/μm. With a 1V potential differences between fixed and moving fingers, the generated electrostatic force causes 4.66 x 10^{-10} static structure movement (Figure 5.10 (c)). By using Equation 3-13 in Chapter 3, the amount of generated current at a sense voltage (Vs) of 8V is approximately 7.76nanoA. Hence, the current, is more than sufficient to be processed by the available readout measurement system. Note that a quick derivation of the output current may be established by estimating the structure displacement, y ($y = (n\varepsilon_o b v^2)/(k_y g)$, Equation 3-10), and the capacitance between the fixed and moving comb-drive resonator, C ($C = 2n\varepsilon_o b\ (y+y_o)/(g)$), Equation 3-11). Then, the value of output current, i_{out} can be estimated from Equation 3-13 by substituting the value of change of capacitance (dC/dy) and natural frequency of the structure, ω.

5.4 Performance Evaluation of the CMRA-v2: Lumped Mass Analysis

5.4.1 Analysis Overview

In general with N coupled resonators, it is possible to produce (2^N – 1) possible output patterns. With 5 coupled resonators, there are 31 possible sensor combinations. For high functionality of the sensor structure, the CMRA structure should produce unique response patterns for all the sensor combinations. This section analyses the performance of the designed CMRA(s) using a lumped model, when the single resonator sensor absorbs a mass. As discussed in Section 4.2, the equation of motion for a lightly damped coupled resonators can be summarized as:-

$$m_n\ddot{x}_n + c_n\dot{x}_n - k_{C_{n-1}}x_{n-1} + (k_{C_{n-1}} + k_n + k_{C_n})x_n - k_{C_n}x_{n+1} = F(t) \qquad \text{(Equation 5-1)}$$

Where, m: mass of the resonator, c: damping parameter, k: stiffness of the resonator, k_c: stiffness of the mechanical coupling, $F(t)$: force used to drive the structure and x_n is the

displacement of the resonator. If we recall Equation 4-8 and Equation 4-9 (Section 4.2), for the equations of motion of the 5 CMRA (with negligible damping); the equations of motion are simplified into the form of the matrix eigenvalue problem:

$$(\omega)^2 \ [X] \quad = \quad [M^{-1}] \ [K] \ [X] \qquad \text{(Equation 5-2)}$$

Where, ω is the eigenvalue or natural frequency of the system, [X] is a displacement matrix of the 5 degrees of freedom of the CMRA, [M] is the mass matrix and [K] is the stiffness matrix of the CMRA.

To solve for the eigenvalue and eigenvectors of the designed CMRA (5 Constant Mass CMRA, 5 Staggered Mass CMRA, and 5 Staggered Stiffness CMRA), the value of k, k_c, and m (Table 5-6) were substituted in the Equation 5-2. The analysis was repeated to determine the overall frequency response of the coupled structure, by applying an excitation force $F(t)$ on the structure array (i.e. at R1, $F1(t)$ = 1 x 10^{-6} [N]). From Equation 5-1 and 5-2 the response of the resonators were computed as follows:-

$$[X]= [F] \ [(K - M \ (\omega)^2)]^{-1} \qquad \text{(Equation 5-3)}$$

Where, [F] is the driving force matrix. The performance of the three CMRA(s) was examined when a maximum of 1 percent of mass of the single resonator (R) (3.0615 x 10^{-11} kg) was added to each resonator (R1, R2, R3, R4, and R5) separately.

To examine and confirm the uniqueness of output signals, the stability of system eigenvectors of the structure and the sensitivity of the mass loading effect on the frequency response pattern, analyses were repeated by adding a mass of 1 x 10^{-11} kg, 1 x 10^{-12}, and 1 x 10^{-13}kg to the single resonators separately for the three CMRA(s). Note that, to analyse the effect of the staggered mass on the CMRA sensor performance, the lumped mass analysis was

performed only based on the effective mass and stiffness of the 5 resonators and effective stiffness of the coupling spring (i.e. neglecting the effect of coupling spring mass). By neglecting the coupling spring mass, the analysed peak to peak modal eigenfrequencies of the three CMRA(s) will be slightly differed when compared to the FEA result.

5.4.2 Result and Discussion: Frequency Response Pattern of CMRA

Figure 5.11, 5.12, and 5.13 are examples of the frequency response analysis result of the three CMRA(s), when the first resonator sensor (R1) and the last resonator (R5) absorbs a mass separately. Note that, all the structures were driven at R1 and the response of the resonators were monitored at R5. The complete unperturbed and perturbed modal eigenfrequencies of the structures were presented in Table 5-7, 5-8 and 5-9 respectively.

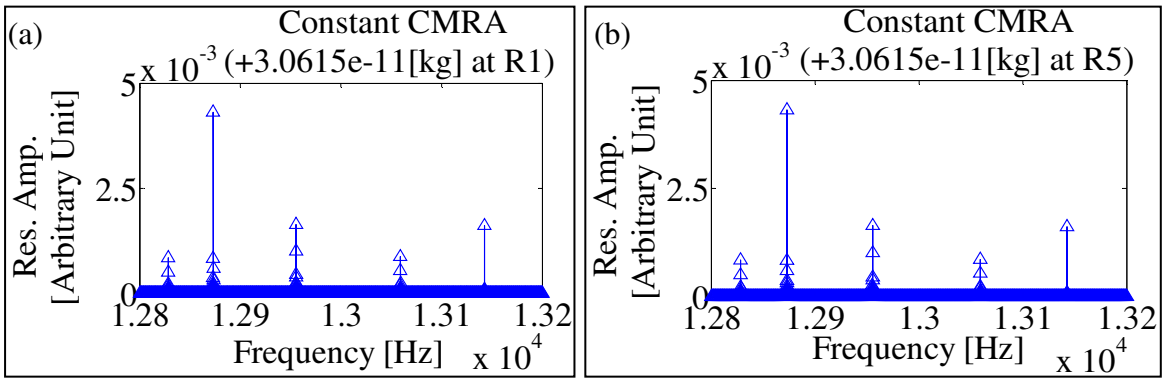

Figure 5.11 Frequency response analysis result of 5 Constant CMRA; (a) 3.0615 x 10^{-11} kg mass added at R1 only ; (b) 3.0615 x 10^{-11} kg mass added at R5 only

Table 5-7 the unperturbed and perturbed modal eigenfrequencies of the 5 Constant Mass CMRA (note: similar colours indicate that the particular modal frequencies are the same with respect to the associated mode)

Perturbed Mass [kg]	5 modal frequencies	Initial	+ At R1	+ At R2	+ At R3	+ At R4	+ At R5
3.0615×10^{-11}	f_{M1}	12857	12828	12837	12839	12837	12828
	f_{M2}	12888	12873	12881	12888	12881	12873
	f_{M3}	12968	12955	12965	12942	12965	12955
	f_{M4}	13066	13059	13042	13066	13042	13059
	f_{M5}	13144	13143	13133	13123	13133	13143
1×10^{-11}	f_{M1}	12857	12851	12852	12853	12852	12851
	f_{M2}	12888	12881	12885	12888	12885	12881
	f_{M3}	12968	12963	12967	12959	12967	12963
	f_{M4}	13066	13063	13058	13066	13058	13063
	f_{M5}	13144	13144	13140	13136	13140	13144
1×10^{-12}	f_{M1}	12857	12857	12857	12857	12857	12857
	f_{M2}	12888	12887	12888	12888	12888	12887
	f_{M3}	12968	12967	12968	12967	12968	12967
	f_{M4}	13066	13065	13065	13066	13065	13065
	f_{M5}	13144	13144	13144	13144	13144	13144
1×10^{-13}	f_{M1}	12857	12857	12857	12857	12857	12857
	f_{M2}	12888	12888	12888	12888	12888	12888
	f_{M3}	12968	12968	12968	12968	12968	12968
	f_{M4}	13066	13066	13066	13066	13066	13066
	f_{M5}	13144	13144	13144	13144	13144	13144

Figure 5.11 shows the frequency response patterns for the 5 Constant CMRA using lumped mass model analyses. Due to the constant mass design, a similar amount of R1 and R5 changes both perturbed conditions generated mirrored frequency response patterns. Table 5-7 clearly indicates, irrespective the amount of mass perturbed in the system, the response of the first half of the coupled resonators are always similar to the second half of the structure (i.e. R1//R5 and R2//R4). The results agreed with the finite element analysis result in Section 3.4.5 for the constant mass structure configuration. Hence, if the 5 Constant CMRA is used to

detect any single species of mass or material (i.e. in the artificial nose application), only 3 resonators will be useful.

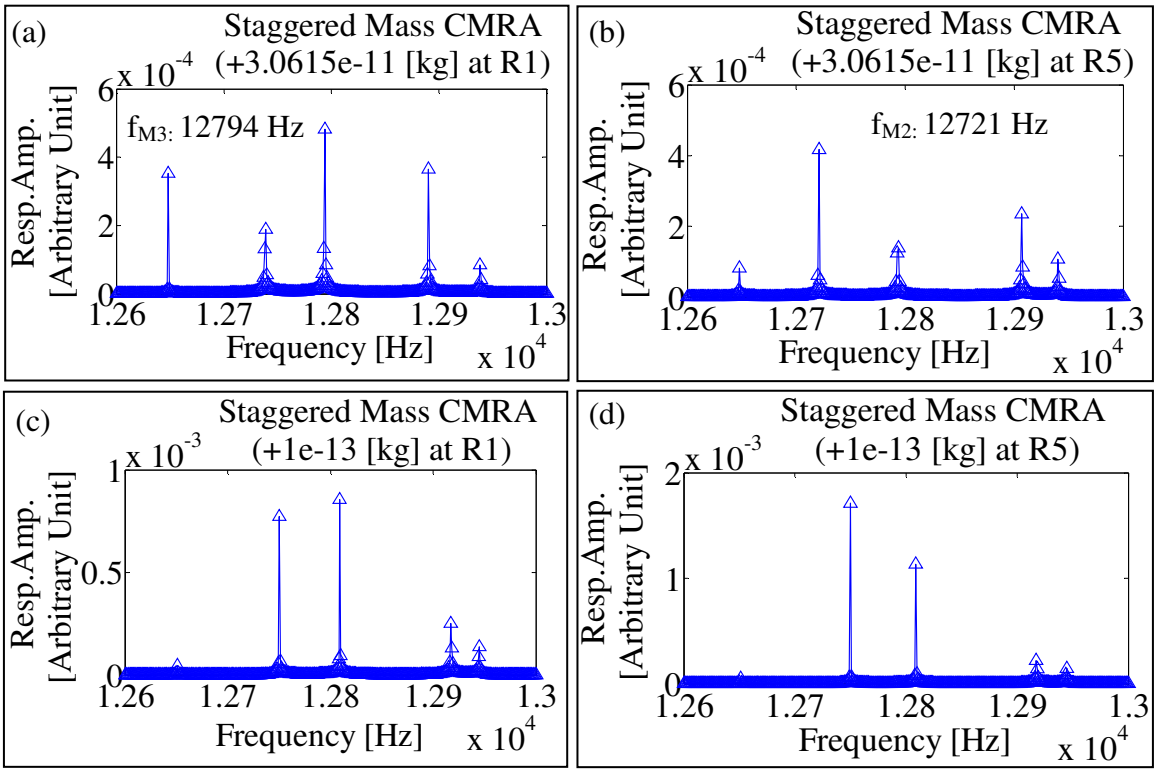

Figure 5.12 Frequency Response Result of 5 Staggered Mass CMRA; (a) 3.0615 x 10^{-11} kg mass added at R1; (b) 3.0615 x 10^{-11} kg mass added at R5; (c) 1 x 10^{-13} kg mass added at R1; (d) 1 x 10^{-13} kg mass added at R5

Figure 5.12 presents the frequency response pattern of the perturbed Staggered Mass CMRA and Table 5-8 compares the modal frequencies of the structure when the single resonator sensor absorbs a mass. From Figure 5.12 it can be seen that 1% of mass (3.0615 x 10^{-11}) or minimum of 1 x 10^{-13}kg of mass absorbed by R1 or R5 , produced different A-F curves due to the staggered mass design of the CMRA. From Table 5-8 modal frequencies, at a maximum of 3.0615 x 10^{-11}kg or 1 x 10^{-11}kg mass absorbed by the single resonator, the modal frequencies of the Staggered Mass CMRA are always distinctive. However, the mass changes

of 1 x 10^{-12} and 1 x 10^{-13}kg produces no change in eigenfrequencies. The distinctiveness of the A-F curve at 1 x 10^{-13}kg (Figure 5.12(c) and (d)) is only associated to the shift of the structure response amplitude. If we consider the shift of the modal eigenfrequencies, the perturbation mass which is less than 1 x 10^{-12}kg may be regarded as being below the detection limit.

Table 5-8 the unperturbed and perturbed modal eigenfrequencies of the 5 Staggered Mass CMRA

Perturbed Mass [kg]	5 modal frequencies	Initial	+ At R1	+ At R2	+ At R3	+ At R4	+ At R5
3.0615 x 10^{-11}	f_{M1}	12651	12648	12630	12613	12639	12648
	f_{M2}	12750	12739	12732	12750	12732	12721
	f_{M3}	12809	12794	12802	12794	12809	12794
	f_{M4}	12917	12890	12909	12917	12895	12907
	f_{M5}	12945	12938	12937	12938	12935	12940
1 x 10^{-11}	f_{M1}	12651	12650	12645	12640	12648	12650
	f_{M2}	12750	12747	12744	12750	12744	12742
	f_{M3}	12809	12804	12806	12803	12809	12803
	f_{M4}	12917	12908	12915	12917	12911	12914
	f_{M5}	12945	12941	12941	12942	12940	12943
1 x 10^{-12}	f_{M1}	12651	12651	12650	12650	12651	12651
	f_{M2}	12750	12750	12750	12750	12750	12749
	f_{M3}	12809	12809	12809	12809	12809	12809
	f_{M4}	12917	12917	12917	12917	12917	12917
	f_{M5}	12945	12944	12944	12944	12944	12944
1 x 10^{-13}	f_{M1}	12651	12651	12651	12651	12651	12651
	f_{M2}	12750	12750	12750	12750	12750	12750
	f_{M3}	12809	12809	12809	12809	12809	12809
	f_{M4}	12917	12917	12917	12917	12917	12917
	f_{M5}	12945	12945	12945	12945	12945	12945

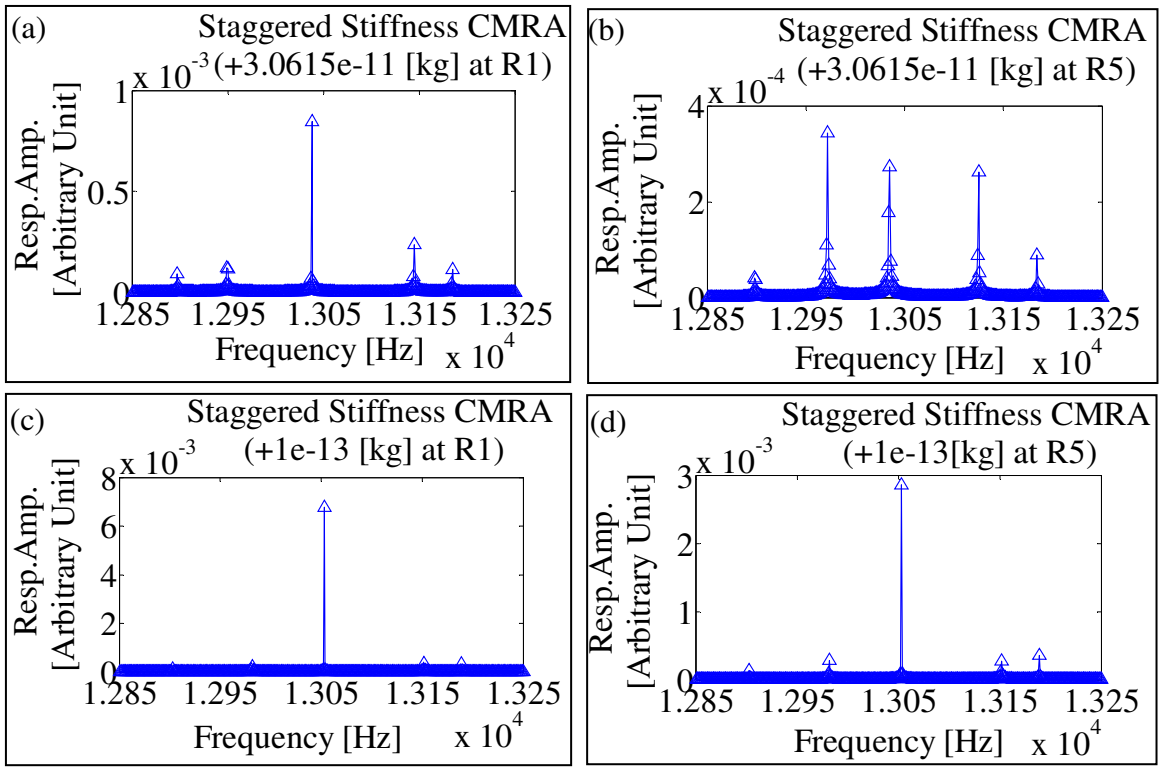

Figure 5.13 Frequency Response Result of 5 Staggered Stiffness CMRA; (a) 3.0615 x 10^{-11}kg mass added at R1; (b) 3.0615 x 10^{-11}kg mass added at R5; (c) 1 x 10^{-13}kg mass added at R1; (d) 1 x 10^{-13}kg mass added at R5

As shown in Figure 5.13, the Staggered Stiffness CMRA produces unique frequency response patterns, when the single resonator sensor (i.e. R1 and R5) absorbs similar amount of mass. By altering the anchor spring length (Section 5.2), we actually stagger the stiffness and mass of the Staggered Stiffness CMRA (e.g. comparing R5 and R3 (Table 5-6), at 0.13% mass change causes 2.52% change in stiffness) . Hence, unique frequency response patterns with distinctive shift of modal frequencies were observed when a maximum of 3.0615 x 10^{-11}kg and 1 x 10^{-11}kg mass absorbed by the single resonator sensor (Table 5-9). Although, 1 x 10^{-13}kg mass is below the detection limit of the structure (no change in modal eigenfrequencies (Table 5-9)); but, the structure still sensitive to produce unique change of response amplitudes due to the different mass and stiffness configuration.

Table 5-9 the unperturbed and perturbed modal eigenfrequencies of the Staggered Stiffness CMRA

Perturbed Mass [kg]	5 modal frequencies	Initial	+ At R1	+ At R2	+ At R3	+ At R4	+ At R5
3.0615 x 10^{-11}	f_{M1}	12903	12897	12889	12869	12876	12898
	f_{M2}	12982	12949	12965	12982	12968	12972
	f_{M3}	13053	13038	13053	13033	13047	13035
	f_{M4}	13152	13145	13131	13152	13142	13125
	f_{M5}	13189	13185	13176	13178	13182	13184
1 x 10^{-11}	f_{M1}	12903	12902	12900	12893	12896	12902
	f_{M2}	12982	12972	12976	12982	12977	12979
	f_{M3}	13053	13047	13053	13046	13051	13048
	f_{M4}	13152	13149	13146	13152	13148	13142
	f_{M5}	13189	13187	13183	13185	13186	13187
1 x 10^{-12}	f_{M1}	12903	12903	12903	12902	12902	12903
	f_{M2}	12982	12981	12981	12982	12981	12982
	f_{M3}	13053	13052	13053	13052	13053	13053
	f_{M4}	13152	13152	13151	13152	13151	13151
	f_{M5}	13189	13189	13189	13189	13189	13189
1 x 10^{-13}	f_{M1}	12903	12903	12903	12903	12903	12903
	f_{M2}	12982	12982	12982	12982	12982	12982
	f_{M3}	13053	13053	13053	13053	13053	13053
	f_{M4}	13152	13152	13152	13152	13152	13152
	f_{M5}	13189	13189	13189	13189	13189	13189

5.4.3 Result and Discussion: Stability of System Eigenvectors of CMRA

Figure 5.14, 5.15 and 5.16 display examples of the stability of the system eigenvectors (mode 1) of the three CMRA(s), when a single resonator sensor (e.g. R1 and R5) absorbs different level of mass (refer to Appendix D and E for a complete eigenvectors stability analysis result for the two staggered CMRA(s)).

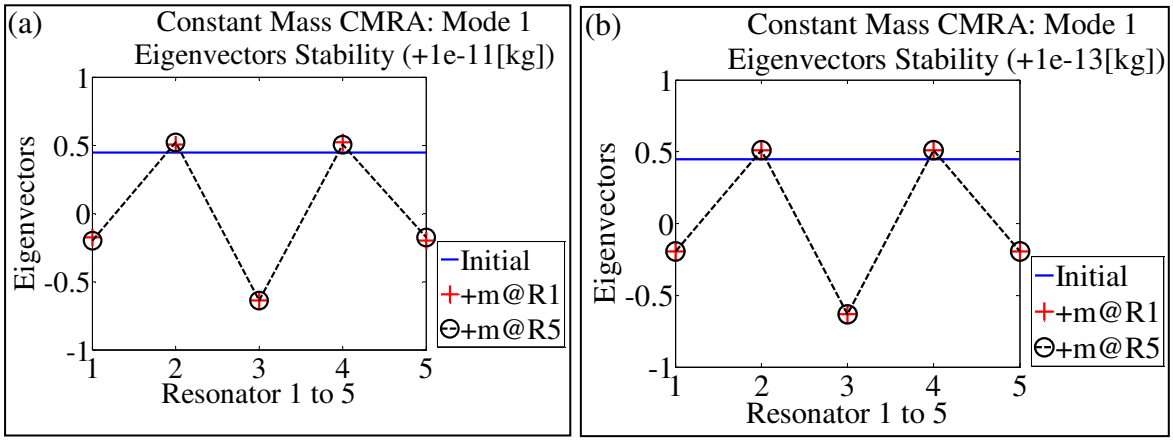

Figure 5.14 Stability of eigenvectors analysis result between unperturbed and perturbed Constant CMRA

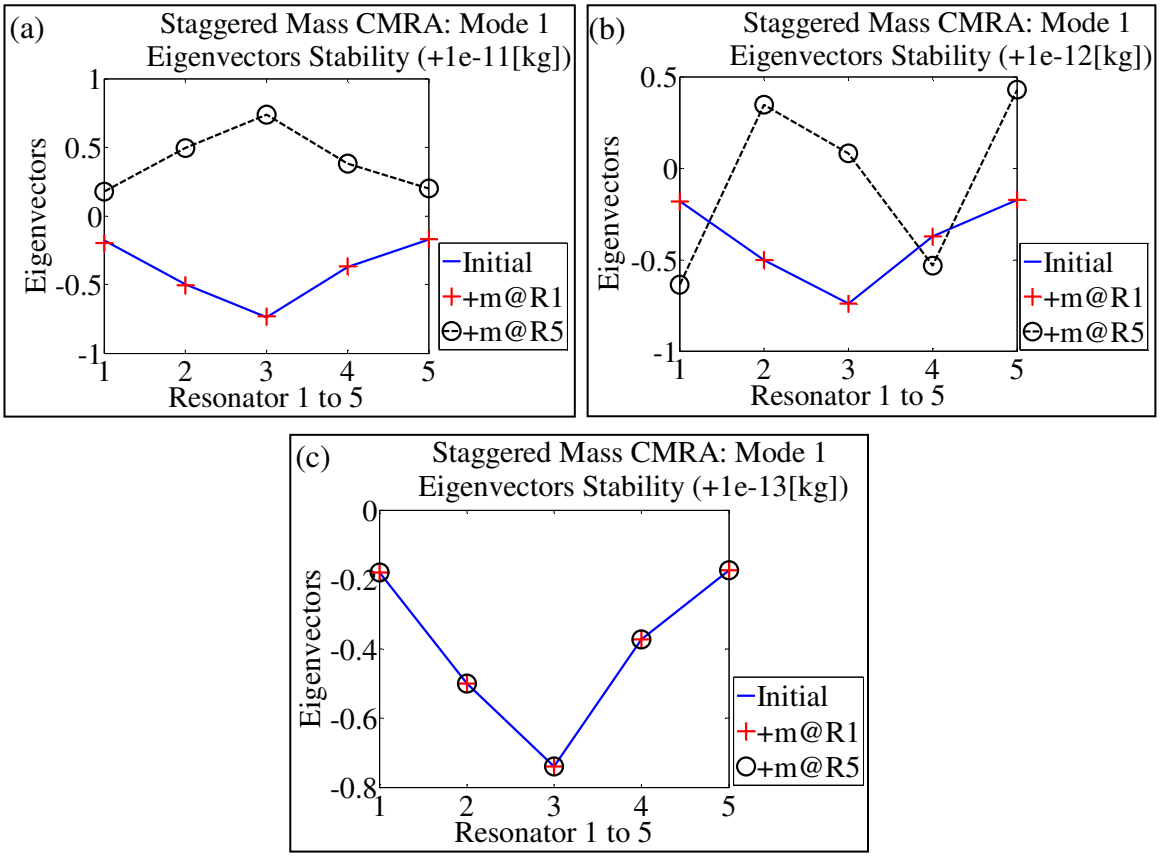

Figure 5.15 Stability of eigenvectors analysis result between unperturbed and perturbed Staggered Mass CMRA

As shown in Figure 5.14, comparing the unperturbed and perturbed eigenvectors of the Constant Mass CMRA, the system eigenvectors are always unstable even though only a small amount of mass (i.e. 1 x 10^{-13}kg) is absorbed by the resonator. Hence, if the unperturbed

eigenvectors are used to estimate the mass change pattern of the perturbed structure (using inverse eigenvalue analysis), a large error is expected to be produced due to the unstable system eigenvectors of the structure.

Figure 5.15 shows an example of the stability analysis results for the Staggered Mass CMRA (refer to Appendix D for the complete analysis results). Referring to the Staggered Mass CMRA design and considering R3 as a reference point, the amount of the staggered mass between the 5 resonators is: R1 compared R2, R1//R2 (9.91×10^{-11}kg) , R2//R3 (3.09×10^{-11}), R4//R3 (6.25×10^{-11}), and R5//R4 (3.53×10^{-11}kg). Following the eigenvectors stability against different perturbing masses, the eigenvectors remain stable when the perturbing mass is significantly smaller than the staggered mass as follows: R1 (at 3.0615×10^{-11}kg perturbation mass), R2 (1×10^{-11}kg), R3 and R4 (1×10^{-12}kg), and R5 (1×10^{-13}kg). The results demonstrate the limit of the amount of perturbation mass that can be perturbed at each single resonator sensor to ensure stable perturbed eigenvectors.

Figure 5.16 shows the stability analysis results of the Staggered Stiffness CMRA (i.e. mode 1; refer to Appendix E for the complete analysis results). As different amount of masses are absorbed by R1 and R5 (i.e. 1×10^{-11}kg, 1×10^{-12}kg or 1×10^{-13}kg) the perturbed eigenvectors are always stable compared to the unperturbed eigenvectors. When the outer CMRA resonators were stiffened (i.e. $k_{R1} > K_{R2} > K_{R3}$ or $K_{R5} > K_{R4} > K_{R3}$) by reducing the length of the anchor spring of the resonator, the mass of the resonators was actually reduced. The configuration of the stiffness of the coupled resonators produced an unsymmetrical staggered mass with the heaviest mass value in the middle of the coupled structure (R3). Such a staggered mass configuration provides an effective way to break the structure symmetry for an effective structure movement. Positioning the stiff resonator at the end of the structure array slightly restrained the eigenvectors at the end of the array. As discussed in Section 4.6.3

such an approach helped to stabilize the structure eigenvectors. Hence the stability of the Staggered Stiffness CMRA improved significantly at levels of absorbed mass.

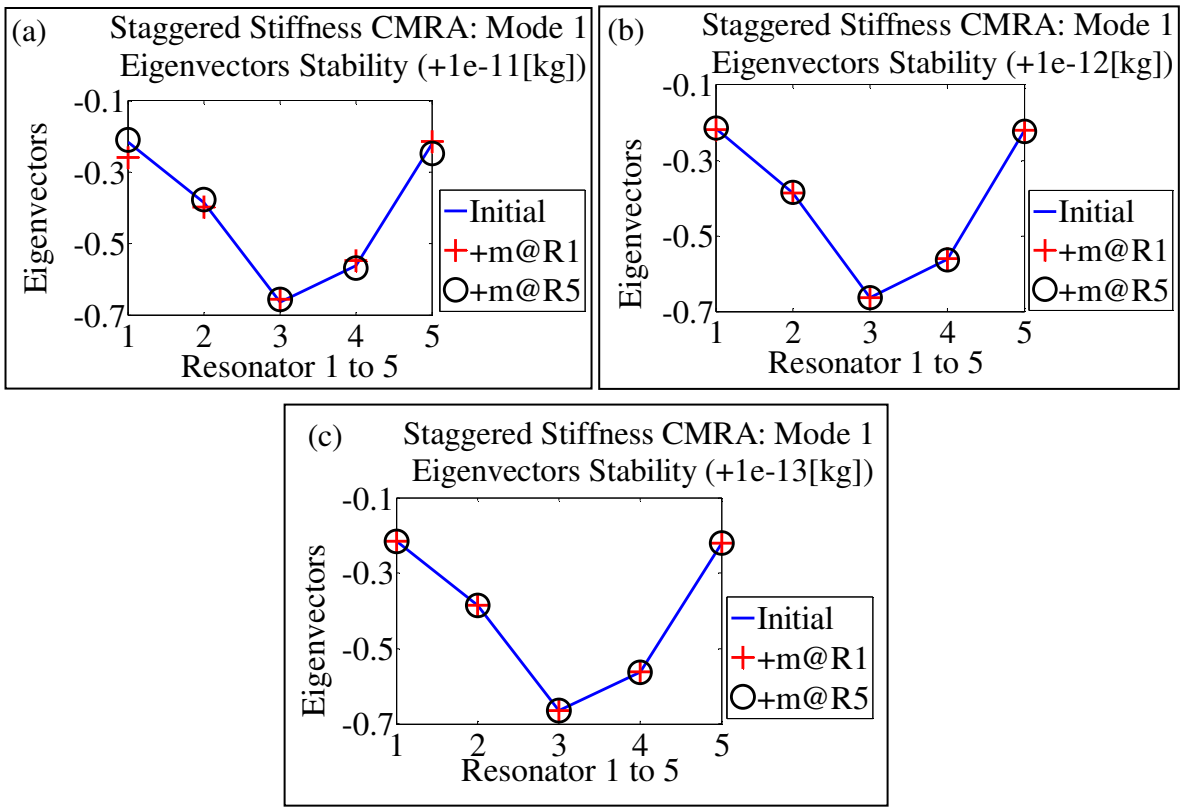

Figure 5.16 Stability of eigenvectors analysis result between unperturbed and perturbed Staggered Stiffness CMRA (single resonator sensor)

5.5 Estimation of Mass Change Patterns of the CMRA Using Inverse Eigenvalue Analysis

5.5.1 Overview and Analysis

When one of the resonators of the CMRA absorbs mass, we can identify which mass has changed by using an inverse eigenvalue analysis; this requires a knowledge of the perturbed eigenvalues (or eigenfrequencies) and perturbed eigenvectors. Since the perturbed eigenvectors are complicated to measure, the unperturbed eigenvectors will be used in the estimation of the mass changes pattern of the CMRA. Hence, it is important to ensure that the

eigenvectors are stable against mass changes. The eigenvectors of the unperturbed system were used to transform the mass and stiffness matrix into a generalised mass matrix [M_G] and generalized stiffness matrix [K_G]. A simple relationship exists between the eigenfrequencies, ω_i and the elements of the generalised mass and stiffness matrices:-

$$\omega_i^2 = \frac{K_{G_{ii}}}{M_{G_{ii}}} \qquad \text{(Equation 5-4)}$$

Assuming, a mass Δm_1 is added to resonator 1 (R1), then a perturbed set of eigenvalues will be obtained; and since the stiffness matrix is unchanged, we may uniquely identify the generalised mass matrix. We can then transform this back to the real mass matrix, so identifying Δm_1, if we have the new eigenvectors or if the unperturbed eigenvectors are sufficiently unchanged. The challenge is to have the CMRA structure design, in which any small change of masses should give insignificant change to the eigenvectors of the unperturbed system.

The performance of the three CMRA(s) (5 Constant Mass CMRA, 5 Staggered Mass CMRA, and 5 Staggered Stiffness CMRA) were examined by adding a mass of 1 x 10^{-11}kg, 1 x 10^{-12} kg, and 1 x 10^{-13} kg separately to each resonator (R1, 2 ,3, 4 and R5). Then the unperturbed eigenvectors were used to estimate the perturbed mass (*epm*). Errors of mass estimation, E_{est} were calculated by comparing the estimated perturbed mass, *epm* and the actual perturbed mass, *apm* added to the structure:

$$E_{est} = |\, epm - apm| \qquad \text{(Equation 5-5)}$$

The performance of the three CMRA(s) was compared by calculating the errors of mass estimation, E_{est} for the sensor structures when absorbing similar amount of mass.

5.5.2 Result and Discussion

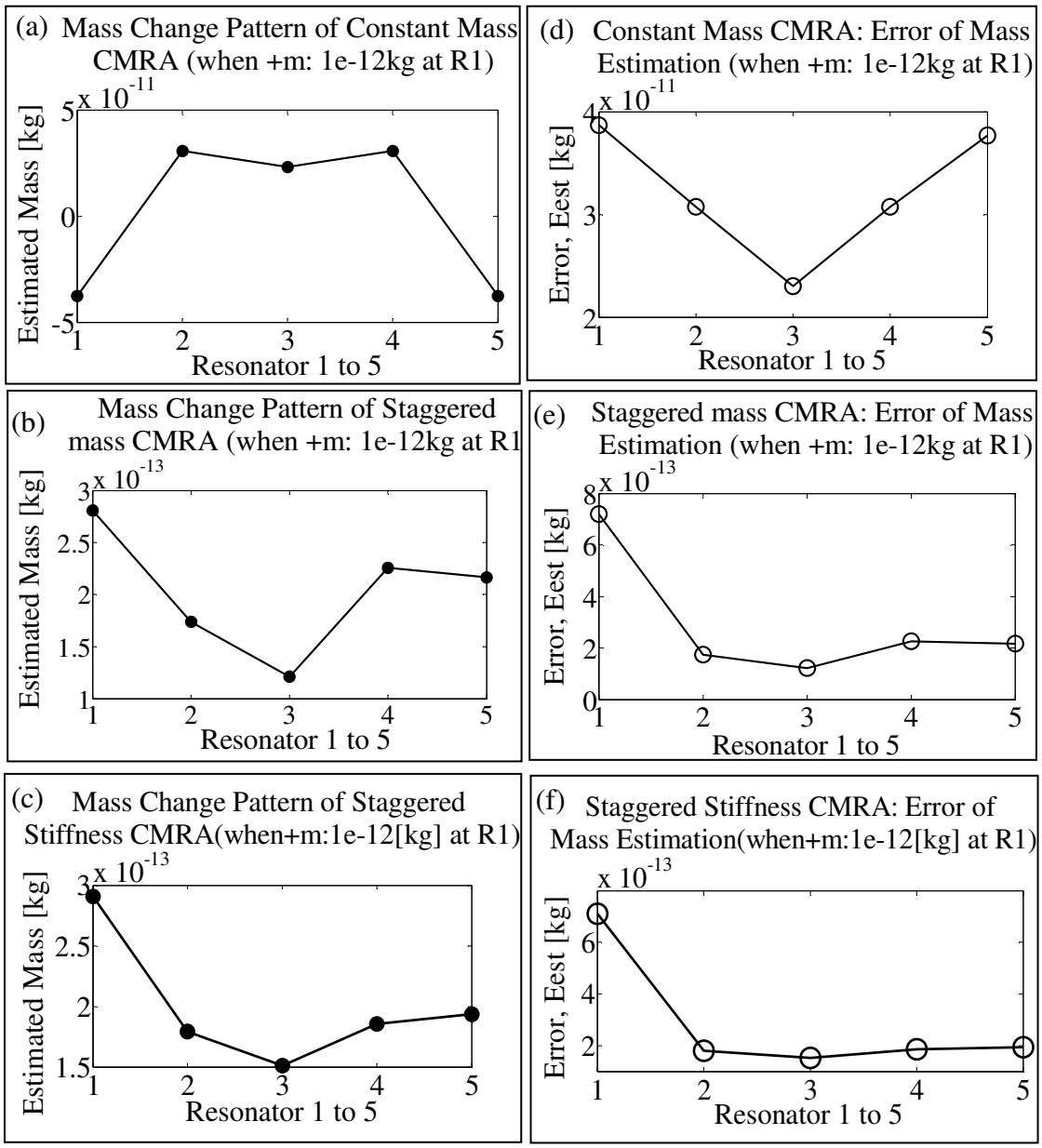

Figure 5.17 Eigenvectors stability analysis; mass change pattern of CMRA estimated using inverse eigenvalue analysis and error of mass estimation: (a), (d) Constant Mass CMRA; (b), (e) Staggered Mass CMRA; (c), (f) Staggered Stiffness CMRA

Figure 5.17(a) (b) and (c) compare examples of the estimated mass using the inverse eigenvalue analysis and the unperturbed eigenvectors of the structure for the 5 Constant Mass CMRA, 5 Staggered Mass CMRA and for 5 Staggered Stiffness CMRA respectively. Comparing the error of mass estimation at R1 between the staggered CMRA and constant

CMRA; the error for the Staggered Mass and Staggered Stiffness CMRA (Figure 5.17 (e) and (f)) was 72% and 71% when the resonator absorbs $1e^{-12}$Kg of mass. However for the Constant CMRA, (Figure 5.17 (d)), the estimations of mass using the unperturbed eigenvectors can be considered invalid, since it causes very high error. Further to emphasize, even though the 70% errors are quite high for the staggered CMRA, we can clearly distinguish the mass change pattern of the five coupled resonators when only R1 absorbs the mass.

Therefore, from the analysis presented above it is clear that staggering the mass of coupled resonators has resulted in the stabilization of the eigenvectors of the structure (refer to Appendix D and E for the new perturbed eigenvectors compared to unperturbed eigenvectors for both staggered structure and a complete stability analysis result). As a result, any small amount of mass absorbed by the resonators, will not affect the designed eigenvectors of the structure. Hence, it is then valid to use the unperturbed eigenvectors to estimate any mass changes absorbed by the resonator.

5.6 Impact of Manufacturing Variation on the CMRA performance

5.6.1 Manufacturing Variation Quantification

5.6.1.1 Overview

Monitoring MEMS fabricated geometries is as fundamentally important as tracking material properties [121]. By measuring the geometrical dimension of the fabricated structure, the level of the process variation can be estimated. In this research, the geometrical dimension of the comb-drive resonators which were fabricated using the INTEGRAM SOI micromachining processes (outsourced) [150] were measured using a scanning electron microscopy (SEM).

Using the data, an analysis was performed to estimate the impact of the manufacturing variation on the performance of the CMRA (Section 5.6.2).

Fundamentally, the key impact parameter is the resonant frequency of the structure:-

Resonant frequency, $\omega = \sqrt{\frac{k}{m}}$ (Equation 5-6)

This means that, $\frac{\Delta\omega}{\omega} = \frac{1}{2}\left[\frac{\Delta k}{k} - \frac{\Delta m}{m}\right]$ (Equation 5-7)

The variation of the fundamental frequency ($\Delta\omega$) relates to the change of the structure stiffness (Δk) and effective mass (Δm) of the structure (Equation 5-7). The change of the structure stiffness or mass due to the change of the nominal designed dimension causes part to part variation (e.g. the variation between single resonators) as well as the overall structure.

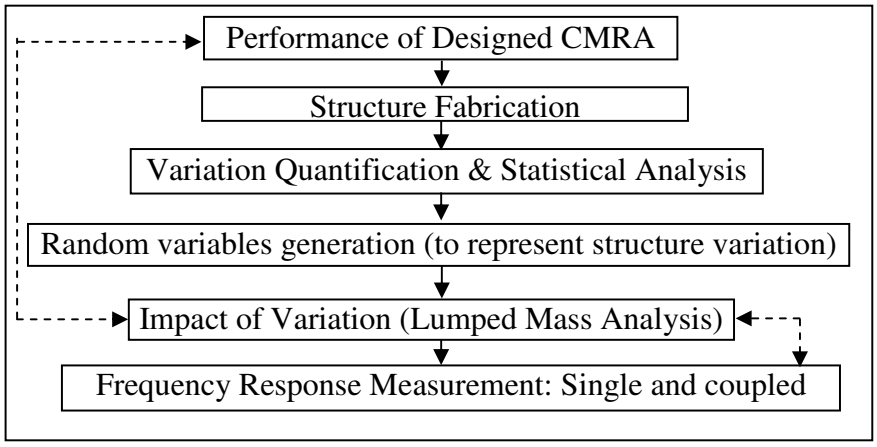

Figure 5.18 Analysis steps - Impact of manufacturing variation analysis on the CMRA performance

Figure 5.18 highlights the analysis steps in quantifying the process variation and analyzing the impact of the manufacturing variation on the CMRA performance. The measured geometrical dimension of the fabricated structure is analyzed using a statistical analysis. The analyzed data is used to generate random variables used to represent the geometrical structure

variations. The generated random variables are then used in the manufacturing variation analysis in order to estimate the impact of the process variation on the designed CMRA.

5.6.1.2 The variation quantification and Statistical Data Analysis

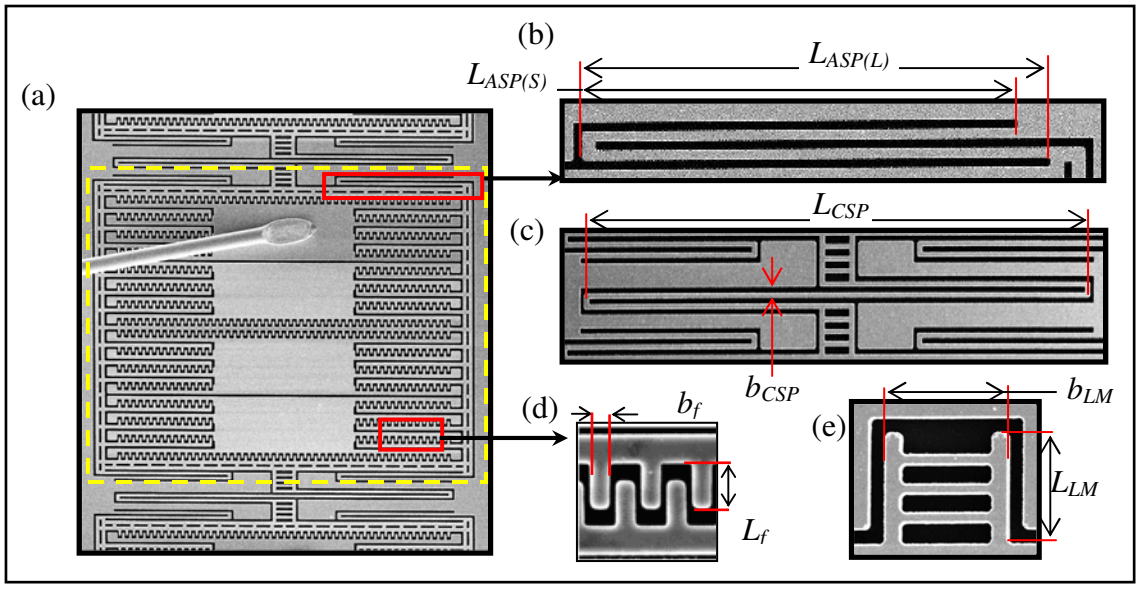

Figure 5.19 (a) Scanning electron microscope (SEM) images of constant coupled resonators; (b) Anchor spring; (c) Coupling spring; (d) Comb fingers; (e) Linked mass

To quantify the variation, 3 INTEGRAM chips (5 x 5 mm in size) which contain single and triple constant mass coupled comb drive resonators were measured using an environmental scanning electron microscope (XL-30 FEG-ESEM). Refer to Table 5-10 for the nominal designed dimension of the INTEGRAM resonators.

The geometrical parameters to be measured are based on the number of repeated elements in the coupled structures (i.e. probability each element will vary due to process variation) which include length and width of the anchor spring (L_{ASP}, b_{ASP}), length and width of the coupling spring (L_{CSP}, b_{ASP}), length and width of the linked mass (L_{LM}, b_{LM}), and length and width of the comb fingers (L_f, b_f). It is important to note that since the integrated comb-drive resonator is a lateral device, the thickness of the device layer has a little effect upon the

resonant frequency of the device and therefore was not measured extensively. Figure 5.19 illustrates the geometrical parameters which were monitored and measured using the SEM. The geometrical measurements were done using the secondary electron detector in the SEM. Before the measurement of the structure, the ESEM system was calibrated using 2 magnification standards (19.7 line per mm (low magnification) and 2160 lines per mm (for high magnification)) [151]. To measure one geometrical dimension of the structure, three measurements were made and an average is taken to establish 1 data sample of the structure dimension.

In order to analyze the variation of the geometrical dimension of the fabricated structure, a simple statistical data analysis was established. The mean (μ) and standard deviation (σ) of the fabricated structure were calculated using 1-sample t test analysis with 90 percent confidence interval. The variation was calculated in terms of a manufacturing tolerance, *V1* (variation between the fabricated and designed structure) ($V1 = ((\mu - \mu_o)/\mu_o)*100$) and a part to part variation of the fabricated structure ($V2 = (\sigma / \mu_o)*100$). Where, μ: population mean of the fabricated samples; μ_o: mean of the nominal designed dimension; and σ: standard deviation of the sample data analysis.

5.6.1.3 Result and Discussion

Figure 5.20 shows an example of one of the measured geometrical dimension for the comb finger length with 9.9μm mean (μ) of the population sample. From the data distribution, the measured dimensions are always less than the nominal design dimension (i.e. 10μm). The manufacturing tolerance and part to part variation for the length of comb finger for the selected INTEGRAM chip (Table 5-10) are -0.94% (always less than the nominal design parameter) and 0.47% respectively.

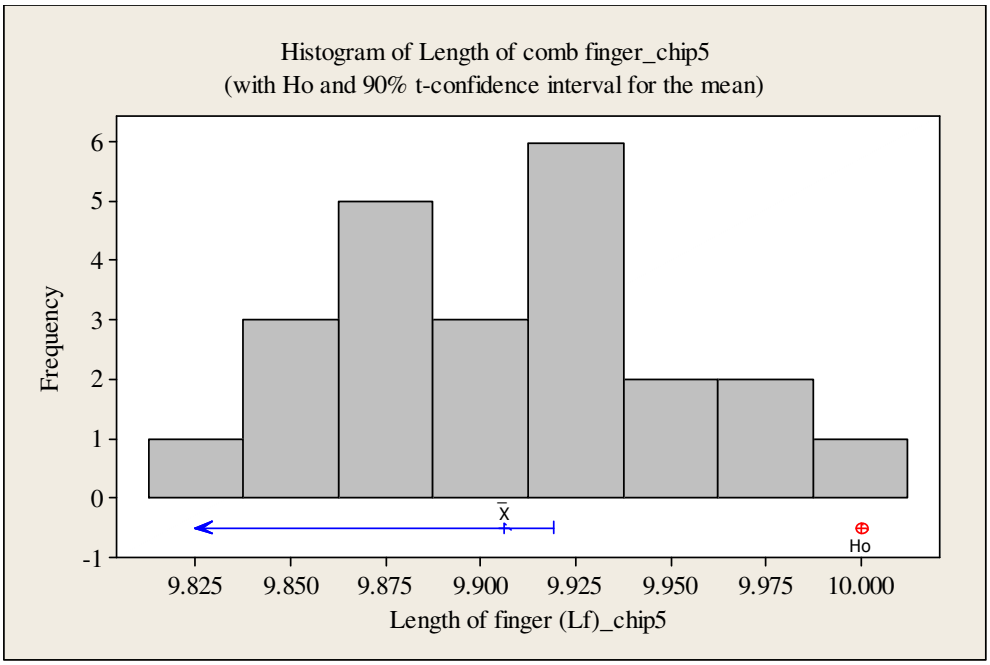

Figure 5.20 Example of comb finger length measured data distribution.

Table 5-10 contains the results of the quantified variation data analysis measured on a single chip. As can be observed, the width of anchor spring (b_{ASP}), coupling spring (b_{CSP}), and the width of finger (b_f) with the smallest nominal design dimension (i.e. 3μm sizes) show the highest manufacturing tolerance and part to part variations. With such level of the part to part variation, we may presume that the variation may significantly change the stiffness and mass of resonators; and hence the frequency response of the resonator. To further confirm the deduction, the quantified variation data were then used in the next section of analysis to analyze the impact of the process variation on the CMRA sensor performance (5 Constant Mass CMRA).

Table 5-10 Manufacturing Variation data analysis – measured on a single INTEGRAM chip

Dimension / (no. of N samples)	Mean - nominal Parameter, μo [μm]	Mean - fabricated parameter, μ [μm]	Standard deviation σ	Manufacturing tolerance $V1$[%]	Part to part variation $V2$ [%]
Anchor Spring width, b_{ASP}/ (24)	3	4.298	0.0460	[43.30]	1.53
Anchor Spring Length, L_{ASP} (24)	201 (s) 216 (L)	200.19 214.07	0.6630 0.7250	[-0.40] [-0.89]	0.33 0.34
Coupling Spring Width, b_{CSP}/ (12)	3	4.295	0.0597	[43.17]	1.99
Coupling Spring Length, L_{ASP} (6)	455	454.37	0.519	[-0.14]	0.11
Width of Linked Mass, b_{LM} (12)	19	20.09	0.0569	[5.72]	0.30
Length of Linked Mass, L_{LM} (12)	38	37.67	0.0940	[-0.87]	0.25
Comb finger Width, b_f (24)	3	4.23	0.0506	[41.06]	1.69
Comb finger Length, L_f(24)	10	9.91	0.0470	[-0.94]	0.47

5.6.2 Impact of Manufacturing Variation Analysis

Due to nature of the manufacturing processes in MEMS, variation is inevitable. However the variation may help to improve some aspects of the CMRA structure design. As we discussed earlier in Chapter 3, and 4 the constant Mass design of the CMRA gives a potential problem in distinguishing any masses absorbed by the sensors since a unique frequency response pattern is not generated. Furthermore, due to the symmetrical mass design, the perturbed eigenvectors of the Constant CMRA structure are always different compared to the unperturbed eigenvectors. In this section an analysis is conducted to identify how the variation may alter the geometrical dimensions of the 5 Constant Mass CMRA (refer to Appendix G for the impact of the variation on a single comb-drive resonator) . Each resonator may have a slightly different mass, which will may help to improve the

distinguishability of the CMRA output signal. In order to analyze the overall CMRA performance and the impact of variation, a lumped mass structure model was established which relates between ω_n , k and m_R of the 5 coupled resonator array structure (from Equation 5-2).

$$(\omega_n)^2 \ [X] \quad = \quad [M^{-1}] \ [K] \ [X]$$

The numerical analysis was undertaken to calculate the effective mass and stiffness of the resonators (refer to Appendix F) so that they are comparable with the FEA value. The numerical derived effective mass and stiffness were then substituted into Equation 5-2. Using MATLAB the 5 eigenfrequencies and eigenvectors of the CMRA were computed. The manufacturing variation was introduced into the model using random variables which were generated based on the quantified μ (mean) and σ (standard deviation) of the fabricated structure which was described earlier in Section 5.6.1.

As an example, a random variable for finger width $RanW_{Fin}$:

$$RanW_{Fin} = LoLW_{Fin} + (UpLW_{Fin} - LoLW_{Fin}) * Rand\ (1,N) \qquad \text{(Equation 5-8)}$$

Where, $LoLW_{Fin}$, is the lower limit of the W_{Fin} variable;

$$= \mu W_{Fin} - (TW_{Fin\ (N)} * \sigma\ W_{Fin}) / \text{sqrt}\ (N + 1) \qquad \text{(Equation 5-9)}$$

$UpLW_{Fin}$ is the upper limit of the W_{Fin} variable;

$$= \mu W_{Fin} + (TW_{Fin\ (N)} * \sigma\ W_{Fin}) / \text{sqrt}\ (N + 1) \qquad \text{(Equation 5-10)}$$

Rand (1,N) is a MATLAB command to generate N random numbers between 0 and 1 (i.e. based on a uniform distribution). $TW_{Fin\ (N)}$ is a statistic 1 sample t test value for the N sample size of the quantified parameters. The generated random variables were then fed into the lumped mass model analysis to represent all the considered geometrical changes due to the

manufacturing variations. The effect of variation (i.e. based on worst case scenario; change of length and width of the anchor spring, comb fingers and linked mass)[2] before and after mass were added to the structure were simulated.

5.6.2.1 Result and discussion

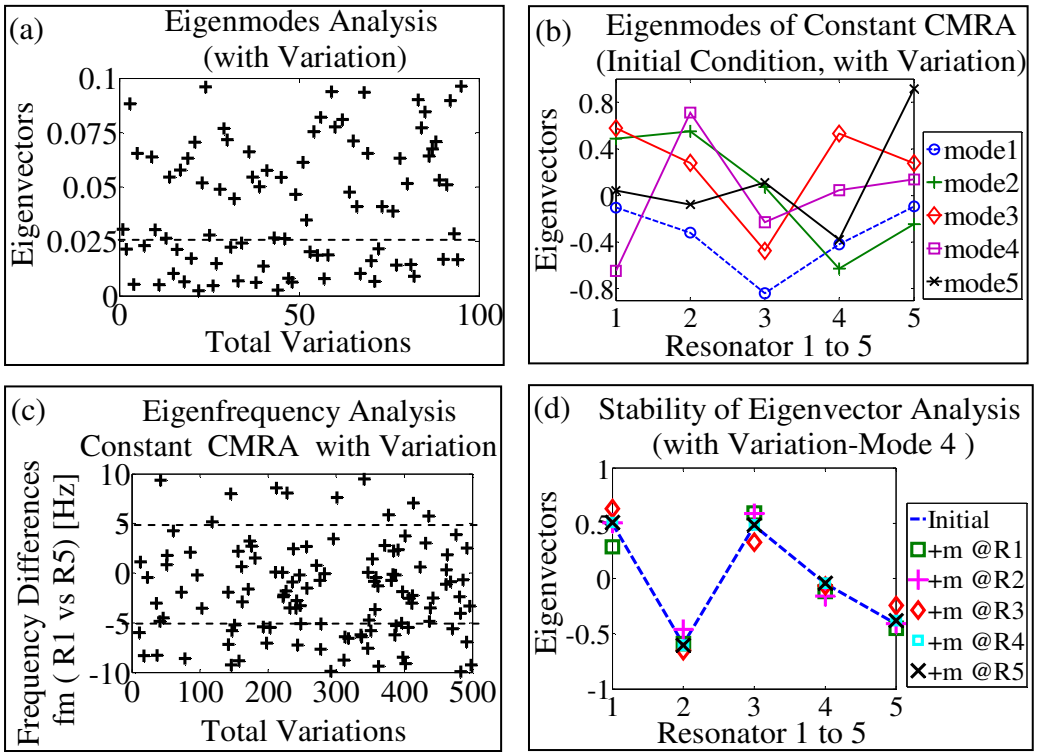

Figure 5.21 The effect of manufacturing variation on the Constant Mass CMRA; (a), (b) Measurability of sensor output signal; (c) Distinctiveness of 5 modal frequencies when single resonator R1 and R5 absorbs similar amount of mass; (d) The eigenvectors of initial and single resonator mass change

[2] A sensitivity analysis such as using the Monte Carlo simulation to indicate which are the most important geometrical parameter in influencing the performance of the CMRA is beyond the scope of the thesis. However, since the CMRA is a lateral device, from the analytical expression for the effective stiffness and mass of the integrated comb-drive resonator (Appendix F, Equation F-1 and F-3), the resonator stiffness (k) is inversely proportional to length cubed (L) and proportional to width cubed (b) of the resonator anchor spring. The sensitivity of change of mass (m) with the change of b and L is less compared to the change in stiffness. The structure thickness (h) has a small effect on the resonator natural frequency (a proportional effect of h on the stiffness and resonator mass is cancelled to each other); So, the stiffness dominates the structure resonant frequency, which is related to the width and length cube of the resonator anchor spring.

Fig. 5.21 shows analysis results of the effect of manufacturing variation on the CMRA sensor performance. The change of the geometrical dimensions due to the process variation, may alter the mass and stiffness of the coupled elements. Considerable increase in some resonator stiffness or mass will reduce some eigenvectors of the structure. As a result some modes of the CMRA frequency response will approach zero; instead of getting 5 response peaks for the 5 CMRA, only 4 peaks or less may be observed when the frequency response of the structure is measured. Figure 5.21(a) displays the effect of variation analysis result on the relative displacement of the coupled resonators on a particular simulation run. Assuming that eigenvectors which less than 0.025 is unable to be measured; out of 100 CMRA variations only 68% may produce 5 response peaks. Figure 5.21(b) shows an example of eigenmode analysis of the unperturbed CMRA; due to the variation, the eigenvectors of mode 1 (i.e. R1) retracted to zero. As a result, if the frequency response of the predicted CMRA is measured at R1, only 4 modal frequencies are expected to be measurable.

However, as a result of the alteration of the mass and stiffness of the coupled elements, some modal frequencies of the structure may be changed, which will enhance the uniqueness of the frequency response of the Constant Mass CMRA. Figure 5.21 (c) demonstrates the plot of eigenfrequency differences of the 5 CMRA when R1 (resonator 1) and R5 absorbs similar amount of mass separately. Instead of having 5 similar modal frequencies due to the constant mass design of the coupled resonators, it can be predicted that the variation may significantly modify the distinctiveness of the frequency response of R1 and R5 single resonator mass change. If we consider a 5Hz frequency difference or below is less distinguishable response; from the impact analysis, 86.6% out of 100 CMRA produces distinctive response pattern (i.e. frequency difference is more than 5 Hz). Figure 5.21(d) shows an example of stable eigenvectors of a single resonator mass change when the variations were imparted in the

analysis. It can be predicted that due to the change of some mass of the coupled resonators, the stability of eigenmodes of some single or multiple resonators sensor may be improved.

5.7 Summary and Conclusion

This chapter presents and discusses the second version of the CMRA design based on the integrated coupled comb-drive resonators. The 5 Constant CMRA was designed in order to examine the effect of the manufacturing variation on the performance of the constant mass CMRA. For uniqueness of the frequency response pattern and stability of the system eigenvectors, the research proposed two staggered CMRA structure designs; (i) 5 Staggered Mass CMRA, and (ii) 5 Staggered Stiffness CMRA.

Driving or monitoring the CMRA structure at different resonators may produce different response patterns, depending on the mass and stiffness configuration of the resonator. For the specific CMRA design, the difference of the response pattern is related to the response amplitude of the structure. The 5 modal frequencies of the structure remain similar with respect to any drive or readout. For example, driving the ideal Constant CMRA from resonator 1 (R1) and measuring the output either at R1 or R5 produce similar response pattern due to the symmetrical structure mass design. However, driving or measuring the staggered CMRA at different resonators will cause different frequency response pattern for the structure. The differences are associated with the unique response amplitude of the resonators due to different mass and stiffness configurations of the resonator.

Although with the CMRA-v2 structure design, flexibility arises in measuring the output signal of the structure (i.e. different drive and readout selections); the drive or readout points need to be selected properly in order to measure all the 5 response peaks of the structure. As analysed for the Constant CMRA, due to the symmetrical design, measuring or driving the

structure at R3 produces only 3 peaks of responses. There are 2 missing eigenfrequencies associated to the eigenmode 2 and 4. Referring to the R3 at the two missing modes, the resonator reacts as a node (0 eigenvector) with zero resonator displacement.

From the FEA analysis result of the unperturbed CMRA, it is confirmed that the second version of the CMRA is measurable with sufficient capacitances to be processed by the readout measurement system. The uniqueness of the frequency response pattern and the stability of the system eigenvectors after mass is added to the resonators (perturbed structure) were then analysed in Section 5.4 using the lumped mass model analysis.

From the lumped mass analysis of the three CMRA(s), it was confirmed that the Constant Mass CMRA always produces similar frequency response pattern for the first and second half of the resonator array. The response of R1 mirrors R5 and R2 mirrors R4. Furthermore the system eigenvectors of the structure is always unstable. The structure was then further analysed in Section 5.6, to examine how the manufacturing process variation may affect the performance of the Constant Mass CMRA.

For the staggered CMRA design, both structures always produce unique frequency response patterns for any single resonator mass changes. Considering the uniqueness of the CMRA modal frequency shift, the perturbing mass which is less than 1×10^{-12}kg may be regarded as being below the detection limit. From the eigenvectors stability analysis, the eigenvectors of the Staggered Mass CMRA remain stable when the perturbing mass is significantly less than the staggered mass. At a minimum and maximum staggered mass of 3.09×10^{-11}kg (R3 compared R2) and 9.91×10^{-11}kg (R2 compared R1), the limit of the perturbing mass for a single resonator mass change is as follows: 3.0615×10^{-11}kg (R1), 1×10^{-11}kg (R2), 1×10^{-12}kg (R3 and R4), and 1×10^{-13}kg (R5). By staggering the length of resonator anchor spring for the Staggered Stiffness CMRA (i.e. at minimum and maximum

staggered mass of 6 x 10^{-13}kg (R2//R1) and 3.2 x 10^{-12}kg (R5// R4)), all the eigenvectors of the single resonator mass change remained stable even though the perturbing mass is slightly higher than the staggered mass (i.e. 1 x 10^{-11}kg). Restraining the resonator displacement at the end of the structure array improves the eigenvectors stability.

To confirm the stability of the system eigenvectors of the three CMRA(s) structure, the inverse eigenvalue analysis was performed to estimate the amount of perturbed mass using unperturbed system eigenvectors in Section 5.5. For the Constant Mass CMRA, the eigenvectors of the perturbed structure are always unstable compared to unperturbed structure; the inverse eigenvalue analysis produced no valid mass change pattern. The determination of mass changes pattern of both staggered CMRA(s) produced an error about 70%. Although the error between the actual perturbed mass and estimated perturbed mass are considered high, but the mass change pattern of the structure was clearly observed.

Manufacturing variation in MEMS fabricated device causes the structure tolerance and part to part variation. From the variation quantification of the INTEGRAM chip, the variation is more significant for smaller nominal geometrical dimensions than larger structures. An example for the 3μm nominal dimension of the anchor spring width, the manufacturing tolerance is about 43%, and part to part variation is estimated around 1.53 percent. From the impact of the manufacturing variation analysis on the Constant Mass CMRA performance, the variation may reduce the measurability of the frequency response output of some of the coupled sensors. However, it can be predicted that the variation may help to naturally stagger the geometrical dimension of the CMRA for uniqueness of the response patterns of the CMRA as the mass detection sensors for the artificial nose. The variation may help to modify the stability of the CMRA system's eigenvectors, so that it will be insensitive to any small amount of mass absorbed by the sensor.

To summarize, in order to confirm the performance of the CMRA sensor (i.e. measurability and uniqueness of the frequency response of the 5 eigenmodes, stability of the structure eigenvectors for estimation of the mass change pattern of the coupled sensors, and the effect of manufacturing variation on the CMRA frequency response), the three CMRA(s) structures (5 Constant Mass, 5 Staggered Mass, and 5 Staggered Stiffness) will be in-house fabricated (Chapter 6). The single comb-drive resonator also will be fabricated in order to examine effect of the input driving voltage, vacuum chamber pressure and mass loading effect on the resonator frequency response. Three similar single resonators of fixed-fixed beams and integrated comb-drive resonators are fabricated on a single chip in order to observe how the process variation may affect the frequency response of the single resonator.

CHAPTER 6 - FABRICATION AND PACKAGING

6.1 Introduction

This chapter describes the fabrication processes of the CMRA, which includes:-

- Single resonator: fixed-fixed beam (CMRA-v1) and comb-drive resonator
- 5 Constant Mass, 5 Staggered Mass and 5 Staggered Stiffness CMRA (CMRA-v2)

The single fixed-fixed beam resonator was fabricated using 5μm SOI (silicon-on- insulator) wafer and the CMRA-v2 was fabricated using 20μm SOI wafer. Section 6.2 begins with the SOI material selection. The fabrication processes are described in Section 6.3. Section 6.4 describes the *Mask Design* in order to realize the CMRA structure. Processes details to fabricate the CMRA are discussed in Section 6.5. The fabricated structure is observed at each major process stage using an Optical Microscope (OM) or SEM (Scanning Electron Microscope). Section 6.6 discusses the observed structure and highlights the constraints in the process fabrication. In order to measure the output signal of the CMRA, the structures are metalized and wire bonded. Both processes are discussed in Section 6.7. To examine the effect of mass loading on the frequency response pattern of the CMRA, a platinum (Pt) mass using a focused ion beam machine (FIB) is deposited on the single and the coupled resonators (CMRA-v2). The experiments and processes related to the FIB machine is highlighted in Section 6.8.

6.2 Single-Crystal Silicon and Silicon-on-Insulator (SOI) Materials

Silicon-on-insulator (SOI) material is a silicon (Si) wafer having an oxide layer buried below the surface of a thin film of single-crystal silicon layer. The SOI is of interest for MEMS because it provides a relatively simple way to fabricate suspended structures in the single-

crystal silicon [131]. The wafer offers great advantages for the resonator technology, where it employs a single sided wafer processing approach with etch selectivity. The suspended structure can be released by removing the buried oxide layer between the silicon device layer and the silicon handle layer. The oxide can be removed either using wet etching or dry etching processes [152].

Table 6-1 SOI wafers thickness for CMRA structure fabrication

SOI wafer layers	Thickness of layer, μm (SingleR-Fixed-fixed beam)	Thickness of layer, μm (Single and CMRA-v2)
Silicon device layer	5	20
Buried oxide layer (BOX)	2	2
Silicon handle layer	450	500

The SOI wafer material (Table 6-1) was chose for the CMRA structure fabrication due to excellent properties of the silicon crystal for the resonator and the available processes to fabricate the structure. The single-crystal silicon has excellent resonating properties such as very high intrinsic Q-factors, it surpasses an aluminium in strength to-weight ratio, does not show mechanical hysteresis or fatigue and has a low thermal expansion coefficient [131]. It therefore, makes an ideal material for the resonators and high performance sensors such as the CMRA.

The MEMS silicon resonator also can be designed to be integrated with electronic circuits, sensors [95] or IC (Integrated Circuit) technology [153]. The silicon and SOI material provides technological advantages for the CMRA fabrication since multiple resonators can be designed, and released on a single chip. Using the SOI material technology, many devices can be realized and fabricated on a single wafer.

6.3 Overview of the Fabrication Process Flow and Structure Packaging

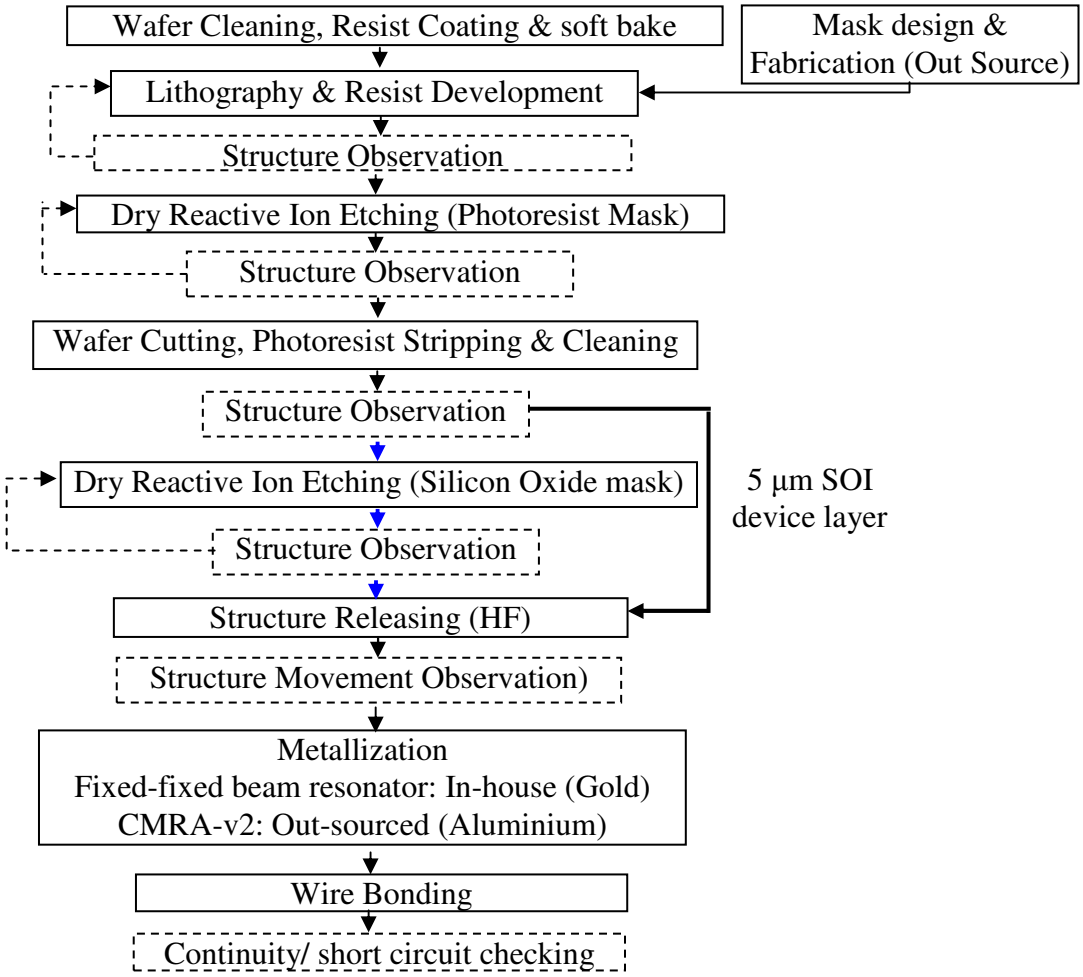

Figure 6.1 Process Flow of CMRA Fabrication (Note: blue arrow is only for 20µm SOI device layer structure (CMRA-v2))

MEMS processes can be divided into bulk micromachining and surface micromachining [17]. Bulk micromachining processes were used to fabricate the CMRA structures. In bulk micromachining processes, material is selectively removed from a substrate by chemical etching [131]. Figure 6.1 summaries the fabrication process. The principal steps are resist coating, pattern transfer using lithography, development process, DRIE (dry reactive Ion etching), and HF released process.

Figure 6.2 is a schematic diagram of the cross section of both the 5µm and 20µm Si devices at each stage of the fabrication process.

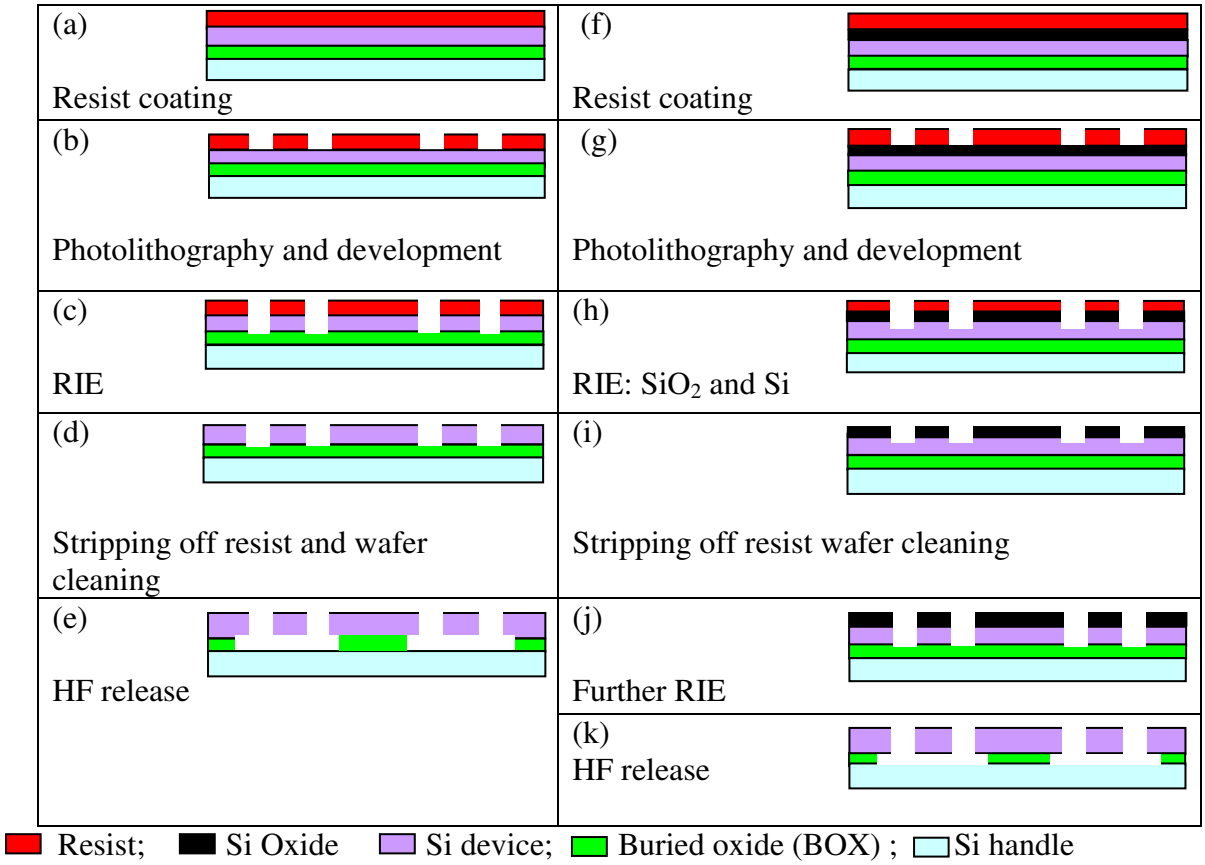

Figure 6.2 schematic diagram of structure device layers at each of process step; (a) – (e): 5µm Si structures; (f) – (k): 20µm Si structures

When fabricating the 5µm Si devices SOI, the photo resist layer was used to etch the 5µm silicon device layer directly (Figure 6.2(a) – (c)). In contrast, the 20µm Si devices employed 2 mask layers (photo resist and SiO_2 mask layer); the photo resist layer was used to etch the SiO_2 mask layer and about one third of the Si device layer (Figure 6.2(f) - (h)). The structures were then finally etched using the oxide mask layer (Figure 6.2(j)) after wafer dicing process and stripping off the resist.

Often, photo resist is not tough enough to withstand a longer etching process (i.e. to deep etch 20μm Si devices). In such case, a thin film of a tougher material is deposited and patterned using a photolithography [154] . In the fabrication of the CMRA-v2, the SOI wafer with a 160nm silicon oxide thin film was deposited on the top layer of the wafer (out-sourced). The oxide film acts as the main etch mask during the etching of the Si material and as the secondary layer to cover the structure during wafer cutting process. The CMRA based on the comb-drive resonator structure is a complex structure with many sub-structure elements. For the 5 coupled resonators, the structure contains 5260 fingers, 20 anchor springs and 4 coupling springs. With such a structure the chances that some of the structural elements may be broken or contaminated during wafer cutting are high. The SiO_2 mask layer is very important in order to cover the structure during wafer dicing process.

Processes details for both 2 different Si devices thicknesses are provided in Section 6.5.

6.4 Mask Design

The mask is crucially important in bulk micromachining processes to transfer the pattern of the structure onto the wafer using a lithography process. The mask not only includes a design and layout of the structures on a single chip, but also arrangements of different chip designs on a wafer. To explain the mask design, this section discusses the mask design for the second version of the CMRA (CMRA-v2). The mask comprises of 4 designs of the CMRA-v2; (1) 5 Constant Mass CMRA, (2) 5 Staggered Mass CMRA, (3) 5 Staggered Stiffness CMRA and (4) Single comb drive resonator. The structures were laid out on 3 separate chips (5 x 5 mm). The mask was designed to ensure the structure will be successfully etched and released; the wafer can be diced to an appropriate chip packaged, wire bonded and electronically tested.

6.4.1 Type of mask

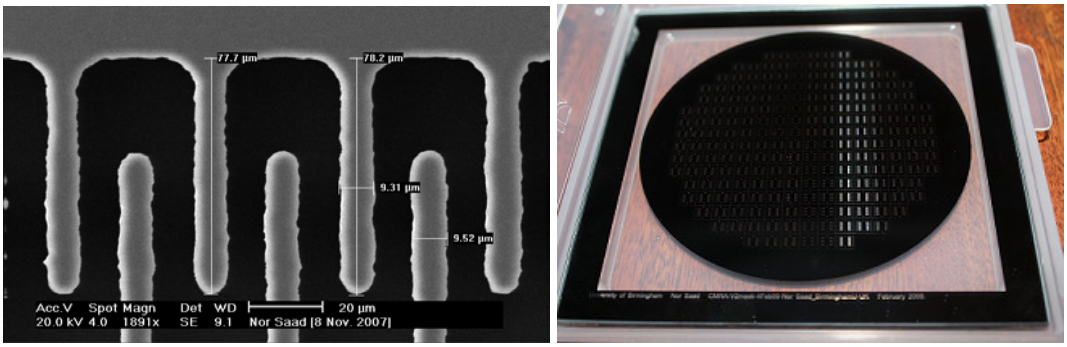

Figure 6.3 (a) SEM image of comb finger, fabricated using polyester film mask; (b) A photo of the chrome glass mask for the CMRA-v2 structure fabrication

The mask material determines the final quality of edge of the fabricated structure. Figure 6.3 (a) is an example of wavy edge comb fingers which were patterned transfer using a polyester film mask. To improve the edge of the structure, glass chrome mask (Figure 6.3 (b)) was used to lithographically transfer the structure pattern.

6.4.2 Etching Channel Aspect Ratio

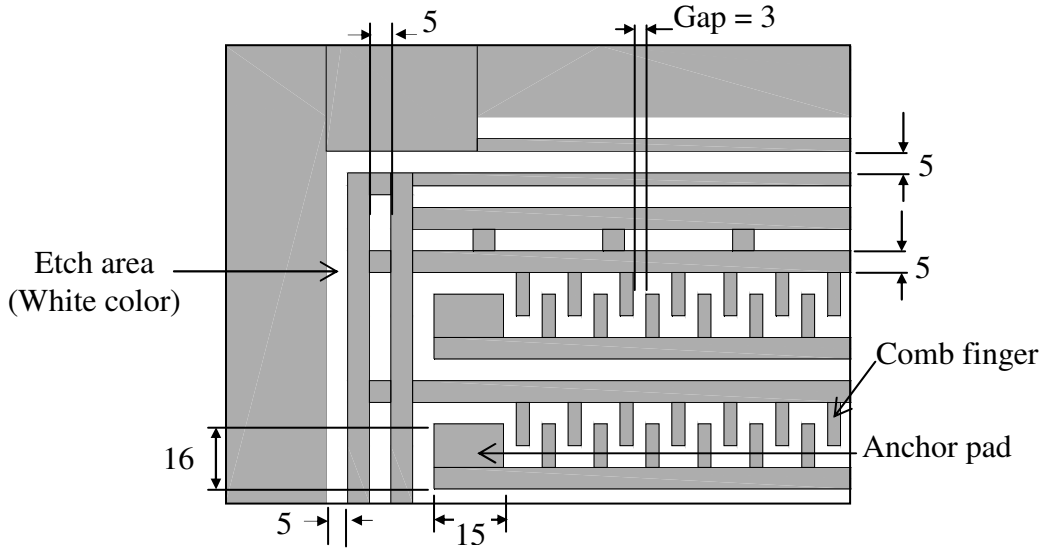

Figure 6.4 Top view of a portion of the resonator design with a minimum channel width of 3µm (Note: all dimensions in µm)

The aspect ratio refers to the ratio between the depth and the width of a channel to be etched using a reactive ion etching process (RIE). As shown in Figure 6.4, the channel to be etched is the area where the resist has been removed after a lithography and development process (positive photo resist). Increase in the aspect ratio, slows the etching process [150]. With 20μm CMRA structure thickness, the channel etching process is controlled by fixing the minimum width of the channel to be etched to 5μm. Hence, the maximum aspect ratio was kept to 4:1. However, the higher aspect ratio (6.7:1) for the gap between the fixed and moving fingers which was designed with 3μm is unavoidable (Figure 6.4). Therefore, more care is required during the structure fabrications to ensure the gap area is properly etched. Furthermore, to ensure the structure is etched uniformly, it is important for all the channels to be designed with even aspect ratios.

6.4.3 Size of the Suspended and Anchored Structure

The CMRA mask was designed to ensure that the suspended structure is successfully released using an HF (hydrofluoric acid) etching process. The important considerations are the maximum size of the suspended structure to be released and also the minimum size of bonded pads to be retained to anchor the fixed structure. To ensure the CMRA is released evenly, all the structures were designed with a maximum of 5μm width. To design the anchor pad size, a guide provided by the INTEGRAM (Europractice) [150] was used. For a maximum of 50μm structure to be released a lateral undercut is in excess of 35μm. Hence, to release the maximum of 5μm beam, the lateral undercut is at least 3.5μm per edge. To securely retain the pad after HF release, the pad was designed at least four times the size of undercut (14 x 14μm).

6.4.4 Size of Wire Bonded Pad

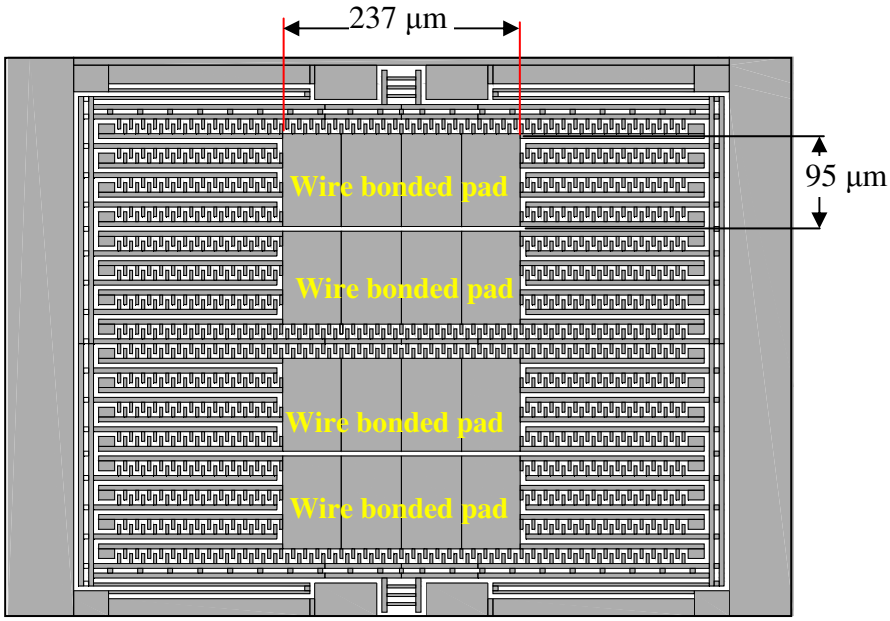

Figure 6.5 Schematic of wire bonded pads of the comb drive resonator

To ensure successful wire bonding process the wire bonded pads need to be designed at least 100 x 100µm sizes. Due to space constraints, the CMRA-v2 wire bonded pads were designed slightly small in terms of the pad width (95µm) but the pad length was increased to 237µm (Figure 6.5).

6.4.5 Gap and Alignment for Chip Dicing Requirement

To ensure the wafer can be diced properly into chips a cutting mark (Figure 6.6) on the wafer is necessary to align the cutting lines during the dicing process. Since, 3 different chips designs were placed and repeated on the mask, a chip identification mark was included (Figure 6.6).

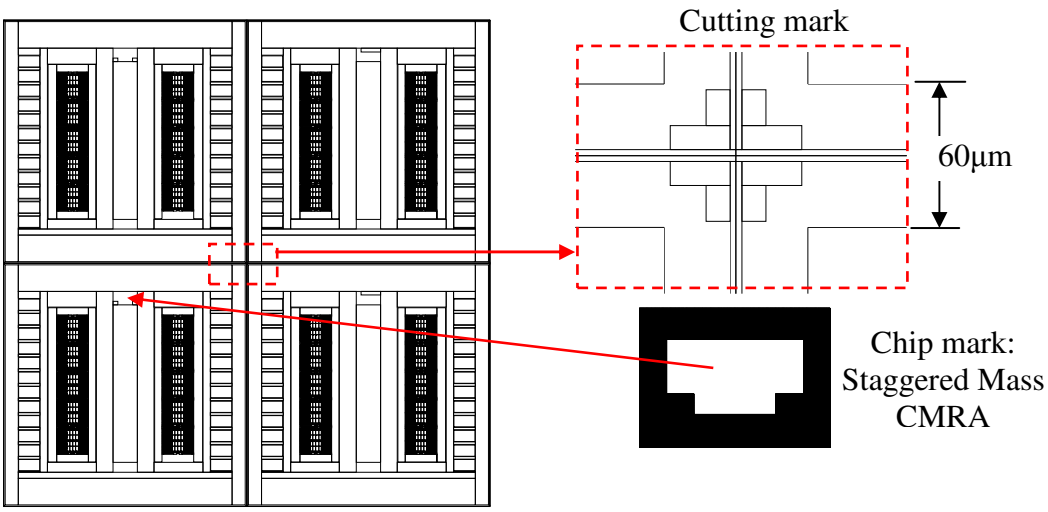

Figure 6.6 A portion of schematic of mask design with cutting mark and cutting width

6.5 Detail Fabrication Processes

6.5.1 Soft Wafer Cleaning

The process is started by cleaning the SOI wafer. While the wafer is placed on the spinner, acetone was sprayed on the wafer surface, and the spinning process started. Before the acetone is dry, the IPA (Isopropyl Alcohol) is sprayed onto the wafer and the speed of the spinner is increased. To dry the wafer, the soft cleaned wafer was pre baked on a hot plate at least for 50 seconds and at 115^{o}C.

6.5.2 Primer and Resist Coating

The research used HMDS (Hexamethyldisilizare) as a primer coating and S1805 a positive photo resist. The HMDS was employed to help an adhesion of the photo resist with the wafer. To ensure clean resist coating, the primer and the resist were applied on the wafer using a syringe and a PVDF filter media (Figure 6.7). Approximately 2 to 3ml HMDS liquid was dropped slowly at the centre of the wafer and the wafer was spun using 3 stages of spinner

speed (480rpm, 10s; 3000rpm, 45s; and 480rpm, 10s). Immediately, after that around 3 to 5ml S1805 was applied and spun on the wafer at 3 stages of spinner speed (200rpm, 10s; 3000rpm, 30s; and 480rpm, 10s). Figure 6.2(a) and (f) show the schematic of the resist layer (red colour) for both 5 and 20μm SOI wafers respectively.

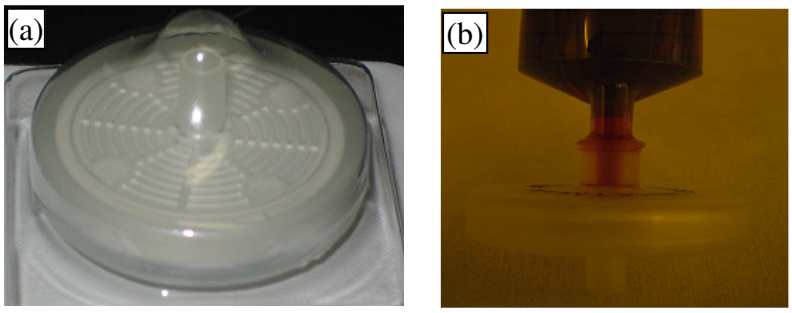

Figure 6.7 (a) PVDF filter media used to filter the resist; (b) The filter fixed to the syringe tip

Before patterning, the wafer was soft baked at a temperature of 115^{o}C on the hot plate for 2 or 3 minutes. It is important to note that the flatness of the spinner and the smoothness of hot plate have significant effects on the evenness of the resist coating across the whole wafer. The soft bake time may have significant effects on the exposure time (lithography) and development process which is further explained in the next section.

6.5.3 Pattern Transfer Using Lithography and Development Process

Using the chrome mask, the SOI wafer which was coated with photo resist is patterned transfer using a Canon Mask Aligner (PLA-501 FN, Figure 6.8). As emphasized by Fedder [155], to ensure an accurate pattern transfer, the exposure and process parameters which need to be considered are wavelength (λ) of the radiation source, resist thickness, exposure time, surface roughness of the structure and temperature of the exposure operation. The wafer was exposed under UV (ultraviolet) light using a hard contact scheme. This is the most crucial

stage to ensure the structure pattern is correctly transferred, with the intended geometrical shape, remains clean, and is free from any defects. The exposed photo resist was then developed using MF 319 to create the desired etch mask for the subsequent dry etching process.

Figure 6.8 Mask aligner machine (PLA-501 FN) for photolithography process

Table 6-2 Experiment data: the effect of different soft bake time, exposure time and development time on comb finger pattern (CMRA-v2)

Experiment	Soft bake time (minutes)	Exposure time (seconds)	Development time (seconds)
Effect of soft bake time	3	3.8	30
	5	3.8	30
Effect of exposure time	2	2	60
	2	4	60
Effect of development time	3	3.6	10
	3	3.6	20

To examine the effect of soft bake time, exposure time and development time, the resist was spun on several plain Si wafers. The effect of the time was examined by soft baking a wafer for 3 and 5 minutes separately and other exposure and development time were fixed (refer to Table 6-2). Then the developed wafer was observed (across the whole wafer based on 3

points observation) using an optical microscope. Particular attention was given to the pattern of the comb fingers. Refer to Section 6.6.1 for the result of observed structures.

CNS and Xie [156] proposed that the S1805 may be soft baked at 3 minutes, exposed between 4 to 5 seconds and developed at 1 minute. After several trial processes, the 5µm device and 20µm device thickness were exposed and developed for 4s, 60s and 3.6s, 20s respectively.

6.5.4 Reactive Ion Etching (RIE) Process

In RIE process, a glow discharge creates chemically reactive ions and radicals of etch gases. The reactive radicals adsorb on the silicon and react to form volatile products. The process also is assisted by ion bombardment which gives the etch process a certain directionality [131, 157]. To etch the silicon a mixture of Sulphur Hexafluoride gas (SF_6), Oxygen (O_2) and Octafluorocyclobutane (C_4F_8) was used. Overall, the gas combinations, pressure and plasma power influence the etch profile of the structure.

Figure 6.9 Surface Technology System (STS machine)

The wafer area which is not protected with the photo resist was dry etched using the surface technology system (STS machine, Figure 6.9). As an example, for the 5µm SOI device the wafer was etched for 2minutes and 40seconds. For 20µm SOI device, at the first etching

stage, the 160 nm oxide mask layer was etched at 6nm per minute and further etching was continued to etch around 1/3 of the Si device layer. In the second stage (after wafer cutting and stripping off resist), the diced and cleaned chips were stuck on a plain silicon wafer using 3195M Thermal Release tape and the remaining 2/3 of the Si layer was etched.

Before a structure release, it is important to ensure that the structure is etched to the buried oxide layer (BOX). This can be confirmed by observing the colour of the etched layer under the optical microscope. The colour may look greenish or light purple depending on the thickness of the Si device and the BOX layer. Due to some tolerance of the Si device layer thickness, multiple mixed colours such as yellow, green, grey and white can be observed across the wafer surface before the etched layer approaches the BOX. The BOX layer is confirmed once all the colours disappear.

6.5.5 Wafer Cutting Process

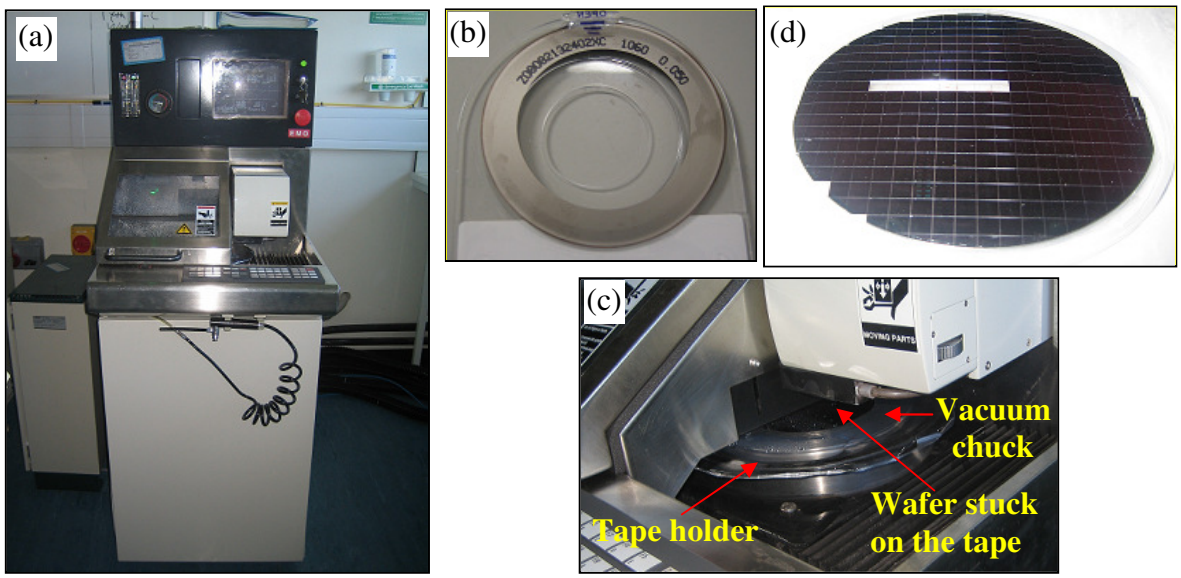

Figure 6.10 (a) DAD 320 (wafer dicing saw machine); (b) Diamond blade; (c) Wafer stuck on the tape holder and clamped on the vacuum chuck during cutting process; (d) Cut wafer

In order to release the suspended structure, the wafer was diced and further processes were carried. To dice the wafer, the research used the wafer dicing saw machine (DAD320, Figure 6.10(a)) and NBC-Z 1060 diamond blade (Figure 6.10(b)) with a size of 56.8 (outer diameter) x 0.05 (thickness) x 40mm (internal Diameter)). Figure 6.10(c) shows the wafer which was stuck on a tape holder and clamped on the vacuum chuck during the cutting process and (d) the wafer after dicing process respectively.

6.5.6 Chip Cleaning and Stripping off Resist

To remove dust and contamination from the cutting process and also to strip off the photo resist mask layer, the selected chips from the diced wafer were cleaned using acetone, and IPA. After cleaning with IPA, the chip was rinsed using the ionised water and blown with nitrogen gun. The cleaning process in acetone and IPA may take few minutes or longer depending on the soft bake time of the wafer after resist coating process. In general, longer soft bake time, harden the resist and hence make it more difficult to remove the resist. If the problem persists, it is necessary to clean the chips using O_2 plasma (STS machine). The cleaning time using O_2 may vary from 3 to 10 minutes depending on the lithography patterning process parameters.

6.5.7 HF Release Process

HF wet etching may be used to release the CMRA structure from the SOI material. The process can be done by dipping the chip which was held with Teflon tweezers, in HF (hydrofluoric) acid at 40% concentration. The HF liquid etches the buried oxide underneath the suspended structure at about 1μm per minute. The etching process was terminated by

dipping and rinsing the chip with deionised water. The chip may be dried using CO_2 (Carbon dioxide) critical point drying or using Cyclohexane freeze drying process. Or using other simple ways, the chip was rinsing in deionised water several times after HF wet etching process; then, the water was replaced with isopropanol (IPA) at least twice. Finally, the chip (still held with tweezers) was placed in a clean bottle slowly dried overnight. In most drying processes the released structure tends to stick to the substrate [131]. For the CMRA-v2 structure the problem is more severe, with stictions occurring between the fixed and moving comb fingers. Refer to Section 6.6.4 for examples of observed structure after HF liquid.

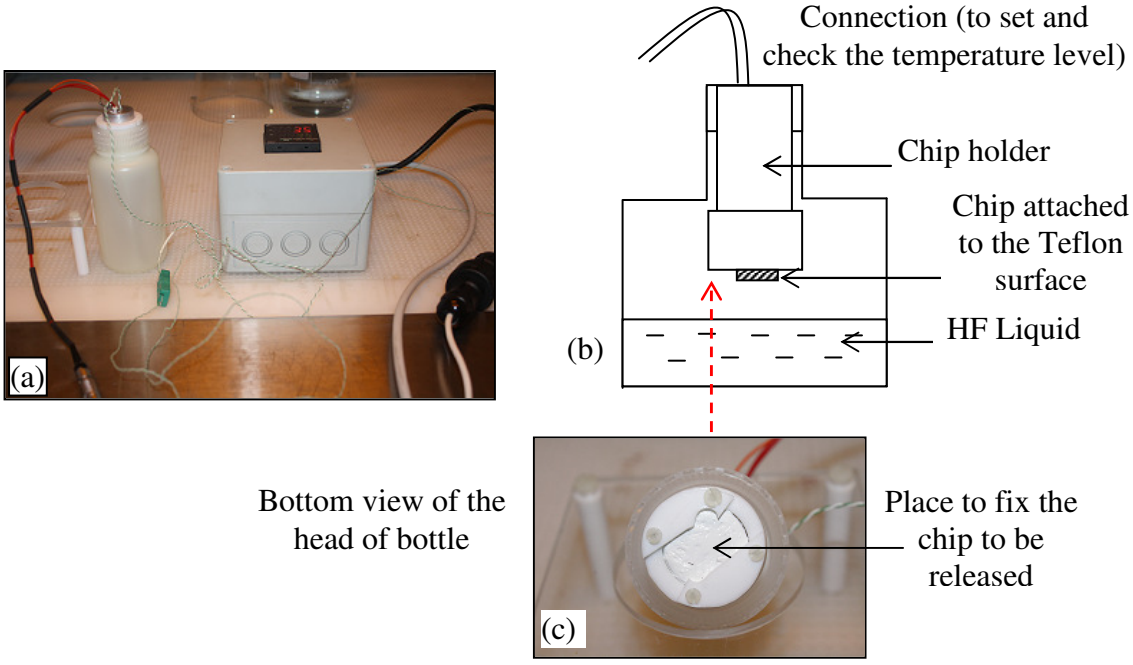

Figure 6.11 HF vapour release kit setup

To solve the problem the research employed HF vapour processing. An HF vapour release kit was developed (developed by Anthony, Figure 6.11). The chip was attached to the bottom surface of the head (chip holder, Figure 6.11(b), (c)) of the teflon bottle and the surface was heated between 32 to 35^{o}C using the connected thermocouple. Once the actual working temperature was achieved, the chip holder was transferred to the bottle which contains HF

liquid (40% concentration). The etch rate using HF vapour may vary between 0.15 to 0.5µm per minute depending on the working temperature during the exposure process. The processing time may vary slightly for each chip to be processed. At the end of the exposure time, the chip holder was removed from the HF bottle and placed in the clean bottle for approximately 10 to 20 seconds. Finally the chip was removed from the holder.

6.5.8 Structure Movement Observation

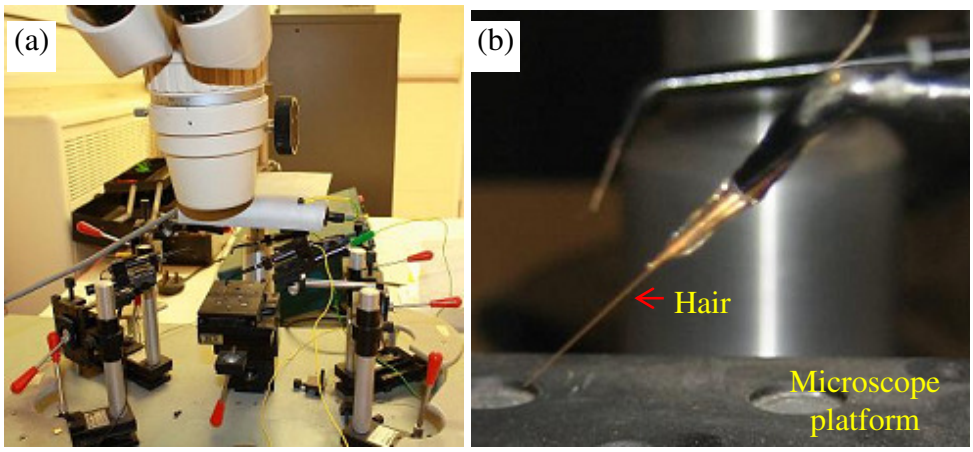

Figure 6.12 (a) Optical microscope with multiple D10 positioners, (b) A hair stuck to the positioner

To ensure the structure is fully released, the structure was gently pushed using a hair and the movement was observed under an optical microscope. Figure 6.12 shows the optical microscope which is equipped with multiple lever controlled positioners. The hair was stuck onto the needle of the positioner (Figure 6.12(b)) and the structure was placed on the microscope platform during the checking procedure.

6.6 Structure Observations

Referring to Figure 6.1 for the process flow of the CMRA fabrication, the fabricated structures were mainly observed at 4 process stages which include:- (1) After lithography and

development process; (2) Reactive Ion etching (RIE); (3) Stripping off resist (before HF process); and (4) After HF release process. The structure was observed using an optical microscope (Ergolux 200, Figure 6.13(a)) and dual beam FIB/SEM system (EDAX DB235, Figure 6.13(b)).

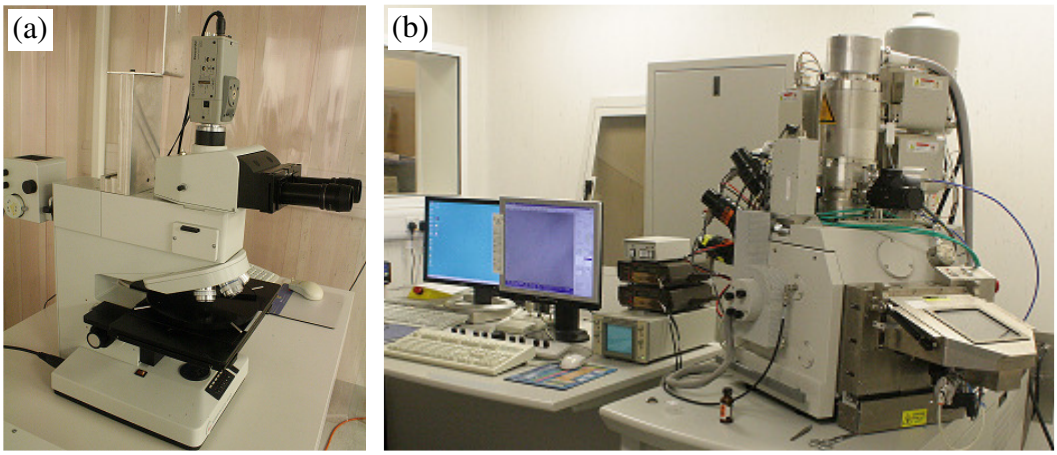

Figure 6.13 (a) Optical Microscope (Ergolux 200); (b) Dual beam FIB/SEM system (EDAX DB235)

6.6.1 Observation 1: Photolithography and Development Process

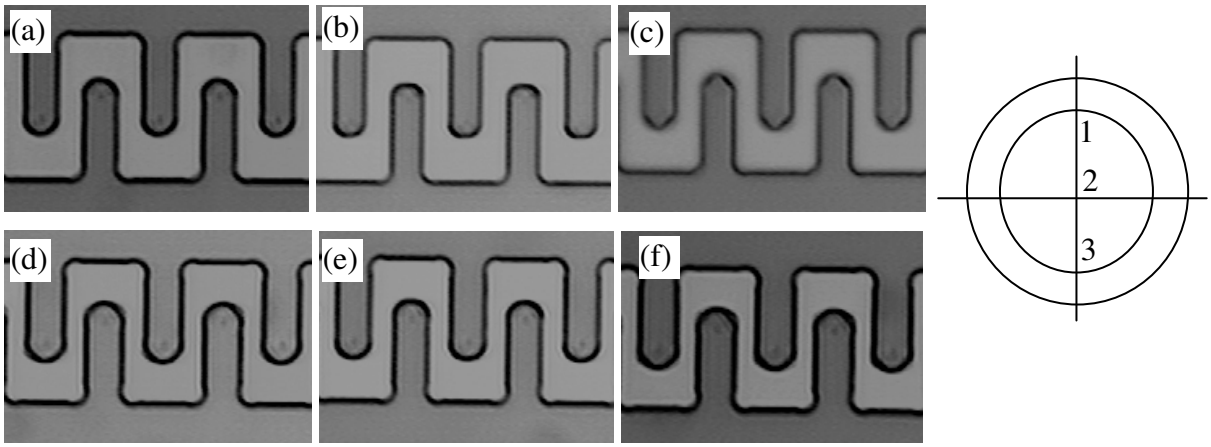

Figure 6.14 The effect of soft bake time (OM image, 3 observation points; micrographs scales at 100x magnification); (a)-(c): 3 minutes soft bake time, 3.8 s exposure, and 30 s development; (d)-(f): 5 minutes soft bake time, 3.8 s exposure, and 30 s development

Figure 6.14 shows the OM image of the comb fingers which were soft baked at 3 minutes ((a)-(c)) and five minutes ((d)-(f)) respectively. 3 minutes soft baking time may be sufficient

to process the CMRA-v2, where the size of the gap between fingers almost similar with the size of the finger (was designed with 3μm gap and 3μm finger width, refer to Chapter 5). Compared to the structure which was baked for 5 minutes, the gap appears to be much smaller. Longer baked time increases the hardness of the resist; hence the resist is more difficult to develop. As can be observed, some finger tips are slightly bigger than the finger base (e.g. (f)). This is expected due to the large exposed area at the finger base, where the UV light is accumulated in the area compared to the finger tip area.

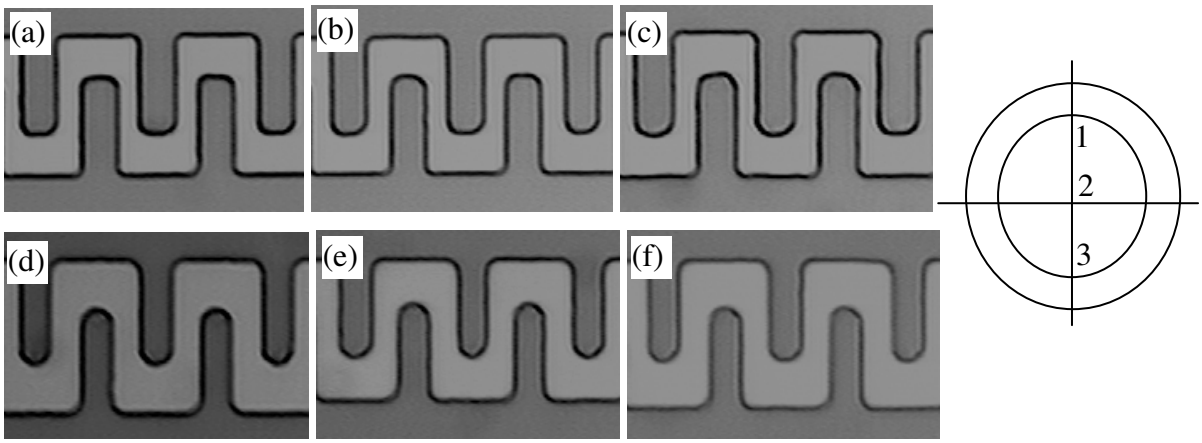

Figure 6.15 The effect of exposure time (micrographs scales at 100x magnification); (a)-(c): 2 minutes soft bake time, 2 s exposure, and 60 s development; (d)-(f): 2 minutes soft bake time, 4 s exposure, and 60 s development

Figure 6.15 illustrates the effect of different exposure times on the structures which were processed on two separate wafers. At similar soft bake time and development time, increasing the exposure time from 2s ((a)-(c)) to 4s ((d)-(f)), definitely decreased the size of the comb finger since the gap between fingers is increased. Increasing the exposure time, increases the softened resist area. Hence, enlarged the gap areas and reduced the size of fingers.

Figure 6.16 shows the result of the structures which were soft baked at 3minutes, exposed at 3.6s and developed at 10s ((a)-(c)) and 20s ((d)-(f)) separately. As can be seen 10s

development time is not sufficient to clean the exposed resist. The structures only properly developed at 20s.

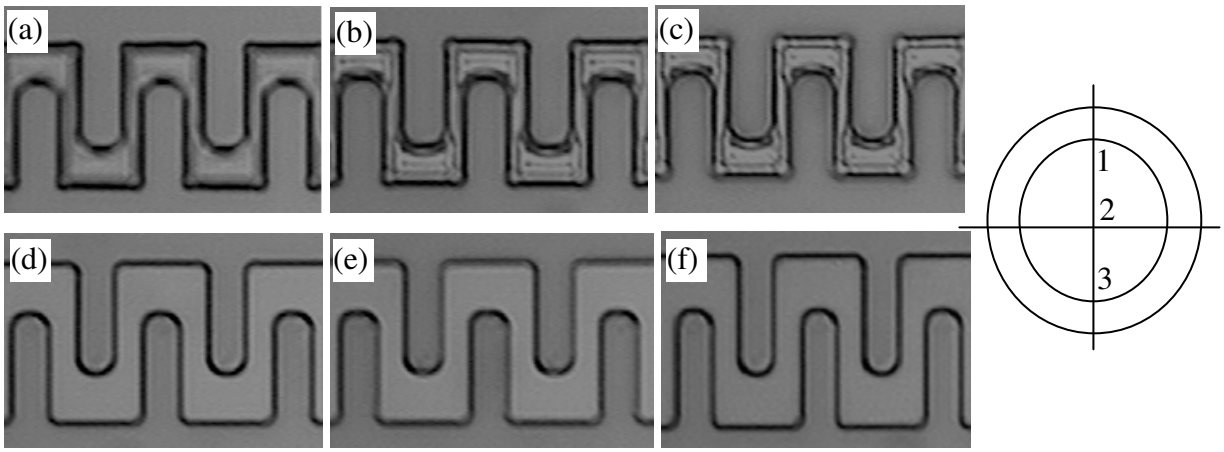

Figure 6.16 The effect of development time (micrographs scales at 100x magnification); (a)-(c): 3 minutes soft bake time, 3.6 s exposure, and 10 s development; (d)-(f): 3 minutes soft bake time, 3.6 s exposure, and 20 s development

It is clear that the soft bake time, exposure time and development time have significant correlation to each other. Appropriate analyses are required to ensure the right pattern is lithographically transferred onto the wafer. Although, most fingers are rectangular with a slight rounding near the finger tip, there are some variations on the finger shape pattern across the whole wafer as observed and discussed earlier (Figure 6.14 – 6.16). It can be confirmed that the variation may significantly affect the final size of the fingers and other resonator elements.

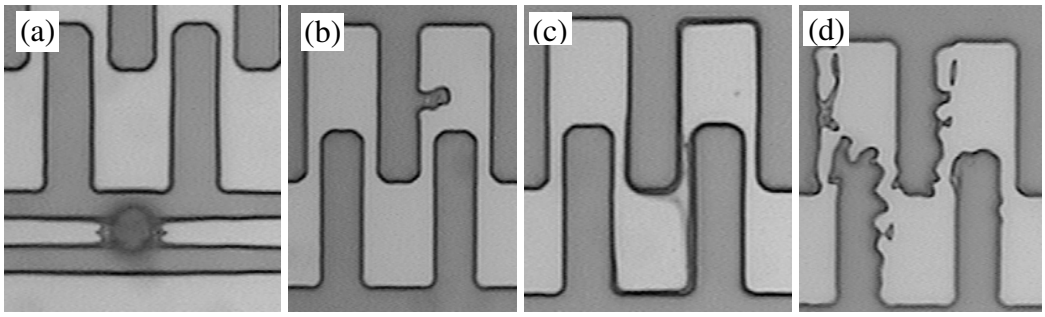

Figure 6.17 Example of observed defects after development process: (a) Foreign material; (b) Resist swelling; (c) Unclean resist (d) Pattern transfer defect

Defects free wafers are hard to achieve. Figure 6.17 illustrates some common defects which were observed after the development process. The research seeks for at least two or three structures for each single and CMRA design to be fabricated so that the response of the structure can be measured and compared.

6.6.2 Observation 2: Reactive Ion Etching (RIE)

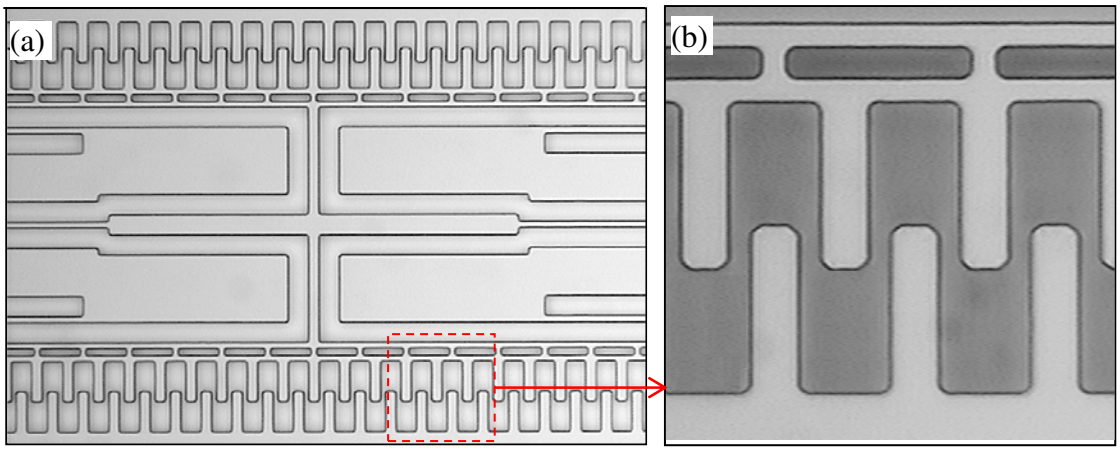

Figure 6.18 (a) Optical microscope image of the mid section of the single fixed-fixed beam resonator after 2 minutes and 40 seconds etching process (at 20x magnification); (b) The fixed and comb fingers at 100x magnification

Figure 6.18 (a) is an example of a single fixed-fixed beam resonator after 2 minutes and 40 seconds dry etched process. The comb fingers (b) show that the structure was properly released. The fingers with rectangular shape and slightly round near the finger tip mimicked the pattern which was transferred to the wafer earlier.

6.6.3 Observation 3: Before HF Release Process

Figure 6.19 shows an example of the Staggered Mass CMRA structure after the second stage etching process in the STS. It is important to ensure that the structure is clean and the Si layer is etched until BOX layer. It is very important at this stage to ensure only structures that are

free defects are further preceded for HF process. Common defects which were found at this stage are illustrated in Figure 6.20. In Figure 6.20(a), where the fingers are connected to each other (not properly etched), the defects originate from the unclean resist in the development process. The debris from dicing processes may also sometimes be stuck between the etched structures (Figure 6.20(b)). Even though the structure is cleaned properly, it is difficult to remove the unwanted debris. Improper wafer handling and the cutting force during the wafer dicing process may also break some structures, which are already partially released after RIE process (Figure 6.20 (c)).

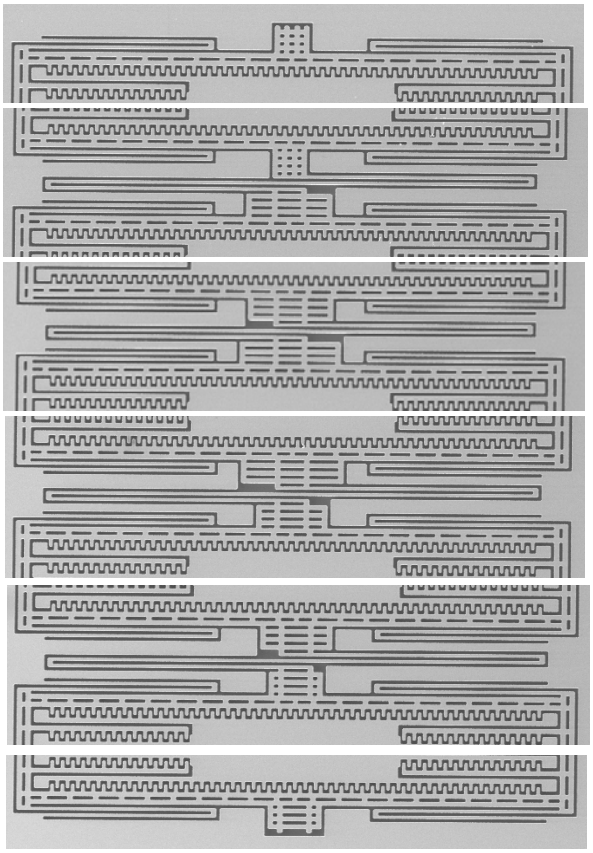

Figure 6.19 OM image of the CMRA-v2 (staggered mass) – ready for HF release process

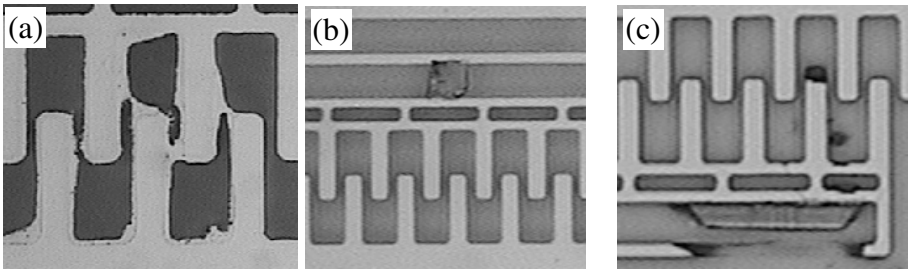

Figure 6.20 Optical microscope images of the defects observed after O_2 plasma cleaning

6.6.4 Observation 4: HF Release Process

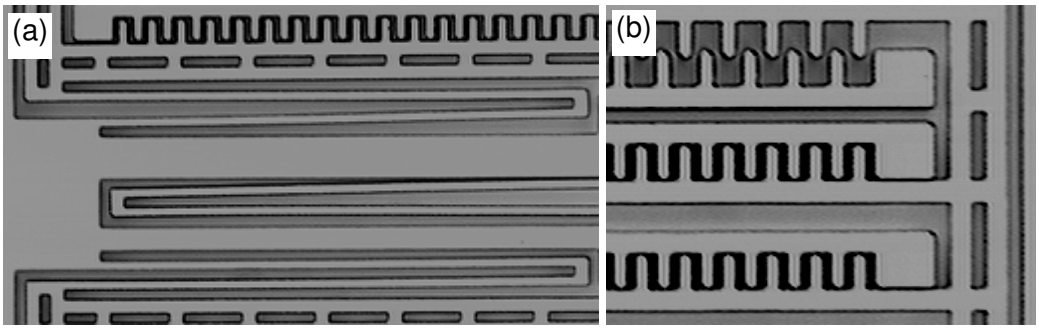

Figure 6.21 Example of defects after HF wet release process; (a) Bending of anchor and coupling spring; (b) Stiction between fixed and moving comb branches

Figure 6.21 illustrates defects which were observed after HF wet etching process. Combination of the surface stress after processing the structure and force of the cleansing and rinsing liquid caused some of the anchor and coupling spring to permanently deform (Figure 6.21(a)). The force and surface tension of the rinsing liquid on the released structure pulled the adjacent surfaces to each other and causing stiction (Figure 6.21(b)), which is very difficult to separate after the structure is dry.

Figure 6.22 is an example of the single fixed-fixed beam resonator which was successfully released using HF vapour processing at 20 minutes and 32 ^{o}C temperatures. Once the movement of the structure is fully confirmed, the structure is then prepared for gold metallization and wire bonding process.

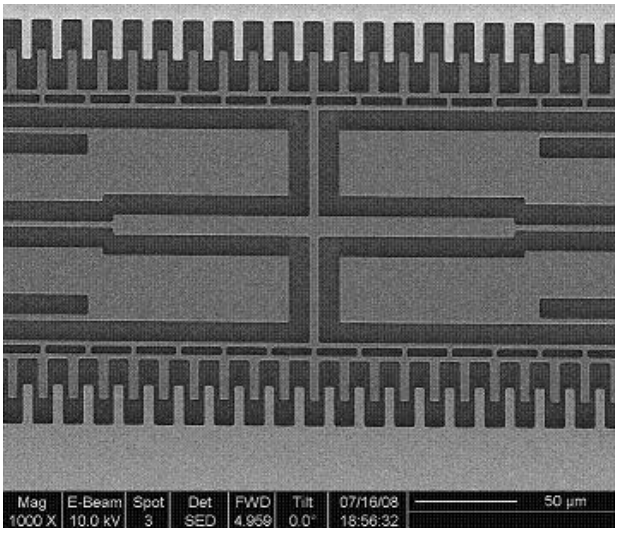

Figure 6.22 SEM image of mid section of single fixed-fixed beam resonator – after HF vapour release

6.6.5 Fabrication Constraints and Discussion

As discussed earlier, the most crucial steps in the CMRA fabrication processes are the wafer preparation, lithography pattern transfer, reactive ion etching process (RIE) and HF released process. The processes need to be repeated few times in order to ensure the quality of the transferred pattern to the wafer and the structure is successfully released.

From the observed structure (Section 6.6.1 – 6.6.4), it can be emphasized that the final quality of the fabricated structure essentially depends on the coated photo resist and the structure pattern which was lithographically transferred to the photo resist mask. It is vitally important to ensure the photo resist is evenly coated on the surface of the SOI wafer and free from any foreign material contamination. Uneven thickness and uneven baking of the photo resist layer induce defects such as swelling of the resist, and in some parts of the structure the resist is very difficult to develop. Unclean resist obstructs the structure preventing proper etching. Then defects are carried forward to the final processes, resulting in failure of the structure fabrication.

It can be argued that the unevenness of the photo resist layer and also variation of the Si device layer thickness supplied by the manufacturer caused some variations in shape and geometrical dimensions of the CMRA structure across the wafer [150]. The defects due to the wafer dicing processes are also unavoidable. Proper care during wafer handling and dicing processes is important to reduce the defects occurrence.

The main problem with the HF wet etching process is stiction. The stiction is either between the moving structure and the fixed structure or between the structure and the substrate (Si handle). The stiction to the substrate is severe if a thin layer of the BOX is used to separate the Si device layer and the handle. The root cause of the stiction is the rinsing liquid which needs to be dried, creating a surface tension forces between the adjacent machined surfaces and also the substrate. As emphasized by Daniel [131] once the contact has been made, the surfaces are held together by hydrogen bridging and van der Waals forces. The stuck surfaces are very difficult to separate. In this research, in order to reduce the stiction problem, the HF vapour released was employed to release the CMRA structure. Occasionally, the stiction problem still appears on some of the CMRA structure elements. The stiction is expected due to the condensed HF vapour left on the structure surface. By careful control the exposure time and temperature, the problem of stiction can be reduced.

6.7 Preparation for Electronic Testing

6.7.1 Gold Metallization

In order to prepare the sample for wire bonding, the single fixed-fixed beam resonator was metalized with 200nm gold. In order to ensure the adhesion of gold material to the silicon surface an adhesion layer of 20 nm titanium was evaporated on the silicon before gold metallization. The titanium was evaporated using an electron beam evaporation at

80miliAmp current and 5kV voltages; and the gold was evaporated using a thermal evaporation at 0.5Amp current. Both the gold and titanium metallisation were done using an Auto 500 Electron Beam - Filament Evaporation System. Figure 6.23 shows the SEM image of the resonator after gold metallization.

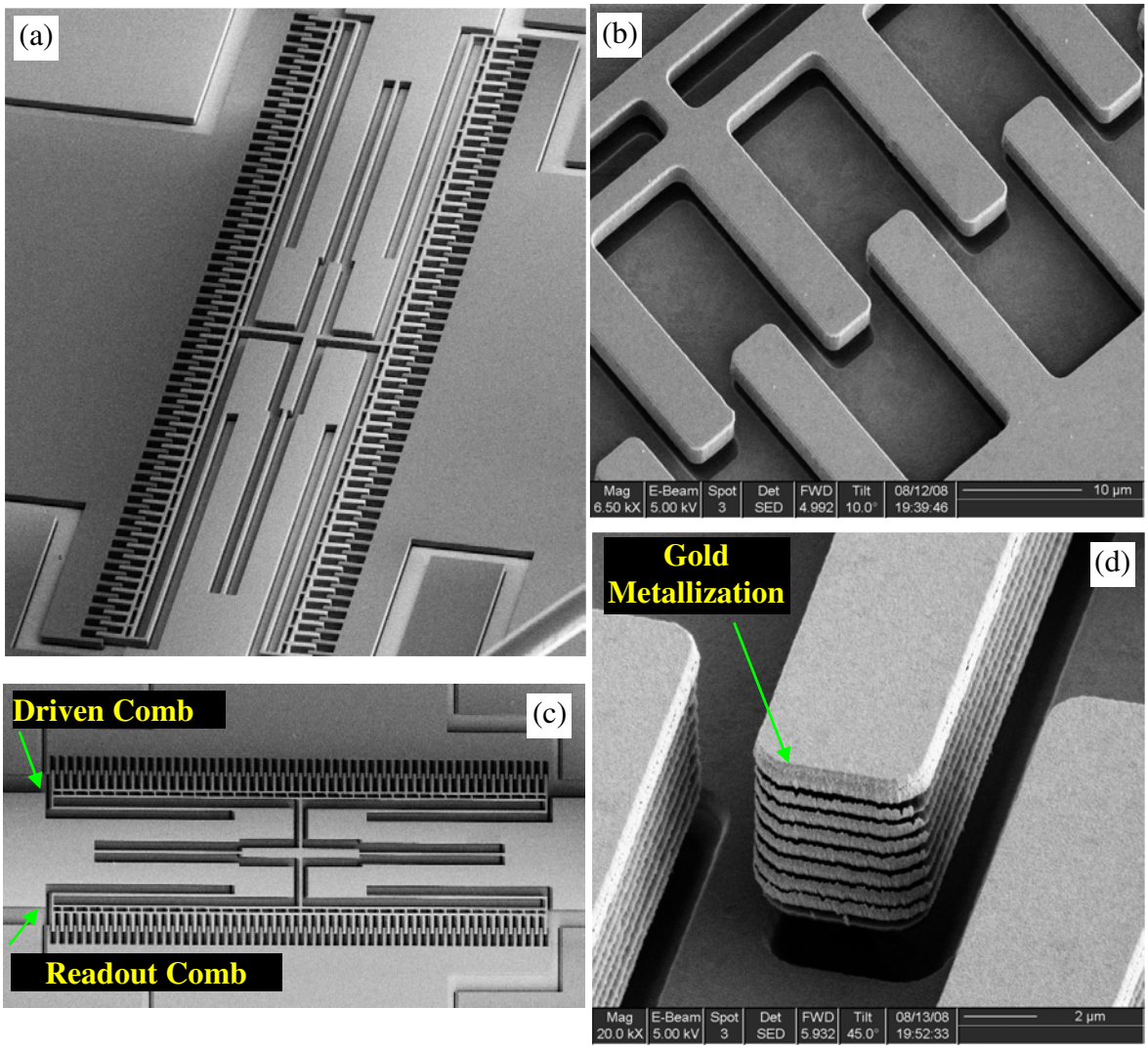

Figure 6.23 SEM image of single R (CMRA-v1) after gold metallization

To prepare for the metallization, the chip contains the structure to be metalized was stuck on a plain silicon wafer by using a copper tape. The wafer was placed in the vacuum chamber of the machine and the metallization material was placed into a ceramic crucible. The machine

was pumped out overnight so that the pressure falls to at least at 1 x 10^{-7}Mbar. Then, the density and thickness of the required coating was set and the evaporation process started (density of gold (Au) = 19.3gcm^{-3}; and titanium (Ti) = 4.5gcm^{-3}).

Two main problems experienced with the gold metallization were shorting and poor bonding adhesion between the bonding wire and the metalized surface. It is hard to visually observe any short between the bonded wires or the fixed and moving comb fingers. Often after electrical connectivity checking, a short circuit will be detected on a bonded chip. Sometimes it is difficult to properly weld the bonding wire onto the metalized gold surface; either the bonded wire lifted off or the gold was detached during the bonding process. To solve the problem the aluminium metallization was used instead of gold.

6.7.2 Aluminium Metallization

Since bonding wire is made of aluminium, aluminium metallization was applied to replace the gold. The aluminium/aluminium bonding is extremely reliable compared to aluminium/gold, because it is not prone to intermetallic formation and corrosion, which will weaken mechanical bonding [158]. Silicon devices are typically metalized using aluminium metal because of its high electrical conductivity and ability to form a protective oxide layer [159]. Furthermore, the aluminium is a low-cost source material and forms low-resistance contacts to n -type or p-type silicon [160].

In this research, due to constraints of in-house equipment, the aluminium metallization was done externally by the QinetiQ Company. The aluminium was metalized by thermal evaporation to a thickness of 150nm. The structure sample was fired in at 425^{o}C in forming gas prior to wire bonding. Figure 6.24 shows an example of a single comb-drive resonator after the aluminium metallization.

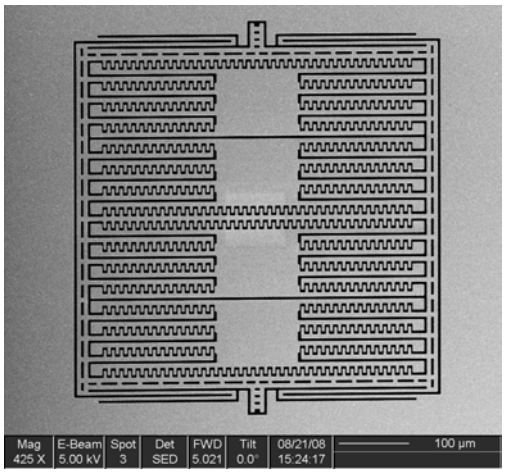

Figure 6.24 SEM image of a single comb drive resonator (CMRA-v2) after aluminium metallization

6.7.3 Wire Bonding and Structure Packaging for Electronic Testing

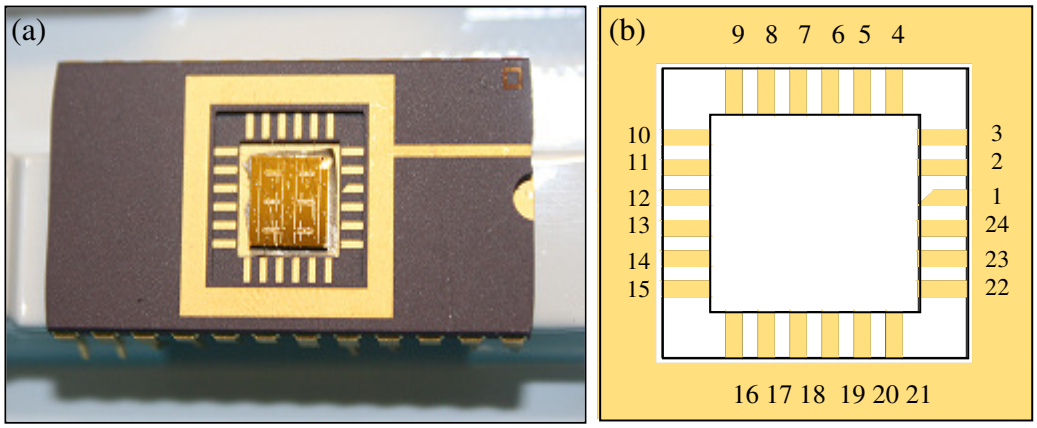

Figure 6.25 (a) Example of a chip stuck on CSB02488 chip carrier; (b) CSB02488

To prepare for wire bonding, the metalized chips were stuck on a 24 pin chip carrier CSB02488 [161] (Figure 6.25(a)). The chip was stuck to the chip carrier using a Staystik Tape (571.003). To simplify the wire bonding connections, all the inputs and ground pads were connected to pins 1 to 12 and the output pads were connected to pins 13 to 24. Figure 6.25 (b) highlights the pins number configuration for the CSB02488 chip carrier.

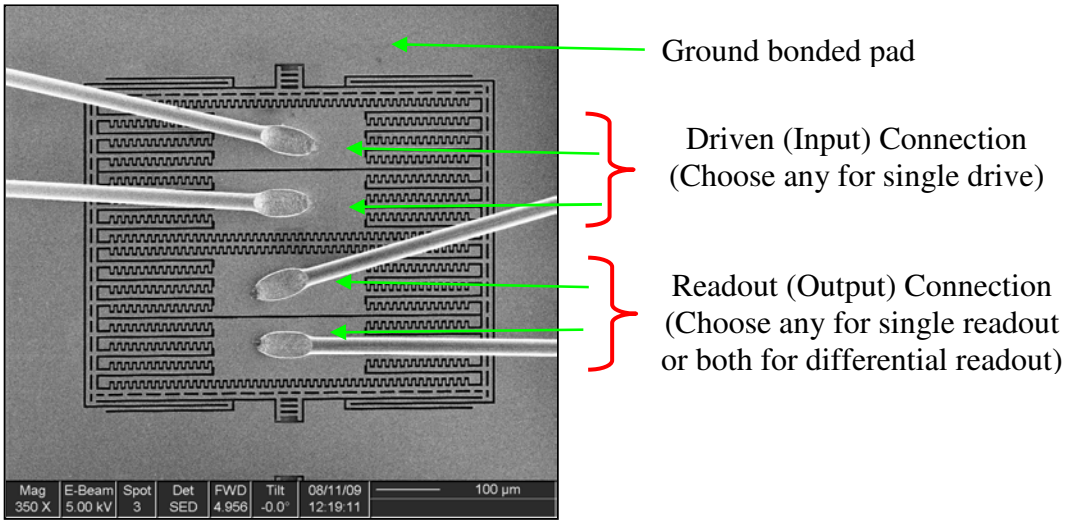

Figure 6.26 SEM image of the wire bonded connection for the comb-drive resonator

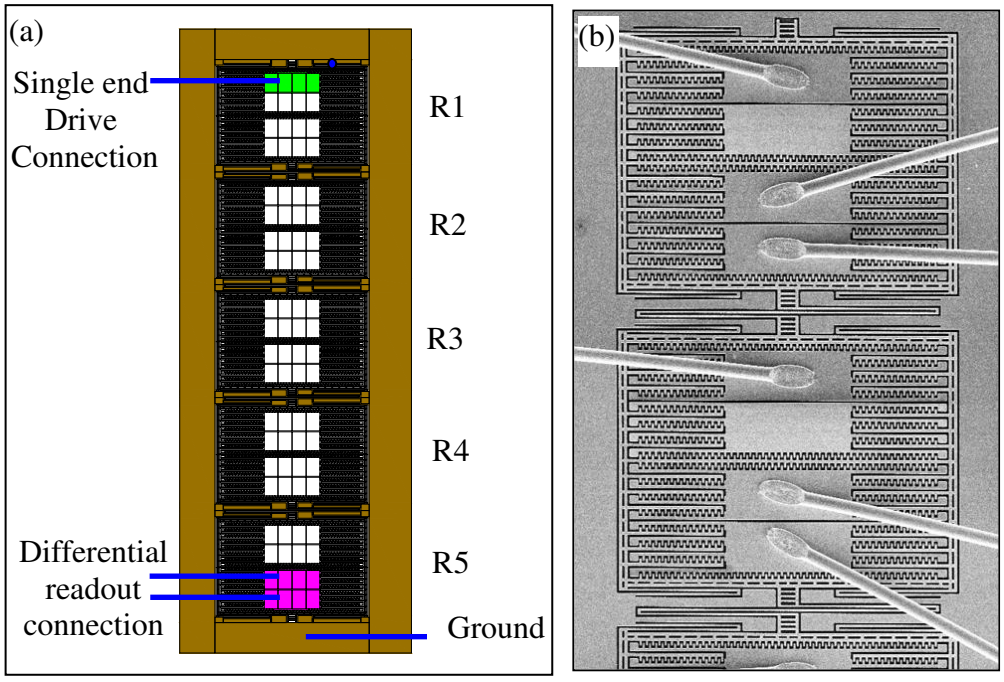

Figure 6.27 (a) Example of bonded scheme of the CMRA; (b) SEM image of wire bonded structure (Constant Mass CMRA)

The structures were wire bonded by using a Delvotek 6319 Ultrasonic Wire Bonder. The machine uses an aluminium wire with the wire diameter of 25µm and welded at 60kHz. Figure 6.26 shows an example of the wire bonded connections for the single comb-drive resonator (CMRA-v2). Only a single connection is required for the single drive or single readout scheme and 2 wires bonded are required for the differential scheme. Similar connections are applied to the coupled resonators depending on the resonators used to drive and readout the CMRA. Figure 6.27 (a) shows an example of a schematic of wire bonded connection of the Constant Mass CMRA, where the first resonator is used to drive the structure and the fifth resonator to measure the output signal of the structure. Figure 6.28 shows example of SEM images of a wire bonded structure of the Staggered Mass CMRA.

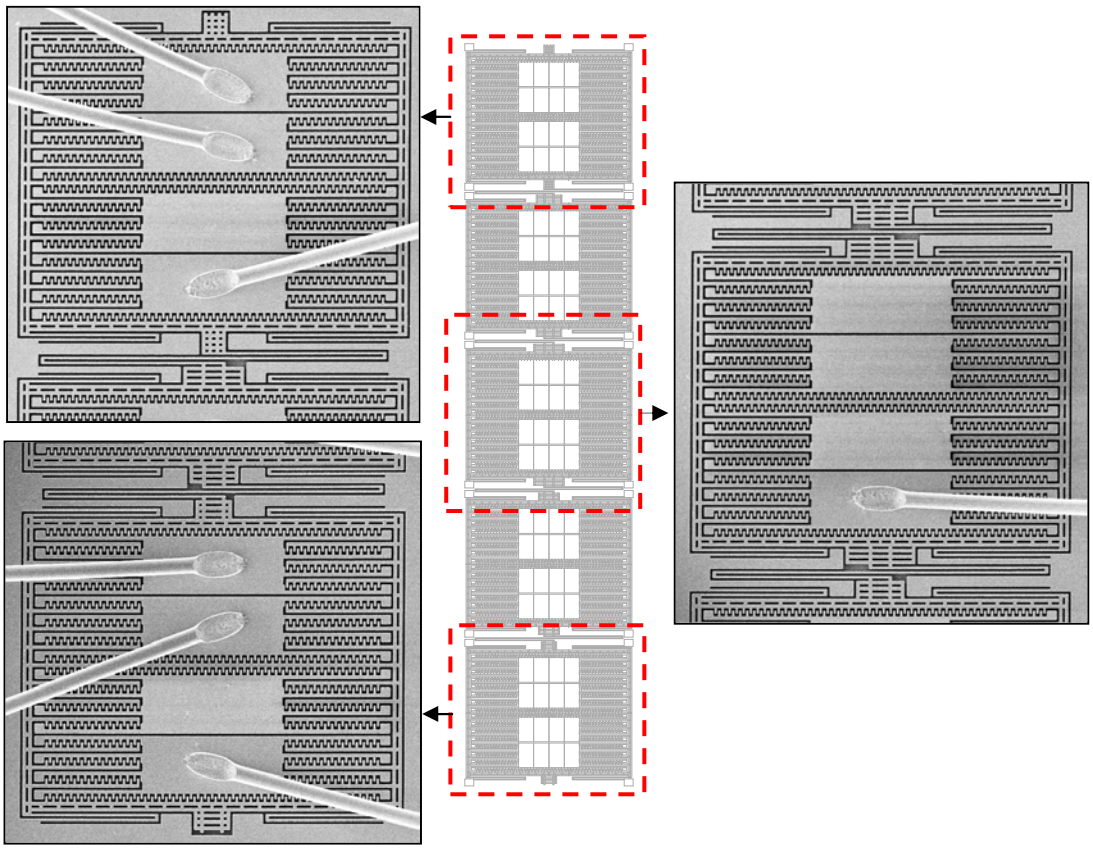

Figure 6.28 Schematic and SEM image of wire bonded structure: Staggered Mass CMRA

6.8 Material Deposition Using FIB

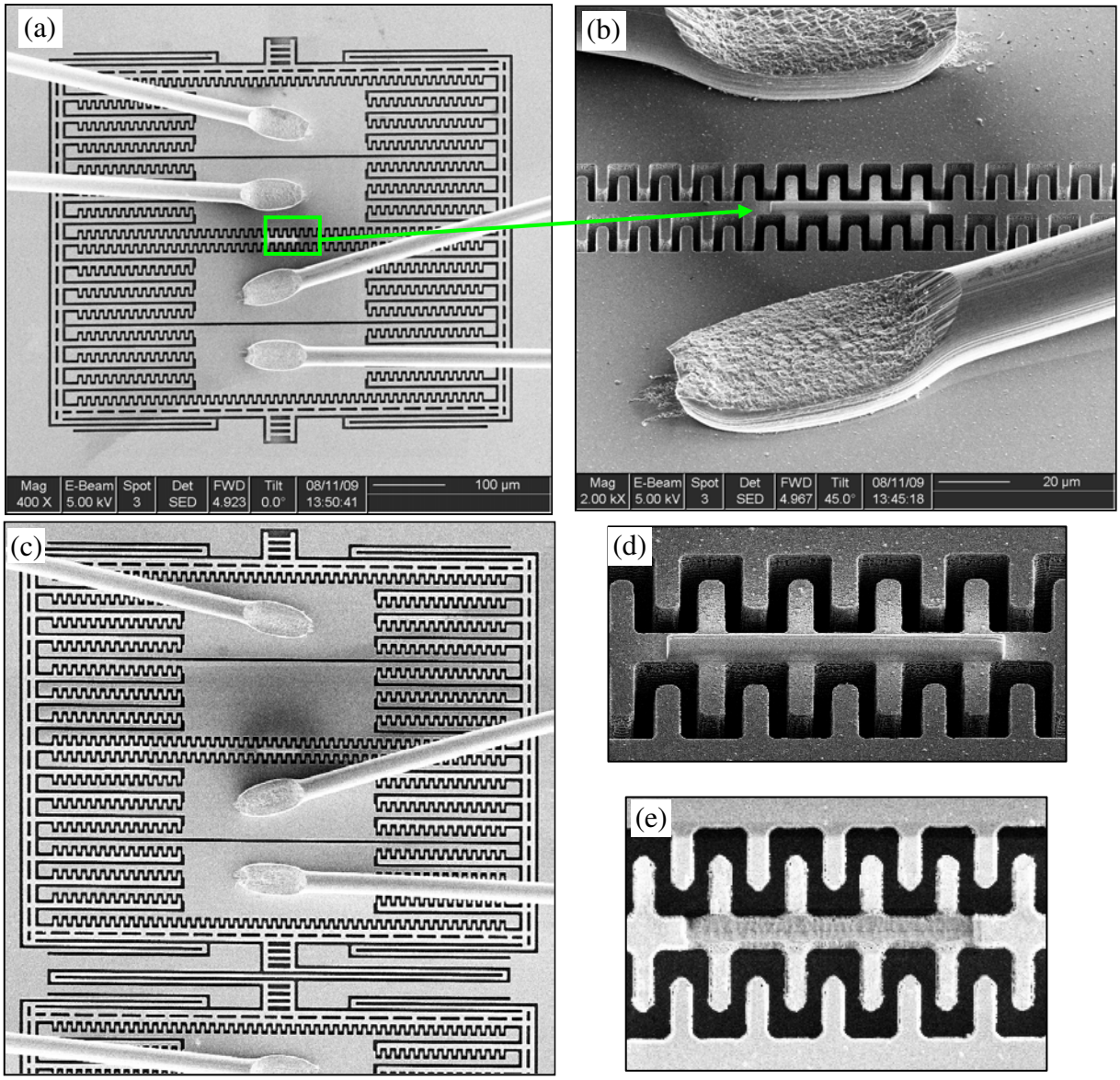

Figure 6.29 SEM images: (a), (b) The position of the platinum mass deposited on the comb drive resonator; (c) A mass deposited on R1 of the Constant CMRA; (d) The enlarged view of the deposited mass (approximate size of 45µm length x 4µm width x 2µm thickness); (e) Deposited platinum which was milled off from the structure

In order to observe the effect of a mass loading on the frequency response pattern of the structure, a platinum mass was deposited using Dual beam FIB/SEM system (EDAX DB235). Specifically, the aims of experiment are:-

- To examine the effect of mass loading on the single comb drive resonator
- To examine and compare the uniqueness of the frequency response pattern of the CMRA sensor structure, the stability of system eigenvectors; and to observe the effect of manufacturing variation on the performance of the CMRA.

Figure 6.29 (a) and (b) show the position where a platinum mass was deposited on the single resonator. To examine the uniqueness of the frequency response pattern and to validate the stability of structure's system eigenvectors , the platinum was deposited on the first resonator (R1) and the fifth resonator (R5) separately. The first step, the mass was deposited on the R1 (Figure 6.29(c)). After measuring the frequency response pattern of the CMRA, then the deposited mass at R1 was milled off and another similar amount of mass was deposited at R5. Approximately, around 0.2 % mass of the single resonator (7.6×10^{-12}kg) was deposited on the structures. The mass was deposited using 550PA ion beam current. Figure 6.29 (d) and (e) show the enlarged image of the deposited mass and the platinum mass which was milled. It can be observed that in Figure 6.29 (e) some silicon have been removed instead of milling the deposited platinum only.

6.9 Summary and Conclusion

This chapter presents and discusses the main issues related to the CMRA fabrication processes and the process to prepare the structure for the frequency response measurement. The mask design in Section 6.4 is an important stage to ensure the successful of the CMRA structure fabrication. The CMRA structure fabrications discussed in Section 6.5 used the standard bulk micromachining processes. The research presented the processes to fabricate 2 separate devices thickness layer of SOI (5 and 20μm). The thin 5μm Si device only requires a photo resist mask to etch the structure. While as, the thicker 20μm Si device employed double mask layers to etch the deeper structure.

Due to the nature of the micromachining processes and the constraints of some fabrication facilities, the fabrications require many considerations and details observations on the processes step for the successful of the structure fabrication (Section 6.6). Detail care and attention are very important to ensure the structure is clean from any possibility of defects during the structure fabrication processes. The processes require special attentions to ensure any possibilities of source of process variations are eliminated.

As discussed in Section 6.5 and 6.6 the tolerance in manufacturing processes initially arises from the lithography processes [162]. The evenness of the resist thickness layer, the exposure and development time have significant impacts on the final profile of the transferred pattern. Those transferred patterns determined the final geometrical shape and dimensions of the fabricated CMRA (length, height, width and structure profile). Even though certain source of the variations are unavoidable (i.e. flatness and smoothness of the hot plate), the CMRA structures were fabricated to ensure that all the defects are reduced, the structures are able to be released, and packaged.

Overall, to evaluate the CMRA performance, the three CMRA(s) structures (discussed in Chapter 5) which include 5 Constant Mass CMRA, 5 Staggered Mass, and 5 Staggered Stiffness CMRA; the singleton of the CMRA-v2 and CMRA-v1 (the integrated comb-drive resonator and fixed-fixed beam resonator) were fabricated. To confirm the performance of the designed CMRA(s), the frequency response of the fabricated structures are then measured and discussed in Chapter 7. The effect of the manufacturing variation will be observed by comparing the frequency response of three similar single resonators which were fabricated on a single chip and the change of the measured frequency response of the CMRA when comparing with the simulated response.

CHAPTER 7 - FREQUENCY RESPONSE MEASUREMENT, RESULT AND DISCUSSION

7.1 Introduction

This chapter presents and discusses the electronic testing of the fabricated CMRA structure, the measurement results and the CMRA performance as a sensor. Section 7.2 highlights aims of the electronic testing. Section 7.3 describes the electronic testing setup and measurement of the CMRA and its single element. Testing procedures and testing samples are highlighted in Section 7.4. Section 7.5 presents and discusses the frequency measurement result of the single resonator (fixed-fixed beam and comb-drive resonator). Performance of the fabricated CMRA(s) which include Constant Mass CMRA, Staggered Mass CMRA and Staggered Stiffness CMRA are discussed and compared in Section 7.6. Section 7.7 discusses the stability of the measured frequency response pattern of the CMRA and its single structure element. Section 7.8 summarizes and discusses the overall performance of the CMRA sensor structure.

7.2 Aim of Electronic Testing

The aims of the electronic testing are:-

7.2.1 To evaluate the performance of the single resonator of the CMRA structure with regard to :

- The effect of input voltage and vacuum pressure level on the resonator frequency response.
- The effect of manufacturing process variations on the frequency response of single resonators.
- Mass loading – frequency response effect of the single resonator.

7.2.2 To measure and evaluate the performance of the three CMRA(s): (1) Constant Mass CMRA, (2) Staggered Mass CMRA, (3) Staggered Stiffness CMRA, in terms of:-

- Measurability and uniqueness of the frequency response of the CMRA(s) before and after the structure is perturbed by deposited mass using focus ion beam technology.
- Stability of the CMRA structure eigenvectors, and the effects of manufacturing variations on performance of the CMRA structures.
- Reliability of the frequency response pattern as a signature for the CMRA sensor structure.

7.3 Electronic Testing Setup and Measurement Scheme

7.3.1 Overview of the Electronic Testing Setup

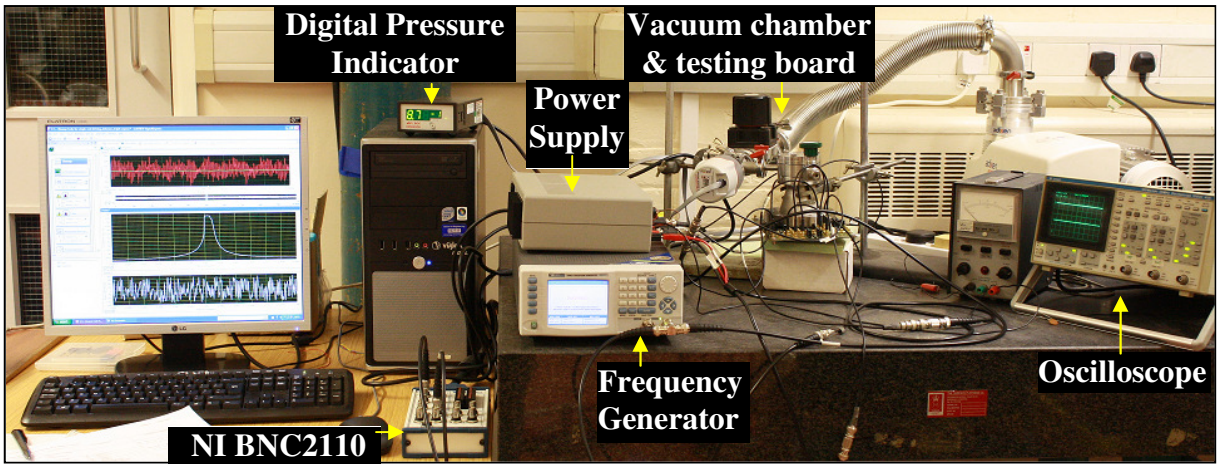

Figure 7.1 Electronic testing setup for frequency response measurement of CMRA

Figure 7.1 shows the electronic testing setup for the frequency response measurement of the CMRA and its single resonator. The testing setup consists of:

- Testing board
- Vacuum chamber system (Adixen DRYTEL 1025)
- Digital Pressure Indicator
- Power supply unit (ISO TECH IPS 1125)

- Oscilloscope (100 Ms/sec 20 MHz Oscilloscope (DSO) 400)
- Frequency generator (50 Ms/sec Waveform Generator WW5061)
- NI BNC 2110 connector block [126]
- Personal computer which is equipped with a data acquisition system (DAQ, NI PCI-6133 [127]) and LabVIEW Signal Express software

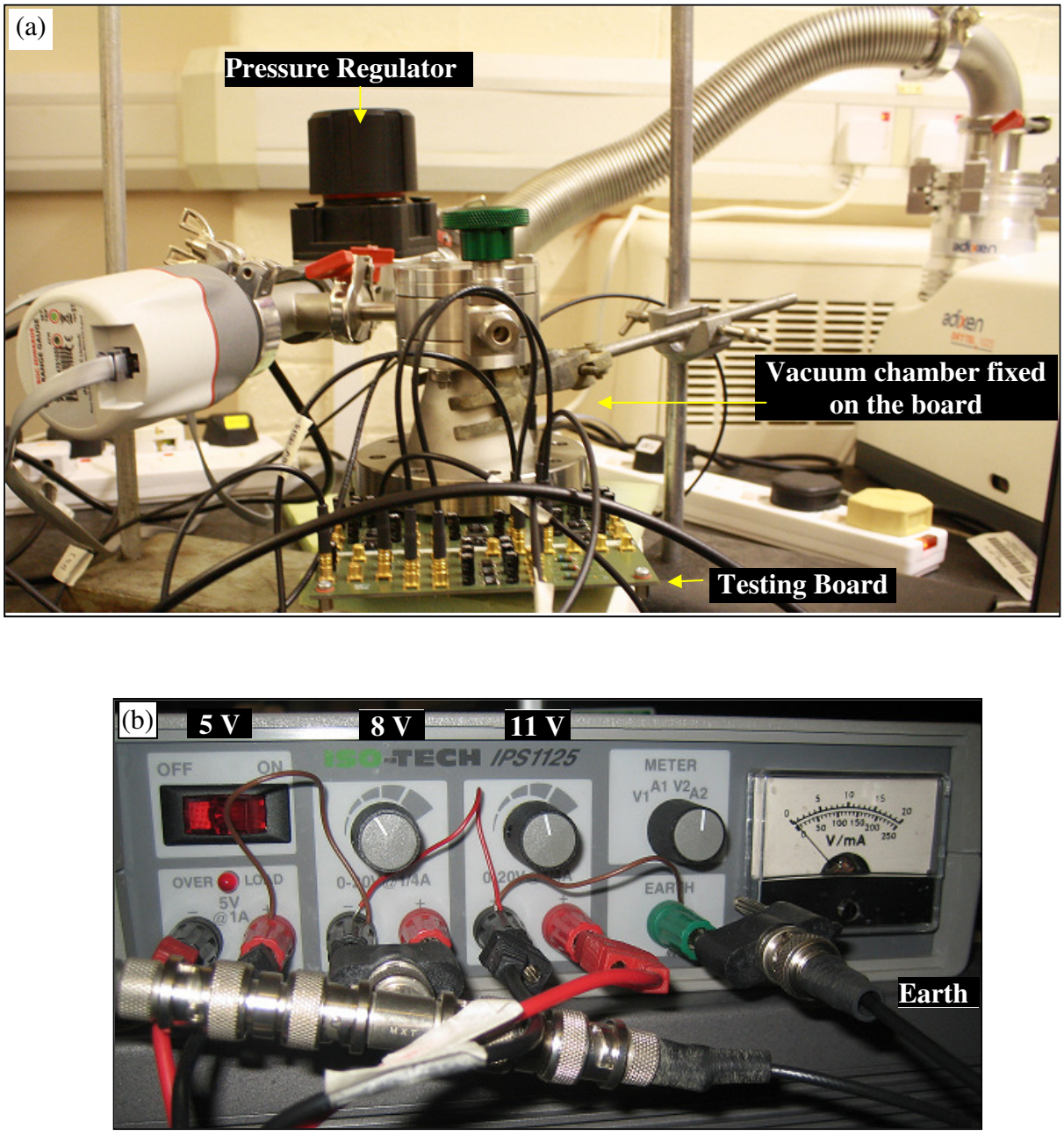

Figure 7.2 (a) Vacuum chamber fixed on the testing board; (b) Power supply connection unit

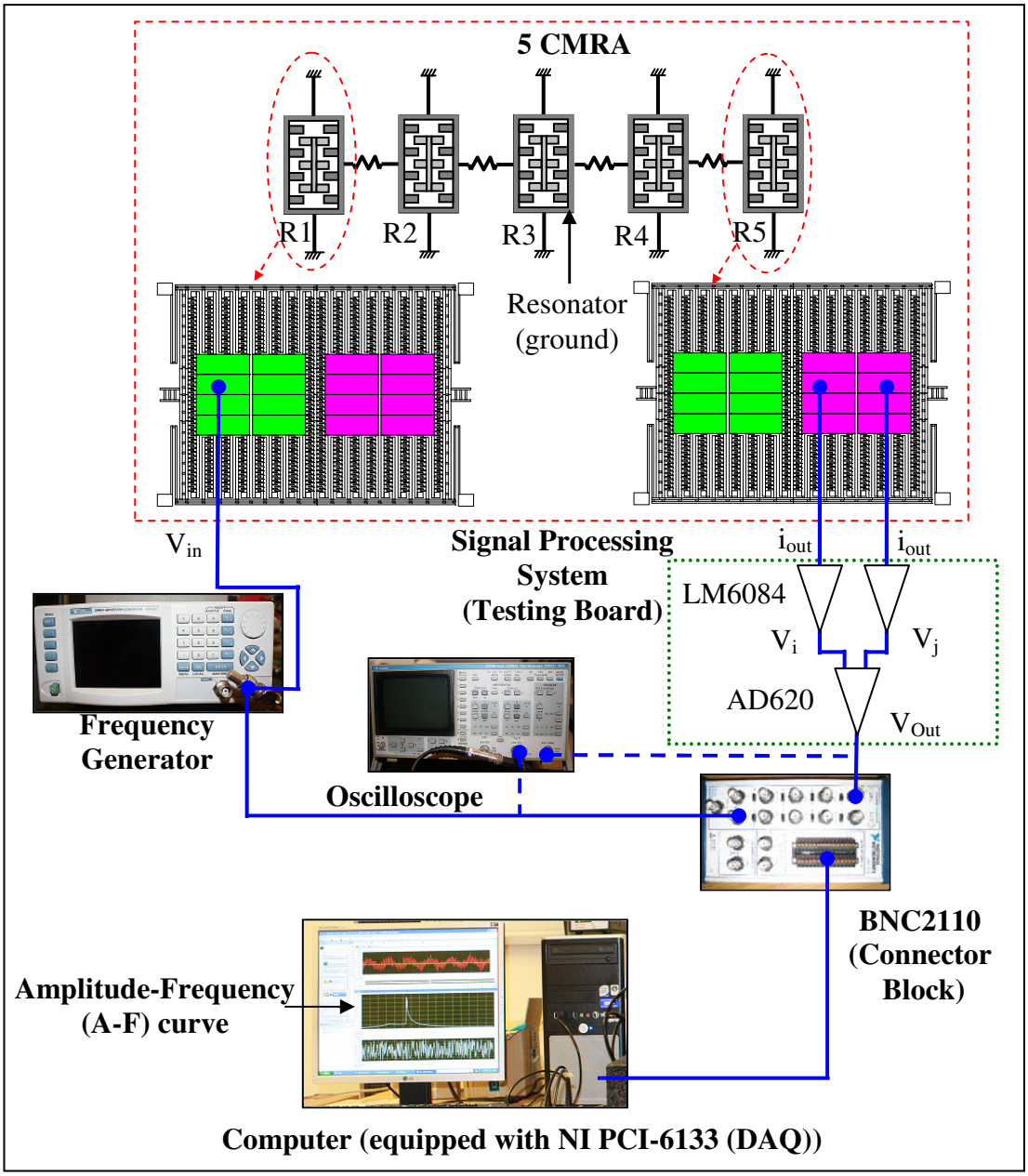

Figure 7.3 Schematic diagram of the frequency response measurement system

The testing board is used to mount the chip and to process the output signal of the resonator sensor structure (note: development of the testing board and overall electronic testing setup configuration for the frequency response measurement are input from Ross Turnbull, a PhD student from the Oxford University). The sensitivity limit of the current developed frequency measurement system is 0.1Hz. The vacuum chamber system is used to pump out and control

the air pressure level, so that the structure can be tested at a reduced air damping condition. As shown in Figure 7.2(a), the chamber was fixed onto the measurement board during the testing process. The digital pressure indicator records the pressure level of the vacuum chamber system. Figure 7.2(b) shows the power supply unit, which was used to supply the DC voltage to amplifiers on the testing board (11V and -5V), and the Transimpedance amplifier (±8V sense voltage) for the readout connections. The oscilloscope was used to observe the resonant frequency of the measured structure by manually sweeping the frequency generator. The BNC2110 connector block was employed to interface the input line (drive pin connection), the output line, and the Data Acquisition System (DAQ) in order to automatically display the frequency response measurement curve of the measured structure on the computer screen. Figure 7.3 illustrates a schematic diagram of the CMRA frequency response measurement system (e.g. CMRA structure with the drive and readout at R1-R5).

7.3.2 Measurement Scheme

Two measurement schemes were used to measure the CMRA and single resonator:-

- Single ended drive – Single readout
- Single ended drive – differential readout

The schemes were selected based upon the design configuration of the structure to be measured. For example, the fixed-fixed beam resonator employs the single ended drive – Single readout measurement scheme; while the integrated comb drive-resonator and the three CMRA(s) structures (5 Constant Mass CMRA, 5 Staggered Mass CMRA, and 5 Staggered Stiffness CMRA) employ the single ended drive – differential readout measurement scheme [163]. Figure 7.4 shows the schematic of the wire bonded scheme of the fixed-fixed beam resonator and the integrated comb drive-resonator structure. The bond pad connected to the

fixed comb structure was used to drive and readout the output signal of the resonator; while the moving structure or resonator was connected to the earth.

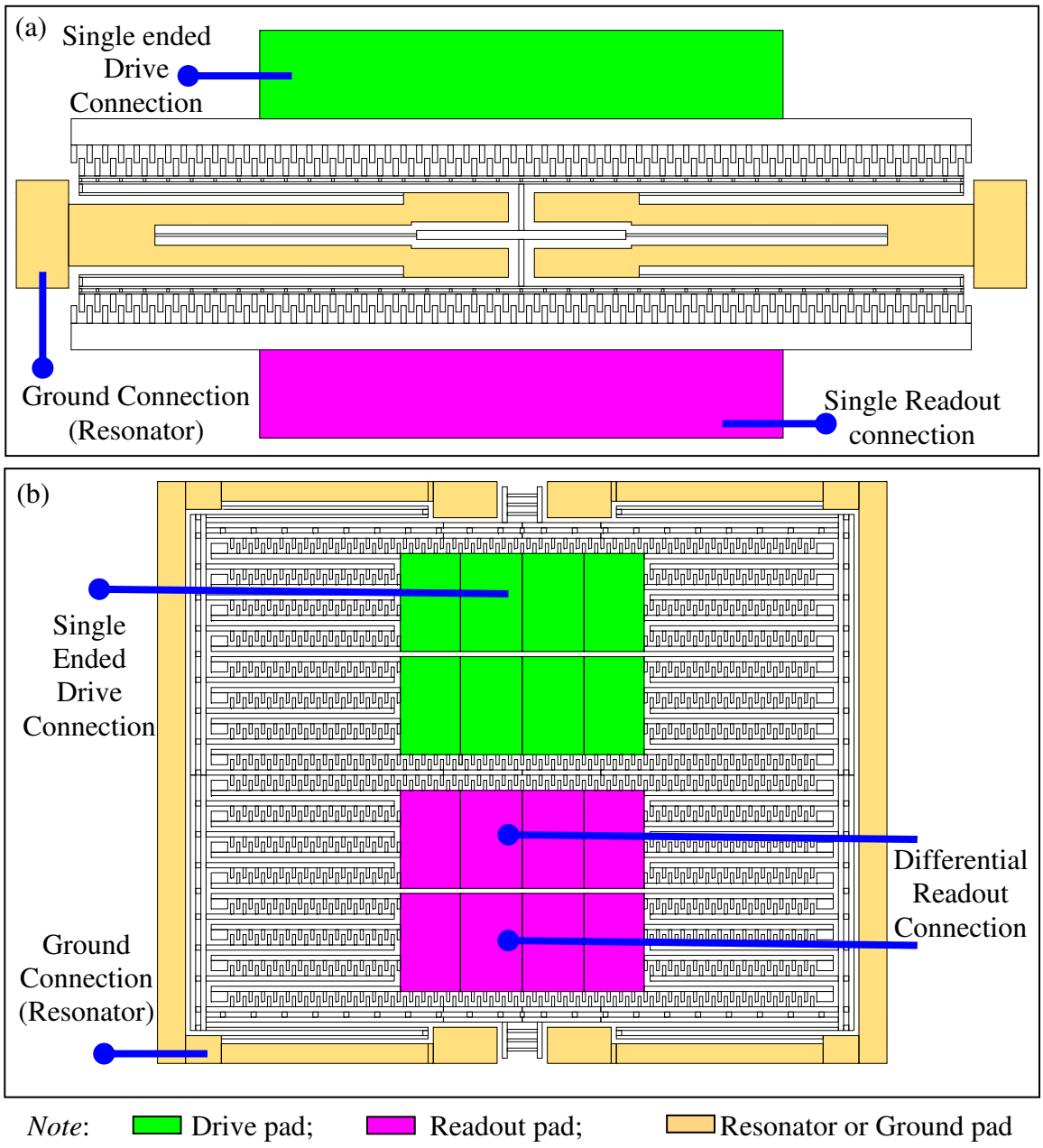

Figure 7.4 (a) Single ended drive – single readout measurement scheme for the fixed-fixed beam resonator; (b) Single ended drive – differential readout measurement scheme for the integrated comb drive resonator

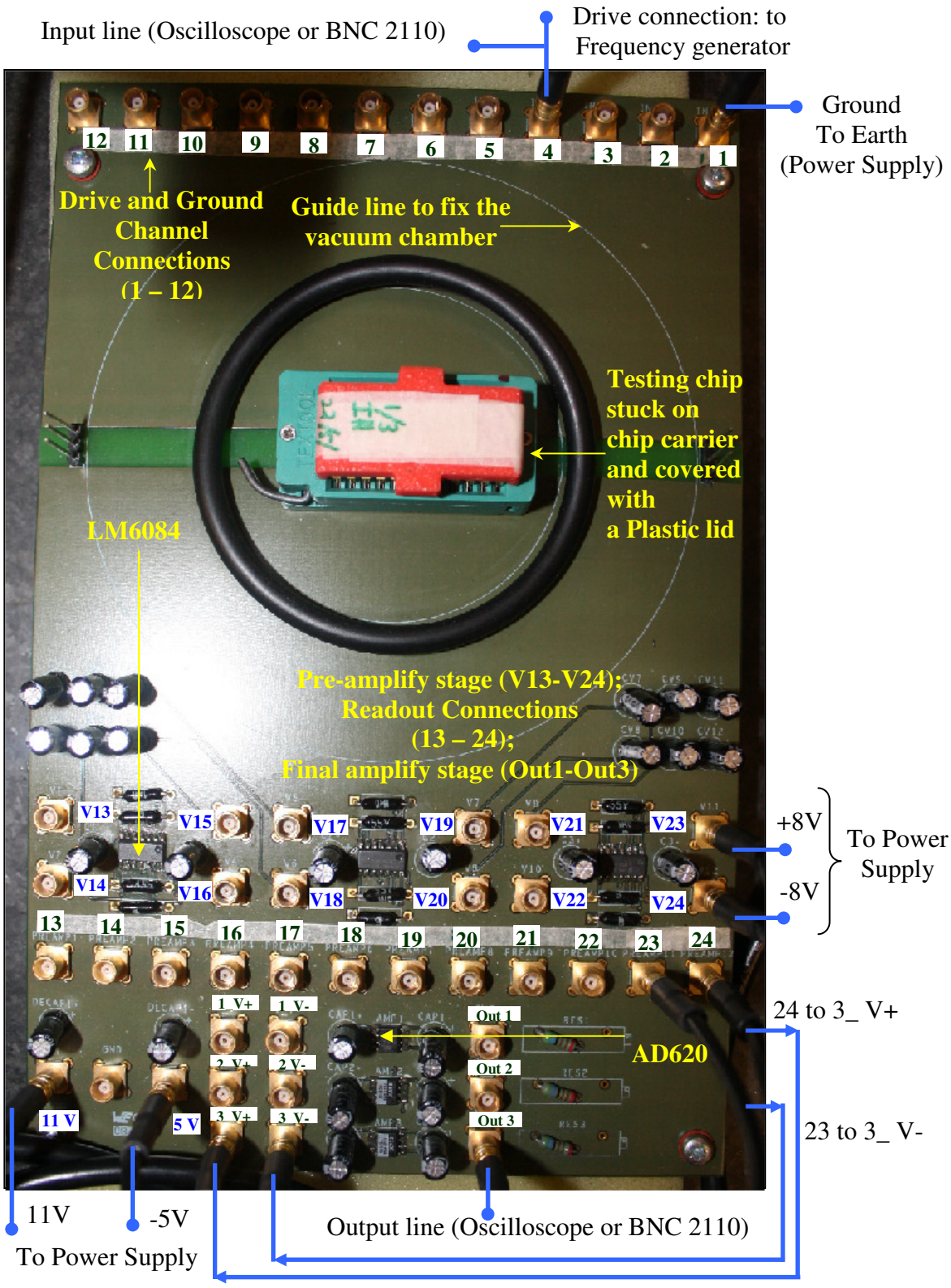

Figure 7.5 Testing chip mounted on electronic testing board; and example of wiring connections for single ended drive and differential readout scheme (drive pin: 4, ground pin: 1, readout pin: 23 and 24, output line: Out3)

Figure 7.5 details the testing board, which consists of the drive and ground channel connections (channel 1 to 12), clamping socket to mount the testing sample, marking line to fix the vacuum chamber, two power supply connections to feed the amplifiers (11V and -5V supply voltage), and the readout channel connections (channel 13 to 24). The output signal processing system comprises Transimpedance amplifiers (LM6084) and Instrumentation amplifiers (AD620).

As presented earlier in Chapter 3 (Section 3.2.1) and Figure 7.3, due to the different voltages fed to the fixed driven comb structure and the grounded resonator, an electrostatic force was generated to vibrate the resonator. The movement of the resonator produces an output signal in the form of current (i_{out}) at the readout channel. To convert the output current (i_{out}) to a useful voltage, ±8V [3]DC sense voltage (V_{DCs}) was fed to the Transimpedance amplifier as illustrated in Figure 7.6. Then the signal is further amplified by the instrumentation amplifiers, AD620.

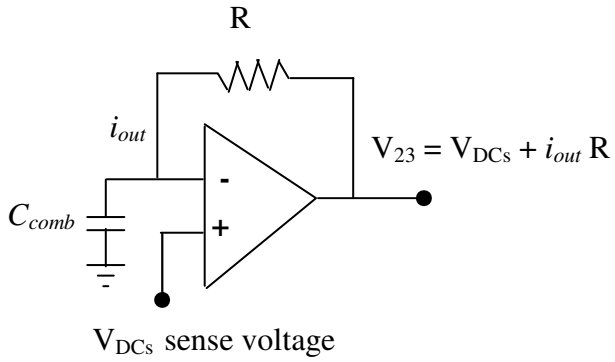

Figure 7.6 The schematic of the Transimpedance amplifier used to convert the output signal of the measured structure (i_{out}) to a useful readout voltage (example for channel 23)

[3] Note that the 8V detection bias will slightly affect the effective resonator spring constant ($K_E = dF_{el}/ dy = - V^2C_o/y_o$). For example with a static capacitance of 1.87 x10^{-13} F (C_o) at an initial displacement of 5µm (y_o), the change of the effective spring constant of a particular resonator is - 0.4787 N/m when the 8V DC voltage is applied to the resonator. The change will likely impact the eigenmodes of the CMRA. To ensure a consistent measurement result it is important to maintain the DC bias voltage for all the device measurement.

Twelve channels (V13 – V24) configured on the testing board (Figure 7.5) were used to supply the V_{DCs} sense voltage to the Transimpedance amplifier for the twelve readout channels (4 x three LM6084 on the testing board). When the differential readout scheme is used to measure the output signal of the structure, the output of V+ and V- channels (two connections) of the Transimpedance amplifier were fed to the Instrumentation amplifier, AD620. If the single readout connection scheme is used, only the output of V+ was fed to the positive channel of the AD620 and V_{DCs} to the negative channel of the amplifier. Figure 7.7 compares the input and output signal of the AD620 amplifier for the single and differential readout measurement scheme. Note that G is gain of the instrumentation amplifier (AD620), dc/dy is the change of capacitance when the resonator moves and dy/dt is the velocity of the resonator.

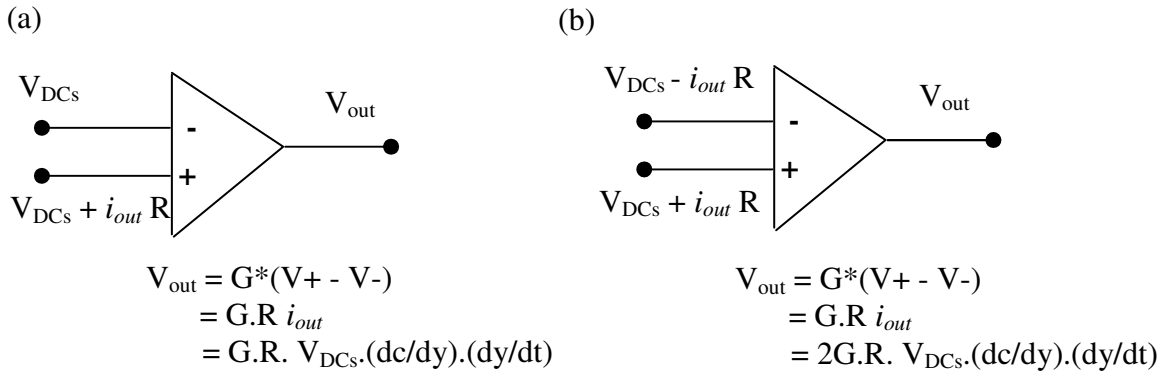

Figure 7.7 The input voltage and output of the AD620 amplifier: (a) Single readout measurement scheme; (b) Differential readout measurement scheme

7.4 Frequency Response Measurement

7.4.1 Testing Procedures

1. After wire bonding the structure and chip connectivity was checked in case there were short circuits between the 24 pins of the chip carrier.

2. If no short circuit was present, the chip carrier was mounted in the clamping socket on the testing board. All the connections on the testing board and overall testing setup were checked (refer to Figure 7.5 as examples of connections on the testing board):

- A driven line (e.g. channel 4) was connected to the frequency generator and an oscilloscope (manual frequency sweeping) or BNC 2110 connector block (automatic frequency sweeping). All grounds and resonator line (e.g. channel 1) were connected to the earth.
- The readout channels (e.g. V23 and V24) were supplied with ±8V DC sense voltage.
- The outputs of pre-amplify stages (channel 23 and 24) were further amplified by connecting to a final amplify stage channels (e.g. 3_V+ and 3_V-).
- The final output line (i.e. Out3) was connected to the oscilloscope (for manual frequency sweeping) or to the BNC2110 connector block (for automatic sweeping). (Note: any lines connected to the substrate of the structure were grounded (to reduce an electrical effect on the measured Si device layer).

3. The personal computer, frequency generator, digital pressure indicator and vacuum chamber motor were switched on.
4. When a light indicator of the vacuum system turns to active mode, the vacuum chamber was fixed onto the testing board. Then, the vacuum system pump was switched on. The air inside the vacuum chamber was released by turning the pressure regulator until the digital pressure indicator shows the pressure level at which the frequency response measurement will be done.
5. Manual frequency sweeping: the power supply unit was switched on. The Vpp voltage (V_{AC}) of the frequency generator was set in order to drive the measured structure. The frequency generator was manually swept through the range of natural frequencies of the

CMRA structure. The resonant frequency was observed on the oscilloscope when the sweeping frequency coincides with the natural frequency of the resonator and the peaks of the sinusoidal output wave become double (Figure 7.8). The range of the frequency bandwidth was noted (when the peaks of the sinusoidal output wave become double and back to the original condition).

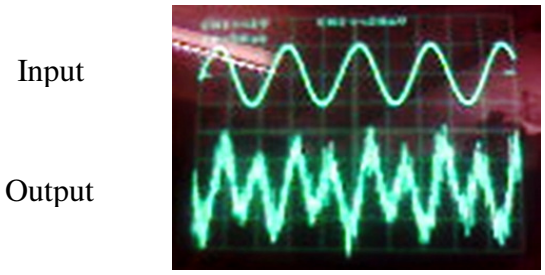

Figure 7.8 Resonant frequency observed on oscilloscope (output wave become double)

6. Automatic frequency sweeping: the input line and output line were connected to the BNC 2110 connector block. The sweeping parameters (Vpp driving voltage, range of sweeping frequency bandwidth and sweeping step, input and output frequency filters) were set on the LabVIEW SignalExpress software window. The frequency response measurement was started by clicking the 'Run Once' button on the menu bar of the LabVIEW window.

7.4.2 Overview of Testing Samples and Testing Conditions

Table 7-1 List of measured chips and details description of the structure on the chip

Chips	Structure Description
Chip1	A single comb drive resonator of the CMRA-v2
Chip2	Three similar single fixed-fixed beam resonators (singleR-v1)
Chip3,Chip4, Chip5	Three similar single comb drive-resonators (singleR-v2)
Chip6, Chip7	5 Constant Mass CMRA
Chip8, Chip9	5 Staggered Mass CMRA
Chip10, Chip11	5 Staggered Stiffness CMRA

As listed in Table 7-1, eleven chips which were in-house fabricated were measured which contained single and coupled resonators. Table 7-2 summarizes all the conducted tests and testing parameters for the eleven chips.

Table 7-2 Summary of conducted test for eleven chips

No	Conducted Test	Chips	Setting Parameter	
			Vacuum Pressure Level (Pa)	Vpp input voltage (V)
1	The effect of vacuum pressure level and Vpp input voltage on frequency response of the single resonator	Chip1	230, 36, 1.6, 0.73, 0.1	0.4
			0.1	0.1, 0.2, 0.3, 0.4, 0.5, 1, 2
2	Mass loading – frequency response effect on single resonator (7.6 x 10^{-12} kg perturbed mass)	Chip1	0.1	0.4
3	The effect of manufacturing variations on frequency response of the single resonators	Chip2	0.1	5
		Chip3	0.1	0.4
		Chip4	0.1	0.4
		Chip5	0.1	0.4
4	Frequency response of three unperturbed CMRA(s) structure: - 5 Constant Mass CMRA (Chip6 and 7) - 5 Staggered Mass CMRA (Chip 8 and 9) - 5 Staggered Stiffness CMRA (Chip10,11)	Chip6	0.1	2
		Chip7	0.1	2
		Chip8	0.1	2
		Chip9	0.1	2
		Chip10	0.1	2
		Chip11	0.1	2
5	Uniqueness and the effect of manufacturing variations on frequency response pattern of three perturbed CMRA(s) structure *(Note: after mass is perturbed separately at resonator 1 (R1) and resonator 5 (R5))*	Chip6	0.1	2
		Chip9	0.1	2
		Chip11	0.1	2
6	Reliability of frequency response pattern of single resonator and CMRA: Comparison between first and second measurement; second measurement was done after 49 days for single resonators (Chip4) and after 45 days for CMRA structure (Chip8)	Chip4	0.1	0.4
		Chip8	0.1	2

Six main tests were conducted in order to evaluate the performance of the CMRA and its singleton. Test no. 1, 2 and 3 were conducted to evaluate the performance of single resonators. Test no. 4, and 5 were carried out to evaluate the performance of the three CMRA(s) structures. Test no. 6 observed the reliability and stability of the frequency response pattern of single resonator and CMRA structure.

When measuring the CMRA structure, several options exist for the drive and readout point depending on the bonded structure. As discussed in Chapter 5, the selection of the drive or readout points will not affect the modal eigenfrequencies of the structure, only the response amplitude of the resonant frequencies will be different. However, the presence of the process variation may slightly modify the effective mass and stiffness of the coupled resonators or coupling springs. Driving or readout of CMRA at different points will produce a different amplitude response. In an extreme case, the response amplitude of the resonant peak may be very tiny and hard to be observed. To measure the expected 5 resonant peaks of the CMRA structures, measurements were taken by fixing the drive point to R1, R3 or R5 and the readout point either at R1 or R5 based on the bonded structure. Unless the resonant peaks were difficult to measure, the drive and readout point for particular CMRA was not changed to simplify the structure measurement.

7.5 Result and Discussion 1: Performance of a Single Resonator

7.5.1 Effect of Vacuum Pressure Level

Figure 7.9 presents the frequency response of the single comb-drive resonator at different air pressure levels. Table 7-3 summarizes the measurement result. Measuring the structure at different pressure levels slightly shifted the resonant frequency of the resonator. For example, comparing the measurement at 230 and 0.73 Pa, the shift of frequency is at a maximum of -

4.4 Hz (-0.03%). The shift of the frequency is considered small. However, measuring the structure at a high pressure level drastically decreased the response amplitude and increased the bandwidth of the measured frequency; hence reducing the Q factor of the resonator. Comparing the response amplitude at the two measured conditions (230 and 0.73 Pa), the reduction in amplitude is 95.6%. The decrease of the response amplitude will reduce the measurability of the frequency response of the measured structure. To ensure measurability of the frequency response pattern of the single or coupled resonators, all measurements were made at 0.1 Pa.

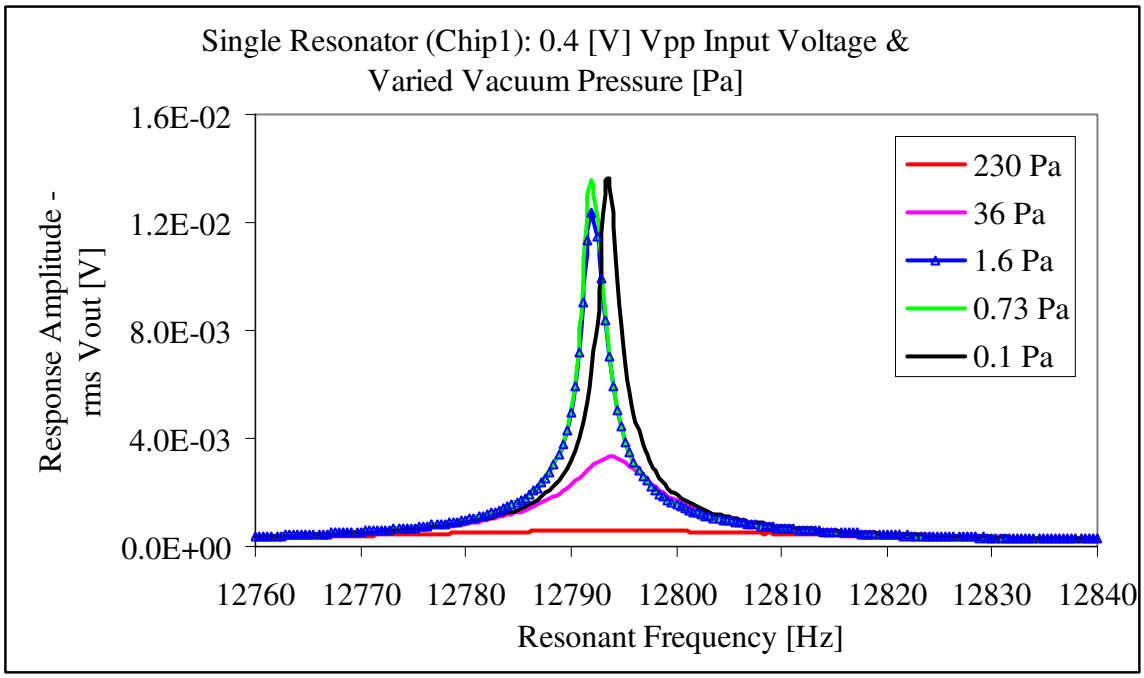

Figure 7.9 The effect of different vacuum pressure levels on frequency response pattern of single resonator

Table 7-3 Summary of the measurement results in Figure 7.9

Vacuum Pressure Level [Pa]	Resonant Frequency [Hz]	Response Amplitude [V]
230	12796.4	5.95×10^{-4}
36	12794.0	3.31×10^{-3}
1.6	12792.0	1.24×10^{-2}
0.73	12792.0	1.35×10^{-2}
0.1	12793.6	1.36×10^{-2}

7.5.2 Effect of Vpp Driving Voltage

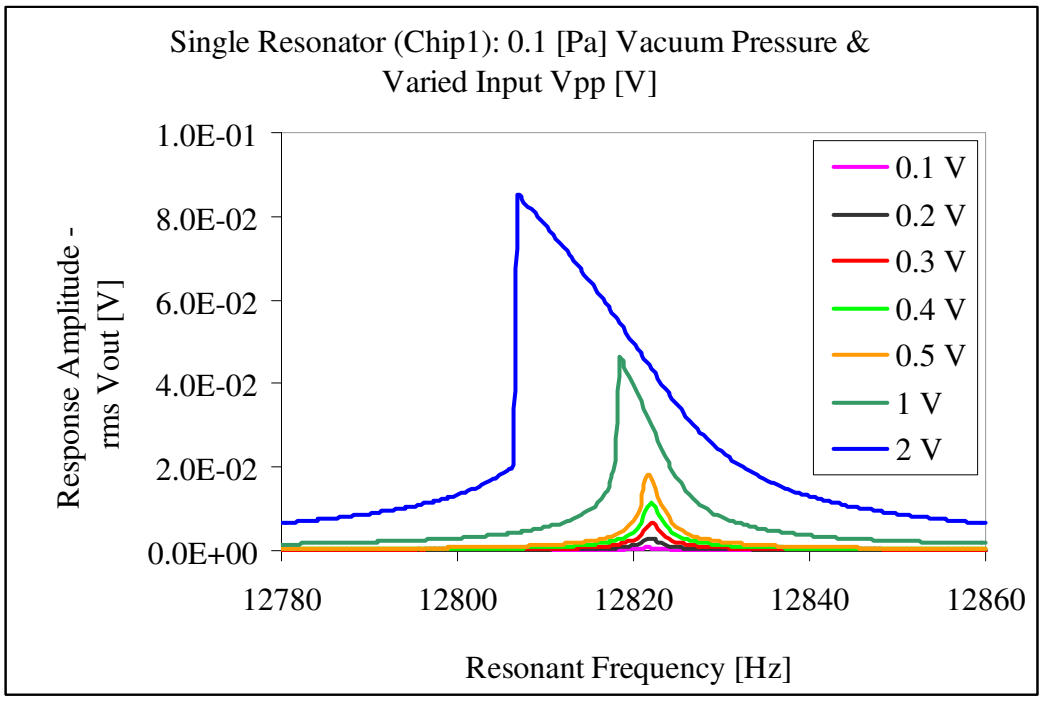

Figure 7.10 The effect of different Vpp input voltage on frequency response pattern of single resonator

Table 7-4 Summary of the measurement results in Figure 7.10

Input voltage [V]	Resonant Frequency [Hz]	Response Amplitude [V]
0.1	12821.6	7.24×10^{-4}
0.2	12822.0	2.91×10^{-3}
0.3	12822.0	6.54×10^{-3}
0.4	12822.0	1.17×10^{-2}
0.5	12821.6	1.84×10^{-2}
1	12818.4	4.63×10^{-2}
2	12806.8	8.53×10^{-2}

Figure 7.10 displays the frequency response of the comb-drive resonator when measured at different drive voltages (Vpp). Table 7-4 lists the measured data. At high input voltage (e.g. 2V) the response amplitude of the A-F curve is considerable and the curve is nonlinear.

Reducing the input voltage (e.g. 0.4V) reduced the response amplitude to 1.17 x 10^{-2}V, which is 7 times lower than the amplitude at 2V. Then the measured frequency response curve is linear.

The cause of the nonlinearity is the electrical spring softening due to the nonlinear change of capacitance at high input voltage. Equation 3-9 (Section 3.5.2) for the electrostatic force generated in the resonator (F_{el} = ½ . $\delta c/\delta y.V^2$), Equation 3-10 and 3-11 further can explain the nonlinear pattern of the measured curve. At high input voltage, the electrostatic force (F_{el}) increases and so displaces the resonator. The increase of the resonator displacement, increases the overlapping distance between the moving and fixed fingers, which raises rate of the generated capacitance in the structure to nonlinear range (Figure 5.10, Section 5.3.4 (generated capacitance for the comb-drive resonator)). With a nonlinear response, the resonant frequency is hard to detect due to the skew of the response curve. Compared to measurements at 0.4V Vpp, at 2V Vpp the shift of the frequency peak is -15.2 Hz (-0.12%); note that the minus sign indicates the frequency is decreased. To ensure a consistent and linear frequency response pattern all the measurement of the single comb drive resonators and the coupled resonators were done at 0.4V Vpp and 2V Vpp respectively. Note that a phase measurement may be used as an alternative to monitor the nonlinear frequency response curve.

7.5.3 Effect of Manufacturing Process Variation on a Single Resonator

Figure 7.11 shows the frequency response measurement results of three similar single resonators from Chip2, Chip3, Chip4 and Chip5. Table 7-5 summarizes the measurement and data analysis of the result. As can be observed, the measured three resonators on each chip display different frequency responses. The process variation has significantly modified the geometrical dimension of the fabricated resonators and altered the response amplitude and

resonant frequency of each resonator. If we consider the shift of the resonant frequency of the comb-drive resonator (Chip3, Chip4 and Chip5), all the measured frequency were larger than the designed structure (12857.3Hz). The resonator R-1 from Chip3 showed the highest frequency shift (14076.4 Hz, 9.48%).

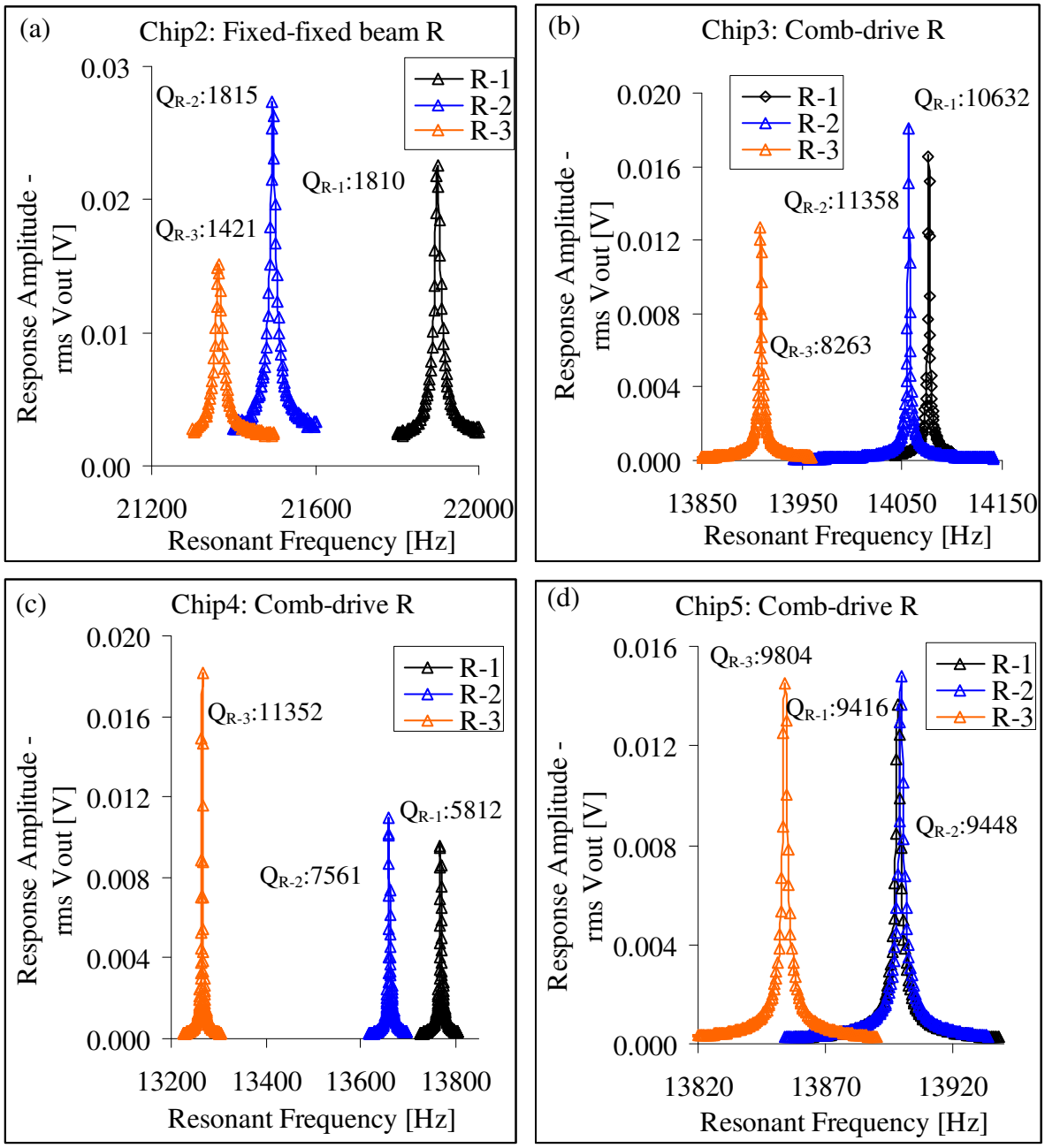

Figure 7.11 Measurement result: (a) three similar fixed-fixed beam resonator fabricated on Chip2; (b), (c) and (d) three similar integrated comb drive-resonator fabricated on Chip3, Chip4 and Chip5

Table 7-5 Summary and analysis of results in Figure 7.11

Peak of Resonant Frequency [Hz] (Response Amplitude [V]) * Percent of frequency shift compared to design value: (Chip2): **22127.1** [Hz]; (Chip3, 4, 5): **12857.3** [Hz] ** Frequency shift difference (%): resonator frequency shift (%) - minimum frequency shift (%) on respective chip			
Chip	(R-1)	(R-2)	(R-3)
Chip2	21900.0Hz (2.25 x 10^{-2}V) * -1.03% -	21496.0Hz (2.74 x 10^{-2}V) * -2.85% ** 1.62%	21364.0Hz (1.51 x 10^{-2}V) * -3.45% ** 2.42%
Chip3	14076.4Hz (1.66 x 10^{-2}V) * 9.48% ** 1.3%	14056.5Hz (1.81 x 10^{-2}V) * 9.33% ** 1.15%	13908.8Hz (1.27 x 10^{-2}V) * 8.18% -
Chip4	13769.2Hz (9.52 x 10^{-3}V) * 7.09% ** 3.91%	13660.4Hz (1.09 x 10^{-2}V) * 6.25% ** 3.07%	13265.6Hz (1.82 x 10^{-2}V) * 3.18% -
Chip5	13898.4Hz (1.37 x 10^{-2}V) * 8.10% ** 0.35%	13899.6Hz (1.48 x 10^{-2}V) * 8.11% ** 0.36%	13854.0Hz (1.45 x 10^{-2}V) * 7.75% -

The increase of the measured frequency of the comb drive resonator can be explained by comparing to the measured geometrical dimension of the comb drive resonator (INTEGRAM chip) and the estimation of impact of process variation on a single comb-drive resonator (Appendix G). For particular INTEGRAM resonators, the process variation has increased the width of the anchor spring and width of the comb finger at about 43.3% and 41.1% respectively (Section 5.6.1, Table 5-10). By considering a 10% similar increase of width of the comb finger (b_f) and the anchor spring width (b_{ASP}), the stiffness of the comb-drive resonator increases about 33.1% compared to 3.2% increase in resonator mass (Appendix G, Table G-1). The considerable increase in stiffness compared to the mass, will increase the

measured frequency of the comb-drive resonator if we consider the fabricated structure is oversized. From the sample measurements and data analysis of the manufacturing tolerances of the in-house fabricated chip (refer to Appendix H (Table H-1, Chip3)), it has been confirmed that the structures on Chip3 were oversized; the increase of the width of the anchor springs (b_{ASP}) and fingers (b_f) were 13.64% and 12.39% respectively. If the maximum variation on each chip is calculated based on differences between the maximum and minimum frequency shift of the resonator; the highest variation for each chip was 2.42% (Chip2), 1.3% (Chip3), 3.91% (Chip4) and 0.36% (Chip5).

Due to the different resonant frequency and response amplitude, each resonator has different quality factor. The highest quality factor for the fixed-fixed beam resonator and integrated comb-drive resonator was 1818 and 11358 respectively. The lower Q factor of the fixed-fixed beam is expected due to the mass and the structure design of the resonator ($Q = m\omega_n/c$, Equation 3-8 (Chapter 3)). The mass (m) and frequency of the fixed-fixed beam (ω_n) which was 8 times smaller than the comb drive resonator (designed value) lowered its Q factor around 6 times. Furthermore, the lower Q of the fixed-fixed beam resonator is expected due to the loss of resonator energy due to strain at the connection between beam and anchor pad (clamping force) to support the resonator [76, 164].

7.5.4 Mass Loading Frequency Response Effect of a Single Resonator

Figure 7.12 shows the frequency response of the single comb drive resonator before and after 7.6×10^{-12}kg platinum was deposited on the structure. The added mass reduced the resonant frequency and the response amplitude of the resonator by 0.031% and 55.5% respectively. The perturbation mass significantly increases the effective mass of the resonator (m) compared to resonator stiffness (k). Hence, reducing the frequency of the resonator, ω (ω =

$(k/m)^{1/2}$) and the resonant amplitude, x ($x = F/(k-m\omega^2)$). The change of the measured response was compared to the lumped mass analysis of the designed comb-drive resonator (Figure 7.13). At no damping condition, adding 7.6 x 10^{-12}kg mass decreased 0.09% the resonant frequency and 60.22% response amplitude. Considering some effect of process variations, the change of the measured frequency response of the perturbed resonator is comparable to the simulated response. The reduction of the Q factor is expected due to the effect of aluminium metallization coated on the surface of the resonators which increases the viscous damping in vacuum [165].

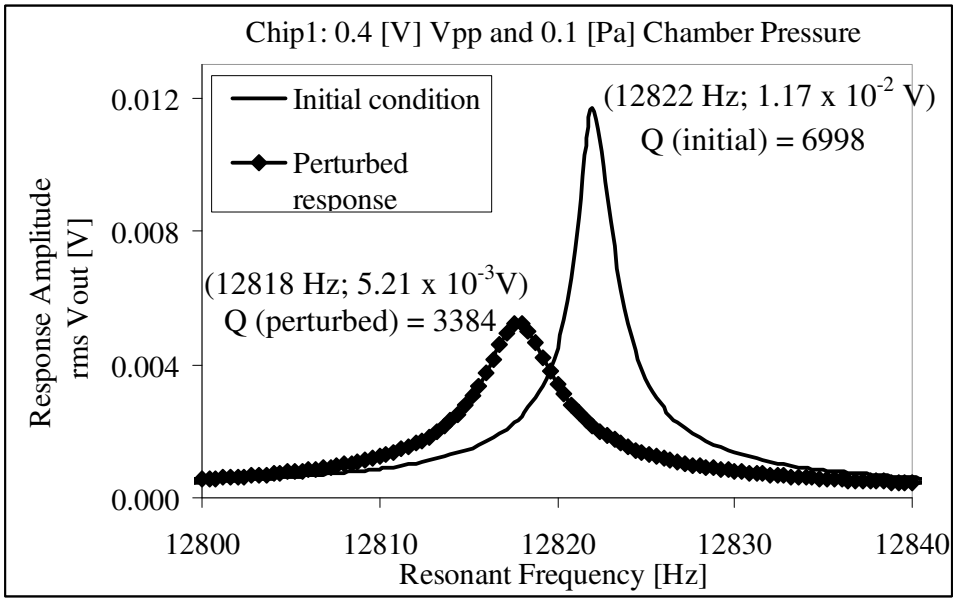

Figure 7.12 Measurement result: mass loading frequency response effect of single comb-drive resonator

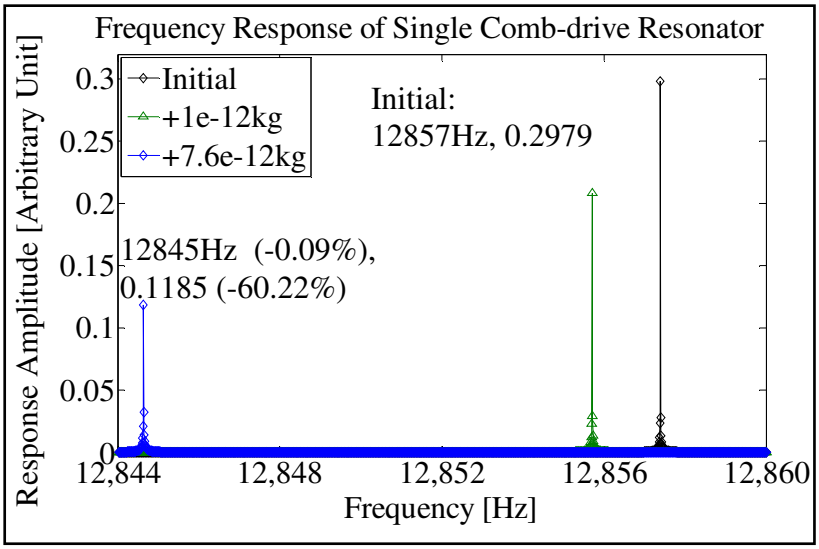

Figure 7.13 Frequency response of unperturbed and perturbed comb-drive resonator (Lumped mass analysis)

7.6 Result and Discussion 2: Performance of CMRA

The performance of the three CMRA(s) was evaluated by comparing the frequency response of the designed and the fabricated structure. The uniqueness of frequency response pattern of the CMRA(s) sensor structure was examined by comparing the response of unperturbed and perturbed structure (after platinum mass was deposited at R1 and R5 separately). The effect of manufacturing variation was determined by observing discrepancies between the measured and simulated frequency response. The inverse eigenvalue analysis was used to estimate the mass change pattern of the perturbed staggered CMRA(s) and to confirm the stability of the eigenvectors of the three CMRA(s).

7.6.1 Constant Mass CMRA

7.6.1.1 Frequency Response of the Unperturbed Structure and the Effect of Process Variation

Figure 7.14 and 7.15 present and compare the simulated frequency response and the measured response of the Constant Mass CMRA fabricated on Chip6 and Chip7 respectively. Table 7-6 summarizes the measured and analyzed data for the structures. For both chips (except for the

mode 5, Chip6), the five measured modal eigenfrequencies were lower than the designed frequencies which were simulated using FEA. The frequency bandwidth between the first and fifth resonant peak for the structures was 650.8Hz (Chip6) and 508.8Hz (Chip7) compared to 467.3Hz for the simulated response.

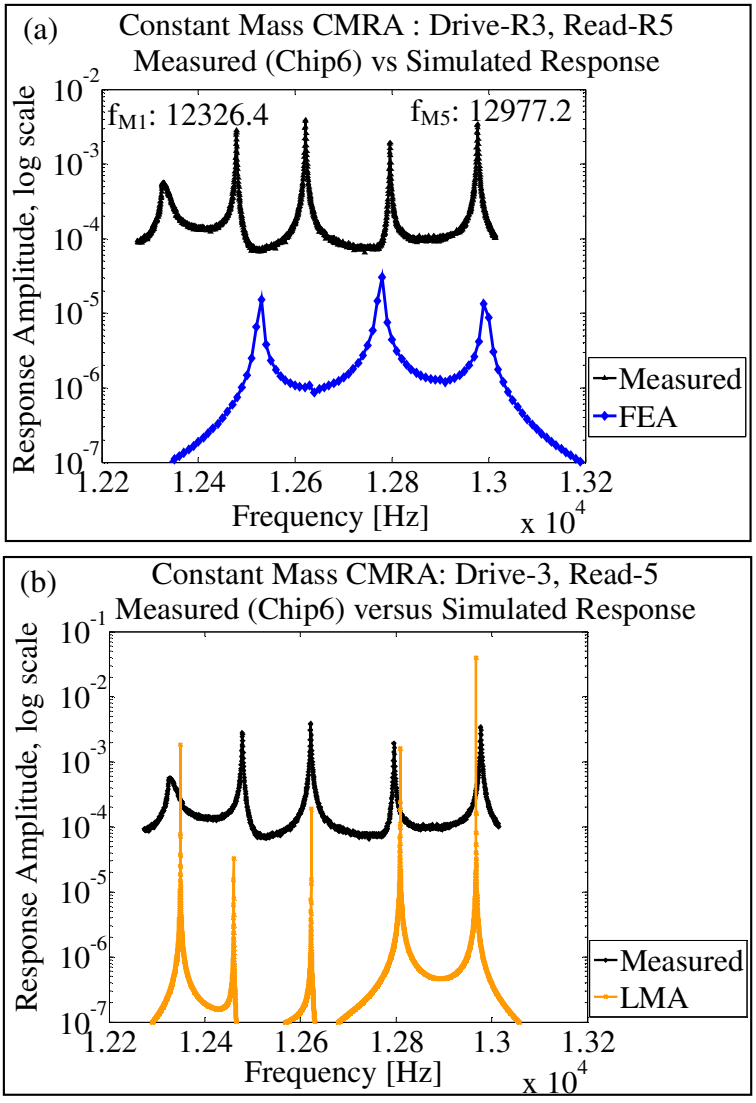

Figure 7.14 Comparison: frequency response of fabricated Constant Mass CMRA (Chip6) and simulated response; (a) Simulated response using FEA; (b) Simulated response at varied resonators stiffness and mass using LMA

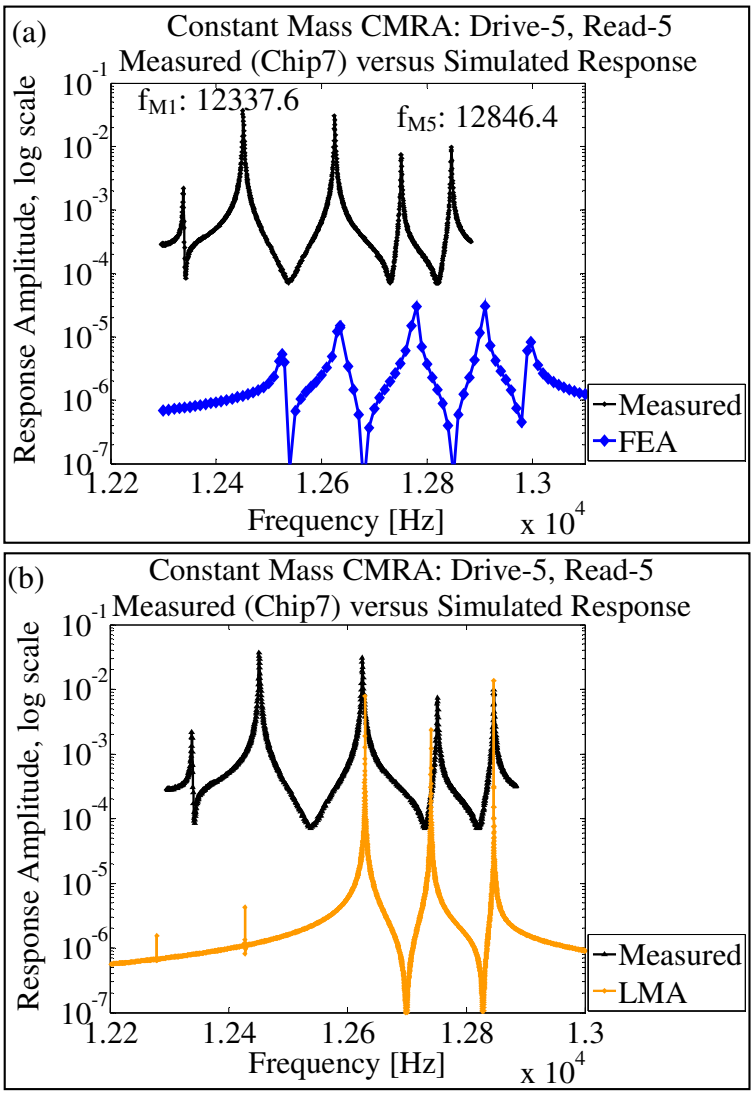

Figure 7.15 Comparison: frequency response of fabricated Constant Mass CMRA (Chip7) and simulated response; (a) Simulated response using FEA (b) Simulated response at varied resonators mass and coupling stiffness using LMA

Considering the 5 Constant Mass CMRA which is driven at R3 and readout at R5 (Chip6); only 3 resonant frequency peaks (mode 1, 3 and 5) are expected to be observed due to the constant and symmetrical designed mass of the resonators (see Section 5.3.2). However, the measurement results of the structure on Chip6 (Figure 7.14 (a)) showed 5 resonant peaks when the structure was driven at R3 and readout at R5. The process variation has modified the mass and stiffness of the coupled structures. Hence, the structure is no longer symmetric.

The effect of process variations can be explained by referring to the SEM measurement of the geometrical dimension of the comb drive resonator from the INTEGRAM chip (as discussed in Chapter 5 and Section 7.5.3); the decrease in the measured frequencies (Chip6 and Chip7, Table 7-6) may be expected due to the effect of structure undersized (i.e. some resonators) which decreases the mass and stiffness of the coupled resonators. Considering at 2.5% decrease in the width of the resonator anchor spring (b_{ASP}) and width of the comb fingers (b_f), the approximate decrease of the comb-drive resonator mass and stiffness is 0.8% and 7.31% respectively (Appendix G, Table G-1). The change of the mass and stiffness decreases the resonator frequency around 3.34%.

Table 7-6 Summary and data analysis of unperturbed Constant Mass CMRA (Figure 7.14 and 7.15)

Chips/ Analysis	[m]Measured Frequencies [Hz] ; (Response Amplitude, rms V_{out} [V]) [d] Designed frequencies (FEA) * Percent (%) of modal frequency shift compared to FEA value **( ) Normalized % of modal frequency shift (over the maximum value) [v]Variation (LMA)				
	Mode1	Mode2	Mode3	Mode4	Mode5
Chip 6 Drive-R3/ Read-R5	[m]12326.4 (5.62×10^{-4})	[m]12478.4 (2.83×10^{-3})	[m]12621.2 (3.92×10^{-3})	[m]12796 (1.93×10^{-3})	[m]12977.2 (3.43×10^{-3})
	[d]12526.8	-	[d]12776.8	-	[d]12994.1
	*-1.6% ** (-1)		*-1.22% ** (-0.76)		*-0.13%; ** (-0.08)
	[v]12349	[v]12460	[v]12622	[v]12814	[v]12967
Chip7 Drive-R5 Read-R5	[m]12337.6 (2.18×10^{-3})	[m]12450.4 (3.65×10^{-2})	[m]12624.4 (3.05×10^{-2})	[m]12751.2 (7.35×10^{-3})	[m]12846.4 (9.73×10^{-3})
	[d]12526.8	[d]12635.7	[d]12776.8	[d]12907.1	[d]12994.1
	*-1.51% ** (-1)	*-1.47% ** (-0.97)	*-1.19% ** (-0.79)	*-1.21% ** (-0.8)	*-1.14% ** (-0.76)
	[v]12284	[v]12432	[v]12625	[v]12737	[v]12842

The same effect of the process variation was considered on the fabricated Constant Mass CMRA (Chip6) and the lumped mass analysis (LMA) were performed to quantify the effect

of the manufacturing variation. As shown in Figure 7.14(b), the analysis produced 5 resonant peaks, when the mass of the 5 constant coupled resonators (R1, R2, R3, R4 and R5) was varied by -0.71%, -0.9%, -0.48%, -1.22% and 0.03% respectively. An average error between the 5 estimated modal eigenfrequencies and the measured frequencies was 0.11% (Table 7-6).

Figure 7.15(b) shows the LMA result of the simulated response for the 5 Constant Mass CMRA on Chip7 when the mass of the resonators were varied by -1.06% (R1), -1.22% (R2), and -0.48% (R3, R4, and R5) and stiffness of the 4 constant coupling springs were changed from 0.2495N/m to 0.22, 0.24,0.20 and 0.23N/m. As can be observed the third and the last modal frequencies are closely fit to the measured response compared to the modal frequencies 1, 2 and 4. The average errors between the 5 estimated and measured modal eigenfrequencies was 0.15% (Table 7-6).

From the measured and simulated modal eigenfrequencies of the CMRA on Chip6 and 7, we can emphasize that the process variation has significantly changed the mass of the coupled resonators. If the structure is to be used as a sensor, it is important to exactly quantify the change of the resonator mass of the fabricated structure; so that any absorbed mass onto each resonator can be determined accurately. Optimization techniques such as Genetic Algorithm may be employed to further analyse and incorporate multi-parameters change of mass, stiffness and frequency response of the couple resonators [166-168] due to the effect of manufacturing variations.

7.6.1.2 Uniqueness of the Frequency Response - Constant Mass CMRA

Figure 7.16 compares the frequency response pattern of the Constant Mass CMRA structure when a mass was perturbed at R1 and R5 separately. For both perturbed conditions, a unique frequency response pattern were observed. Table 7-7 summarizes the measured data.

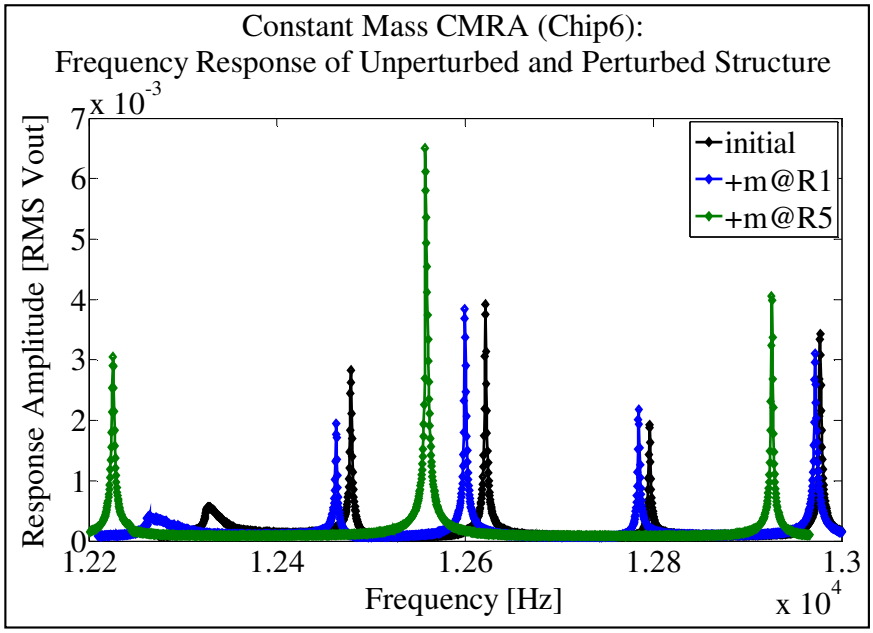

Figure 7.16 Comparison: frequency response pattern of unperturbed and perturbed Constant Mass CMRA

Table 7-7 Summary of measurement data (Figure 7.16) and data analysis

Measurement / Analysis Chip6	Modal Frequencies, f_M [Hz] (Response Amplitude, rms Vout [V]) Note:- Frequency and amplitude difference = perturbed value – initial value				
	Mode1	Mode2	Mode3	Mode4	Mode5
Initial	12326.4 (5.62×10^{-4})	12478.4 (2.83×10^{-3})	12621.2 (3.92×10^{-3})	12796 (1.93×10^{-3})	12977.2 (3.43×10^{-3})
+m at R1	12264.4 (4.25×10^{-4})	12462.8 (1.95×10^{-3})	12599.6 (3.84×10^{-3})	12784.4 (2.18×10^{-3})	12971.6 (3.11×10^{-3})
Frequency difference	-62 -0.50%	-15.6 -0.13%	-21.6 -0.17%	-11.6 -0.09%	-5.6 -0.04%
Amplitude difference	-1.37×10^{-4}, -24.38%	-8.8×10^{-4}, -31.1%	-8.0×10^{-5}, -2.04%	2.5×10^{-4}, 12.4%	-3.2×10^{-4}, -0.09%
+m at R5	12225.6 (3.05×10^{-3})	-	12577.2 (6.5×10^{-3})	-	12925.6 (4.04×10^{-3})
Frequency difference	-100.8 -0.82%	-	-44.0 -0.35%	-	-51.6 -0.4%
Amplitude difference	2.5×10^{-3} 444.8%	-	2.6×10^{-3} 66.33%	-	6.1×10^{-4} 17.78%

Table 7-8 Eigenvalue analysis result of Constant Mass CMRA (ideal condition) using lumped mass analysis (7.6 x 10^{-12} kg mass was perturbed at R1 and R5 separately)

Analysis	f(mode1)	f(mode2)	f(mode3)	f(mode4)	f(mode5)
Initial [Hz]	12857	12888	12968	13066	13144
+m at R1 [Hz]	12853	12882	12964	13064	13144
+m at R5 [Hz]	12853	12882	12964	13064	13144

The perturbation mass at R1 reduced the 5 unperturbed modal frequencies. The highest and lowest frequency shift occurred at mode1 and mode 5 (Table 7-7). After the deposited mass at R1 was milled off and 7.6 x 10^{-12}kg platinum mass was deposited at R5, the measurement result shows only 3 resonant peaks (mode1, 3 and 5). It can be claimed that, the variation in the milling process (i.e. a slight over milled the silicon material (see Section 6.8)), and the perturbation mass at R5 have balanced the masses discrepancy between R1 and R5; hence 3 resonant peaks were produced when driving and measuring the structure at R3 and R5.

The frequency response pattern of the measured structure may be further explained by referring to the eigenvalue analysis result of the designed structure (Table 7-8 and Section 5.4.2, Chapter 5). Due to the symmetrical designed mass of the resonators, similar resonant frequencies shift were produced when adding mass at R1 or R5. In contrast, the fabricated structure (Chip6) showed unique frequency response patterns when platinum mass was perturbed separately at R1 and R5. Hence, the process variation has evidently staggered some mass and stiffness of the designed constant mass coupled resonators as discussed in Section 7.6.1.1. The variation of the perturbation mass deposited at R1 and R5 also affected the frequency response pattern of the measured structure. As a result the Constant Mass CMRA (Chip6) produced a unique frequency response pattern for a single perturbed resonator sensor (i.e. for R1and R5).

7.6.1.3 Stability of the Structure Eigenvectors

To confirm the stability of system eigenvectors between the designed and the fabricated structure, the inverse eigenvalue analysis was considered (refer to Section 5.5). The designed eigenvectors and the measured eigenvalues were used to determine the mass change pattern of the unperturbed and perturbed structure. Figure 7.17(a) shows the inverse eigenvalue analysis result of the structure on Chip6 before and after a mass was perturbed at R1. As expected, the perturbed eigenvectors of the Constant Mass CMRA are always unstable compared to the unperturbed designed structure. Using the designed eigenvectors to estimate the mass change pattern of the resonators always cause errors; i.e. the estimated mass for R1 always mirrors the estimated mass at R5 when mass only perturbed at R1 (Figure 7.17(b)) . It is interesting to further research a new set of the unperturbed eigenvectors of the fabricated structure. We then can confirm how the process variation may naturally stabilize the structure eigenvectors; and estimate the mass change pattern of the perturbed structure using inverse eigenvalue analysis.

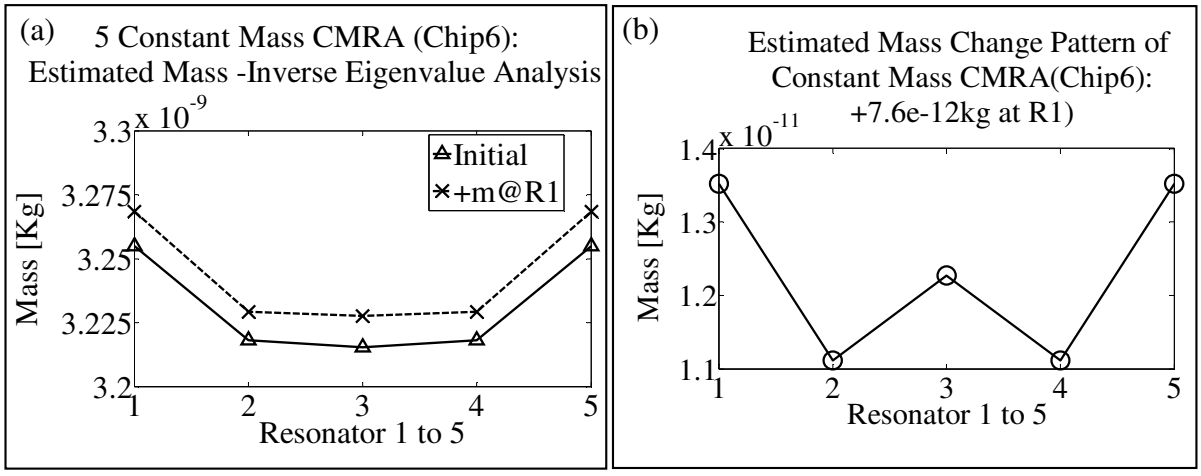

Figure 7.17 (a) Estimation of mass of unperturbed and perturbed Constant Mass CMRA (Chip6) using Inverse Eigenvalue Analysis; (b) Mass change pattern of structure (perturbed mass at R1)

7.6.2 Staggered Mass CMRA

7.6.2.1 Frequency Response of the Unperturbed Structure and the Effect of Process Variation

Figure 7.18 presents and compares the measured frequency response of the 5 Staggered Mass CMRA from Chip8 and Chip9 and the simulated response from FEA. The frequency bandwidth between the first and fifth peaks for both structures are 502.2Hz (Chip8) and 647.2Hz (Chip9); while the simulated modal frequencies bandwidth is 508.4Hz. Table 7-9 details the measured and simulated responses.

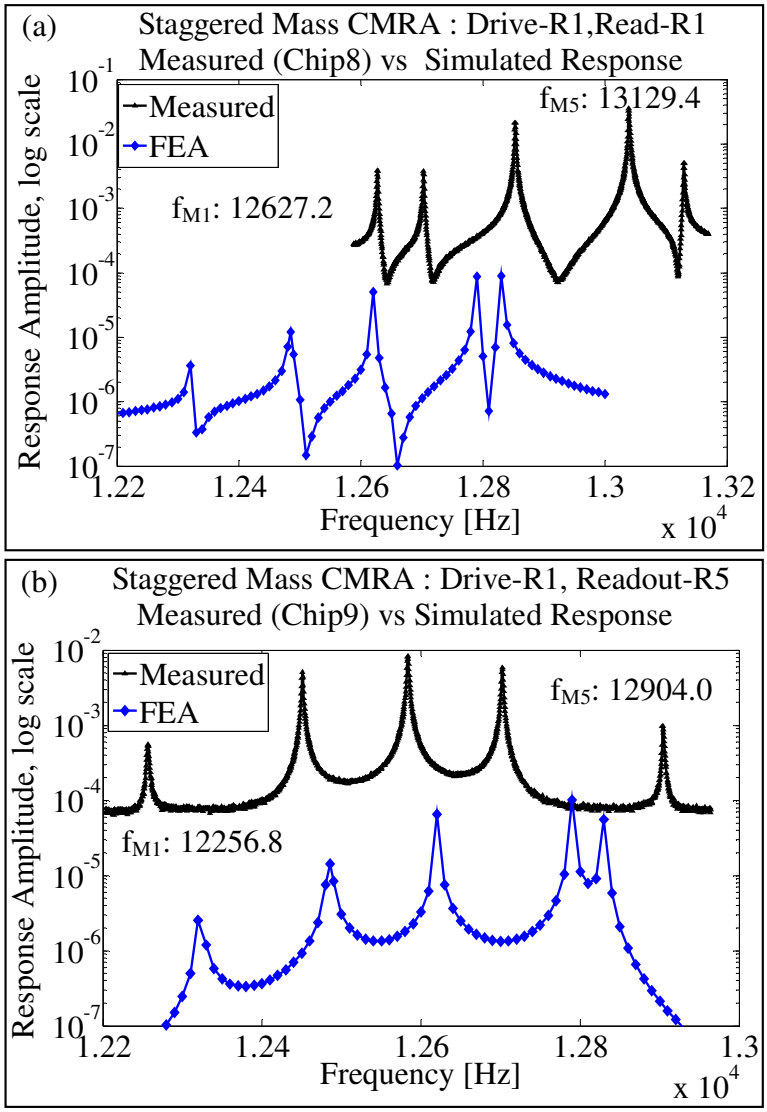

Figure 7.18 Comparison: frequency response of fabricated Staggered Mass CMRA and Simulated response (FEA); (a) Chip8; (b) Chip9

Considering the structure on Chip8 (Figure 7.18(a)), the measured 5 modal frequencies are higher compared to the simulated eigenfrequencies (Table 7-9). We may expect that the structure is slightly oversized; the increase in stiffness of the resonators is higher than the increase in mass of the structure, when the process variation altered the geometrical dimension of the structure. Therefore, the measured eigenfrequencies are higher than the simulated response. From the sample measurements and data analysis of the manufacturing tolerances on Chip8 have confirmed that the structures were oversized (refer to Appendix H (Table H-2)); the increase of the width of the anchor springs (b_{ASP}) and fingers (b_f) were 6.51% and 5.78% respectively. The variation has affected the Staggered Mass CMRA on Chip9 differently. The first four measured modal frequencies are lower compared to the simulated response, but the last modal frequency is higher compared to the simulated eigenfrequency. Hence, we may expect that some of the coupled structures are slightly undersized, which reduces the measured modal frequencies; and some resonators are oversized.

Table 7-9 Summary of the measurement results of unperturbed Staggered Mass CMRA

Chips	[m]Measured Frequencies [Hz] ; (Response Amplitude, rms V_{out} [V]) [d] Designed frequencies (FEA) * Percent (%) of modal frequency shift compared to FEA value **( ) Normalized % of modal frequency shift (over the maximum value)				
	Mode1	Mode2	Mode3	Mode4	Mode5
Chip8 Drive-R1/ Readout-R1	[m]12627.2 (3.9×10^{-3})	[m]12702.8 (3.81×10^{-3})	[m]12852.8 (2.13×10^{-2})	[m]13038.8 (3.51×10^{-2})	[m]13129.4 (5.06×10^{-3})
	[d] 12322.9	[d] 12485.1	[d] 12621.0	[d] 12789.0	[d] 12831.3
	* 2.47% **(1)	* 1.74% **(0.70)	*1.84% **(0.74)	* 1.95% **(0.79)	* 2.32% **(0.94)
Chip9 Drive-R1/ Readout-R5	[m]12256.8 (5.57×10^{-4})	[m]12451.2 (5.11×10^{-3})	[m]12583.6 (8.23×10^{-3})	[m]12702.0 (5.88×10^{-3})	[m]12904.0 (9.81×10^{-4})
	[d] 12322.9	[d] 12485.1	[d] 12621.0	[d] 12789.0	[d] 12831.3
	* -0.54% **(-0.79)	* -0.27% **(-0.40)	* -0.3% **(-0.44)	* -0.68% **(-1)	* 0.57% **(0.84)

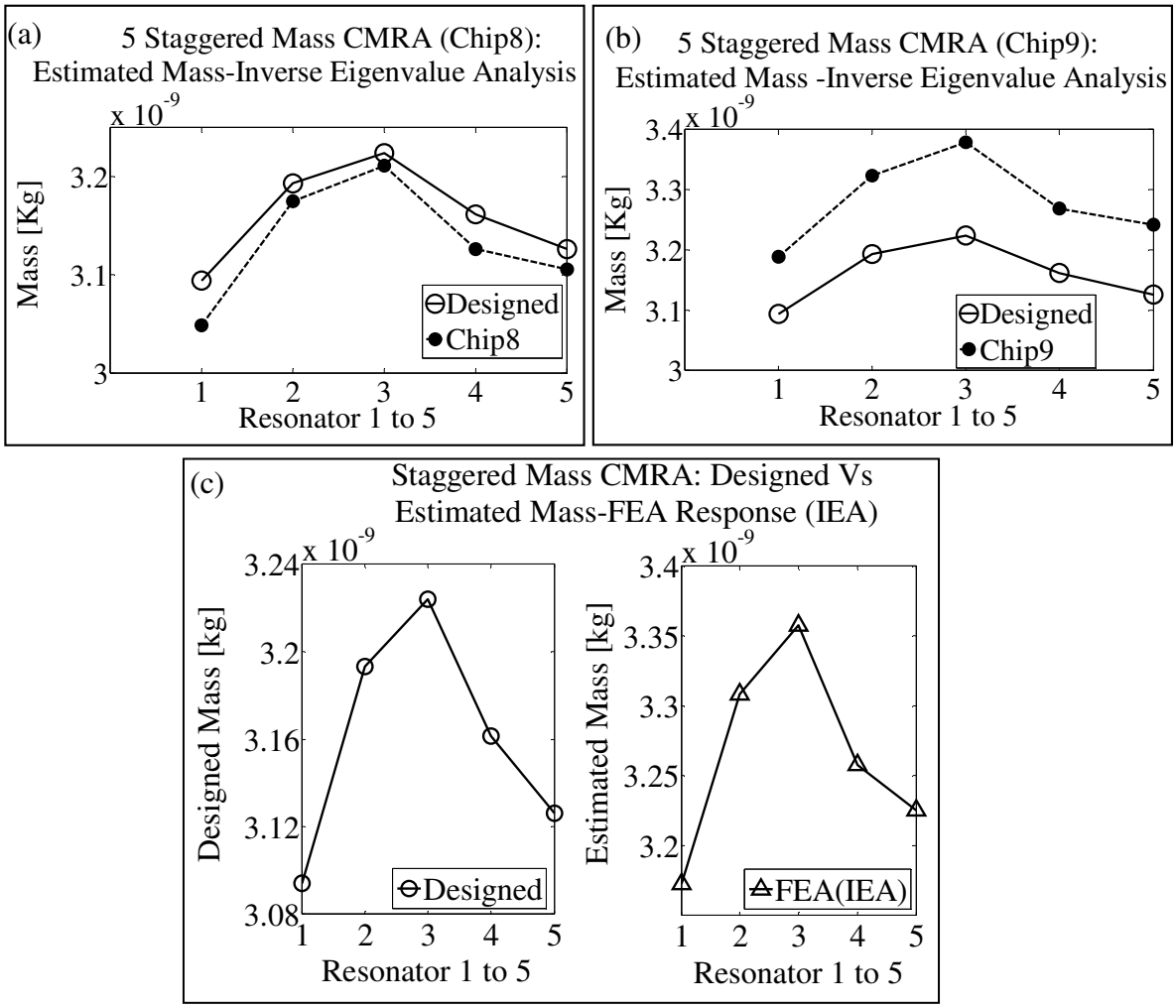

Figure 7.19 Comparison: designed mass and estimated mass of Staggered Mass resonators (using inverse eigenvalue analysis); (a) Chip8; (b) Chip9; (c) Designed mass and estimated mass from the FEA simulated response

Table 7-10 Staggered Mass CMRA: comparison- designed mass and estimated mass of the fabricated structure using inverse eigenvalue analysis

Resonator(R)	R1	R2	R3	R4	R5
Designed Mass nanokg]	3.0941	3.1932	3.2241	3.1616	3.1263
Chip8: Estimated Mass [nanokg]	3.049 (-1.46%)	3.175 (-0.57%)	3.211 (-0.41%)	3.127 (-1.09%)	3.106 (-0.65%)
Chip9:Estimated Mass: [nanokg]	3.189 (3.07%)	3.324 (4.10%)	3.379 (4.80%)	3.269 (3.40%)	3.242 (3.70%)

The discrepancies between the fabricated and the designed structure was further analysed by considering the inverse eigenvalue analysis (IEA) to approximately quantify the mass change

of the fabricated coupled resonators. Figure 7.19 displays the analysis result and Table 7-10 summarizes the data. By assuming a small change in the stiffness of the resonator, the estimated mass for the 5 resonators on Chip8 are lower than the designed mass (Figure 7.19(a)). The maximum mass change is -1.46% for R1. While the estimated masses for the structure on Chip9 are higher than the designed mass, with the maximum mass change is 4.80% for R3 (Figure 7.19(b)). Figure 7.19(c) shows the comparison between the designed mass of the coupled resonators and the estimated mass (using IEA) of the FEA simulated response (see Figure 7.18(a)). Considering the differences of the resonator mass in Figure 7.19(c); and comparing between the modal frequency bandwidth for the structure on Chip8 (502.2Hz), Chip9 (647.2Hz) and the simulated response (508.4Hz), the estimated masses for both fabricated structure is considered sensible at no or small change in the resonator stiffness.

alculating the differences between the maximum and minimum change of mass; the maximum mass variation estimated for both structure are 1.05% (Chip8) and 1.73% (Chip9). As exemplified by the Chip8 and Chip9, the manufacturing variation may affect the fabricated CMRA differently. Therefore, a calibration is important for each fabricated CMRA to exactly quantify the change of the mass, before the structure can be used as a sensor.

7.6.2.2 Uniqueness of the Frequency Response - Staggered Mass CMRA

Figure 7.20 shows comparison of the frequency response pattern of the unperturbed Staggered Mass CMRA and after mass was perturbed at R1 and R5 separately. As can be observed, each single perturbed resonator (R1 and R5) produced a unique frequency response pattern to present a signature for that particular resonator sensor.

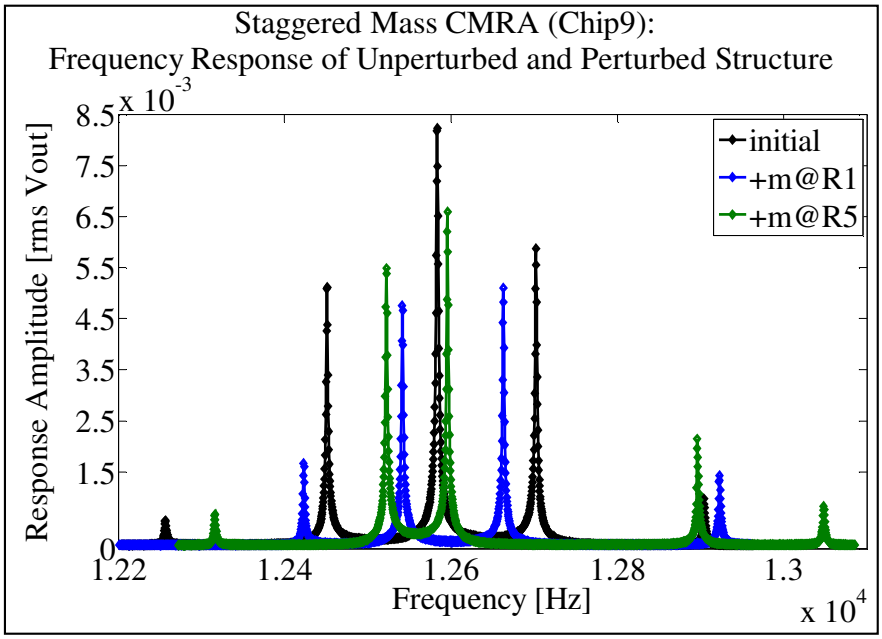

Figure 7.20 Comparison: frequency response pattern of unperturbed and perturbed Staggered Mass CMRA

Table 7-11 Summary of measurement result (Figure 7.20) and data analysis

Measurement / Analysis Chip9	Modal Frequencies, f_M [Hz] (Response Amplitude, rms Vout [V]) Note:- Frequency and amplitude difference = perturbed value –initial value				
	Mode1	Mode2	Mode3	Mode4	Mode5
Initial measurement	12256.8 (5.57×10^{-4})	12451.2 (5.11×10^{-3})	12583.6 (8.23×10^{-3})	12702.0 (5.88×10^{-3})	12904.0 (9.81×10^{-4})
+m at R1	-	12422.8 (1.67×10^{-3})	12541.6 (4.75×10^{-3})	12662.8 (5.1×10^{-3})	12922.8 (1.43×10^{-3})
Frequency difference	-	-28.4 -0.23%	-42 -0.33%	-39.2 -0.31%	18.8 0.15%
Amplitude difference	-	-3.44×10^{-3} -67.3%	-3.48×10^{-3} -42.3%	-7.8×10^{-4} -13.3%	4.49×10^{-4} 45.77%
+m at R5	12316.4 (6.76×10^{-4})	12522.4 (5.49×10^{-3})	12596.0 (6.6×10^{-3})	12896.0 (2.14×10^{-3})	13048.4 (8.3×10^{-4})
Frequency difference	59.6 0.49%	71.2 0.57%	12.4 0.1%	194 1.53%	144.4 1.1%
Amplitude difference	1.19×10^{-4} 21.4%	3.8×10^{-4} 7.4%	-1.63×10^{-3} -19.8%	-3.74×10^{-3} -63.6%	-1.51×10^{-4} -15.4%

When an approximate 7.6 x 10^{-12}kg mass was added at R1, the measured structure shows only 4 resonant peaks. The missing peak is associated to the response of mode 1. Considering the mode 4 with the least reduction in the response amplitude (7.8 x 10^{-4}V, Table 7-11); the mass is considerably large to reduce the response amplitude of the first resonant peak (i.e. mode 1) which is initially 5.57 x 10^{-4}V.

When the deposited mass at R1 was milled off and a mass was deposited at R5, five resonant peaks are observed. It can be argued that the removal mass at R1 significantly reduces the mass of the structure; hence increases response amplitude of mode 1 and the 5 measured modal frequencies after mass was added at R5 (the resonant frequency, $\omega = (k/m)^{1/2}$ and the response amplitude, $x = F/(k-m\omega^2)$) . As discussed in Chapter 6, some silicon (R1) also has been milled instead of removing only platinum. Furthermore, considering the lumped analysis result of the designed structure (Table 7-12); due to the staggered mass design the analysis produced unique modal frequencies when mass was perturbed at R1 and R5.

Table 7-12 Eigenvalue analysis result of Staggered Mass CMRA (ideal condition) using lumped mass analysis (7.6 x 10^{-12} kg mass was perturbed at R1 and R5 separately)

Analysis	Mode1	Mode2	Mode3	Mode4	Mode5
Initial [Hz]	12651	12750	12809	12917	12945
+m at R1[Hz]	12650	12748	12806	12911	12942
+m at R5 [Hz]	12650	12744	12804	12915	12943

Overall, the staggered mass design of the coupled resonators and the altered mass due to the effect of process variations have helped to stagger the structure to produce unique frequency response pattern for single resonator sensors.

7.6.2.3 Stability of the Structure Eigenvectors

Figure 7.21 (a) compares the inverse eigenvalue analysis result of the unperturbed structure and after mass was perturbed at R5. Note that the mass change pattern of the perturbed R1 can not be estimated using the inverse eigenvalue analysis since only 4 modal eigenfrequencies are available (Table 7-11). The 7.6 x10^{-12}kg mass used to validate the mass change pattern of the perturbed R5 in Figure 7.21(b) confirmed that the unperturbed eigenvectors are unstable to accurately determine the mass change pattern of the resonator. The mass variation effect (i.e. maximum of 1.73% for Chip9) and the 7.6 x10^{-12}kg deposited mass have affected the stability of the structure eigenvectors; the designed eigenvectors were no more comparable to estimate the mass change pattern of the fabricated structure when mass was deposited at R5.

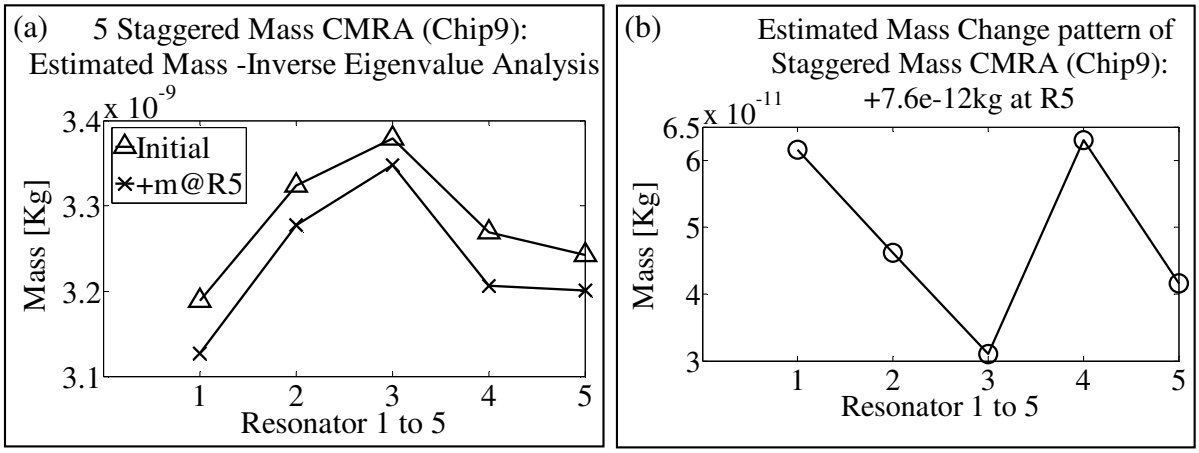

Figure 7.21 (a) Estimation of mass of Staggered Mass CMRA (Chip9) using Inverse Eigenvalue Analysis; (b) Mass change pattern of the perturbed structure

7.6.3 Staggered Stiffness CMRA

7.6.3.1 Frequency Response of the Unperturbed Structure and the Effect of Process Variation

Figure 7.22 presents the measurement result of the unperturbed Staggered Stiffness CMRA which was fabricated on Chip10 and Chip11. The modal frequency bandwidth between the

first and fifth resonant peak of the structure is 679.2Hz (Chip10) and 644Hz (Chip11); while the simulated frequency bandwidth is 502.6Hz. Table 7-13 summarizes the measured data.

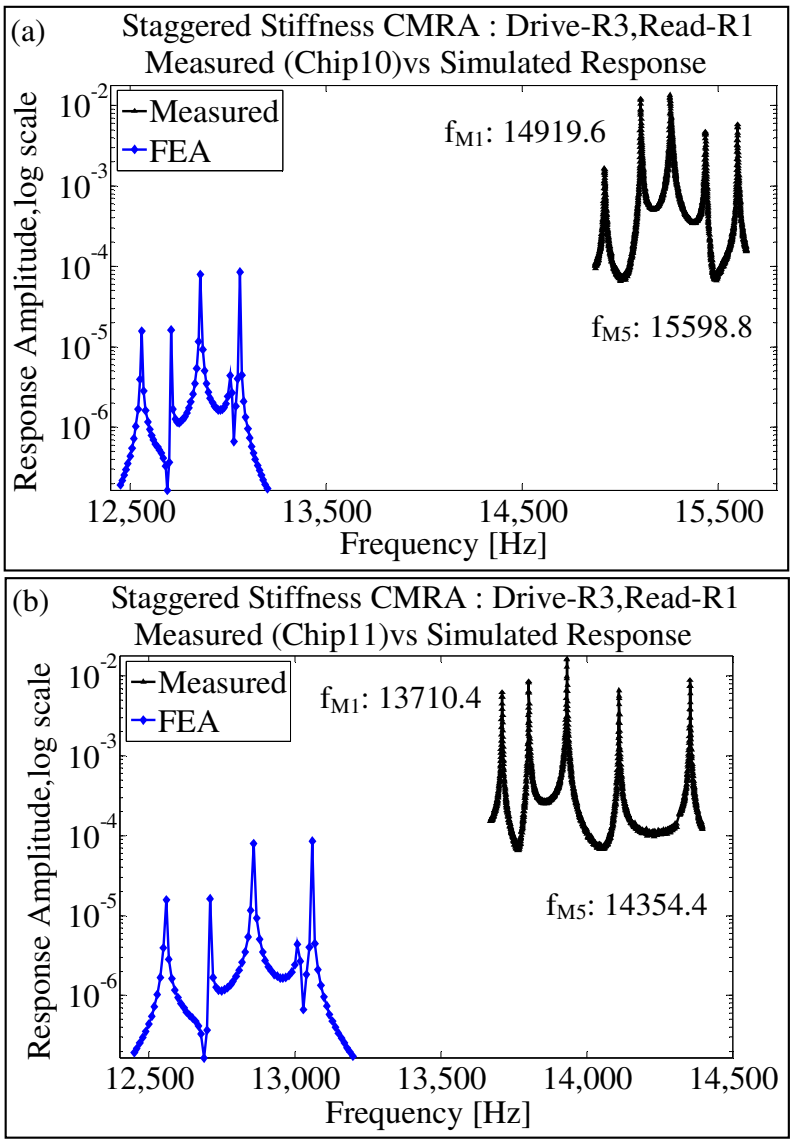

Figure 7.22 Comparison: frequency response of fabricated Staggered Stiffness CMRA and Simulated response (FEA); (a) Chip10; (b) Chip11

Table 7-13 Summary of the measurement results of unperturbed Staggered Stiffness CMRA (Figure 7.22)

Chips	[m]Measured Frequencies [Hz] ; (Response Amplitude, rms V_{out} [V]) [d] Designed frequencies (FEA) *Percent (%) of modal frequency shift compared to FEA value **( ) Normalized % of modal frequency shift (over the maximum value)				
	Mode1	Mode2	Mode3	Mode4	Mode5
Chip10 Drive-R3/ Readout-R1	[m]14919.6 (1.65×10^{-3})	[m]15104.0 (1.21×10^{-2})	[m]15254.4 (1.34×10^{-2})	[m]15434.4 (4.76×10^{-3})	[m]15598.8 (5.86×10^{-3})
	[d] 12557.9	[d] 12709.4	[d]12858.7	[d]13015.9	[d]13060.5
	*18.81% **(0.97)	*18.84% **(0.97)	*18.63% **(0.96)	*18.58% **(0.96)	*19.43% **(1)
Chip11 Drive-R3/ Readout-R1	[m]13710.4 (6.21×10^{-3})	[m]13801.6 (8.54×10^{-3})	[m]13932.0 (1.64×10^{-2})	[m]14110.4 (6.62×10^{-3})	[m]14354.4 (8.8×10^{-3})
	[d] 12557.9	[d] 12709.4	[d]12858.7	[d]13015.9	[d]13060.5
	* 9.18% **(0.93)	* 8.59% **(0.87)	* 8.35% **(0.84)	* 8.41% **(0.85)	* 9.91% **(1)

Comparing the measured and simulated responses, since the measured modal frequencies are much higher than the simulated response, we can expect that both fabricated structures are oversized due to the effect of process variation. If we consider the increase of the width of anchor spring, b_{ASP} is similar as the increase of the comb finger width, b_f (comparing to the observed INTEGRAM chip), the increase of the resonator stiffness will be much higher than the increase of mass (i.e. from estimation of the stiffness of an anchor spring, $k = Eh(b_{ASP})^3/(L_{ASP})^3$ (Equation F-2, Appendix F)) . The effect of change of the stiffness compared to resonator mass is more significant for the Staggered Stiffness CMRA, since length of the resonator anchor springs were staggered. Hence, we observe the measured modal frequencies are higher than the simulated response. The sample measurements and data analysis of the manufacturing tolerances on Chip10 (refer to Appendix H (Table H-3)) have confirmed that the structures on the chip were oversized, with 25.59% and 26.6% increase of the width of the anchor springs (b_{ASP}) and fingers (b_f).

The effect of over-sizing due to the process variation was further analysed using the inverse eigenvalue analysis to estimate the mass change of the fabricated structure. Figure 7.23 displays the analysis result and Table 7-14 summarizes the estimated mass. Comparing the estimated masses and the designed mass (at no change of the structure stiffness), the highest differences for both structures are -27.20% (Chip10, R5) and -13.32% (Chip11, R2). If the variation for the structure is calculated based on differences between the maximum and minimum change of the resonator mass, the maximum variations for Chip10 and Chip11 are 0.76% and 0.93%.

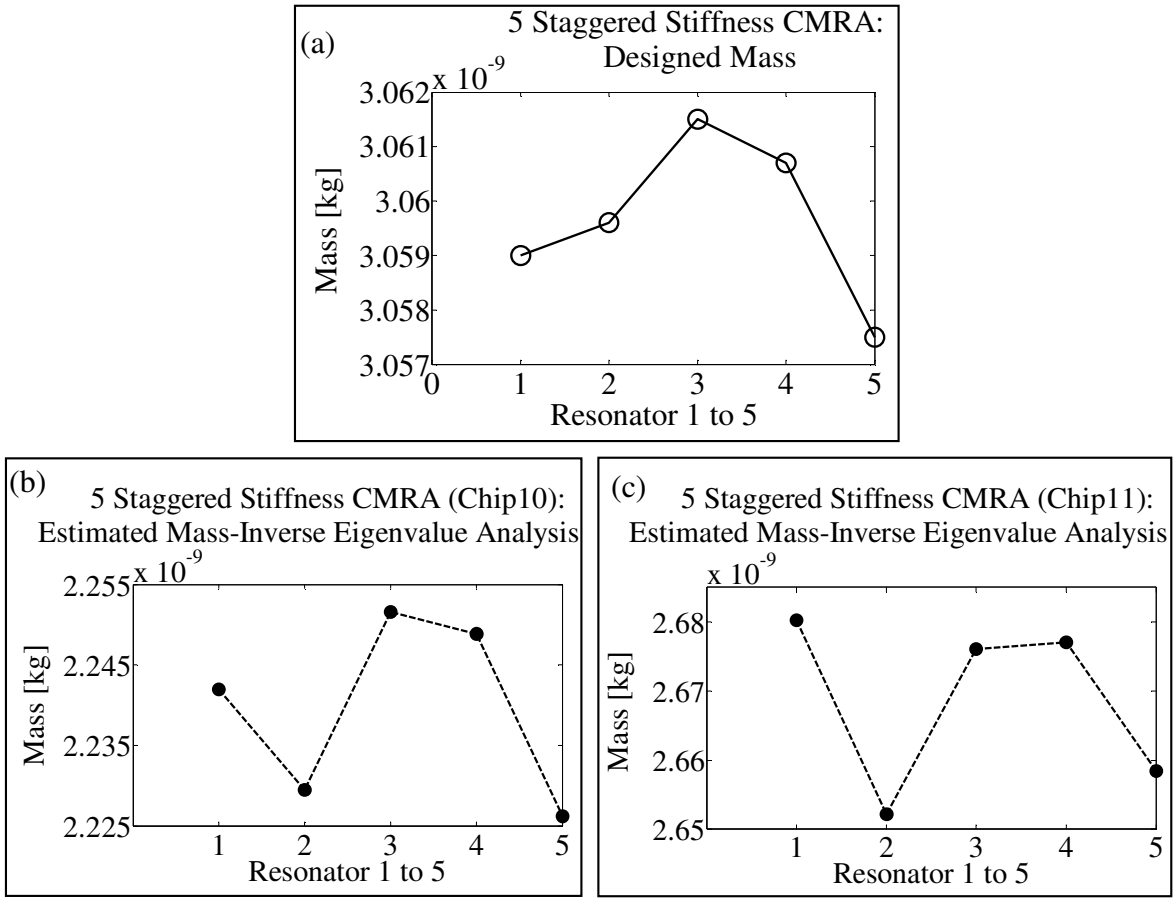

Figure 7.23 Comparison: designed mass and estimated mass of Staggered Stiffness CMRA (using inverse eigenvalue analysis); (a) Designed mass; (b) Chip10; (c) Chip11

Table 7-14 Staggered Stiffness CMRA: comparison- designed mass and estimated mass of the fabricated structure using inverse eigenvalue analysis

Resonator(R)	R1	R2	R3	R4	R5
Designed Mass nanokg]	3.0590	3.0596	3.0615	3.0607	3.0575
Chip10: Estimated Mass [nanokg]	2.242 (-26.71%)	2.229 (-27.15%)	2.252 (-26.44%)	2.249 (-26.52%)	2.226 (-27.20%)
Chip11:Estimated Mass: [nanokg]	2.680 (-12.39%)	2.652 (-13.32%)	2.676 (-12.59%)	2.677 (-12.54%)	2.658 (-13.07%)

7.6.3.2 Uniqueness of the Frequency Response - Staggered Stiffness CMRA

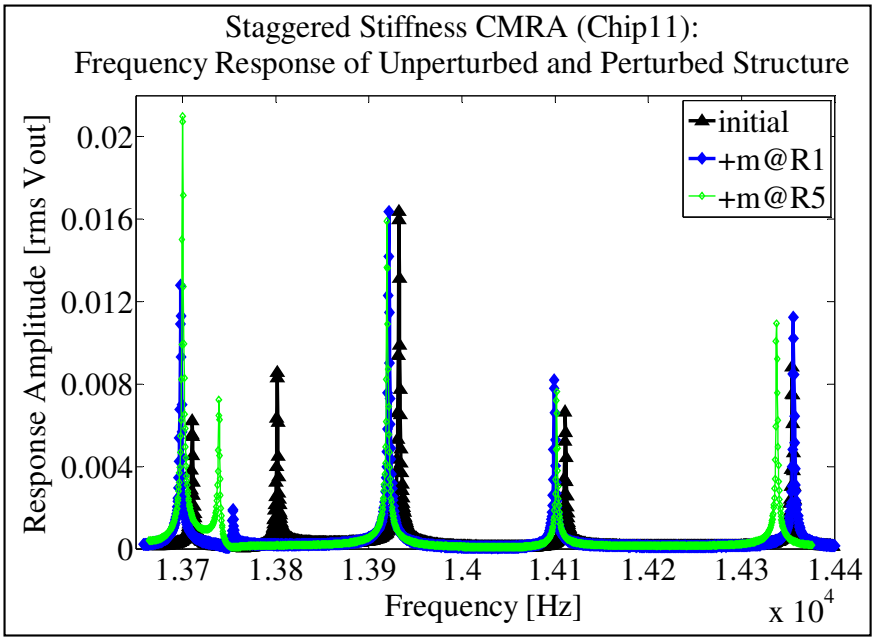

Figure 7.24 Comparison: frequency response pattern of unperturbed and perturbed Staggered Stiffness CMRA

Figure 7.24 compares the measured frequency response pattern of the unperturbed and perturbed Staggered Stiffness CMRA structure (Chip11). Overall, the measured perturbed responses are unique. However, the shift of some modal frequencies for both perturbed conditions (i.e. mode 1, 3 and mode 4) are more or less similar. Table 7-15 summarizes the measured and analyzed data of the structure.

To understand the effect of mass loading on the frequency response pattern of the Staggered Stiffness CMRA and the effect of process variation on the fabricated structure, the eigenvalue analysis result of the designed structure was considered (Table 7-16). Due to the staggered stiffness design, the shift of modal frequencies for mode 1 is similar and mode 3, and 5 are almost similar when mass is perturbed at R1 and R5. Considering the measured responses (Table 7-15), three modal eigenfrequencies (mode 1, 3 and 4) are nearly similar when mass was perturbed at R1 and R5. The differences of the three frequencies are 2.4Hz (mode1), 1.6Hz (mode 3), and 2.4Hz (mode4). Comparing the measured (Table 7-15) and the designed modal frequencies (Table 7-16), it can be argued that the impact of process variation is slightly affected the modal frequency of mode 4 and 5. The mass changes of the structure due to process variation (as discussed in Section 7.6.3.1) has slightly reduced the distinguishability of the frequency shift of mode 4 and significantly increased the frequency shift of mode 5.

Table 7-15 Summary of measurement data (Figure 7.24) and data analysis

Measurement / Analysis Chip11	Modal Frequencies, f_M [Hz] (Response Amplitude, rms Vout [V]) Note:- Frequency and amplitude difference = perturbed value – initial value				
	Mode1	Mode2	Mode3	Mode4	Mode5
Initial measurement	13710.4 (6.21×10^{-3})	13801.6 (8.54×10^{-3})	13932.0 (1.64×10^{-2})	14110.4 (6.62×10^{-3})	14354.4 (8.8×10^{-3})
+m at R1	13698.0 (1.28×10^{-2})	13754.4 (1.9×10^{-3})	13921.2 (1.63×10^{-2})	14099.2 (8.19×10^{-3})	14355.6 (1.12×10^{-2})
Frequency difference	-12.4 -0.09%	-47.2 -0.34%	-10.8 -0.08%	-11.2 -0.08%	1.2 0.01%
Amplitude difference	6.6×10^{-3}, 106.3%	-6.6×10^{-3} -77.8%	-1×10^{-4} -0.61%	1.57×10^{-3} 23.7%	2.4×10^{-3} 27.3%
+m at R5	13700.4 (2.1×10^{-2})	13739.2 (7.21×10^{-3})	13919.6 (1.59×10^{-2})	14101.6 (7.64×10^{-3})	14337.6 (1.09×10^{-2})
Frequency difference	-10 -0.07%	-62.4 -0.45%	-12.4 -0.09%	-8.8 -0.06%	-16.8 -0.12%
Amplitude difference	1.48×10^{-2}, 238.3%	-1.3×10^{-3}, -15.2%	-5.0×10^{-4}, -3.1%	1.02×10^{-3}, 15.4%	2.1×10^{-3} 23.9%

Table 7-16 Eigenvalue analysis result of Staggered Stiffness CMRA (ideal condition) using lumped mass analysis (7.6 x 10^{-12} kg mass was perturbed at R1 and R5 separately)

Analysis	Mode1	Mode2	Mode3	Mode4	Mode5
Initial (Hz)	12903	12982	13053	13152	13189
+m at R1(Hz)	12902	12975	13048	13150	13188
+m at R5 (Hz)	12902	12980	13049	13144	13187

7.6.3.3 Stability of the Structure Eigenvectors

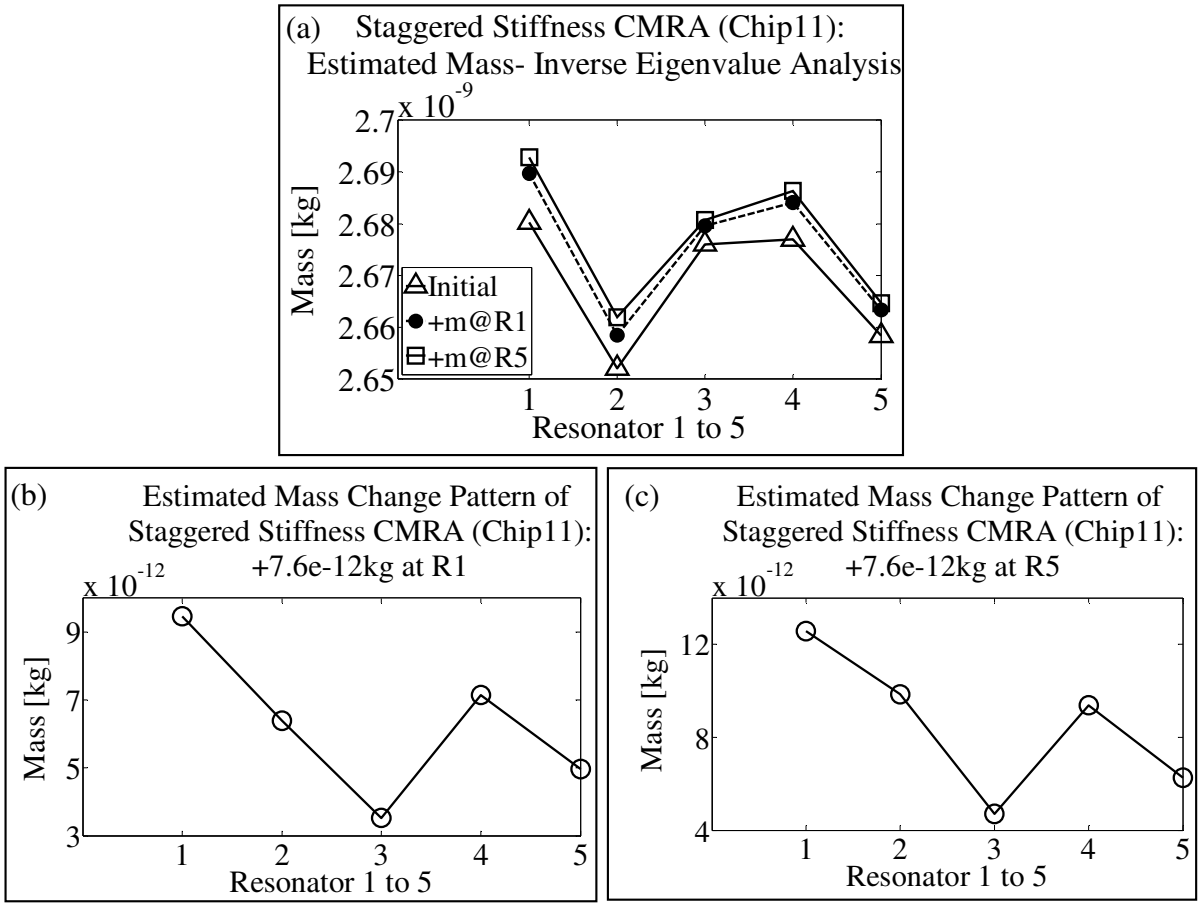

Figure 7.25 (a) Comparison – Estimated mass of unperturbed and perturbed Staggered Stiffness CMRA (Chip11) using Inverse Eigenvalue Analysis; (b) Mass change pattern of the structure (mass perturbed at R1); (c) Mass change pattern of the structure (mass perturbed at R5)

Figure 7.25 (a) compares the estimated mass of the coupled resonators for the unperturbed and perturbed structure using the inverse eigenvalue analysis. Comparing between the unperturbed mass and when structure was perturbed at R1 (Figure 7.25(b)), the analysis shows that the maximum mass changes is at R1. However, the analysis also shows that the

maximum mass change at R1 when mass was perturbed at R5 (Figure 7.25(c)). Therefore, it can argue that the eigenvectors of the fabricated structure are remained stable when 7.6 x10^{-12}kg mass was perturbed at R1 (i.e. agreeable with modelling analysis (Chapter 5)). Hence, the analysis using the designed eigenvectors correctly identified the mass change pattern of the resonator. The effect of process variation and when mass was milled off at R1 caused the eigenvectors of the fabricated structure were no more stable compared to the designed eigenvectors. The inverse eigenvalue analysis causes error when using the designed eigenvectors to estimate the perturbed mass at R5.

7.7 Stability of the Measured Response

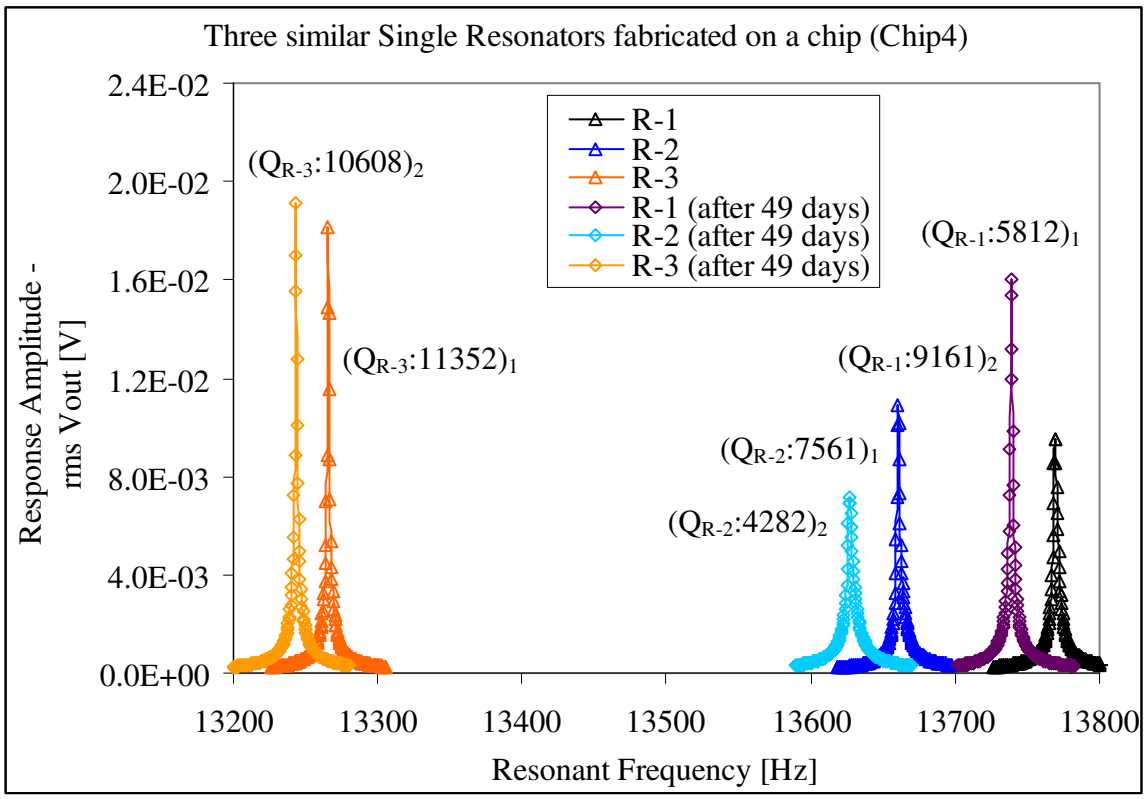

Figure 7.26 Measurement result: frequency response comparison of Single resonators (second measurement: 49 days after the first measurement)

The stability of the measured frequency response pattern was examined by comparing between the first and second batch of the measurements. Figure 7.26 displays and compares the frequency response of three single comb-drive resonators (Chip4) between the first and second measurement. Table 7-17 details the measurement result.

Table 7-17 Summary of data analysis of measured structure (Figure 7.26)

Measurement/ analysis (Chip4)	Peak of Resonant Frequency [Hz] (Response Amplitude [V]) Differences = Measurement 2 – Measurement 1		
	(R-1)	(R-2)	(R-3)
Measurement 1 (Initial)	13769.2Hz (9.52×10^{-3}V)	13660.4Hz (1.09×10^{-2}V)	13265.6Hz (1.82×10^{-2}V)
Measurement 2 (After 49 days)	13739.2Hz (1.61×10^{-2}V)	13626.8 Hz (7.17×10^{-3}V)	13243.2 Hz (1.92×10^{-2}V)
Frequency Difference	-30Hz -0.22%	-33.6 Hz -0.25%	-22.4Hz -0.17%
Amplitude Difference	6.6×10^{-3}V 69.33%	-3.7×10^{-3}V -33.9%	1.0×10^{-3}V 5.5%

As can be observed after 49 days, the resonant frequency of the three resonators decreased, with R-2 resonator shows the highest decrement followed by R-1 and R-3. While, the response amplitude of R-1 and R-3 resonator increased, and R-2 resonator decreased. The change of the response amplitude and the resonant frequency has changed the performance of the single resonators. As a result, the quality factors of R-1 was increased by 57.6%; while, the quality factor of R-2 and R-3 resonator were decreased by 43.4% and 6.6% respectively.

The decrease of the resonant frequency of the three single resonators may be because of a slight increase of the resonator mass. One possible reason of the increase of the resonator mass is due to an oxidation of the aluminium material which was metallized on the surface of the resonators. However, further research such as X-ray diffraction analysis (XRD) may be performed to determine the phase change of the material before the argument can be

confirmed. The change of the performance of the single resonator has exemplified that the same effect may occur on the CMRA sensor structure. Figure 7.27 compares the first and second measurement result of the unperturbed Staggered Mass CMRA (Chip8). Table 7-18 summarizes the measured and analyzed data.

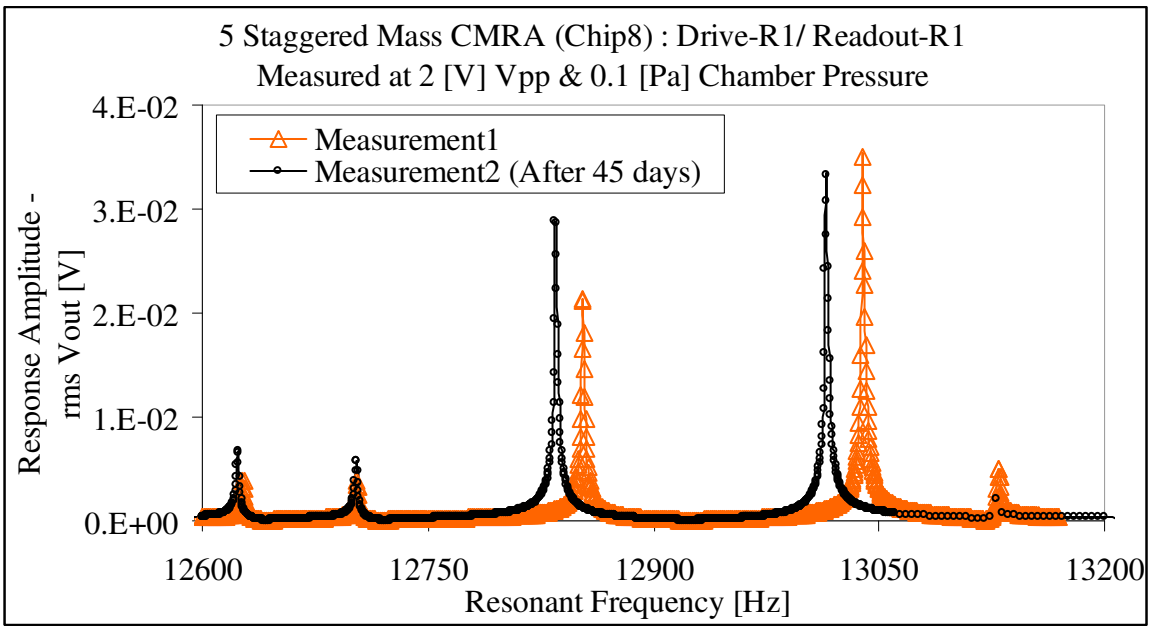

Figure 7.27 Measurement result: frequency response comparison of 5 staggered Mass CMRA (second measurement: 45 days after the first measurement)

Table 7-18 Summary of data analysis of measured structure (Figure 7.27)

Measurement/ Analysis (Chip8)	Peak of Resonant Frequency [Hz] (Response Amplitude [V]) Differences = Measurement 2 – Measurement 1				
	Mode 1	Mode 2	Mode 3	Mode 4	Mode 5
Measurement1 (Initial)	12627.2 (3.9×10^{-3})	12702.8 (3.81×10^{-3})	12852.8 (2.13×10^{-2})	13038.8 (3.51×10^{-2})	13129.4 (5.06×10^{-3})
Measurement2 (after 45 days)	12624.0 (6.78×10^{-3})	12702.8 (5.77×10^{-3})	12834.8 (2.88×10^{-2})	13014.8 (3.32×10^{-2})	13128.0 (2.17×10^{-3})
Frequency Difference	-3.2Hz -0.03%	0	-18Hz -0.14%	-24Hz -0.18%	-1.4Hz -0.01%
Amplitude Difference	2.9×10^{-3}V 74.4%	2.0×10^{-3}V 52.5%	7.5×10^{-3}V 35.2%	-1.9×10^{-3}V -5.4%	-2.2×10^{-3}V -43.5%

As shown in Figure 7.27, after 45 days from the first measurement of the structure, some structure modal frequencies and the resonant peaks were changed. Except for the modal frequency of the mode 2, all other modal frequencies were decreased. The response amplitude of the mode 1, 2 and 3 were increased and mode 4 and 5 were decreased.

As discussed earlier for the single resonator, the shift of the modal frequencies and response amplitude may be due to the increase of resonator mass after certain period of time. To estimate the change of the structure mass, the inverse eigenvalue analysis was considered. From the analysis result in Figure 7.28, the maximum estimated increase of mass are 0.20% (R1), followed by 0.16% (R5), 0.12% (R3), 0.096% (R4) and 0.095%(R2).

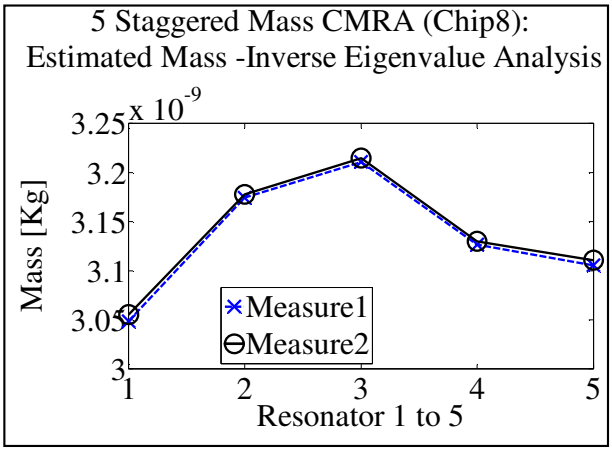

Figure 7.28 Inverse eigenvalue analysis result: estimated mass of Staggered Mass CMRA (comparison between measurement1 and 2)

Although, the frequency response pattern of the structure is changed after certain time, but the five peaks of the structure modal frequencies are remained measurable. Hence, the frequency response pattern of the CMRA structure is still reliable to be used as a signature for the coupled resonators sensor. Only a calibration is required before mass is perturbed on the structure; to ensure accurate prediction of the perturbed mass when comparing between the unperturbed and perturbed frequency response pattern. However, more measurement and

analysis are required to confirm the rate of change of the frequency response pattern of the CMRA structure over a period of time.

7.8 Summary and Conclusion

To confirm the performance of the CMRA structure, 11 Chips were tested which involves 6 tests of the three CMRA(s) structure (Constant Mass CMRA, Staggered Mass CMRA and Staggered Stiffness CMRA) and its single resonators (integrated comb-drive resonator) and also the single fixed-fixed beam resonator.

From the performance evaluation of the single resonator (Chip1) which was measured at different vacuum level (Section 7.5.1) shows that the air pressure level give a very small effect on the shift of the resonant frequency. However, the air pressure level has large effect, decreasing the response amplitude of the resonator signal and increasing the resonant frequency bandwidth of the measured response.

The input voltage (Vpp) has a proportional effect on the response amplitude of the resonant frequency curve. As discussed in Section 7.5.2, at high range of the input voltage (i.e. more than 0.4 V) the A-F curve of the single resonator is nonlinear and the shift of the resonant frequency is unpredictable. To ensure stable and predictable frequency response curve for a linear sensor characteristic the single resonator and the CMRA structure was driven at 0.4 V and 2V Vpp voltage respectively.

Process variation is inevitable as exemplified by the frequency response measurement of the single resonators fabricated on Chip2, Chip3, Chip4 and Chip5 (Section 7.5.3). Three similar single resonators on each chip exhibit different resonant frequency and different response amplitude. The maximum frequency variations between the fabricated single resonators are 3.91% (Chip4) followed by 2.42% (Chip2), 1.3% (Chip3) and 0.36% (Chip5).

From the mass loading frequency response effect analysis of the single resonators (Section 7.5.4), showed that when an approximate 7.6 x 10^{-12}kg platinum mass was deposited on the single resonator (Chip1), the resonant frequency and the response amplitude of the resonator decreases by 0.03% and 55% respectively.

As discussed in Section 7.6, the performances of the three fabricated CMRA(s) are summarized as follows:-

Constant Mass CMRA:

The measurements of the unperturbed structure confirm that all the resonant peaks of the 5 modal frequencies are measurable. Both measured responses (Chip6 and Chip7) showed significant differences when compared to the simulated responses from finite element analysis. As discussed in Section 7.6.1.1 the process variation has significantly modified the mass and stiffness of the structures. The maximum mass change estimated using lumped mass analysis was -1.22% for both structures. When the Constant Mass CMRA (Chip6) was perturbed at R1 and R5 separately, the structure showed distinctive response patterns for both perturbed conditions (Section 7.6.1.2). The process variation has naturally staggered the Constant Mass CMRA to produce unique frequency response pattern for the coupled resonator sensors.

Staggered Mass CMRA:

The measurement results of the Staggered Mass CMRA (Section 7.6.2.1) confirmed that the 5 modal frequencies of the structure are measurable. The process variation has significantly altered the mass of the coupled resonators and changed the measured modal eigenfrequencies. By using the inverse eigenvalue analysis, the maximum variations between the estimated masses of 5 resonators were 1.05% (Chip8) and 1.73% (Chip9). Due to the effect of process variation and the staggered mass design of the coupled resonators the Staggered Mass CMRA

(Chip9) produced a unique frequency response pattern as a single resonator sensor when mass was perturbed at R1 and R5 (Section 7.6.2.2). However, the mass changes due to the process variation on Chip9 (i.e. the errors which is more than 1% compared to the amount of staggered mass) have modified the designed mass of the coupled resonators; hence using the inverse eigenvalue analysis, the mass change pattern of the perturbed platinum mass at R5 was unable to be determined.

Staggered Stiffness CMRA:

The measurement results of the structure showed that the measured 5 modal frequencies for both Chip10 and Chip11 are higher than the simulated response (Section 7.6.3.1). The shift of the frequencies was expected due to the effect of structure oversized and the structure design of the staggered stiffness. From the inverse eigenvalue analysis result, the maximum estimated change of mass was -27.20% (Chip10) and -13.32% (Chip11) and the maximum estimated mass variations for both chips were 0.76% (Chip10) and 0.93% (Chip11). When the structure (Chip11) was perturbed at R1 and R5 separately, the measurement results showed distinctive frequency response patterns. It can be claimed that the process variation has impacted less the Staggered Stiffness CMRA. As a result, the structure eigenvectors remained stable to determine the mass change pattern of the structure sensor when mass was perturbed at R1. However, the effect of the process variation and the variation of the platinum deposited mass, caused the inverse eigenvalue analysis no more sensitive to estimate the mass change pattern due to the perturbed mass at R5.

The stability analysis of the frequency response of the 3 single comb-drive resonators on Chip4 exemplify that some resonator quality factor was increased and some was decreased after a period of 49 days. The analysis of the Staggered Mass CMRA after 45 days showed that least effect occurs on the CMRA structure. The average reduction of the 5 modal

frequencies are 9.32Hz compared to 28.67Hz for single resonator. Since the resonators are coupled together the effect of high and low quality factors are mitigated among neighbourhood elements of the coupled resonators and the coupling springs.

Overall, this type of sensor structure requires a calibration before mass is perturbed on its resonator sensor to ensure accurate comparison of the sensor output signal before and after mass is perturbed on the structure. Since the process variation is in place, a technique to accurately calibrate the fabricated CMRA and to extract a new set of the structure eigenvectors is required; knowing the new set of the fabricated CMRA eigenvectors, the inverse eigenvalue analysis may be used to estimate the mass change pattern of the coupled resonator sensor.

CHAPTER 8 - CONCLUSION AND FUTURE RECOMMENDATIONS

8.1 Conclusion

The main objective of this research was the development of a new sensor structure of the coupled micro resonator array (CMRA) for use in the artificial nose. The research motivation was the realization of multiple resonant sensors with a simplified readout system. The drive and readout of the sensor output was based on an electrostatic drive and capacitive detection. The frequency response curve of the coupled structure is the signature output of the CMRA sensor. Any change of mass of one of the resonators changed the frequency response of the coupled structure. Knowing the change of mass of the coupled resonators allows the determination of mass species on the resonators, since the CMRA resonator sensors were designed to selectively absorb particular mass.

Chapter 5 presented three final CMRA(s) structure, (1) 5 Constant Mass CMRA, (2) 5 Staggered Mass CMRA, and (3) 5 Staggered Stiffness CMRA. The mass loading effect on the CMRA frequency response was tested by a platinum mass deposition using the focused ion beam (FIB) technology. There are several challenges to be overcome to successfully develop the CMRA sensor:

1. Balanced effective mass of the coupled elements for measurable frequency response:

The first key performance criteria of the CMRA was measurability of the frequency response of the coupled structure. The mass and stiffness configuration of the coupled elements determined the relative displacement and the measurability of all eigenmodes of the structure. As demonstrated by the first version of the CMRA (Section 3.5.5, Chapter 3), due to large mass of the comb drive actuators, the actuator failed to drive the coupled fixed-fixed beam resonators. The large mass of the driven comb which was rigidly coupled to the first

resonator (R1) reduced the relative displacement of the first coupled element (i.e. creating a node), which desynchronised the motion of the first element and the next coupled elements. The 5 Constant Mass CMRA which was based on the integrated coupled comb-drive resonators enhanced the measurability of the structure output signal. The constant mass balanced the relative displacement of the 5 coupled resonators for all the 5 structure eigenmodes.

2. Amount of staggered mass and staggered approach for unique, measurable frequency response and stable eigenvectors:

A unique frequency response pattern is very important as a finger print of the CMRA sensor structure. The research used the inverse eigenvalue analysis to estimate the mass change pattern of the coupled resonators. Since the unperturbed eigenvectors were used in the inverse eigenvalue analysis, it is important to stabilize the eigenvectors against the perturbing mass.

Although the Constant Mass CMRA provided an advantage for a measurable output signal, the structure produced no unique frequency response pattern for the entire single resonator sensors and the eigenvectors were always unstable. Breaking the symmetry of the structure by staggering the mass of the coupled resonators helped to produce unique frequency response patterns and stabilize the structure eigenvectors. However, determination of amount of the staggered masses and the staggered approach is important to ensure the measurability of the 5 eigenmodes of the CMRA. As exemplified by the uniform step staggered approach (Section 4.6.2), with 5% total mass differences between R1 and R5 reduced the relative displacement of the R1 (mode 1) and R5 (mode 5) to approach zero. As a result only four modal eigenfrequencies are expected measurable when the readout is at R1 or R5.

The Staggered Mass and Staggered Stiffness CMRA which were based on the unsymmetrical staggered - balanced mass distribution between the first and second half of the coupled array with the heaviest mass in the middle of the structure array improved the structure measurability. Positioning the heaviest mass at the middle of the structure array helped to balance the relative displacement of the 5 coupled resonators; the impact of the large mass is reduced by segregating it to both half of the array. With the unsymmetrical-balanced mass, the approach staggered the coupled resonators for a unique frequency pattern of the coupled resonator sensor, while balancing the relative displacement of the coupled structure on both half of the array. A balanced relative displacement between the 5 resonators reduces a risk that some of the modal eigenfrequencies of the coupled structure at the resonator with the smallest displacement is unable to be measured. For both staggered CMRA(s) the minimum limit of perturbing mass for a unique detectable response is 1×10^{-12}kg.

The staggered CMRA(s) were designed to stabilize the eigenvectors due to a small change of absorbed mass (i.e. for a single resonator mass change). The structure eigenvectors are stable if the eigenvectors and the eigenmodes of the coupled structure remain comparable before and after a mass is added to the structure. For the Staggered Mass CMRA, the eigenvectors of the single resonator sensor remained stable when the perturbing mass was 3.0615×10^{-11}kg (R1), 1×10^{-11}kg (R2), 1×10^{-12}kg (R3 and R4) and 1×10^{-13}kg (R5). For the Staggered Stiffness CMRA the perturbed eigenvectors remained stable when the single resonator sensor absorbs 1×10^{-11}kg mass.

3. The CMRA fabrication process and the impact of process variation:

The CMRA fabrication used the bulk micromachining processes which relies essentially on the lithography process to transfer the structure pattern. It is the nature of the MEMS processes, that a slight variation in the process parameters varies the final profile of the

fabricated structure. As discussed in Chapter 6, the sources of the process variation of the fabricated structure were originated from the photo resist preparation and the process to transfer the pattern onto the wafer (photolithography and development processes). The variation of the thickness of the SOI material layer supplied by the manufacturer caused the processing time to etch the Si device layer varies from one chip to another chip, which also affected the device profile.

The quantified variation of the INTEGRAM chip showed that for the particular measured geometrical dimensions the minimum and maximum part to part variations were 0.25% and 1.99% respectively (Section 5.6.1). The numbers give an idea, the level of variation which is expected to vary the fabricated structure (e.g. length, width); it can be suggested that more chips are required to be quantified across the whole wafer in order to confirm the level of the variation for particular facilities and technique to fabricate the MEMS structure.

The frequency response measurement of the three similar single resonators which were fabricated on a single chip (Chip2, Chip3, Chip4 and Chip5) showed the level of variation for the particular chips. The minimum and maximum frequency variation of the single resonator were 0.35% (Chip5) and 3.91% (Chip4). A such variation level will significantly affect the performance of the fabricated CMRA sensor structures. Comparing the designed and the fabricated CMRA structures on the 6 different chips, the maximum estimated mass variation between the 5 coupled resonators was 1.19% (Chip6), 0.74% (Chip7), 1.05% (Chip8), 1.73% (Chip9), 0.76% (Chip10) and 0.93% (Chip11). Although the variation provides an advantage to naturally stagger the Constant Mass CMRA (Chip6); the variation also reduces some response amplitude of the coupled structure. The mass change of the fabricated structure which was significantly higher than the amount of staggered mass caused the

approach of using the inverse eigenvalue analysis to estimate the mass change pattern of the perturbed resonator is less suitable.

4. Suitability of the inverse eigenvalue analysis to estimate the mass change of the perturbed CMRA

Although using the inverse eigenvalue analysis could not accurately determine the amount of perturbed mass for the single resonator mass change, but the analysis is sufficient to estimate the mass change pattern of the perturbed staggered CMRA as discussed in Section 5.5. However, the impact of the manufacturing variation has limited the use of the inverse eigenvalue analysis. Due to the effect of manufacturing variations, only 4 modal eigenfrequencies were measurable when R1 of the Staggered Mass CMRA (Chip9) was perturbed with 7.6 x 10^{-12}kg platinum; as a result, the stability of the structure eigenvectors could not be validated using the inverse eigenvalue analysis. The effect of process variation caused the approach was unable to estimate the mass change pattern of the Staggered Stiffness CMRA (Chip11) when platinum mass was perturbed at R5.

Overall the three CMRA(s) structures were successfully demonstrated the multiple resonant sensors with a simplified readout. The 5 Constant Mass CMRA (Chip6) which has been naturally staggered by the process variations showed unique frequency response patterns when platinum mass was perturbed separately at R1 and R5. With the staggered designs, both Staggered Mass (Chip9) and Staggered Stiffness CMRA (Chip11) also showed unique frequency response pattern for the single perturbed resonator sensor. The second measurement of the Staggered Mass CMRA (Chip8) showed that the structure frequency response remained stable after 45 days from the first measurement. Although some modal frequencies were slightly decreased, but all the structure eigenmodes were measurable. In order to use the CMRA as a sensor structure, an approach to accurately quantify the mass

change pattern of the perturbed coupled resonator is required; since the mass of the fabricated structure was changed due to the process variation, the CMRA sensor structure requires a calibration before any mass is perturbed on the structure.

In conclusion the CMRA structure development is successful. The CMRA sensor structure showed potential to present large resonant sensors array for the artificial nose. By only monitoring the frequency response of the coupled resonators, the complexity of the readout and signal processing system of large sensing system will be simplified. Using the CMRA, requirement to integrate different sensors response is eliminated; hence, simplifying the mathematical modelling to characterize different sensor responses.

8.2 Future Recommendations

In order to use the CMRA sensor structure in the artificial nose there are still many further studies required:

1. An approach to estimate the mass change of the perturbed CMRA resonator

The impact of the process variation which changed some structure eigenvectors and reduced the measurability of the eigenmodes, cause the approach of the inverse eigenvalue analysis to become less suitable to estimate the mass change of the CMRA sensor structure; unless the new set of eigenvectors of the fabricated CMRA are determined. Otherwise, an alternative technique to compare the two states of the Amplitude-Frequency curve (A-F curve) (before and after mass was perturbed on the structure) is required to determine the change of mass of the perturbed CMRA.

2. Redesign the CMRA to include the effect of manufacturing variation

In order to use the inverse eigenvalue analysis to estimate the mass change pattern, it is important to redesign the CMRA so that the structure eigenvectors are insensitive to the manufacturing variation.

3. Using the electrostatic or mechanical tuning to compensate the manufacturing variability

It is interesting to research an approach of a frequency tuning using the electrostatic comb drive [169] to alter the resonant frequencies of the CMRA structure. The mechanical frequency tuning approach using the focused ion beam platinum deposition also may be explored.

4. An Approach to analyse and optimize the CMRA structure design

An approach such as Genetic Algorithm may be used to further analyse the CMRA performance or optimize the CMRA structure design. The approach may be used to estimate the amount of change of mass or stiffness of the coupled structure which affected by the process variation. Knowing the change value will determine the new set of eigenvectors of the fabricated CMRA. The technique may also be used to explore other alternatives to break the CMRA structure symmetry such as staggering the coupling spring, and optimizing the performance of the CMRA (e.g. optimizing the design parameter to improve the Q-factor of the sensor structure).

5. Alternative method to drive and readout the CMRA sensor structure

The electrostatic drive and capacitive readout constrains the size of the CMRA structure. Small CMRA structure is hard to be realised in order to ensure enough capacitance for the drive and readout measurement. Large mass of the CMRA sensor reduces the sensitiveness of the sensor to detect a small amount of perturbed mass. Other approach of drive and readout such as a piezoelectric excitation and an optical detection may be explored, so that the CMRA sensor can be operated in higher scale of resonant frequency (Mega hertz or gigahertz).

6. Mass loading frequency effect based on real test of odour absorption – desorption

Even though many researches are important before the CMRA can be properly established for the artificial nose, it is interesting to experiment the effect of the odour absorption - desorption process on the sensitivity and stability of the Amplitude-Frequency curve (A-F curve) of the CMRA structure. Then the structure can be further improved to be sensitive within the threshold of the species of odour to be measured.

A likely sequence of operations of the final device are:

A chemically sensing membrane material which will react with the odorant molecules will be coated on the surface of the resonator. A calibration step is required to observe the effect of the coated material on the shift of the resonant frequency curve (note: the device will be operated in a vacuum test chamber). An odour or a sample gas to be tested will be introduced and directed to the coated sensing membrane material by using a flow control valve unit. The sensor is then allowed to vibrate in few minutes before the final frequency response curve is measured.

APPENDIX A

Consideration - Finite Element Analysis (COMSOL Multiphysics)

1. Modeling using graphical user interface (GUI, predefined physics modes or PDEs)

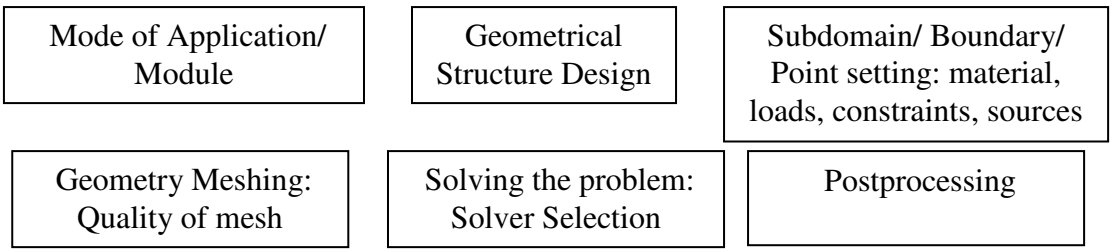

2. Stability of mesh: minimum element quality (3D structure: at least 0.1; and 2D: at least 0.3 [169])

3. The effect of mesh quality on the simulation result.

Table A-1 Example of fundamental frequency of fixed-fixed beam resonator compared to minimum element quality of mesh and time to run the simulation

Mesh Statistics Parameter/ Others	(1)	(2)	(3)	(4)	(5)	(6)	(7)
DOF	17228	9622	7362	6302	6306	5022	3642
Number of mesh points	2277	1312	1022	884	884	718	538
Number of elements	4061	2188	1638	1384	1386	1076	746
Number of boundary element	493	436	406	384	382	360	330
Number of vertex elements	24	24	24	24	24	24	24
Element area ratio	0.0028	9.29e-4	2.5e-4	3.09e-4	1.86e-4	9.66e-5	9.51e-5
Minimum element quality	0.6047	0.7054	0.7058	0.7059	0.6985	0.6435	0.6328
Resonator frequency [Hz]	48761.71	48765.35	48763.09	48760.54	48759.97	48760.36	48766.58
Predefined mesh size	Extremely fine	Extra fine	Finer	Fine	Normal	Coarse	Extra Coarser
Solution Time [s]	1.438	0.766	0.547	0.438	0.453	0.344	0.235

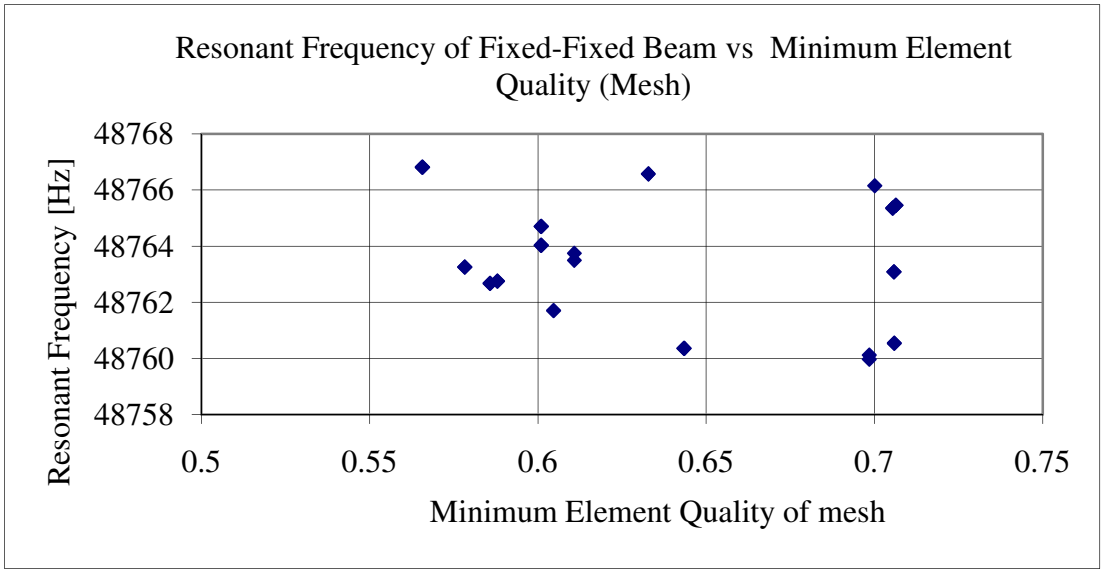

Figure A.1 Simulated Frequency response of fixed-fixed beam using COMSOL Multiphysics at different quality of mesh.

APPENDIX B

MATLAB CODES – Eigenvalue and Eigenvectors Analysis

```
clc
clf

% insert the stiffness of R1 (resonator1), R2, R3 R4 and R5
k1=stiffnessR1;
k2=stiffnessR2;
k3=stiffnessR3;
k4=stiffnessR4;
k5=stiffnessR5;

% insert the four coupling stiffness of kc1, kc2, kc3, and kc4
kc1=coupling_stiffness_kc1;
kc2=coupling_stiffness_kc2;
kc3=coupling_stiffness_kc3;
kc4=coupling_stiffness_kc4;

% insert the mass of R1 , R2, R3 R4 and R5
m1=massR1;
m2=massR2;
m3=massR3;
m4=massR4;
m5=massR5;

% Initial mass matrix of the 5 resonators (unperturbed Resonators)
M=[m1,0,0,0,0;0,m2,0,0,0;0,0,m3,0,0;0,0,0,m4,0;0,0,0,0,m5]  ;

% Stiffness matrix (resonator stiffness & coupling constant)
K=[(k1+kc1), -kc1,0,0,0;-kc1, (k2+kc1+kc2),-kc2,0,0;0,-kc2,(k3+kc2+kc3),-
kc3,0;0,0,-kc3,(k4+kc3+kc4),-kc4;0,0,0,-kc4,(k5+kc4)];

Force=[0; 0; 1e-6; 0;0];

% The natural frequency of the uncoupled single degree of freedom system
% (R1, R2, R3, R4, & R5)
f1=(1/(2*pi))*(k1/m1)^0.5; % Natural frequency of R1
f2=(1/(2*pi))*(k2/m2)^0.5; % Natural frequency of R2
f3=(1/(2*pi))*(k3/m3)^0.5; % Natural frequency of R3
f4=(1/(2*pi))*(k4/m4)^0.5; % Natural frequency of R4
f5=(1/(2*pi))*(k5/m5)^0.5; % Natural frequency of R5

%************************************************************************
**********************************
%  EIGENVALUE AND EIGENVECTORS ANALYSIS

E=(M^-1)*K;

% The column eigenvector matrix,v and diagonal eigenvalue matrix, d of the
unperturbed five degree of freedom system are:
[V,d]=eig(E);

% five unsorted modal eigenfrequencies of 5 coupled resonators:-
fc1=(1/(2*pi))*d(1,1)^0.5;
fc2=(1/(2*pi))*d(2,2)^0.5;
fc3=(1/(2*pi))*d(3,3)^0.5;
```

```
fc4=(1/(2*pi))*d(4,4)^0.5;
fc5=(1/(2*pi))*d(5,5)^0.5;
% the sorted 5 modal eigenfrequencies (the lowest: mode1;..; the highest:%
mode 5)
yR = [fc1; fc2; fc3; fc4; fc5]; [sortyR, OrderR]=sort (yR);

% x=[1,2,3,4,5]

% The eigenvectors of the 5 coupled resonators (note: the eigenvectors for-
% mode1, mode2, mode3, mode4 and mode5 were determined based on the sorted-
% order of the 5 modal eigenfrequencies;

% If the sorted order is 1,2,3,4, and 5; then the eigenvectors are:-
mode1=V(:,1);
mode2=V(:,2);
mode3=V(:,3);
mode4=V(:,4);
mode5=V(:,5);

%*************************************************************************
% PLOTTING THE EIGENMODES

% figure(1) % Eigenmodes of 5 coupled resonators

plot(x,mode1,x,mode2,x,mode3,x,mode4,x,mode5),title('Eigenmodes of
Unperturbed 5 CMRA'), xlabel('Resonator 1 to 5'),ylabel('Eigenvectors'),
legend('mode1','mode2','mode3','mode4','mode5'),  style=-1
```

Eigenvectors Stability: Alternative 1 (Chapter 4)

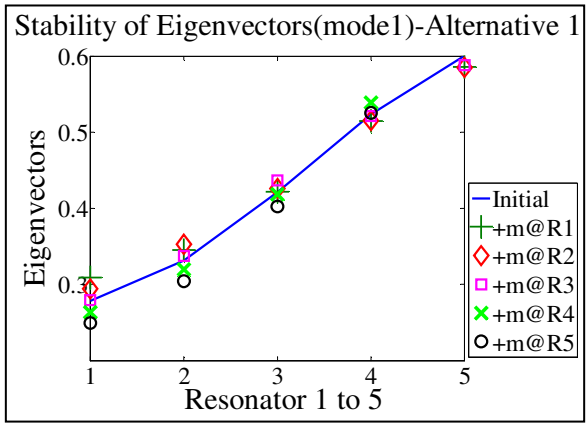

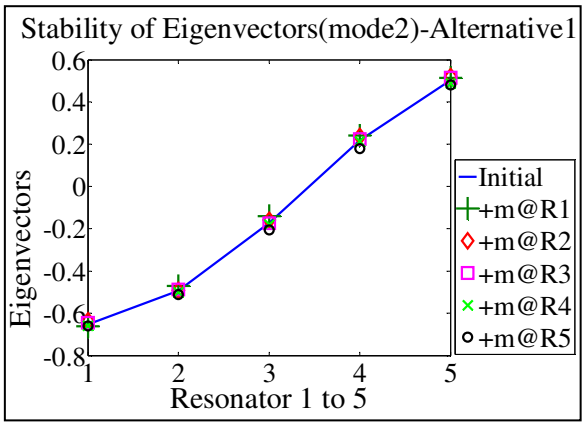

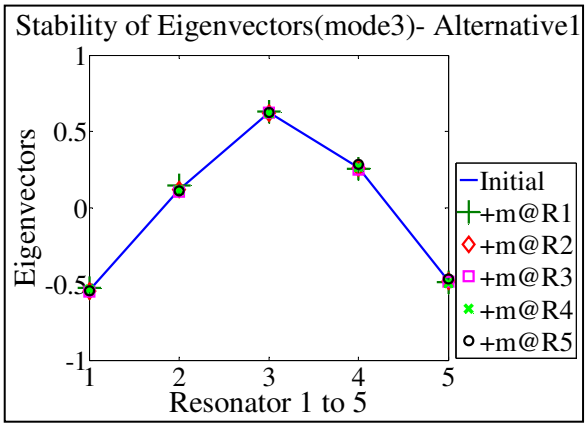

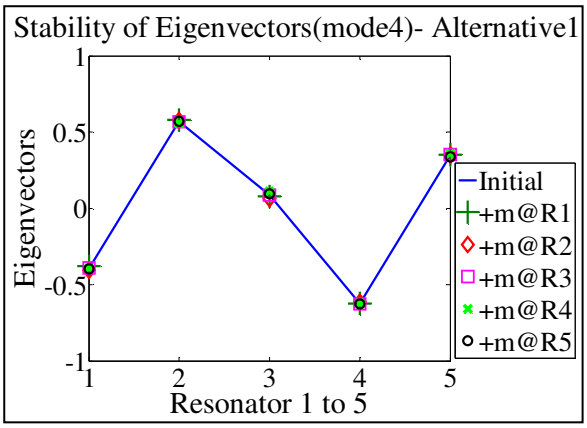

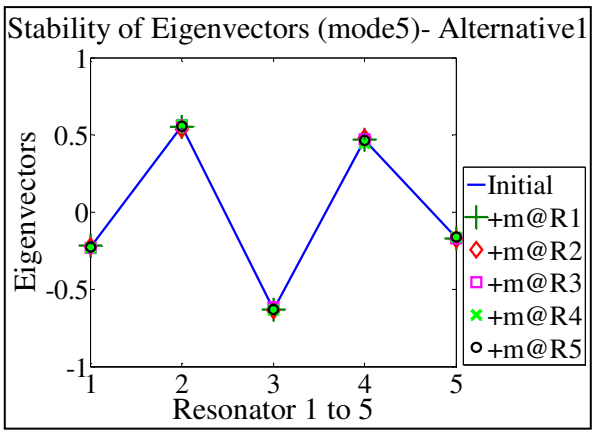

Eigenvectors Stability: Alternative 2

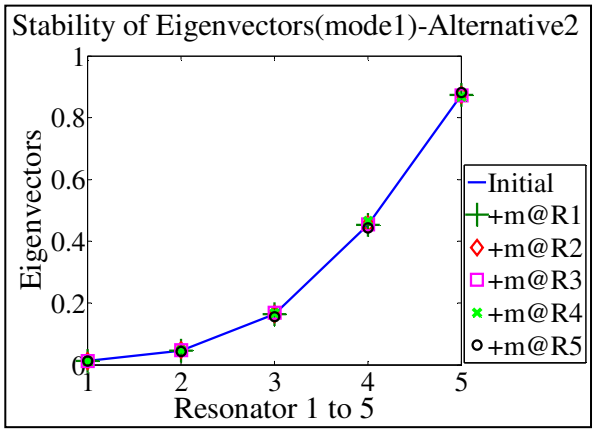

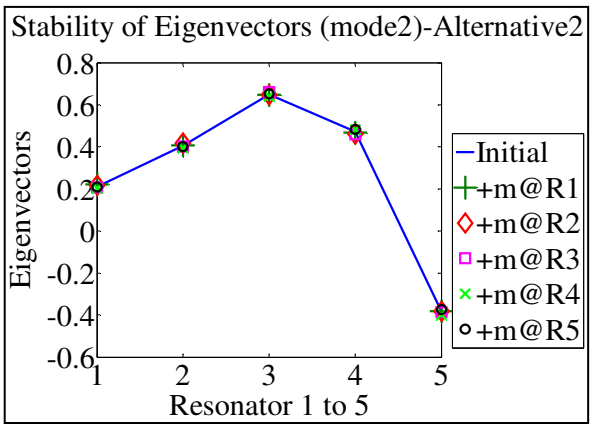

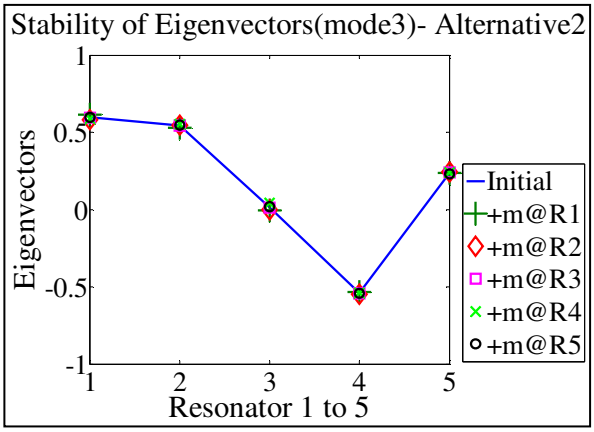

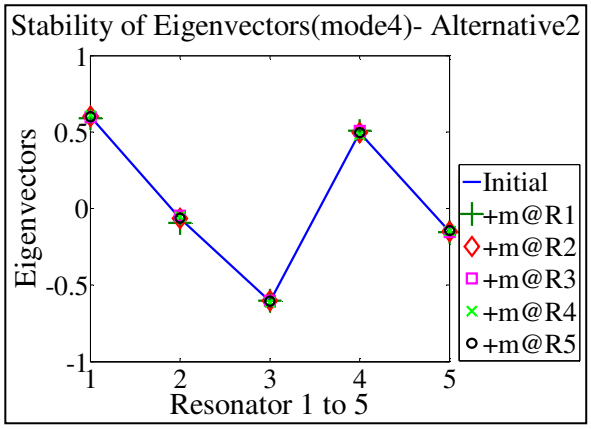

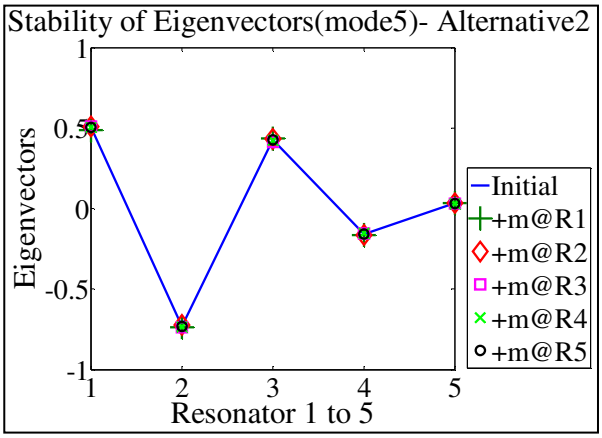

Eigenvectors Stability: Alternative 3

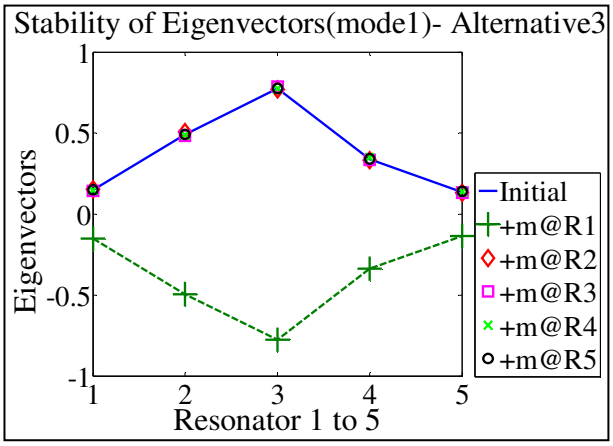

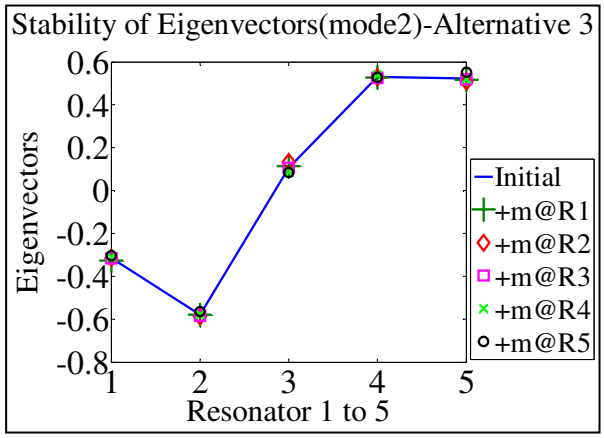

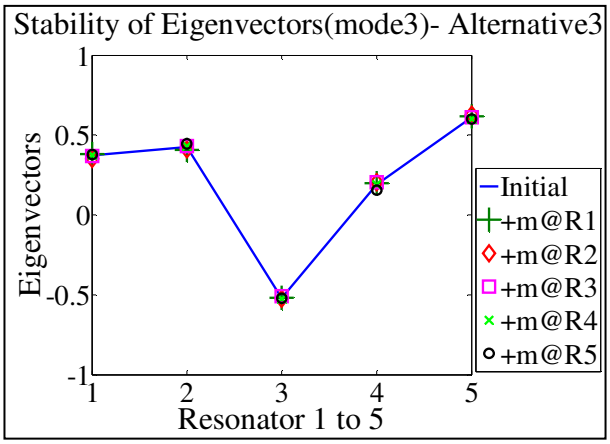

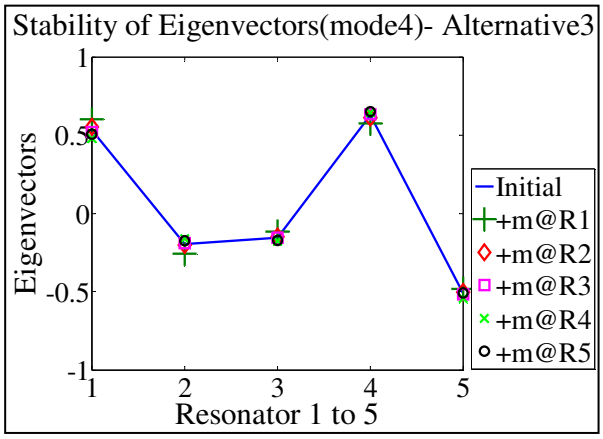

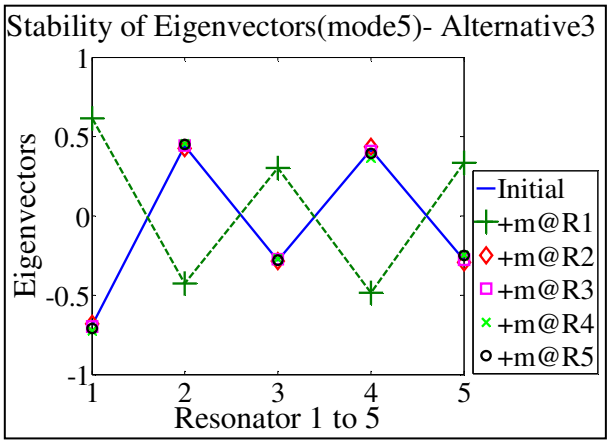

Eigenvectors Stability: Alternative 4

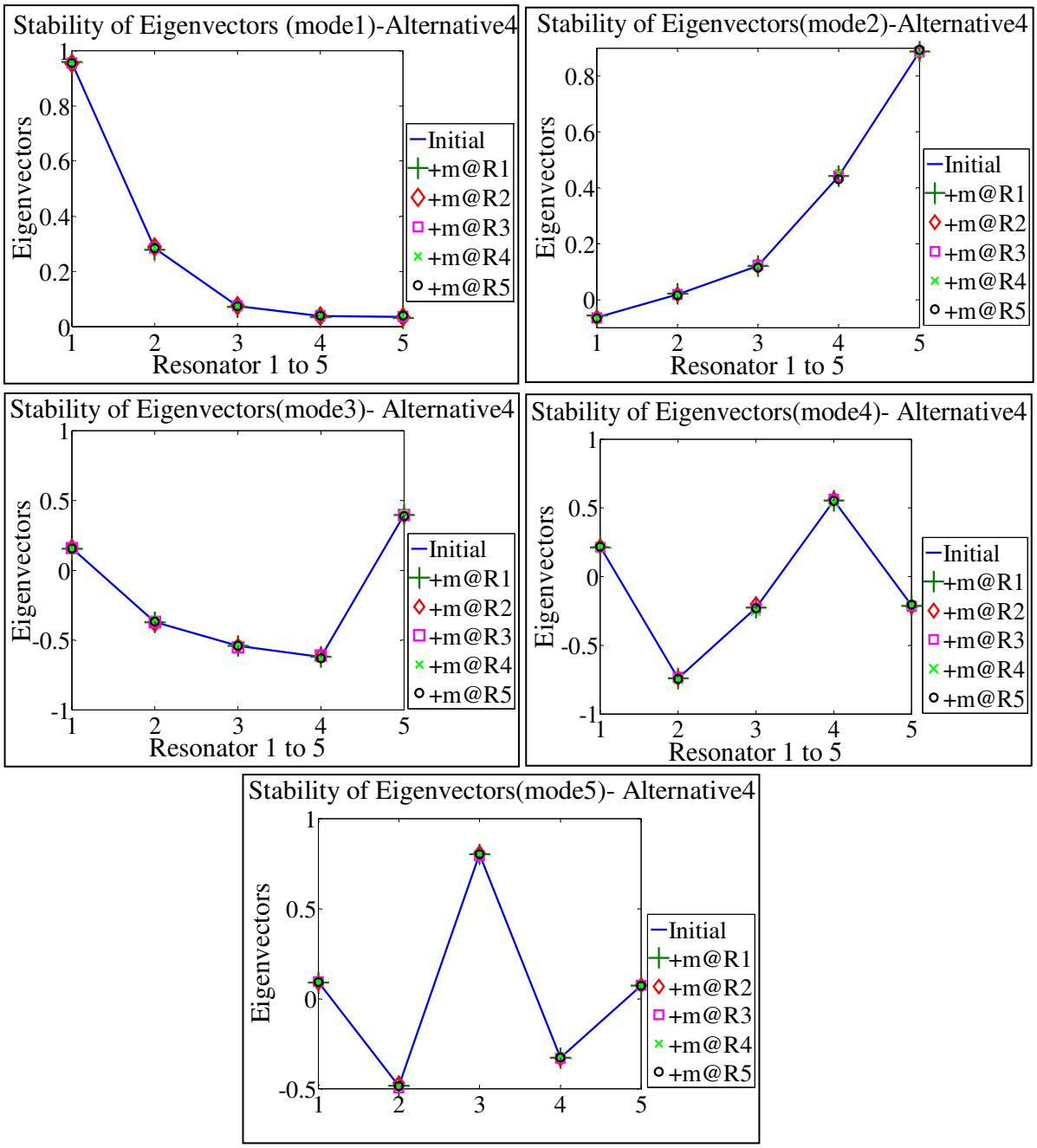

Eigenvectors Stability: Alternative 5

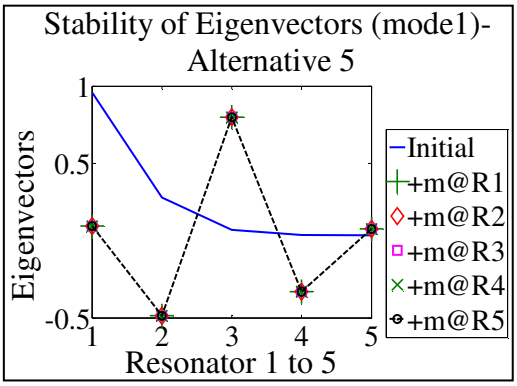

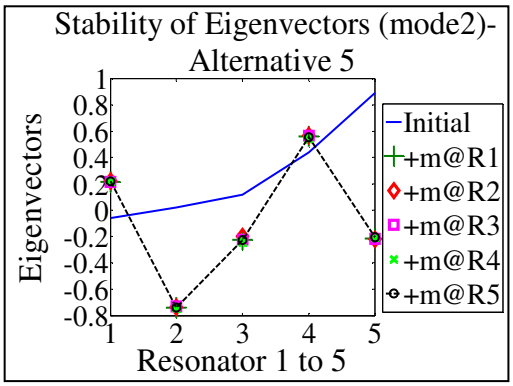

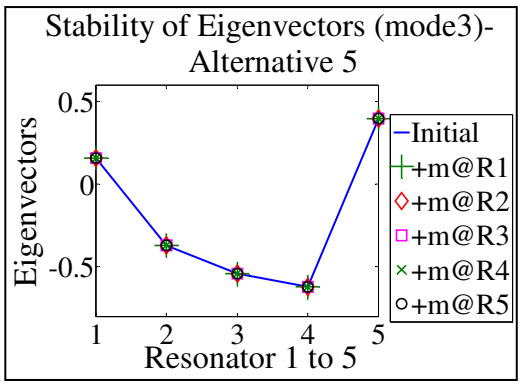

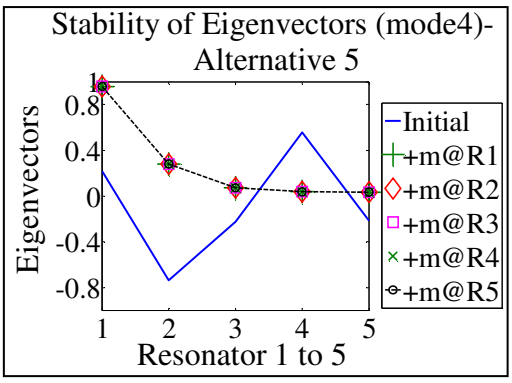

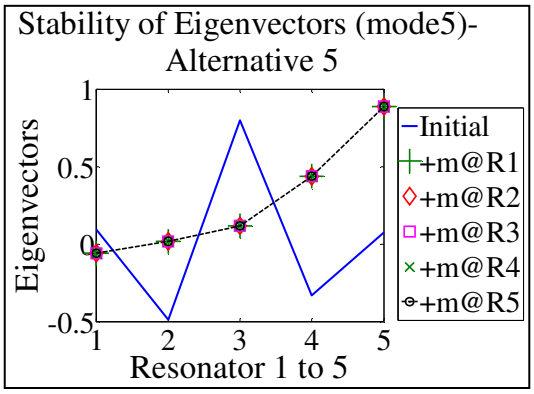

Eigenvectors Stability: Alternative 6

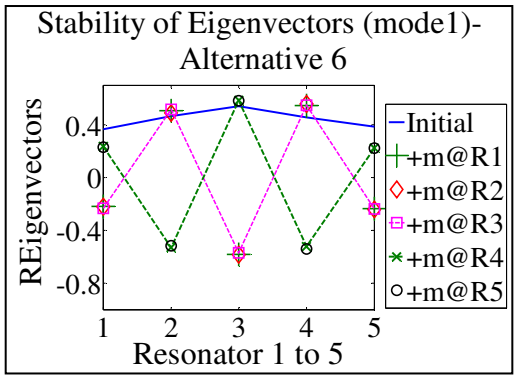

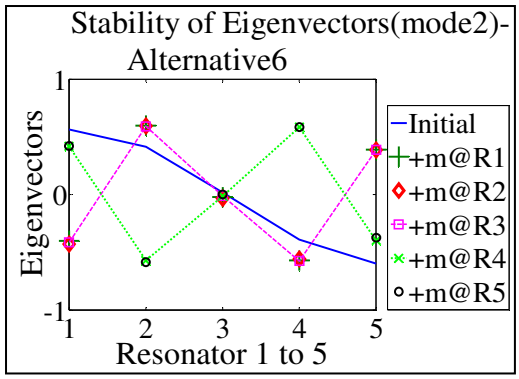

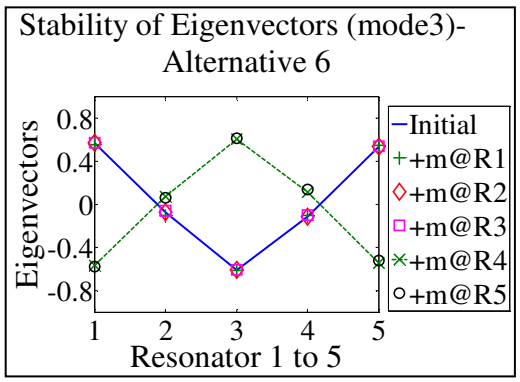

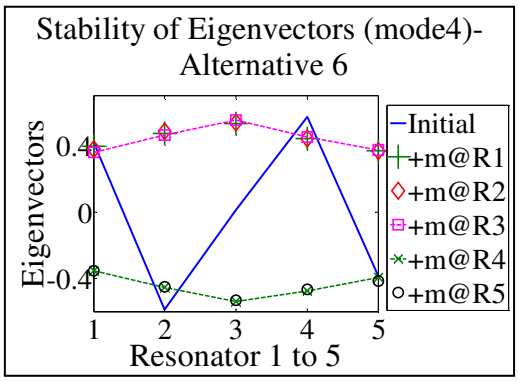

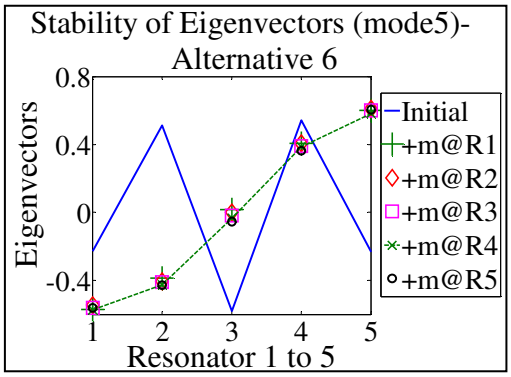

APPENDIX D

Eigenvectors of 5 Staggered Mass CMRA (Unperturbed (Initial) and Perturbed): Analysed using Lumped Mass Analysis (Chapter 5)

Note:

1. **IEA: Determination of mass change pattern of the resonator using Inverse Eigenvalue Analysis, Y-Successful; N-Failed
2. (*) Original ranked perturbed eigenvectors;
   (***) perturbed eigenvectors (ranked based on the unperturbed eigenvectors)
3. Highlighted eigenvectors:-
   - Incomparable perturbed eigenvectors;
   - Symmetrical perturbed eigenvectors

Table D-1 Perturbed mass: 3.0615 x 10^{-11}kg

Eigenvector/ Analysis Perturbed Mass [kg]	mode1	mode2	mode3	mode4	mode5
Initial	-0.1797	-0.3397	0.4649	-0.6413	-0.4920
	-0.5010	-0.5276	0.3787	0.3523	0.4400
	-0.7398	0.0438	-0.5412	0.0744	-0.3727
	-0.3734	0.5230	0.0948	-0.5231	0.5495
	-0.1731	0.5751	0.5818	0.4305	-0.3514
(*)(***)	-0.2535	-0.5280	0.5051	-0.6132	-0.1908
(+) 3.0615 x 10^{-11} at	-0.5190	-0.4810	0.1081	0.6194	0.3101
R1	-0.7174	0.1869	-0.5054	-0.1634	-0.3928
	-0.3544	0.4894	0.2326	-0.3029	0.7001
(**IEA:Y)	-0.1617	0.4641	0.6508	0.3492	-0.4722
(*)	-0.2162	-0.2943	0.3204	0.8202	0.3247
(+) 3.0615 x 10^{-11} at	-0.6572	-0.5219	0.2888	-0.3626	-0.2595
R2	-0.6527	0.2929	-0.5820	0.0158	0.3701
	-0.2853	0.5584	0.1676	0.3281	-0.6866
(**IEA:N)	-0.1183	0.4934	0.6687	-0.2965	0.4678
(***)	0.8202	-0.2943	0.3204	0.3247	-0.2162
	-0.3626	-0.5219	0.2888	-0.2595	-0.6572
	0.0158	0.2929	-0.5820	0.3701	-0.6527
	0.3281	0.5584	0.1676	-0.6866	-0.2853
	-0.2965	0.4934	0.6687	0.4678	-0.1183
(*)	0.1274	-0.3530	0.4517	0.5995	-0.5596
(+) 3.0615 x 10^{-11} at	0.4142	-0.5489	0.4551	-0.3266	0.4522
R3	0.8304	0.0443	-0.4527	-0.0754	-0.2888
(**IEA:N)	0.3274	0.5094	0.2088	0.5603	0.5229
	0.1247	0.5592	0.5834	-0.4629	-0.3542
(***)	0.5995	-0.3530	0.4517	-0.5596	0.1274
	-0.3266	-0.5489	0.4551	0.4522	0.4142
	-0.0754	0.0443	-0.4527	-0.2888	0.8304
	0.5603	0.5094	0.2088	0.5229	0.3274
	-0.4629	0.5592	0.5834	-0.3542	0.1247

(*)	0.1456	-0.3224	-0.4851	-0.3857	0.7139
(+) 3.0615 x 10^{-11} at	0.4268	-0.5746	-0.3983	0.1040	-0.5562
R4	0.7011	-0.1358	0.5627	0.2484	0.3129
	0.5067	0.5564	-0.0900	-0.6018	-0.2371
(**IEA:N)	0.2201	0.4877	-0.5303	0.6454	0.1639
(***)	-0.4851	-0.3857	0.7139	-0.3224	0.1456
	-0.3983	0.1040	-0.5562	-0.5746	0.4268
	0.5627	0.2484	0.3129	-0.1358	0.7011
	-0.0900	-0.6018	-0.2371	0.5564	0.5067
	-0.5303	0.6454	0.1639	0.4877	0.2201
(*)	-0.1664	-0.2234	-0.5162	0.5517	0.6096
	-0.4700	-0.4285	-0.5215	-0.2322	-0.5118
(+) 3.0615 x 10^{-11} at	-0.7142	-0.1781	0.5160	-0.2089	0.3671
R5	-0.4016	0.3795	0.1754	0.6838	-0.4420
	-0.2829	0.7686	-0.4058	-0.3613	0.1906
(**IEA:Y)					
(***)	-0.5162	-0.2234	-0.1664	0.5517	0.6096
	-0.5215	-0.4285	-0.4700	-0.2322	-0.5118
	0.5160	-0.1781	-0.7142	-0.2089	0.3671
	0.1754	0.3795	-0.4016	0.6838	-0.4420
	-0.4058	0.7686	-0.2829	-0.3613	0.1906

Table D-2 Perturbed mass: 1 x 10^{-11}kg

Eigenvector/ Analysis Perturbed Mass [kg]	mode1	mode2	mode3	mode4	mode5
Initial	-0.1797	-0.3397	0.4649	-0.6413	-0.4920
	-0.5010	-0.5276	0.3787	0.3523	0.4400
	-0.7398	0.0438	-0.5412	0.0744	-0.3727
	-0.3734	0.5230	0.0948	-0.5231	0.5495
	-0.1731	0.5751	0.5818	0.4305	-0.3514
(*)(***)	-0.1990	-0.3927	0.4929	-0.6781	-0.3434
(+) 1 x 10^{-11} at	-0.5061	-0.5222	0.3025	0.4729	0.3827
R1	-0.7345	0.0816	-0.5356	-0.0264	-0.3911
	-0.3686	0.5165	0.1334	-0.4155	0.6375
(**IEA: Y)	-0.1702	0.5474	0.6007	0.3783	-0.4198
(*)(***)	-0.1929	-0.3316	0.4115	-0.7141	-0.4357
(+) 1 x 10^{-11} at	-0.5509	-0.5390	0.3490	0.3680	0.3711
R2	-0.7172	0.1278	-0.5603	0.0378	-0.3754
	-0.3473	0.5351	0.1214	-0.4535	0.6091
(**IEA: Y)	-0.1561	0.5449	0.6165	0.3841	-0.4006
(*)	-0.1612	-0.3440	0.4611	0.6280	0.5158
(+) 1 x 10^{-11} at	-0.4720	-0.5346	0.4082	-0.3441	-0.4442
R3	-0.7732	0.0440	-0.5135	-0.0748	0.3419
(**IEA: N)	-0.3591	0.5187	0.1364	0.5356	-0.5424
	-0.1562	0.5700	0.5818	-0.4413	0.3545

(***)	0.6280	-0.3440	0.4611	0.5158	-0.1612
	-0.3441	-0.5346	0.4082	-0.4442	-0.4720
	-0.0748	0.0440	-0.5135	0.3419	-0.7732
	0.5356	0.5187	0.1364	-0.5424	-0.3591
	-0.4413	0.5700	0.5818	0.3545	-0.1562
(*)	0.1702	-0.3328	-0.4719	-0.5366	-0.6068
(+) 1 x 10^{-11} at	0.4810	-0.5408	-0.3854	0.2506	0.5058
R4	0.7313	-0.0104	0.5487	0.1548	-0.3556
	0.4120	0.5411	-0.0933	-0.5926	0.4159
(**IEA: N)	0.1877	0.5512	-0.5647	0.5236	-0.2768
(***)	-0.5366	-0.3328	-0.4719	-0.6068	0.1702
	0.2506	-0.5408	-0.3854	0.5058	0.4810
	0.1548	-0.0104	0.5487	-0.3556	0.7313
	-0.5926	0.5411	-0.0933	0.4159	0.4120
	0.5236	0.5512	-0.5647	-0.2768	0.1877
(*)	0.1768	-0.2975	-0.4862	0.6030	0.5466
(+) 1 x 10^{-11} at	0.4943	-0.4907	-0.4347	-0.3029	-0.4747
R5	0.7348	-0.0262	0.5382	-0.1302	0.3736
	0.3806	0.4908	0.0086	0.5955	-0.5072
(**IEA: Y)	0.1990	0.6551	-0.5338	-0.4160	0.2814
(***)	0.1768	-0.2975	-0.4862	0.6030	0.5466
	0.4943	-0.4907	-0.4347	-0.3029	-0.4747
	0.7348	-0.0262	0.5382	-0.1302	0.3736
	0.3806	0.4908	0.0086	0.5955	-0.5072
	0.1990	0.6551	-0.5338	-0.4160	0.2814

Table D-3 Perturbed mass: 7.6 x 10^{-12}kg

Eigenvector/ Analysis Perturbed Mass [kg]	mode1	mode2	mode3	mode4	mode5
Initial	-0.1797	-0.3397	0.4649	-0.6413	-0.4920
	-0.5010	-0.5276	0.3787	0.3523	0.4400
	-0.7398	0.0438	-0.5412	0.0744	-0.3727
	-0.3734	0.5230	0.0948	-0.5231	0.5495
	-0.1731	0.5751	0.5818	0.4305	-0.3514
(*)(***)	-0.1940	-0.3790	0.4871	-0.6760	-0.3735
(+) 7.6 x 10^{-12} at	-0.5048	-0.5241	0.3220	0.4481	0.3955
R1	-0.7359	0.0717	-0.5374	-0.0047	-0.3888
(**IEA: Y)	-0.3699	0.5184	0.1235	-0.4376	0.6220
	-0.1709	0.5548	0.5958	0.3882	-0.4074
(*)(***)	-0.1898	-0.3343	0.4238	-0.6979	-0.4497
(+) 7.6 x 10^{-12} at	-0.5387	-0.5374	0.3563	0.3655	0.3870
R2	-0.7231	0.1076	-0.5563	0.0461	-0.3752
	-0.3539	0.5323	0.1152	-0.4701	0.5961
(**IEA: Y)	-0.1603	0.5519	0.6088	0.3953	-0.3897

(*)(***) (+) 7.6 x 10^{-12} at **R3** (**IEA: Y)	-0.1655 -0.4789 -0.7655 -0.3626 -0.1602	-0.3430 -0.5329 0.0439 0.5197 0.5713	0.4620 0.4015 -0.5204 0.1268 0.5818	-0.6312 0.3461 0.0748 -0.5326 0.4387	-0.5102 0.4432 -0.3489 0.5443 -0.3540
(*) (+) 7.6 x 10^{-12} at **R4** (**IEA: N)	-0.1726 -0.4861 -0.7336 -0.4023 -0.1841	-0.3344 -0.5374 0.0030 0.5373 0.5574	-0.4703 -0.3839 0.5470 -0.0936 -0.5688	-0.5613 0.2741 0.1374 -0.5809 0.5035	0.5836 -0.4933 0.3608 -0.4462 0.2947
(***)	-0.5613 0.2741 0.1374 -0.5809 0.5035	-0.3344 -0.5374 0.0030 0.5373 0.5574	-0.4703 -0.3839 0.5470 -0.0936 -0.5688	0.5836 -0.4933 0.3608 -0.4462 0.2947	-0.1726 -0.4861 -0.7336 -0.4023 -0.1841
(*) (+) 7.6 x 10^{-12} at **R5** (**IEA: Y)	0.1776 0.4961 0.7362 0.3787 0.1921	-0.3078 -0.4998 -0.0089 0.5000 0.6367	-0.4813 -0.4218 0.5394 -0.0154 -0.5470	0.6113 -0.3138 -0.1180 0.5804 -0.4208	0.5353 -0.4677 0.3738 -0.5168 0.2963
(***)	0.1776 0.4961 0.7362 0.3787 0.1921	-0.3078 -0.4998 -0.0089 0.5000 0.6367	-0.4813 -0.4218 0.5394 -0.0154 -0.5470	0.6113 -0.3138 -0.1180 0.5804 -0.4208	0.5353 -0.4677 0.3738 -0.5168 0.2963

Table D-4 Perturbed mass: 1 x 10^{-12}kg

Eigenvector/ Analysis Perturbed Mass [kg]	mode1	mode2	mode3	mode4	mode5
Initial	-0.1797 -0.5010 -0.7398 -0.3734 -0.1731	-0.3397 -0.5276 0.0438 0.5230 0.5751	0.4649 0.3787 -0.5412 0.0948 0.5818	-0.6413 0.3523 0.0744 -0.5231 0.4305	-0.4920 0.4400 -0.3727 0.5495 -0.3514
(*)(***) (+) 1 x 10^{-12} at **R1** (**IEA: Y)	-0.1815 -0.5015 -0.7393 -0.3729 -0.1728	-0.3445 -0.5273 0.0472 0.5225 0.5727	0.4681 0.3717 -0.5409 0.0983 0.5836	-0.6488 0.3665 0.0632 -0.5108 0.4242	-0.4746 0.4341 -0.3758 0.5614 -0.3604
(*)(***) (+) 1x 10^{-12} at **R2** (**IEA: Y)	-0.1810 -0.5059 -0.7378 -0.3709 -0.1714	-0.3392 -0.5293 0.0521 0.5242 0.5720	0.4593 0.3758 -0.5435 0.0975 0.5856	-0.6491 0.3545 0.0706 -0.5162 0.4260	-0.4867 0.4328 -0.3732 0.5561 -0.3568

(+) 1x 10^{-12} at	-0.1778	-0.3401	0.4645	-0.6400	-0.4945
R3	-0.4981	-0.5283	0.3818	0.3515	0.4404
(**IEA: Y)	-0.7433	0.0438	-0.5386	0.0745	-0.3694
	-0.3720	0.5226	0.0991	-0.5244	0.5489
	-0.1714	0.5746	0.5818	0.4316	-0.3518
(*)(***)	-0.1788	-0.3389	0.4656	-0.6311	-0.5054
(+) 1x 10^{-12} at	-0.4992	-0.5288	0.3794	0.3421	0.4481
R4	-0.7391	0.0386	-0.5420	0.0832	-0.3717
	-0.3770	0.5251	0.0946	-0.5324	0.5358
(**IEA: Y)	-0.1745	0.5730	0.5801	0.4408	-0.3443
(*)	0.1794	-0.3356	-0.4671	-0.6371	-0.4984
(+) 1x 10^{-12} at	0.5004	-0.5241	-0.3844	0.3469	0.4442
R5	0.7394	0.0371	0.5412	0.0806	-0.3730
	0.3740	0.5205	-0.0841	-0.5315	0.5451
(**IEA: N)	0.1754	0.5834	-0.5780	0.4298	-0.3435
(***)	-0.6371	-0.3356	-0.4671	-0.4984	0.1794
	0.3469	-0.5241	-0.3844	0.4442	0.5004
	0.0806	0.0371	0.5412	-0.3730	0.7394
	-0.5315	0.5205	-0.0841	0.5451	0.3740
	0.4298	0.5834	-0.5780	-0.3435	0.1754

Table D-5 Perturbed mass: 1 x 10^{-13}kg

Eigenvector/ Analysis Perturbed Mass [kg]	mode1	mode2	mode3	mode4	mode5
Initial	-0.1797	-0.3397	0.4649	-0.6413	-0.4920
	-0.5010	-0.5276	0.3787	0.3523	0.4400
	-0.7398	0.0438	-0.5412	0.0744	-0.3727
	-0.3734	0.5230	0.0948	-0.5231	0.5495
	-0.1731	0.5751	0.5818	0.4305	-0.3514
(*)(***)	-0.1799	-0.3402	0.4652	-0.6421	-0.4902
(+) 1 x 10^{-13} at	-0.5011	-0.5276	0.3780	0.3538	0.4394
R1	-0.7398	0.0441	-0.5412	0.0733	-0.3730
	-0.3733	0.5230	0.0951	-0.5219	0.5507
(**IEA: Y)	-0.1731	0.5749	0.5820	0.4299	-0.3523
(*)(***)	-0.1798	-0.3396	0.4644	-0.6421	-0.4915
(+) 1x 10^{-13} at	-0.5015	-0.5278	0.3784	0.3525	0.4393
R2	-0.7396	0.0446	-0.5415	0.0740	-0.3727
	-0.3731	0.5231	0.0951	-0.5225	0.5502
(**IEA: Y)	-0.1729	0.5748	0.5822	0.4301	-0.3520
(*)(***)	-0.1795	-0.3397	0.4649	-0.6412	-0.4922
(+) 1x 10^{-13} at	-0.5007	-0.5277	0.3790	0.3522	0.4400
R3	-0.7402	0.0438	-0.5410	0.0744	-0.3723
(**IEA: Y)	-0.3732	0.5230	0.0952	-0.5233	0.5495
	-0.1729	0.5751	0.5818	0.4306	-0.3515

(*)(***)	-0.1796	-0.3396	0.4650	-0.6403	-0.4934
(+) 1x 10^{-13} at	-0.5008	-0.5277	0.3787	0.3513	0.4408
R4	-0.7398	0.0432	-0.5413	0.0753	-0.3726
	-0.3737	0.5232	0.0948	-0.5241	0.5481
(**IEA: Y)	-0.1732	0.5749	0.5817	0.4316	-0.3507
(*)(***)	-0.1797	-0.3393	0.4651	-0.6409	-0.4927
(+) 1x 10^{-13} at	-0.5010	-0.5273	0.3792	0.3518	0.4404
R5	-0.7398	0.0431	-0.5412	0.0750	-0.3727
	-0.3734	0.5228	0.0937	-0.5240	0.5491
(**IEA: Y)	-0.1733	0.5760	0.5815	0.4305	-0.3506

APPENDIX E

Eigenvectors of 5 Staggered Stiffness CMRA (Unperturbed (Initial) and Perturbed): Analysed using Lumped Mass Analysis (Chapter 5)

Note:

1. **IEA: Determination of mass change pattern of the resonator using Inverse Eigenvalue Analysis, Y-Successful; N-Failed
2. (*) Original ranked perturbed eigenvectors;
   (***) perturbed eigenvectors (ranked based on the unperturbed eigenvectors)
3. Highlighted eigenvectors:-
   - Incomparable perturbed eigenvectors;
   - Symmetrical perturbed eigenvectors

Table E-1 Perturbed mass: 3.0615 x 10^{-11}kg

Eigenvector/ Analysis Perturbed Mass [kg]	mode1	mode2	mode3	mode4	mode5
Initial	-0.2153	0.6307	0.5632	-0.3659	0.3240
	-0.3851	0.5064	-0.0537	0.4931	-0.5910
	-0.6638	0.0261	-0.5846	-0.0552	0.4619
	-0.5621	-0.4948	0.3218	-0.3987	-0.4199
	-0.2207	-0.3167	0.4843	0.6789	0.3950
(*) (***)	0.4112	-0.7391	0.3928	-0.2877	0.2036
(+) 3.0615 x 10^{-11} at	0.4342	-0.2928	-0.2857	0.6027	-0.5312
R1	0.6119	0.2406	-0.5614	-0.1728	0.4730
	0.4837	0.4964	0.4356	-0.3224	-0.4773
(**IEA:Y)	0.1846	0.2523	0.5091	0.6483	0.4741
(*)	-0.2788	0.4975	0.5926	0.5407	0.1825
(+) 3.0615 x 10^{-11} at	-0.5470	0.5064	-0.0551	-0.5853	-0.3027
R2	-0.6247	-0.1440	-0.5692	0.2926	0.4249
	-0.4529	-0.6008	0.3147	0.1620	-0.5569
(**IEA:Y)	-0.1664	-0.3381	0.4719	-0.5031	0.6200
(***)	-0.2788	0.4975	0.5926	0.1825	0.5407
	-0.5470	0.5064	-0.0551	-0.3027	-0.5853
	-0.6247	-0.1440	-0.5692	0.4249	0.2926
	-0.4529	-0.6008	0.3147	-0.5569	0.1620
	-0.1664	-0.3381	0.4719	0.6200	-0.5031
(*) (***)	-0.1567	0.6209	0.5620	-0.3902	0.3508
(+) 3.0615 x 10^{-11} at	-0.3464	0.4989	0.0860	0.5249	-0.5911
R3	-0.7804	0.0265	-0.5064	-0.0566	0.3535
(**IEA:Y)	-0.4705	-0.5088	0.4371	-0.3807	-0.4308
	-0.1584	-0.3256	0.4788	0.6512	0.4659
(*) (***)	-0.1223	0.5957	0.6300	-0.2681	-0.4035
(+) 3.0615 x 10^{-11} at	-0.2606	0.5832	-0.0156	0.3265	0.6976
R4	-0.5617	0.2635	-0.6373	0.0318	-0.4580
	-0.7330	-0.4207	0.2627	-0.3767	0.2610
(**IEA:N)	-0.2537	-0.2420	0.3574	0.8238	-0.2696

(*) (***)	-0.1892	0.5543	-0.6108	-0.3665	0.3900
(+) 3.0615 x 10^{-11} at	-0.3494	0.5150	-0.0842	0.3678	-0.6869
R5	-0.6287	0.1786	0.5576	0.1790	0.4806
	-0.5843	-0.4137	-0.0413	-0.6126	-0.3348
(**IEA:Y)	-0.3247	-0.4738	-0.5543	0.5684	0.1817

Table E-2 Perturbed mass: 1 x 10^{-11}kg

Eigenvector/ Analysis Perturbed Mass [kg]	mode1	mode2	mode3	mode4	mode5
Initial	-0.2153	0.6307	0.5632	-0.3659	0.3240
	-0.3851	0.5064	-0.0537	0.4931	-0.5910
	-0.6638	0.0261	-0.5846	-0.0552	0.4619
	-0.5621	-0.4948	0.3218	-0.3987	-0.4199
	-0.2207	-0.3167	0.4843	0.6789	0.3950
(*) (***)	-0.2583	0.6919	0.5110	-0.3408	0.2743
(+) 1 x 10^{-11} at	-0.3978	0.4522	-0.1465	0.5408	-0.5691
R1	-0.6556	-0.0524	-0.5808	-0.1025	0.4686
	-0.5473	-0.4814	0.3675	-0.3688	-0.4448
(**IEA:Y)	-0.2136	-0.2867	0.4950	0.6670	0.4283
(*) (***)	-0.2360	0.5913	0.5727	-0.4370	0.2764
(+) 1 x 10^{-11} at	-0.4324	0.5161	-0.0542	0.5557	-0.4821
R2	-0.6564	-0.0234	-0.5798	-0.1472	0.4591
	-0.5330	-0.5280	0.3196	-0.3149	-0.4860
(**IEA:Y)	-0.2057	-0.3235	0.4804	0.6159	0.4941
(*) (***)	-0.1959	0.6275	0.5623	-0.3738	0.3355
(+) 1 x 10^{-11} at	-0.3744	0.5040	-0.0036	0.5035	-0.5939
R3	-0.7051	0.0263	-0.5640	-0.0557	0.4224
(**IEA:Y)	-0.5332	-0.4994	0.3639	-0.3930	-0.4240
	-0.1997	-0.3196	0.4830	0.6702	0.4201
(*) (***)	-0.1836	0.6186	0.5890	-0.3310	-0.3577
(+) 1 x 10^{-11} at	-0.3452	0.5360	-0.0407	0.4315	0.6374
R4	-0.6365	0.1108	-0.6063	-0.0186	-0.4636
	-0.6217	-0.4802	0.3028	-0.4006	0.3579
(**IEA:Y)	-0.2355	-0.2953	0.4383	0.7372	-0.3504
(*) (***)	-0.2087	0.6122	0.5743	-0.3522	-0.3588
(+) 1 x 10^{-11} at	-0.3763	0.5102	-0.0155	0.4304	0.6427
R5	-0.6558	0.0653	-0.5815	0.0386	-0.4755
	-0.5689	-0.4795	0.2423	-0.4917	0.3825
(**IEA:Y)	-0.2475	-0.3615	0.5226	0.6689	-0.2929

Table E-3 Perturbed mass: 7.6 x 10^{-12}kg

Eigenvector/ Analysis Perturbed Mass [kg]	mode1	mode2	mode3	mode4	mode5
Initial	-0.2153	0.6307	0.5632	-0.3659	0.3240
	-0.3851	0.5064	-0.0537	0.4931	-0.5910
	-0.6638	0.0261	-0.5846	-0.0552	0.4619
	-0.5621	-0.4948	0.3218	-0.3987	-0.4199
	-0.2207	-0.3167	0.4843	0.6789	0.3950
(*) (***)	-0.2467	0.6788	0.5245	-0.3470	0.2852
(+) 7.6 x 10^{-12} at	-0.3944	0.4667	-0.1256	0.5307	-0.5742
R1	-0.6580	-0.0329	-0.5822	-0.0921	0.4674
	-0.5515	-0.4840	0.3572	-0.3755	-0.4395
(**IEA: Y)	-0.2156	-0.2935	0.4926	0.6696	0.4212
(*) (***)	-0.2309	0.6012	0.5704	-0.4209	0.2887
(+) 7.6 x 10^{-12} at	-0.4205	0.5145	-0.0541	0.5436	-0.5082
R2	-0.6586	-0.0109	-0.5809	-0.1257	0.4613
	-0.5406	-0.5198	0.3201	-0.3354	-0.4720
(**IEA: Y)	-0.2095	-0.3218	0.4814	0.6317	0.4721
(*) (***)	-0.2005	0.6283	0.5624	-0.3719	0.3330
(+) 7.6 x 10^{-12} at	-0.3772	0.5045	-0.0153	0.5010	-0.5935
R3	-0.6954	0.0262	-0.5695	-0.0556	0.4315
(**IEA: Y)	-0.5403	-0.4983	0.3542	-0.3944	-0.4231
	-0.2047	-0.3189	0.4834	0.6723	0.4143
(*) (***)	-0.1912	0.6214	0.5832	-0.3392	-0.3503
(+) 7.6 x 10^{-12} at	-0.3551	0.5292	-0.0438	0.4458	0.6274
R4	-0.6437	0.0908	-0.6015	-0.0266	-0.4636
	-0.6075	-0.4848	0.3075	-0.4011	0.3719
(**IEA: Y)	-0.2322	-0.3009	0.4490	0.7243	-0.3610
(*) (***)	-0.2104	0.6171	0.5713	-0.3537	-0.3522
(+) 7.6 x 10^{-12} at	-0.3786	0.5094	-0.0253	0.4428	0.6332
R5	-0.6579	0.0550	-0.5827	0.0181	-0.4735
	-0.5672	-0.4839	0.2627	-0.4720	0.3906
(**IEA: Y)	-0.2405	-0.3501	0.5143	0.6751	-0.3134

Table E-4 Perturbed mass: 1 x 10^{-12}kg

Eigenvector/ Analysis Perturbed Mass [kg]	mode1	mode2	mode3	mode4	mode5
Initial	-0.2153	0.6307	0.5632	-0.3659	0.3240
	-0.3851	0.5064	-0.0537	0.4931	-0.5910
	-0.6638	0.0261	-0.5846	-0.0552	0.4619
	-0.5621	-0.4948	0.3218	-0.3987	-0.4199
	-0.2207	-0.3167	0.4843	0.6789	0.3950

(*) (***)	-0.2190	0.6375	0.5586	-0.3636	0.3185
(+) 1 x 10^{-12} at	-0.3862	0.5017	-0.0636	0.4986	-0.5887
R1	-0.6632	0.0186	-0.5845	-0.0604	0.4628
	-0.5609	-0.4933	0.3267	-0.3955	-0.4228
(**IEA: Y)	-0.2201	-0.3136	0.4854	0.6776	0.3988
(*) (***)	-0.2173	0.6269	0.5641	-0.3734	0.3199
(+) 1x 10^{-12} at	-0.3895	0.5077	-0.0538	0.5007	-0.5803
R2	-0.6633	0.0215	-0.5841	-0.0645	0.4624
	-0.5595	-0.4980	0.3216	-0.3907	-0.4273
(**IEA: Y)	-0.2193	-0.3174	0.4840	0.6731	0.4056
(*) (***)	-0.2134	0.6303	0.5631	-0.3667	0.3253
(+) 1x 10^{-12} at	-0.3841	0.5061	-0.0485	0.4942	-0.5914
R3	-0.6681	0.0262	-0.5829	-0.0552	0.4578
(**IEA: Y)	-0.5593	-0.4953	0.3262	-0.3981	-0.4204
	-0.2186	-0.3170	0.4842	0.6781	0.3976
(*) (***)	-0.2122	0.6294	0.5660	-0.3624	0.3278
(+) 1x 10^{-12} at	-0.3812	0.5095	-0.0524	0.4868	-0.5962
R4	-0.6614	0.0347	-0.5870	-0.0512	0.4623
	-0.5681	-0.4939	0.3200	-0.3994	-0.4133
(**IEA: Y)	-0.2223	-0.3148	0.4796	0.6853	0.3906
(*) (***)	-0.2147	0.6290	0.5642	-0.3636	0.3285
(+) 1x 10^{-12} at	-0.3843	0.5068	-0.0502	0.4855	-0.5978
R5	-0.6631	0.0297	-0.5845	-0.0448	0.4641
	-0.5628	-0.4936	0.3145	-0.4094	-0.4158
(**IEA: Y)	-0.2231	-0.3209	0.4885	0.6801	0.3827

Table E-5 Perturbed mass: 1 x 10^{-13}kg

Eigenvector/ Analysis Perturbed Mass [kg]	mode1	mode2	mode3	mode4	mode5
Initial	-0.2153	0.6307	0.5632	-0.3659	0.3240
	-0.3851	0.5064	-0.0537	0.4931	-0.5910
	-0.6638	0.0261	-0.5846	-0.0552	0.4619
	-0.5621	-0.4948	0.3218	-0.3987	-0.4199
	-0.2207	-0.3167	0.4843	0.6789	0.3950
(*) (***)	-0.2157	0.6313	0.5627	-0.3657	0.3235
(+) 1 x 10^{-13} at	-0.3852	0.5059	-0.0547	0.4937	-0.5907
R1	-0.6638	0.0254	-0.5846	-0.0557	0.4620
	-0.5620	-0.4947	0.3223	-0.3983	-0.4202
(**IEA: Y)	-0.2206	-0.3164	0.4844	0.6788	0.3954
(*) (***)	-0.2155	0.6303	0.5633	-0.3667	0.3236
(+) 1x 10^{-13} at	-0.3855	0.5065	-0.0537	0.4939	-0.5899
R2	-0.6638	0.0257	-0.5846	-0.0561	0.4620
	-0.5619	-0.4952	0.3218	-0.3979	-0.4207
(**IEA: Y)	-0.2205	-0.3168	0.4843	0.6784	0.3961

(*) (***)	-0.2151	0.6306	0.5632	-0.3660	0.3242
(+) 1x 10^{-13} at	-0.3850	0.5063	-0.0532	0.4932	-0.5910
R3	-0.6643	0.0261	-0.5844	-0.0552	0.4615
(**IEA: Y)	-0.5619	-0.4949	0.3223	-0.3986	-0.4200
	-0.2205	-0.3168	0.4843	0.6788	0.3953
(*) (***)	-0.2150	0.6305	0.5635	-0.3656	0.3244
(+) 1x 10^{-13} at	-0.3847	0.5067	-0.0536	0.4925	-0.5915
R4	-0.6636	0.0270	-0.5849	-0.0548	0.4620
	-0.5627	-0.4948	0.3216	-0.3988	-0.4192
(**IEA: Y)	-0.2208	-0.3165	0.4839	0.6796	0.3946
(*) (***)	-0.2152	0.6305	0.5633	-0.3657	0.3245
(+) 1x 10^{-13} at	-0.3850	0.5064	-0.0534	0.4924	-0.5917
R5	-0.6638	0.0265	-0.5846	-0.0541	0.4622
	-0.5622	-0.4947	0.3211	-0.3998	-0.4195
(**IEA: Y)	-0.2209	-0.3171	0.4848	0.6791	0.3938

Effective Mass and Stiffness of Comb-Drive Resonator

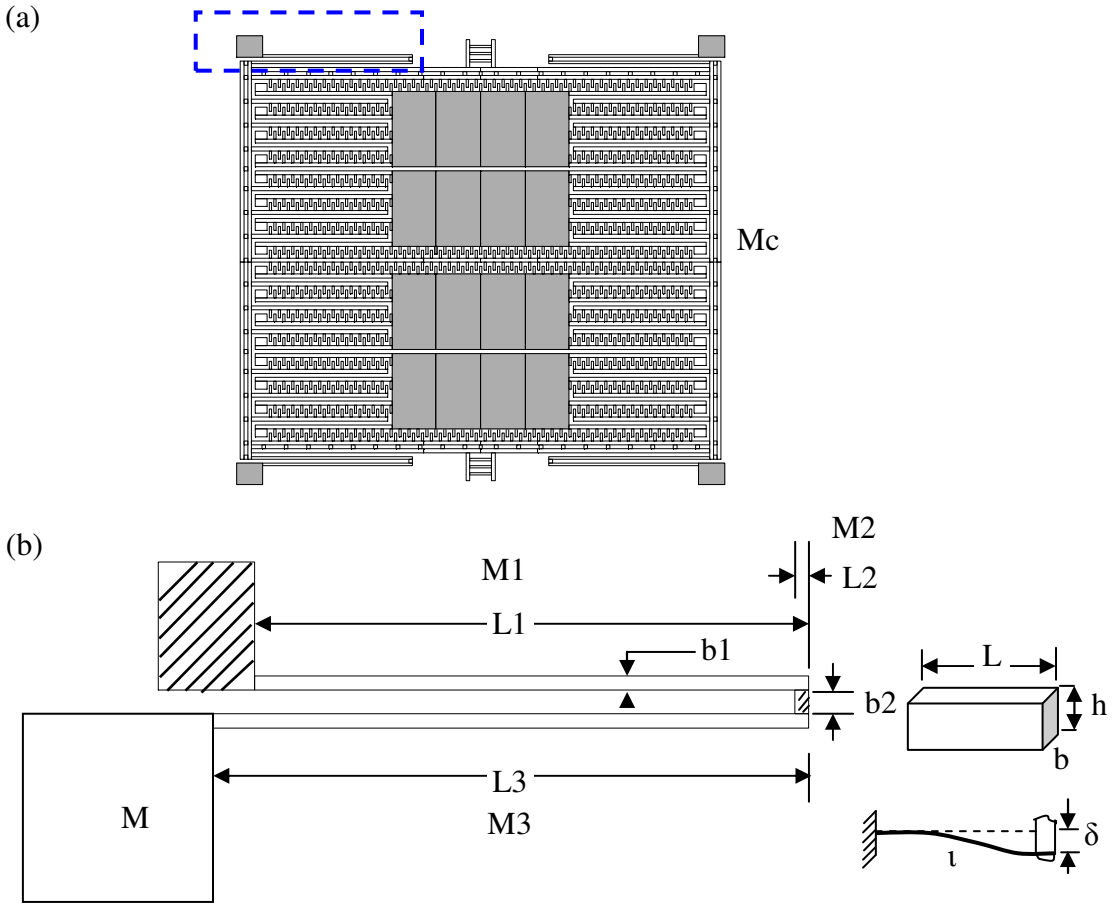

Figure F.1 (a) Integrated comb-drive resonator; (b) An anchor spring of the resonator

By assuming beam 2 is rigid, and two beams of beam 1 and beam 3 are in series, stiffness of an anchor spring, k [1];

$$k=\frac{k_1 k_3}{k_1+k_3};\quad k_1=\frac{12EI_1}{(L_1)^3};\quad k_3=\frac{12EI_3}{(L_3)^3};\ I_1=\frac{h(b_1)^3}{12};\ I_3=\frac{h(b_3)^3}{12}$$

Assuming width of beam 1, b1 = b3 = b; Stiffness of an anchor spring, k;

$$k=\frac{Ehb^3}{(L_1)^3+(L_3)^3} \qquad \text{(Equation F-1)}$$

or if L1 = L3, then;

$$k=\frac{Ehb^3}{2L^3} \qquad \text{(Equation F-2)}$$

Where E: Young's Modulus; k: beam stiffness; h: thickness of device; b: width of the beam; I: second moment of area

Effective mass of resonator,

$$M_R = M_c + \frac{13M_1}{35} + \frac{M_2}{4} + M_3\left[\frac{13}{35}\left(\frac{L_3}{L_1}\right)^6 + 1 + 2\left(\frac{L_3}{L_1}\right)^2 - \left(\frac{L_3}{L_1}\right)^3\right]$$

(Equation F-3)

Where M_c: concentrated mass of resonator (refer to Figure 1(a)), M_1-M_3: mass of anchor spring element (refer to Figure F.1(b))

Parameter/ Method Estimation	Finite Element Analysis	Numerical Analysis	Error (%) Numerical Analysis// FEA
Stiffness of Resonator, k_R	19.9796 N/m	21.6977 N/m	8.6%
Effective mass of resonator, m_R	3.0615nkg	3.1728nkg	3.64%
Natural Frequency	12857.3 Hz	13161Hz	2.36%

Bibliography:

1. W.T. Thomson and M.D. Dahleh. *Theory of Vibration and Applications*, 5th Edition: Prentice Hall, 1998.
2. Rayleigh–Ritz method. http://en.wikipedia.org/wiki/Rayleigh-Ritz_method, 2008 (Accessed).

Manufacturing Variation Impact on Frequency Response of A Single Comb-Drive Resonator

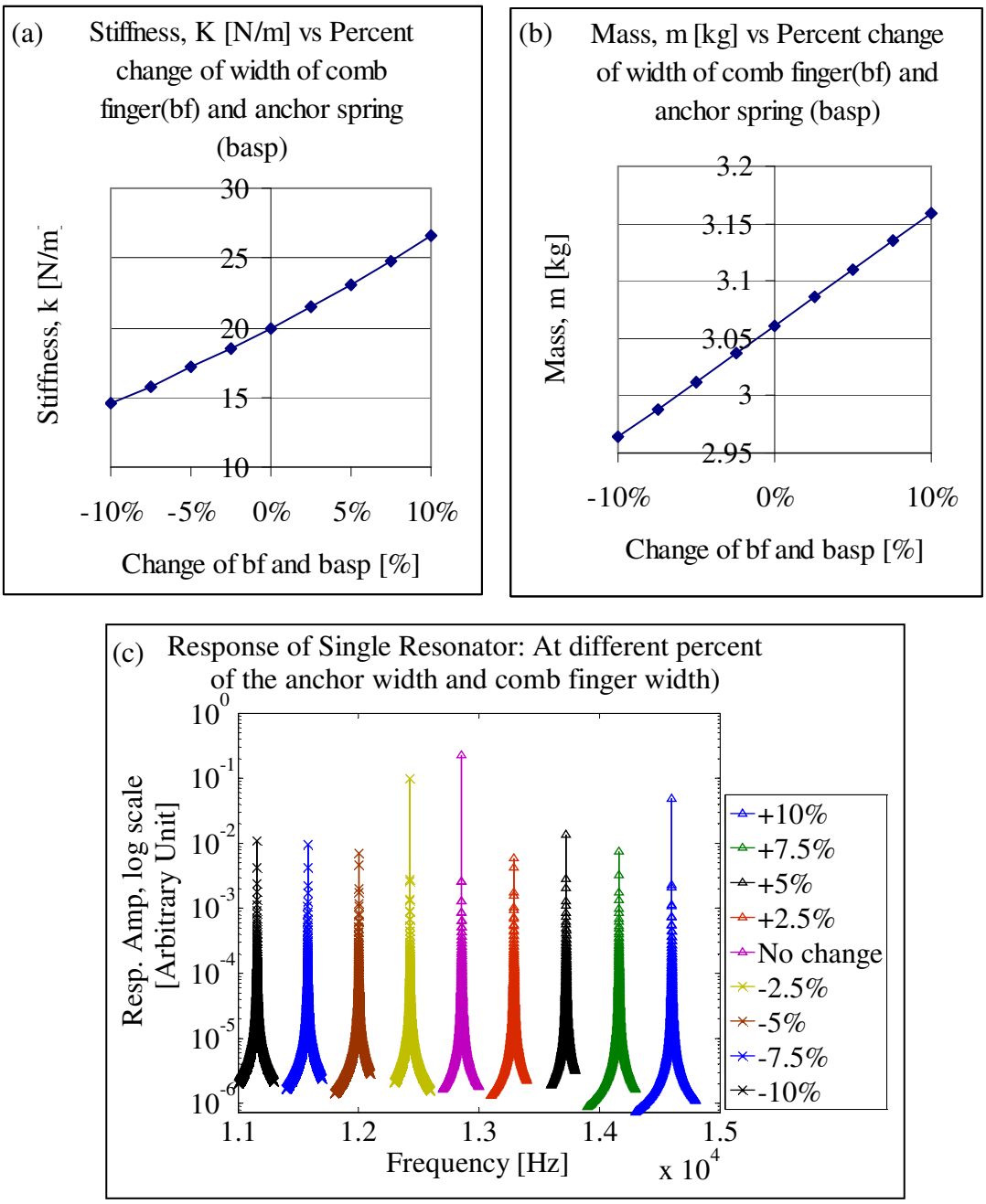

Figure G.1 Estimated change of effective mass, stiffness and frequency response of comb-drive resonator using numerical analysis (refer to Appendix F); (assumption: only width of resonator anchor spring (b_{ASP}) and width of comb fingers (b_{ASP}) vary at similar amount of change)

Table G-1 Details of analysis result (Figure G.1)

% of change of b_f and b_{ASP}	Resonator Stiffness, k [N/m]	Resonator Mass, m [nkg]	Ratio: % of $\Delta k/\Delta m$	Resonant Frequency [Hz]
-10%	14.5625	2.9635	8.5	11158
-7.5%	15.8110	2.9880	8.7	11578
-5.0%	17.1274	3.0125	8.9	12002
-2.5%	18.5158	3.0370	9.2	12428
0	19.976	3.0615	0	12858
+2.5%	21.5122	3.0860	9.6	13290
+5.0%	23.1242	3.1105	9.9	13725
+7.5%	24.8162	3.1350	10.1	14162
+10.0%	26.5881	3.1595	10.3	14602

APPENDIX H

Sample of Geometrical Measurements and Manufacturing Data Analysis – Measured on a Single In-House Chip

Table H-1 Sample of measurements and manufacturing variation data analysis – measured on a single in-house chip (Single integrated comb-drive resonator, SingleR-v2 (Chip3))

Dimension / (no. of N samples)	Mean - nominal Parameter, μo [μm]	Mean - fabricated parameter, μ [μm]	Standard deviation σ	Manufacturing tolerance $V1$[%]	Part to part variation $V2$ [%]
Anchor Spring width, b_{ASP} / (24)	3	3.4093	0.0503	[13.64]	1.68
Anchor Spring Length, L_{ASP} (24)	201 (s) 216 (L)	198.9260 214.1720	0.6030 0.4870	[-1.03] [-0.85]	0.30 0.23
Width of Linked Mass, b_{LM} (12)	39	38.7423	0.3045	[-0.60]	0.78
Length of Linked Mass, L_{LM} (12)	35	34.588	0.3136	[-1.18]	0.90
Comb finger Width, b_f (24)	3	3.3717	0.0591	[12.39]	1.97
Comb finger Length, L_f(24)	10	9.9591	0.0706	[-0.41]	0.71

Table H-2 Sample of measurements and manufacturing variation data analysis – measured on a single in-house chip (Staggered Mass CMRA (Chip8))

Dimension / (no. of N samples)	Mean - nominal Parameter, μo [μm]	Mean - fabricated parameter, μ [μm]	Standard deviation σ	Manufacturing tolerance $V1$[%]	Part to part variation $V2$ [%]
Anchor Spring width, b_{ASP} / (20)	3	3.1954	0.0495	[6.51]	1.65
Anchor Spring Length, L_{ASP} (20)	201 (s) 216 (L)	198.4890 213.2570	0.3280 0.5040	[-1.25] [-1.27]	0.16 0.23
Comb finger Width, b_f (20)	3	3.1733	0.0503	[5.78]	1.68
Comb finger Length, L_f(20)	10	10.0385	0.0758	[0.39]	0.76

Table H-3 Sample of measurements and manufacturing variation data analysis – measured on a single in-house chip (Staggered Stiffness CMRA (Chip10))

Dimension / (no. of N samples)	Mean - nominal Parameter, μo [μm]	Mean - fabricated parameter, μ [μm]	Standard deviation σ	Manufacturing tolerance $V1$[%]	Part to part variation $V2$ [%]
Anchor Spring width, b_{ASP} / (20)	3	3.7676	0.0316	[25.59]	1.05
Comb finger Width, b_f (20)	3	3.7980	0.0507	[26.60]	1.69
Comb finger Length, L_f (20)	10	9.8629	0.0580	[-1.37]	0.58

LIST OF REFERENCES

[1] J.W. Gardner and P.N. Bartlett. A brief history of electronic noses. *Sensors and Actuators B*, 18-19(1-3):211-220, 1994.

[2] Alpha M.O.S. Electronic noses. *http://www.alpha-mos.com/products_technology/electronic_nose.html*, 2008 (Accessed).

[3] M. Karen. Electronic Nose. *http://science.nasa.gov/headlines/y2004/06oct_enose.htm*, 2004.

[4] W. Jatmiko, T. Fukuda, F. Arai, and B. Kusumoputro. Artificial Odour Discrimination System Using Multiple Quartz Resonator Sensors and Neural Network for Recognizing Fragrance Mixtures. *IEEE Sensors*, 6:223-233, 2006.

[5] T. Tan, Q. Lucas, L. Moy, J.W. Gardner, and P.N. Bartlett. The electronic Nose- A New Instrument for sensing vapours. *LC-GC International*, 8(4):198-200, 1995.

[6] J.W. Gardner and P.N. Bartlett. Performance Definition and Standardisation of Electronic Noses. *Sensors and Actuators B*, 33:60-67, 1996.

[7] J.W. Gardner and J. Yinon (Editor). *Electronic Noses & Sensors for the Detection of Explosives,* NATO Science Series (II. Mathematics, Physics, and Chemistry – volume 159): Kluwers Academic Publishers, The Netherlands, 2004.

[8] J.W. Gardner and W.E. Gardner. The role of the electronic nose in condition monitoring. *36th Annual British Conference on NDT*, 39(12):865-869, 1997.

[9] T.C. Pearce, J.W. Gardner, and F. Sharon. Electronic Nose for Monitoring the Flavour of Beers. *ANALYST*, 118:371-377, 1993.

[10] E. Llobet, E.L. Hines, J.W. Gardner, P.N. Bartlett, and T.T. Mottram. Fuzzy ARTMAP based electronic nose data analysis. *Sensors and Actuators B*, 61:183-190, 1999.

[11] Ritaban Dutta, Aruneema Das, Nigel G. Stocks, and David Morgan. Stochastic-resonance based electronic nose: a novel way to classify bacteria. *Sensors and Actuators B*, 115:17-27, 2006.

[12] J.A. Covington, J.W. Gardner, A. Hamilton, T. C. Pearce, and S.L. Tan. Towards a truly Biomimetic Olfactory Microsystems: An Artificial Olfactory Mucosa. *IET Nanobiotechnology*, 1(2):15-21, 2007.

[13] J.W. Gardner and P.N. Bartlett (Editor). *Sensors and sensory systems for an electronic nose,* NATO ASI Series, Series E (Applied Sciences – volume 212): Kluwers Academic Publishers, The Netherlands, 1992.

[14] H. Troy Nagle, Ricardo Gutiekrez-Osuna, and Susan S. Schiffman. The How and Why of Electronic noses. *IEEE Spectrum*, 35(9):22-31, 1998.

[15] Keith J. Albert, Nathan S. Lewis, Caroline L. Schauer, Gregory A. Sotzing, Shannon E. Stitzel, Thomas P. Vaid, and David R. Walt. Cross-Reactive Chemical Sensor Arrays. *Chem. Rev.*, 100:2595-2626, 2000.

[16] H.V. Shurmer and J.W. Gardner. Odour discrimination with an electronic nose. *Sensors and Actuators B*, 8:1-11, 1992.

[17] E. Llobet, J. Rubio, X. Vilanova, J. Brezmes, X. Correig, J.W. Gardner, and E.L. Hines. Electronic nose simulation tool centred on Pspice. *Sensors and Actuators B*, 76:419-429, 2001.

[18] Takamichi Nakamoto, Katsufumi Fukunishi, and Toyosaka Moriizumi. Identification capability of odour sensor using quartz-resonator array and neural-network pattern recognition. *Sensor and Actuators B*, 1:473-476, 1990.

[19] T. Nakamoto, A. Fukuda, and T. Moriizumi. Perfume and flavour identification by odour-sensing system using quartz-resonator sensor array and neural-network pattern recognition. *Sensor and Actuators B*, 10:85-90, 1993.

[20] Nicola Ulivieri, Cosimo Distante, Tondi Luca, Santina Rocchi, Pietro Siciliano. IEEE1451.4: A way to standardize gas sensor. *Sensors and Actuators B*, 114:141-151, 2006.

[21] Peter R Hauptmann. Selected examples of intelligent (micro) sensor systems: state-of-the-art and tendencies. *Measurement Science and Technology*, 17:459-466, 2006.

[22] Laura A. Oropeza-Ramos, Christopher B. Burgner, and Kimberly L. Turner. Robust micro-rate sensor actuated by parametric resonance. *Sensors and Actuators A*, 152:80-87, 2009.

[23] M. Shavezipura, K. Ponnambalamb, A. Khajepoura, and S.M. Hashemic. Fabrication uncertainties and yield optimization in MEMS tunable capacitors. *Sensors and Actuators A*, 147:613-622, 2008.

[24] Rong Liu, Brad Paden, and Kimberly Turner. MEMS Resonators That Are Robust to Process-Induced Feature Width Variations. *Journal of Microelectromechanical Systems*, 11(5):505-511, 2002.

[25] Odorant receptors and the organization of the olfactory system. *http://nobelprize.org/nobel_prizes/medicine/laureates/2004/odorant_high_eng.jpg*, 2008 (Accessed).

[26] Eric H. Chudler. Smell - The Nose Knows. *http://faculty.washington.edu/chudler/nosek.html*, 1996-2008.

[27] John C. Leffingwell. Olfaction - A review. *http://www.leffingwell.com/olfaction.htm*, 1999.

[28] Stuart Firestein. How the olfactory system makes sense of scents. *Nature*, 413(6853):211-218, 2001.

[29] Yale Center for Advanced Instructional Media. Cranial Nerve I - Olfactory Nerve. *http://www.med.yale.edu/caim/cnerves/cn1/cn1_2.html*, 1998.

[30] Kensaku Mori, Harald von Campenhausen, and Yoshihiro Yoshihara. Zonal organization of the mammalian main and accessory olfactory systems. *Philosophical Transactions of the Royal Society B: Biological Sciences*, 355(1404):1801-1812, 2000.

[31] Anna Menini, Laura Lagostena, and Anna Boccaccio. Olfaction: From Odorant Molecules to the Olfactory Cortex. *News in Physiological Sciences*, 19:101-104, 2004.

[32] P.K. Gupta. The 2004 Nobel Prize in Physiology or Medicine: 'Odorant receptors and organization of the olfactory system'. *Current Science*, 87(11):1500-1504, 2004.

[33] A.I. Athamneh, B.W. Zoecklein, and K. Mallikarjunan. Electronic Nose Evaluation of Cabernet Sauvignon Fruit Maturity. *Journal of Wine Research*, 19:69-80, 2008.

[34] L. Moy, T. Tan, and J.W. Gardner. Monitoring the stability of perfume and body odours with an electronic nose. *Perfumer & Flavorish*, 19(4):11-16, 1994.

[35] B. Wilfrid Bourgeois, Anne-Claude Romain, Jacques Nicolas and Richard M. Stuetz. The use of sensor arrays for environmental monitoring: interests and limitations. *Environmental Monitoring*, 5:852-850, 2003.

[36] G. Dodd, P.N. Bartlett, and J.W. Gardner. Complex sensor systems: odour detection by the sense of smell and by electronic noses. *Biochemical Society Transactions*, 19(1):36-39, 1991.

[37] M.A. Craven, J.W. Gardner, and P.N. Bartlett. Electronic noses-development and future prospects. *Trends in analytical Chemistry*, 15(9):486-493, 1996.

[38] R. D. Erik. *Development of Calibration Standards for accurate measurements of geometry in microelectromechanical systems*.: Department of Electrical Engineering and Computer Science, Master of Science thesis, Department of Electrical Engineering and Computer Science, Massachusetts Institute of Technology, 1998.

[39] E.R. Thaler, F.C. Bruney, D.W. Kennedy, and C.W. Hanson. Use of an Electronic Nose to Distinguish Cerebrospinal Fluid from Serum. *Arch Otolaryngology Head & Neck Surgery*, 126(1):71-74, 2000.

[40] John R. Vig. Temperature-insensitive dual-mode resonant sensors – A review. *IEEE Sensors Journal*, 1(1):62-68, 2001.

[41] M. Penza and G. Cassano. Application of Principle Component Analysis and Artificial Neural Networks to recognize the individual VOCs of methanol/3-proponol in a binary mixture by SAW multi-sensor array. *Sensors and Actuators B*, 89(3):269-284, 2003.

[42] G.R. Jordan. Sensor technologies of the future. *Journal of Physics E: Scientific Instruments*, 18(9):729-735, 1985.

[43] Barry E. DeMartini, Jeffrey F. Rhoads, Steven W. Shaw, and Kimberly L. Turner. A single input–single output mass sensor based on a coupled array of microresonators. *Sensors and Actuators A*, 137(1):147-156, 2007.

[44] Barry E. DeMartini, Jeffrey F. Rhoads, Mark A. Zielke, Kyle G. Owen, Steven W. Shaw, and Kimberly L. Turner. A single input-single output coupled micro resonator array for the detection and identification of multiple analytes. *Applied Physics Letters,* 93: 054102-1-3, 2008.

[45] John R. Vig, Raymond L. Filler, and Yoonkee Kim. Chemical Sensor based on quartz microresonator. *Journal of Microelectromechanical Systems*, 5(2):138-140, 1996.

[46] A Gregory A. Sotzing, Jennifer N. Phend, Robert H. Grubbs, and Nathan S. Lewis. Highly Sensitive Detection and Discrimination of Biogenic Amines Utilizing Arrays of Polyaniline/ Carbon Black Composite Vapour Detectors. *Chemistry of Materials*, 12:592-595, 2000.

[47] Michael S. Freund and Nathan S. Lewis. A Chemically Diverse Conducting Polymer-Based "Electronic Nose". *Proc. Natl. Acad. Sci.*, 92:2652-2656, 1995.

[48] Jan Dijksterhuis and Robert A. Samson (Editors). *Food Mycology: A multifaceted Approach to Fungi and Food*, Mycology (volume 25): CRC press, Taylor & Francis Group, 2007.

[49] Navid Yazdi, Farrokh Ayazi, and Khalil Najafi. Micromachined Inertial Sensors. *Proceedings of the IEEE*, 86(8):1640-1659, 1998.

[50] Gao Daqi and Chen Wei. Simultaneous estimation of odour classes and concentrations using an electronic nose with function approximation model ensembles. *Sensors and Actuators B*, 120:584–594, 2007.

[51] M.S. Nayak, R. Dwivedi, and S.K. Srivastava. Application of iteration technique in association with multiple regression method for identification of mixtures of an integrated gas-sensor array. *Sensor and Actuators B*, 21:11-16, 1994.

[52] S. Capone, M. Epifani, F. Quaranta, P. Siciliano, A. Taurino, and L. Vasanelli. Monitoring of rancidity of milk by means of an electronic nose and a dynamic PCA analysis. *Sensors and Actuators B*, 78:174-179, 2001.

[53] G. Huyberechts, P. Szecowka, J. Roggen, and B.W. Licznerski. Simultaneous quantification of carbon monoxide and methane in humid air using a sensor array and an artificial neural network. *Sensor and Actuators B*, 45:123–130, 1997.

[54] A. Szczurek and M. Maciejewska. Relationship between odour intensity assessed by human assessor and TGS sensor array response. *Sensor and Actuators B*, 106:13-19, 2005.

[55] F. Liang Feng, Yongjun Liu, Xiaodong Zhou, and Jiming Hu. The fabrication and characterization of a formaldehyde odour sensor using molecularly imprinted polymers. *Journal of Colloid and Interface Science*, 284:378–382, 2005.

[56] Peter Hauptmann, Ralf Borngraeber, Jens Schroeder, and Joerg Auge. Application of Novel Sensor Electronics for Quartz Resonators in Artificial Tongue. *2000 IEEE/EIA International Frequency Control Symposium and Exhibition*, pp. 100-105, 2000.

[57] Karsten Boholt, Kjær Andreasen, Frans den Berg, and Thomas Hansen. A new method for measuring emission of odour from rendering plant using the Danish Odour Sensor System (DOSS) artificial nose. *Sensors and Actuators B*, 106:170-176, 2005.

[58] Rajendra Bunkar, Ram Asrey, K.D. Vyas, V.K. Rao, Sunil Kumar, A.R. Srivastava, and M.P. Kaushik. Polyepichlorohydrin modified quartz crystal microbalance sensor for sulphur mustard vapour detection. *Indian Journal of Science and Technology*, 3(2):139-142, 2010.

[59] Jones Edward Barry, White Neil M., Tudor John M., and Beeby Stephan P..
US Patent 7498721 - Resonant sensor assembly.
http://www.patentstorm.us/patents/7498721/description.html, Brunel University, 2009.

[60] Zheng Cui, Deyong Chen, and Shanhong Xia. Modelling and Experiment of a Silicon Resonant Pressure Sensor. *Analog Integrated Circuits and Signal Processing*, 32:29-35, 2002.

[61] Ville Kaajakari, Tomi Mattila, Antti Lipsanen, and Aarne Oja. Nonlinear Mechanical Effects in Silicon Longitudinal Mode Beam Resonators. *Sensors and Actuators A*, 120(1):64-70, 2005.

[62] G. Stemme. Resonant silicon sensors. *Journal of Micromechanics and Microengineering*, 1(2):113-125, 1991.

[63] M. Elwenspoek and R. Wiegerink. *Mechanical Microsensor*, Microtechnology and MEMS: Berlin, London Springer, 2001.

[64] W.T. Thomson and M.D. Dahleh. *Theory of Vibration and Applications*, 5th Edition: Prentice Hall, 1998.

[65] Clark T.-C. Nguyen and Roger T. Howe. Quality factor control for Micromechanical Resonators. *International Electron Devices meeting* (*IEDM)*, pp.505-508, 1992.

[66] X.M.H. Huang, C.A. Zorman, M. Mehregany, and M.L. Roukes. Quality Factors Issues in Silicon Carbide Nanomechanical Resonators. *The 12th International Conference an Solid State Sensors, Actuators and Microsystems,* IEEE, pp.722-725, 2003.

[67] Manu Agarwal, Saurabh A. Chandorkar, Rob N. Candler, Bongsang Kim, Matthew A. Hopcroft, Renata Melamud, Chandra M. Jha, Thomas W. Kenny, and Boris Murmann. Optimal drive condition for nonlinearity reduction in electrostatic microresonators. *Applied Physics Letters*, 89: 214105-1-3, 2006.

[68] Ville Kaajakari, Tomi Mattila, Aarne Oja, and Heikki Seppä. Nonlinear Limits for Single-Crystal Silicon Microresonators. *Journal of Microelectromechanical Systems*, 13(5):715-724, 2004.

[69] F. Ayela and T. Fournier. An experimental study of anharmonic micromachined silicon resonators. *Measurement Science and Technology*, 9:1821-1830, 1998.

[70] Qingfei Chen, Liang Huang, and Ying-Cheng Lai. Chaos-induced Intrinsic Localized Modes in Coupled Micro cantilever Arrays. *Applied Physics Letters*, 92:241914-1-3, 2008.

[71] R.M. Langdon. Resonator sensors -a review. *Journal of Physics E: Scientific Instruments*, 18(2): 103-115, 1985.

[72] Siavash Pourkamali, Akinori Hashimura, Reza Abdolvand, Gavin K. Ho, Ahmet Erbil, and Farrokh Ayazi. High-Q Single Crystal Silicon HARPSS Capacitive Beam Resonators With Self-Aligned Sub-100-nm Transduction Gaps. *Journal of Microelectromechanical Systems*, 12(4):487-496, 2003.

[73] J.E.-Y. Lee and A.A. Seshia. 5.4-MHz single-crystal silicon wine glass mode disk resonator with quality factor of 2 million. *Sensor and Actuators A*, 156:28-35, 2009.

[74] D. A. Hall and C.E. Millar (Editors). *Proceeding of Sensors and Actuators*, Manchester Business School (1996): IOM Communication Ltd, 1999.

[75] Murali K. Ghatkesar, V. Barwich, T. Braun, A.H. Bredekamp, U. Drechsler, M. Despont, H. P. Lang, M. Hegner, and Ch. Gerber. Real-Time Mass Sensing by Nanomechanical Resonators in Fluid. *Proceedings of the IEEE Sensors 2004*, 2:1060-1063, 2004.

[76] P. Mohanty, D.A. Harrington, K.L. Ekinci, Y.T. Yang, M.J. Murphy, and M.L. Roukes. Intrinsic Dissipation in high-frequency micromechanical resonators. *Physical Review B*, 66:1-15, 2002.

[77] Mustafa U. Demirci, Mohamed A. Ahdelmoneum and Clark T.-C. Nguyen. Mechanically Corner-Coupled Square Microresonator Array for reduced Series

Motional Resistance. *TRANSDUCERS '03, 12th International Conference on Solid-State Sensors, Actuators and Microsystems*, 2:955-958, 2003.

[78] Seungbae Lee and Clark T.-C. Nguyen. Mechanically-Coupled Micromechanical Resonator Arrays for Improved Phase Noise. *Proceedings of the 2004 IEEE International Frequency Control Symposium and Exposition, A Conference of the IEEE Ultrasonics, Ferroelectrics, and Frequency Control Society (UFFC-S)*, pp.144-150, 2004.

[79] John F. Lindner, Brian K. Meadows, and William L. Ditto. Array Enhanced Stochastic Resonance and Spatiotemporal Synchronization. *Physical Review Letters*, 75(1):3-6, 1995.

[80] M.E. Inchiosa and A.R. Bulsara. Signal Detection Statistics of Stochastic Resonators. *Physical Review E*, 53(3): 2021-2024, 1996.

[81] Dimitri Galayko, Andreas Kaiser, Lionel Buchaillot, Dominique Collard, Chantal Combi. Microelectromechanical Variable Bandwidth IF Frequency Filters with Tunable Electrostatical Coupling Spring. *Proceedings IEEE Sixteenth Annual International Conference on Micro Electro Mechanical Systems*, pp.153-156, 2003.

[82] Kun Wang and Clark T.-C. Nguyen. High-Order Medium Frequency Micromechanical Electronic Filters. *Journal of Microelectromechanical Systems*, 8(4):534-557, 1999.

[83] Siavash Pourkamali, and Farrokh Ayazi. Electrically coupled MEMS bandpass filters - Part I: With coupling element. *Sensors and Actuators A*, 122(2):307-316, 2005.

[84] Siavash Pourkamali, and Farrokh Ayazi. Electrically coupled MEMS bandpass filters - Part II: Without coupling element. *Sensors and Actuators*, 122(2):317-325, 2005.

[85] Chun-Sheng Ma, Yuan-Zhe Xu, Xin Yan, Zheng-Kun Qin, and Xian-Yin Wang. Optimization and Analysis of series-coupled microring resonator arrays. *Optics Communications*, 262(1):41-46, 2006.

[86] John A. Judge, Brian H. Houston, Douglas M. Photiadis, and Peter C. Herdic. Effects of disorder in one- and two-dimensional micromechanical resonator arrays for filtering. *Journal of Sound and Vibration*, 290:1119-1140, 2006.

[87] Maxim K. Zalalutdinov, Jeffrey W. Baldwin, Martin H. Marcus, Robert B. Reichenbach, Jeevak M. Parpia, and Brian H. Houston. Two-dimensional Array of Coupled Nanomechanical Resonators. *Applied Physics Letters*, 88(14):143504-1-3, 2006.

[88] Matthew Spletzer, Arvind Raman, Hartono Sumali and John P. Sullivan. Highly Sensitive Mass Detection and Identification using Vibration Localization in Coupled Microcantilevers Arrays. *Applied Physics Letters*, 92(11):114102-1-3, 2008.

[89] Matthew Spletzer, Arvind Raman, Alexander Q. Wu, and Xianfan Xu. Ultrasensitive Mass Sensing using Mode Localization in Coupled Microcantilevers. *Applied Physics Letters*, 88(25): 254102-1-3, 2006.

[90] Eyal Buks and Michael L. Roukes. Electrically Tunable Collective Response in a Coupled Micromechanical Array. *Journal of Microelectromechanical Systems*, 11(6):802-807, 2002.

[91] M. Sato, B. E. Hubbard, and A. J. Sievers. Observation of Locked Intrinsic Localized Vibrational Modes in a Micromechanical Oscillator Array. *Physical Review Letters*, 90(4): 044102-1-4, 2003.

[92] F. Roman, S. Dirk, D. Wolfram, and M. Jan. Tunable Frequency Selective Vibration Detection with MEMS Force Coupled Oscillators. *EUROSENSORS XXII*, pp.1573-1576, 2008.

[93] Rajeev J. Ram, Ralph Sporer, Hans-Richard Blank, and Robert A. York. Chaotic Dynamics in Coupled Microwave Oscillators. *IEEE Transactions on Microwave Theory and Techniques*, 48(11):1909-1916, 2000.

[94] Yu-Wei Lin, Sheng-Shian Li, Zeying Ren, and Clark T.-C. Nguyen. Low Phase Noise Array-Composite Micromechanical Wine Glass Disk Oscillator. *IEEE International Electron Devices Meeting, 2005 IEDM - Technical Digest*, pp.278-281, 2005.

[95] Hiroyuki Fujita. Microactuators and micromachines. *Proceedings of the IEEE*, 86(8):1721-1732, 1998.

[96] Clark T.-C. Nguyen, and Roger T. Howe. An Integrated CMOS Micromechanical Resonator High-Q Oscillator. *IEEE Journal of Solid-State Circuits*, 34(4):440-455, 1999.

[97] Brian D. Jensen, , Senol Mutlu, Sam Miller, Katsuo Kurabayashi, and James J. Allen. Shaped Comb Fingers for Tailored Electromechanical Restoring Force. *Journal of Microelectromechanical Systems*, 12(3):373-383, 2003.

[98] Wenjing Ye, Subrata Mukherjee, and Noel C. MacDonald. Optimal Shape Design of an Electrostatic Comb Drive in Microelectromechanical Systems. *Journal of Microelectromechanical Systems*, 7(1):16-26, 1998.

[99] Wenjing Ye and Subrata Mukherjee. Optimal Shape Design of Three-dimensional MEMS with Applications to Electrostatic Comb drives. *International Journal of Numerical Methods in Engineering*, 45(2):175-194, 1999.

[100] Rob Legtenberg, A.W. Groeneveld and M. Elwenspoek. Comb-drive actuators for large displacements. *Journal of Micromechanics and Microengineering*, 6(3):320-329, 1996.

[101] Walied A. Moussa, Hesham Ahmed, Wael Badawy, and Medhat Moussa. Investigating the reliability of electrostatic comb-drive actuators utilized in microfluidic and space systems using finite element analysis. *Canadian Journal of Electrical and Computer Engineering*, 27(4):195-200, 2002.

[102] Toshiki Hirano, Tomotake Furuhata, Kaigham J. Gabriel, and Hiroyuki Fujita. Design, Fabrication, and Operation of Submicron Gap Comb-Drive Microactuators. *Journal of Microelectromechanical Systems*, 1(1):52-59, 1992.

[103] David Elata and Vitaly Leus. How slender can comb drive fingers be?. *Journal of Micromechanics and Microengineering*, 15(5):1055-1059, 2005.

[104] John D. Grade, Hal Jerman, and Thomas W. Kenny. Design of Large Deflection Electrostatic Actuators. *Journal of Microelectromechanical Systems*, 12(3): 335-343, 2003.

[105] Chihchung Chen, and Chengkuo Lee. Design and Modelling for comb drive actuator with enlarged static displacement. *Sensors and Actuators A*, 115(2-3):530-539, 2004.

[106] Kun Wang, Ark-Chew Wong, and Clark T.-C. Nguyen. VHF Free-free Beam High-Q Micromechanical Resonators. *Journal of Microelectromechanical Systems*, 9(3):347-360, 2000.

[107] Guangya Zhou and Philip Dowd. Tilted folded-beam suspension for extending the stable travel range of comb-drive actuators. *Journal of Micromechanics and Microengineering*, 13(2):178-183, 2003.

[108] M.A. Rosa, S. Dimitrijev, and H.B. Harrison. Enhanced electrostatic force generation capability of angled comb finger design used in electrostatic comb-drive actuators. *Electronics Letters*, 34(18):1787-1788, 1998.

[109] M.A. Rosa, S. Dimitrijev, and H.B. Harrison. Improved operation of micromechanical comb drive actuators through the use of a new angled comb finger design. *Journal of Intelligent Material Systems and Structures*, 9(4):283-290, 1998.

[110] Chris S.B. Lee, Sejin Han and Noel C. MacDonald. Single crystal silicon (SCS) XY-stage fabricated by DRIE and IR alignment. *Proceedings IEEE Thirteenth Annual International Conference on Micro Electro Mechanical Systems*, pp.28-33, 2000.

[111] Andryas Mawardi and Ranga Pitchumani. Design of Microresonators Under Uncertainty. *Journal of Microelectromechanical Systems*, 14(1):63-69, 2005.

[112] Scott G. Adams, Fred M. Bertsch, Kevin A. Shaw, Peter G. Hartwell, Noel C.MacDonald, and Francis C. Moon. Capacitance Based Tunable Micromechanical Resonators. *International Conference on Solid-State Sensors and Actuators, and Eurosensors IX, Proceedings*, 1:438-441, 1995.

[113] Allen Dewey, Hong Ren, and Tianhao Zhang. Behavioural Modelling of Microelectromechanical Systems (MEMS) with Statistical Performance-Variability Reduction and Sensitivity Analysis. *IEEE Transactions On Circuits And Systems, Analog And Digital Signal Processing*, 47(2):105-113, 2000.

[114] Shyam Praveen Vudathu, Kishore Kumar Duganapalli, Rainer Laur, Dorota Kubalinska, and Angelika Bunse Gerstner. Parametric Yield Analysis of MEMS Via Statistical Methods. *DTIP of MEMS & MOEMS*, 2006.

[115] Jonathan W. Wittwer, Michael S. Baker, and Larry L. Howell. Robust Design and Model Validation of Nonlinear Compliant Micromechanisms. *Journal of Microelectromechanical Systems*, 15(1):33-41, 2006.

[116] Christoph Germer, Ulli Hansen, Hans-Joachim Franke, and Stephanus Buttgenbach. Computer Aided Tolerance Analysis and Synthesis in Micro Systems (ToAST). *Analog Integrated Circuits and Signal Processing*, 40(2):131-140, 2004.

[117] Irina Codreanu, A. Martowicz, and T. Uhl. Influence of Uncertain Parameters on the Performance of A Micro-Comb Resonator. *19th Micromechanics Europe Workshop*, 2008.

[118] Guchuan Zhu, Julien Penet, and Lahcen Saydy. Robust Control of an Electrostatically Actuated MEMS in the Presence of Parasitic and Parametric Uncertainties. *Proceedings of the 2006 American Control Conference*, pp.1233-1236, 2006.

[119] Dana Weinstein, Sunil A. Bhave, Masahiro Tada, Shun Mitarai, Shinya Morita, and Koichi Ikeda. Mechanical Coupling of 2D Resonator Arrays for MEMS Filter Application. *Proceedings of the IEEE International Frequency Control Symposium and Exposition,* pp.1362-1365, 2007.

[120] Luca Schenato, Wei-Chung Wu, Laurent El Ghaoui and Kristofer Pister. Process Variation Analysis for MEMS Design. *Proceedings of the SPIE - The International Society for Optical Engineering*, 4239:272-279, 2001.

[121] Raj K. Gupta. Electronically probed measurements of MEMS geometries. *Journal of Microelectromechanical Systems*, 9(3):380-389, 2000.

[122] Jonathan W. Wittwer, Troy Gomm and Larry L. Howell. Surface micromachined force gauges: uncertainty and reliability. *Journal of Micromechanics and Microengineering*, 12(1):13-20, 2002.

[123] J. Li, A.Q. Liu, and Q.X. Zhang. Tolerance Analysis for comb-drive actuator using DRIE Fabrication. *Sensors and Actuators A*, 125(2):494-503, 2006.

[124] Yoon Shik Hong, Jong Hyun Lee and Soo Hyun Kim. A laterally driven symmetric micro-resonator for gyroscopic applications. *Journal of Micromechanics and Microengineering*, 10(3):452-458, 2000.

[125] Nor Hayati Saad, Xueyong Wei, Carl Anthony, Hossein Ostadi, Raya Al-Dadah, and Michael C.L. Ward. Impact of Manufacturing Variation on the performance of Coupled Micro Resonator Array for Mass Detection Sensor. *Procedia Chemistry*, 1(1): 831-834, 2009.

[126] National Instruments Corporation. NI BNC-2110: Shielded Connector Block with BNC for X Series and M Series. *http://sine.ni.com/nips/cds/view/p/lang/en/nid/1865*, 2009.

[127] National Instruments Corporation. NI PCI-6133: 14-Bit, 2.5 MS/s/ch, Simultaneous Sampling Multifunction DAQ. *http://sine.ni.com/nips/cds/view/p/lang/en/nid/201937*, 2009.

[128] National Semiconductor Corporation. LMC6084: Precision CMOS Quad Operational Amplifier. *http://www.national.com/mpf/LM/LMC6084.html#Overview*, 2004.

[129] One Technology Way, Analog Devices, USA. Low Cost Low Power Instrumentation Amplifier AD620. *http://www.mit.tut.fi/MIT-1016/AD620.pdf*, 2004.

[130] Canon Inc., Japan. *Canon Mask Aligner PLA-501FA Operation Manual (PUB.B-1E-3001F)*: 2008 (Accessed).

[131] Jurgen H. Daniel. *Micromachining Silicon for MEMS*: MTP, D.F.MooreTrinity Hall, 1999.

[132] Delta Mask, the Netherlands. Services & Equipment. *http://www.deltamask.nl/frames.html*, 2008 (Accessed).

[133] Julien Arcamone, Gemma Rius, Gabriel Abadal, Jordi Teva, Nuria Barniol, and Francesc Perez-Murano. Micro/nanomechanical resonators for distributed mass sensing with capacitive detection. *Microelectronic Engineering*, 83(4-9):1216-1220, 2006.

[134] William T. Thomson and Marie Dillon Dahleh. *Theory of Vibrations with Applications*, 5th Edition: Prentice Hall, 1998.

[135] K.H. Low. Closed-Form Formulas for Fundamental Vibration Frequency of Beams Under Off-Centre Load. *Journal of Sound and Vibration*, 201(4):528-533, 1997.

[136] Robert D. Blevins. *Formulas for Natural Frequency and Mode Shape*: Van Nostrand Reinhold, 1979.

[137] William T. Thomson. *Theory of Vibration with Applications*, 3rd Edition: Allen & Unwin, 1988.

[138] COMSOL, COMSOL Multiphysics. *Structural Mechanics Module User's Guide*: Version 3.4, 2007.

[139] M. Naseer, Th. Bechteler, M. Parlak and Y. Gurbuz. Coupling Spring Design and Insertion Loss Minimization of Second Order Microelectromechanical Filters. *Nanotech 2003*, 1:388-391, 2003.

[140] Yasar Gurbuz, Mustafa Parlak, Thomas F. Bechteler, and Ayhan Bozkurt. An Analytical Design Methodology for Microelectromechanical (MEM) filters. *Sensors and Actuators A*, 119(1):38-47,2005.

[141] Didem Ozevin, Stephen Pessiki, Akash Jain, David W. Greve, and Irving J. Oppenheim. Development of a MEMS Device for Acoustic Emission Testing. *Proceedings of the SPIE - The International Society for Optical Engineering*, 5057:64-74, 2003.

[142] J.M. Haemer, S.K. Sitaraman, D.K. Fork, F.C. Chong, S. Mok, D.L. Smith, and F. Swiatowiec. Flexible Micro-Spring Interconnects for High Performance Probing. *2000 Proceedings, 50th Electronic Components and Technology Conference*, pp.1157-1163, 2000.

[143] Kyu-Yeon Park, Chong-Won Lee, Yong-Su Oh, and Young-Ho Cho. Laterally oscillated and force-balanced micro vibratory rate gyroscope supported by fish hook shape springs. *Sensor and Actuators A*, 64(1):69-76, 1998.

[144] Nor Hayati Saad, Raya K. Al-Dadah, Carl J. Anthony, and Michael C.L. Ward. Analysis of MEMS Mechanical Spring for Coupling Multimodal Micro Resonators Sensor. *Microelectronic Engineering*, 86(4-6):1190-1193, 2009.

[145] P.J. Stephanou, G. Piazza, C. D. White, M.B.J. Wijesundara, and A.P. Pisano. Design of Novel Mechanical Coupling for Contour Mode Piezoelectric RF MEMS Filter. *Journal of Physics: Conference Series*, 34(1):342 - 349, 2006.

[146] COMSOL, COMSOL Multiphysics. *MEMS Module Model Library*: Version 3.4, pp. 44-53, 2007.

[147] Isabelle P.F. Harouche, and C. Shafai. Comb Drive. *MEMS Module - Model Library*: COMSOL, 2007.

[148] M. Leonard. *Elements of Vibration Analysis*, 2nd Edition: McGraw-Hill, 1986.

[149] Nor Hayati Saad, Carl J. Anthony, Raya Al-Dadah, Michael C.L. Ward. Exploitation of Multiple Sensor Arrays in Electronic Nose. *2009 IEEE Sensors*, pp.1575-1579, 2009.

[150] INTEGRAM Deep Protyping Kit. *SOI Micromachining Design Handbook*, Revision 2nd Edition: Qinetiq Ltd, Coventor Sarl, 2004.

[151] 3 EM Calibration Standard: SIRA Calibration Specimens (S212). *http://www.taab.co.uk/pdf-details/5_taab_sections_1204015335.pdf*, 2008 (Accessed).

[152] P.T. Docker, P. Kinnell, and M.C.L. Ward. A dry single-step process for the manufacture of released MEMS structures. *Journal of Micromechanics and Microengineering*, 13(5):790-794, 2003.

[153] Rob M. C. Mestrom, Rob H. B. Fey, and Henk Nijmeijer. Phase Feedback for Nonlinear MEM Resonators in Oscillator Circuits. *IEEE/ASME Transactions on Mechatronics*, 14(4):423-433, 2009.

[154] Danny Banks. *Microengineering, MEMS, and Interfacing: A Practical Guide*: CRC Press, Taylor and Francis Group, 2006.

[155] Gary K. Fedder. MEMS Fabrication. *ITC International Test Conference, IEEE*, pp.691-698, 2003.

[156] CNS and L.Xie. Overview of Photolithography. *http://www.cns.fas.harvard.edu/facilities/Cleanroom/Report/Optical%20Lithography.pdf*, 2005.

[157] B. Stark and W.C. Tang. Chapter 5: MEMS Device Processing. *http://parts.jpl.nasa.gov/docs/JPL%20PUB%2099-1E.pdf* , pp.69-90, 2008.

[158] Zonghe Lai and Johan Liu. Chapter A: Wire Bonding. *http://extra.ivf.se/ngl/A-WireBonding/ChapterA.htm*, 2009.

[159] J.D. Minford. *Handbook of Aluminium Bonding Technology and Data*: Taylor & Francis Inc., 1993.

[160] George L.S. and Ralph S.K. Aluminium Metallization - Advantages and Limitations for Integrated Circuit Applications. *Proceedings of The IEEE*, 57(9):1570-1580, 1969.

[161] CSB02488. *http://www.spectrum-semi.com/products/private/drawings/CSB02488.pdf*, 2007.

[162] D. Scheibner, J. Mehner, D. Reuter, T. Gessner, and W. Dotzel. A spectral vibration detection system based on tunable micromechanical resonators. *Sensors and Actuators A*, 123-124:63-72, 2005.

[163] Carl J. Anthony, and Ross Turnbull. A MEMS Resonator with differential drive and readout: fabrication, theory and Q-control. *Second STIMESI Workshop on MEMS and Microsystems Research and Teaching, Berlin-Brandenburg Academy of Sciences and Humanities, Germany*, 2008.

[164] Clark T.-C. Nguyen, and Roger T. Howe. CMOS Micromechanical Resonator Oscillator. *Technical Digest - International Electron Devices Meeting (IEDM)*, pp. 199-202, 1993.

[165] A.R. Klempner, R.T. Marinis, P. Hefti, and R.J. Pryputniewicz. Experimental determination of the Q-factors of microcantilevers coated with thin metal films. *Strain*, 45:295-300, 2009.

[166] J. Meltaus, P. Hämäläinen, M.M. Salomaa, and V.P. Plessky. Genetic Optimization Algorithms in the Design of Coupled SAW Filters. *IEEE International Ultrasonics, Ferroelectrics, and Frequency Control Joint 50th Anniversary Conference*, 3:1901-1904, 2004.

[167] Bjorn Lindmark, Peter Slattman, and Anders Ahlfeldt. Genetic algorithm optimization of cylindrical reflectors for aperture-coupled patch elements. *IEEE Antennas and Propagation Society International Symposium*, pp.442-445, 1999.

[168] Min Liu, Kurt Maute, and Dan M. Frangopol. Multi-objective design optimization of electrostatically actuated microbeam resonators with and without parameter uncertainty. *Reliability Engineering and System Safety*, 92(10):1333-1342, 2007.

[169] B.L. Ki, and C. Young-Ho. Frequency tuning of a laterally driven microresonator using an electrostatic comb array of linearly varied length. *International Conference on Solid-State Sensors and Actuators*, Chicago, 1997.